

PhD Thesis

2017

Constitutive modelling of soils and fibre-reinforced
soils

Thomas A. Bower

Under the supervision of Tony Jefferson and Peter Cleall



Abstract

This thesis covers two major themes: the first relates to the development of a constitutive soil model, and the second is the development of a model to predict the behaviour of fibre-reinforced soils.

The hardening soil (HS) model is an advanced constitutive plasticity model which is applicable to the analysis of many soil types including sands and clays (Schanz et al., 1999; Benz, 2007). This model is explored in depth, and several improvements to the model are proposed. The first improvement is the formulation of a new hardening shear yield surface to replace the previous hardening shear surface and failure surface. The second is the implementation of the model in a robust return mapping scheme. The scheme used is the closest point projection method of Simo and Hughes (2006), which is tailored specifically to this implementation of the model. This constitutive soil model and return mapping scheme is hereinafter referred to as the HS-LC model.

The HS-LC model is then used in finite element analyses and compared to published experimental and predicted data obtained from the prior versions of the HS model. It was found that the new HS-LC model was able to reproduce results from both the experimental data and the previous models. The numerical stability of the proposed model was also tested with a step size study, a mesh density study, and investigation of convergence rates for simulations.

The second main theme of this thesis is fibre-reinforced soils. The motivation for reinforcing soils is first explored, then a literature review is conducted on different reinforcement types; focussing on fibre-reinforcement. Experimental results from the literature are then discussed, along with several models which predict the behaviour of fibre-reinforced soil.

Results from an experimental study (Chatzopoulos, 2015; Wang, 2015) of fibre-reinforced sand are presented and discussed. A series of triaxial compression tests were conducted; in which fibre content, fibre length, and fibre type were varied. It

was found that some fibre types added a significant amount of strength to the soil, where other types added little strength. All fibres studied here were manufactured from polypropylene, it was therefore concluded that the geometry had a significant impact on the strength contribution for the composite. This study also found that when the fibre diameter was too large or too fine relative to the sand particle size, then the particles would not bind to the fibre. An additional unique study was also carried out in relation to fibre composites. This was a series of fibre pullout tests, where a fibre was pulled through a prescribed length of compressed, dry soil. In this test it was found that the peak bond strength was linked to the compressive stress acting on the fibre.

A novel fibre-soil composite model was also formulated which is based on micro-mechanical relationships between soil and fibre, from findings of the literature review and the experimental study. The proposed model is based on the well known shear lag model (Cox, 1952) and is modified to also include the effects of fibre debonding. The model takes the form of a representative volume element (RVE), which is homogenised using a statistical approach (Bažant and Oh, 1986). The proposed fibre model is then combined with the new HS-LC model using the rule of mixtures. The composite model is then used to predict the behaviour of the tests in the experimental study. Predictions of the triaxial tests closely matched the experimental results in the shear stress response, however, were less accurate for the prediction of volumetric strains. It was concluded that further work is required in the development of this model before it can be considered in routine design.

Contents

1	Introduction	1
1.1	Objectives of this thesis	2
1.2	Thesis structure	3
1.3	Finite element analysis	4
1.4	Behaviour of soils	10
1.5	Reinforcement of soils	13
1.6	Sign convention	16
1.7	Tensor and invariant definitions	17
2	The hardening soil model	19
2.1	Model parameters	21
2.1.1	Stiffness parameters	21
2.1.2	Failure parameters	24
2.1.3	Dilatancy	25
2.2	Hardening shear yield surface	29
2.2.1	Shear surface in the original HS model	30
2.2.2	Shear surface in the HS-smooth model	33
2.3	Hardening cap surface	34
2.3.1	Cap surface in original HS model	34
2.3.2	Cap surface in the HS-smooth model	36
2.4	Failure criteria	38
2.4.1	Mohr-Coulomb criterion	38
2.4.2	Matsuoka-Nakai criterion	40
2.5	Tension limit	41
2.6	Other contributions to the HS model	41

3	A robust implementation of the HS model	43
3.1	Motivation	43
3.2	Changes to the shear yield surface	45
3.3	Changes to the cap yield surface	52
3.4	Tension yield surface	52
3.5	Summary of the proposed model	54
3.6	Auxiliary parameters	55
3.7	Summary of parameters in the HS-LC model	57
3.8	The closest point projection method	57
3.8.1	CPP algorithms	60
3.8.2	Consistent tangent matrix	68
3.8.3	Return strategy	69
3.9	Stiffness update	71
4	HS-LC model validation	75
4.1	Oedometer tests	76
4.2	Triaxial tests	85
4.3	Circular footing	94
4.4	Leesburg footing	102
5	A literature review on fibre-reinforced soils	111
5.1	Experimental studies	112
5.2	Previously proposed soil-fibre models	115
5.2.1	Statistical distribution model with shear strength increase . .	115
5.2.2	Energy-based homogenisation method	120
5.2.3	Fibre contribution matrix with empirical debonding	122
5.2.4	Fibre pullout model in clay	127
5.2.5	Shear lag soil model	129
5.2.6	Summary of soil-fibre models	133
6	Experimental program	135
6.1	Material properties	136

6.1.1	Leighton Buzzard sand	136
6.1.2	Fibres	137
6.2	Testing setup and procedures	139
6.2.1	Triaxial tests	139
6.2.2	Fibre pullout tests	140
6.2.3	Sample dissection	142
6.3	Experimental results	143
6.3.1	Triaxial tests	143
6.3.2	Fibre pullout tests	150
6.3.3	Sample dissection	151
7	A new soil-fibre model	155
7.1	A finite element study of soil-fibre interaction	156
7.1.1	Elastic soil and fully bonded fibre	158
7.1.2	Elasto-plastic soil and fully bonded fibre	160
7.2	Model formulation	163
7.2.1	Behaviour of a single fibre	163
7.2.2	Fully bonded fibre	165
7.2.3	Debonding fibre	168
7.2.4	Comparison with finite element study	173
7.3	Homogenisation	175
7.3.1	Fibre radius of influence	175
7.3.2	Fibre orientation distribution	177
7.4	Parametric study	183
7.4.1	Shear radius R/r_f	185
7.4.2	Fibre modulus E_f	190
7.4.3	Fibre volume fraction v_f	190
7.4.4	Slip stiffness k_s	190
7.4.5	Fibre length l_f	190
7.4.6	Fibre radius r_f	191
7.4.7	Orientation exponent n	191

7.4.8	Bond strength κ_b	191
7.4.9	Residual strength κ_r (debonded)	192
7.4.10	Fibre modulus E_f (debonded)	192
7.4.11	Fibre volume fraction v_f (debonded)	192
7.4.12	Fibre length l_f (debonded)	192
8	Fibre model validation	195
8.1	Unreinforced triaxial tests	195
8.2	Triaxial fibre concentration study	198
8.3	Triaxial fibre type study	199
8.4	Triaxial fibre length study	203
8.5	Triaxial sample preparation study	207
9	Conclusions	213
9.1	Future work	216
	Bibliography	219
	Nomenclature	231
	CPP algorithms	239

Chapter 1

Introduction

Civil engineering is a discipline which covers the design and construction of buildings, bridges, railways, highways, tunnels, irrigation systems and many more. Every one of these structures is either built resting on soil, constructed within soil, or composed of soil. It is therefore vital that the behaviour of soil is fully understood, and can be predicted accurately in the design process of these structures.

This thesis explores two main topics; the first is the constitutive modelling of soil, and the second is the behaviour of fibre-reinforced soil. This work uses many previously defined theories such as the finite element method, plasticity, models for different aspects of soil behaviour, and composite theory. Due to the diverse nature of this thesis, each theme exploited is introduced in this chapter. More detailed background to each theme can be found later in the thesis. The first main goal of this work is to improve an existing constitutive soil model, particularly focusing on its robustness. The second goal of this work is to produce a new model to describe the behaviour of fibre reinforced soils, which is used in conjunction with the proposed constitutive soil model.

For many soil design problems, it may be sufficient to use derived analytical methods, such as Terzaghi's formulae for calculating the bearing capacity of shallow foundations (Terzaghi et al., 1996), and the analysis of slope stability problems using Bishop's, or the Swedish method of slices (Craig, 2004). More complex prob-

lems, to which such models are not applicable, require a more generalised approach. Complexities here may include difficult geometry, abnormal loading conditions, and different soil behaviours. Finite element analysis is one such method which can be used to capture the behaviour of soils in a wide range of geotechnical design problems.

1.1 Objectives of this thesis

The main themes of this thesis are the constitutive modelling of soils, analysis with the finite element method (FEM), and reinforcement of soils. The main goals of this thesis are to produce an improved version of an existing constitutive soil model (the hardening soil model), and a new model to describe the behaviour of fibre-reinforced soil. These main goals are to be attained with the following objectives:

- To evaluate an existing advanced constitutive soil model, known as the hardening soil (HS) model
- To clarify some of the implementational aspects of the HS model
- To reformulate the HS model in order to improve both its performance and numerical robustness
- To validate the accuracy and assess the performance of the improved HS model by comparing to experimental results and predictions using the previous versions of the model
- To investigate the behaviour of soil-fibre composites through a review of experimental studies
- To evaluate the current state of existing models which predict the behaviour of fibre-reinforced soils
- To document and interpret results from an experimental study of fibre-reinforced soils

- To develop a new constitutive model for the prediction of the behaviour of soil reinforced with short fibres
- To validate the accuracy of the proposed soil-fibre model by comparing predicted results to experimental results

1.2 Thesis structure

- Chapter 1 - A basic overview of FEM and geotechnical engineering in general, standard definitions for various parameters are also defined
- Chapter 2 - An in-depth overview of the HS model is conducted, including its modification by several authors
- Chapter 3 - Issues with the previous version of the HS model are identified and resolved, the proposed HS-LC model is described fully, and an implicit return mapping procedure is described
- Chapter 4 - The proposed HS-LC model is used in several analyses, and results are compared with published experimental results, and published results from prior versions of the HS model
- Chapter 5 - A literature review on fibre-reinforced soils is conducted, with consideration for both experimental and modelling work
- Chapter 6 - Experimental work on fibre-reinforced soils from two MSc projects which the author co-supervised is documented, this includes triaxial testing, investigation of fibre pullout behaviour, and dissection of prepared samples
- Chapter 7 - The interaction between soil and fibre is investigated further through a finite element study, and a new soil-fibre composite model is formulated based on micro-mechanical interactions and findings from the literature review, experimental study, and finite element study

- Chapter 8 - The proposed soil-fibre composite model is combined with the HS-LC model, and results are compared with the experimental study
- Chapter 9 - Conclusions are made on both the performance of the HS-LC model and the proposed soil-fibre model, and potential future work is discussed

The remainder of this chapter provides a basic overview of finite elements, soil plasticity, and soil reinforcement. More detailed background material specific to the objectives of this thesis is described in Chapters 2 and 5.

1.3 Finite element analysis

The finite element method (FEM) is a powerful analysis tool, which is highly adaptable for a variety of applications including stress-strain analysis (Owen and Hinton, 1980; Zienkiewicz and Taylor, 2000), fluid dynamics (Reddy and Gartling, 2010), heat transfer (Lewis et al., 1996; Reddy and Gartling, 2010), and viscosity (Owen and Hinton, 1980; Gunzburger, 2012).

The purpose of FEM is to provide a framework for which to base simple governing equations, and apply them to complex problems which would be otherwise unsolvable using conventional calculations. Perhaps the simplest example of finite elements is the one dimensional spring model, which relates the force applied to the end of a spring to the extension of the spring, through a linear stiffness constant. In the finite element method, this same relationship applies, albeit with many more degrees of freedom:

$$\mathbf{F} = \mathbf{k}\mathbf{u} \tag{1.1}$$

where \mathbf{F} represents a vector of forces applied to a system, \mathbf{u} is the vector of displacements for each degree of freedom in the system, and the matrix \mathbf{k} represents the stiffness of each degree of freedom and is related to the geometric and material

properties of the system.

There are many types of finite elements which can be used to model various problems. The relationship between forces and displacements are different for each type of finite element, due to their varying boundary conditions. Continuous structures such as soils can be analysed using a selection of continuum elements:

- Plane strain - This two-dimensional element type is suitable for modelling geometries which are effectively infinite in one direction (Figure 1.1), such that strains are only transferred in one plane. Tangential to this plane, stresses develop due to material surrounding both sides of the plane. Examples of problems suited to this element type are embankments, earth dams, strip footings, and tunnels.
- Axisymmetric - This element is used for modelling circular geometry with a two-dimensional mesh (Figure 1.2). Typically, analyses are performed on one unit radian, and the axis of symmetry must be defined. Examples of uses of this element are soil triaxial tests, soil oedometer tests, circular footings, and single pile foundations.
- General stress space - This three-dimensional element type can be used for any given soil problem where the geometry cannot be approximated by one of the aforementioned element types (Figure 1.3). This type of element is typically reserved for more complex design work.

For many materials, the relationship between force and displacement is more complex than the basic Hookean relationship (Equation 1.1). Plasticity, time dependent behaviour, and coupling effects each require more complex models to capture the required behaviour. One of the main aspects of this thesis is plasticity in soils; here it is required that the relationship between stress and strain is appropriately defined. Once this ‘constitutive model’ is defined, then the stresses and strains can be translated into forces and displacements and used in the global solution algorithm.

Stress in a material is comprised of several independent components, which repre-

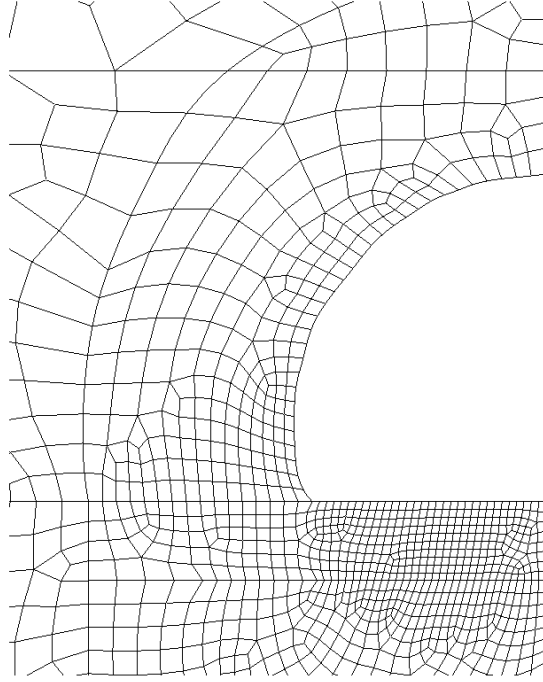


Figure 1.1: Plane strain mesh used to model a tunnel

sent the direct and shear stresses on each orthogonal Cartesian plane. The stress tensor for full three-dimensional space is given by Equation 1.2. In the two-dimensional cases, several of these components are not present; for example, in the plain strain case, $\sigma_{xz} = \sigma_{zx} = \sigma_{yz} = \sigma_{zy} = 0$ and $\varepsilon_z = \varepsilon_{xz} = \varepsilon_{zx} = \varepsilon_{yz} = \varepsilon_{zy} = 0$.

$$\boldsymbol{\sigma} = \begin{bmatrix} \sigma_x & \sigma_{xy} & \sigma_{xz} \\ \sigma_{yx} & \sigma_y & \sigma_{yz} \\ \sigma_{zx} & \sigma_{zy} & \sigma_z \end{bmatrix} \quad (1.2)$$

To determine if a material is yielding according to a particular material model, it is common to describe this stress tensor in terms of simple and meaningful measures, for example, the mean stress p , or the shear stress q ; these are defined in Section 1.7. These terms are known as invariants of stress, as they do not change when the stress coordinate axis is rotated.

These stress invariants can be used to detect yielding in materials. The von Mises material model (as described by Owen and Hinton (1980) and shown in Figure 1.4a)

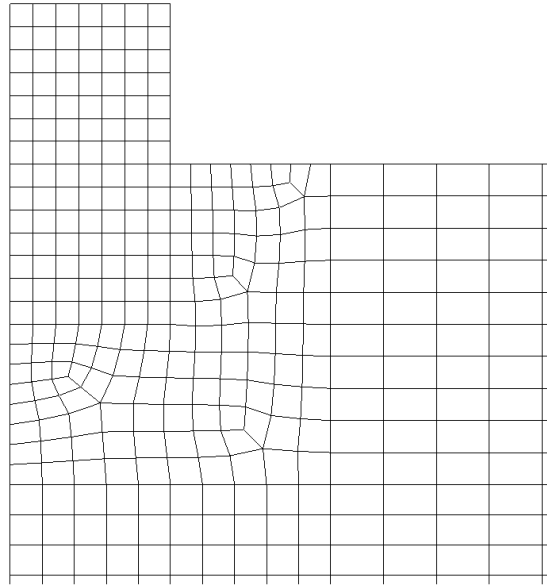


Figure 1.2: Axisymmetric mesh used to model a circular footing

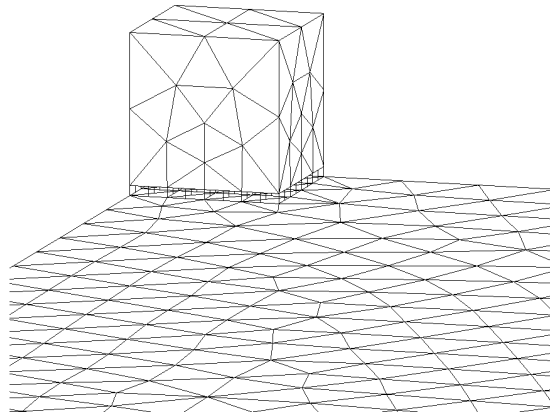


Figure 1.3: Three-dimensional mesh used to model a square footing

places a limit on the shear stress. The yield criterion for the von Mises model is given by

$$f_{VM} = q - \sigma_y \quad (1.3)$$

where σ_y is a material parameter defining the yield strength of the material. The Drucker-Prager model (Drucker et al., 1952), shown in Figure 1.4b, also takes the mean stress into account, such that the shear yield limit increases along with the compressive stress. The yield function for the Drucker-Prager model is given by

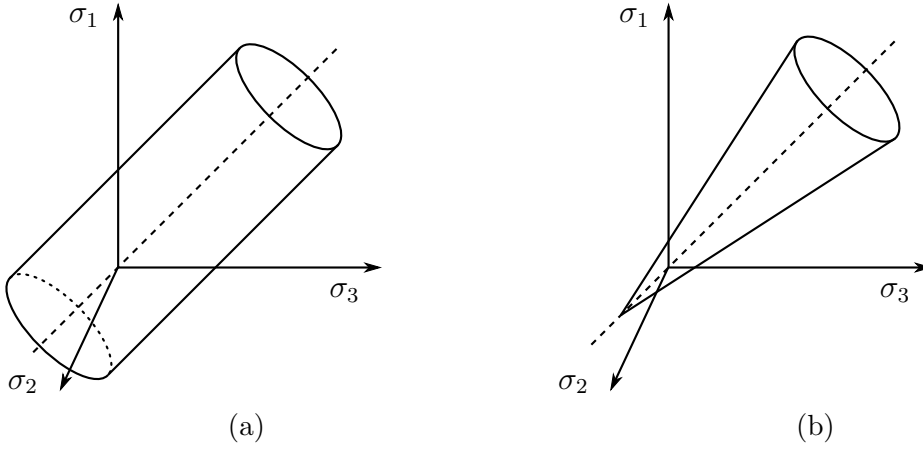


Figure 1.4: Yield surfaces for von Mises (a) and Drucker-Prager (b) plasticity models, the dashed line represents the line $\sigma_1 = \sigma_2 = \sigma_3$

$$f_{DP} = q + \frac{6 \sin \varphi}{3 - \sin \varphi} (p + c \cot \varphi) \quad (1.4)$$

where φ is the friction angle, which relates to the internal friction between soil particles, and describes the rate at which the shear strength increases with the mean stress; and c is the cohesion, which describes the inter-particle bonding of soils, and controls the position of the apex of the yield surface.

The von Mises yield surface (Figure 1.4a) is a cylinder in the three-dimensional stress space because the criterion is based on the shear stress q only. The radius of the cylinder is equal to the yield stress σ_y . With the Drucker-Prager surface (Figure 1.4b), the radius of the yield surface is dependent on the mean stress p .

If the yield function, e.g. f_{VM} , is negative, then the material is said to be in an elastic state; if f_{VM} is equal to zero then the current stress state is on the yield surface. The yield function defines the allowable boundaries of stress, therefore $f_{VM} > 0$ would represent an illegal stress state. Some material models allow hardening of the yield surface. This is where the yield surface grows according to some pre-defined component of plastic strain, for example, the plastic shear strain can be used as a hardening variable in the von Mises model.

The hardening gradient describes the rate at which the plastic strains expand or contract the yield surface. Figure 1.5 shows an example load path for a hardening

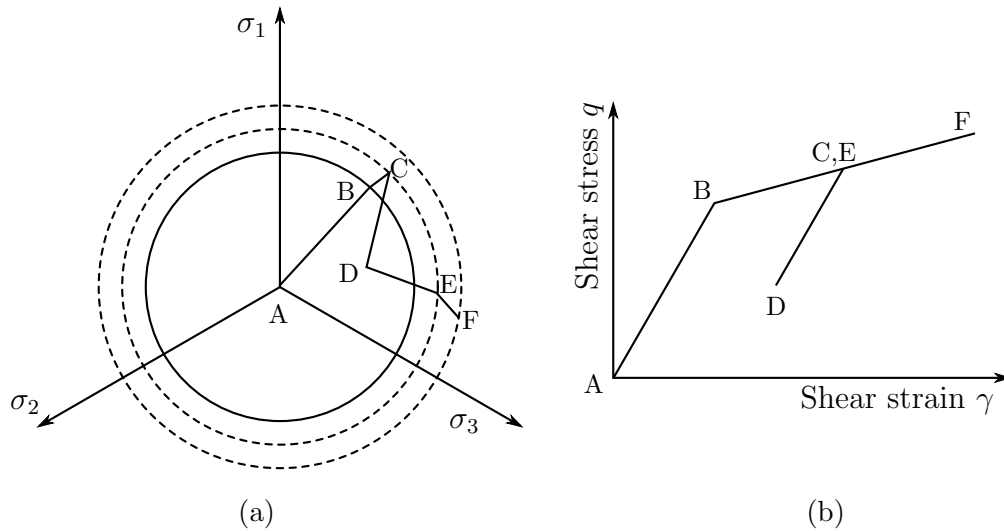


Figure 1.5: Hardening load paths for the von Mises model in principal stress space (a) and the corresponding stress-strain path (b)

material. Under initial loading (AB), elastic behaviour is observed and the stiffness is initially high. Once the yield criterion is exceeded, the yield surface begins to harden and expand (BC); here the stiffness is reduced. Unloading follows the initial gradient back to the elastic domain (CD) and leaves the yield surface in the current position at C. Reloading (DE) observes elastic behaviour again until the yield surface is reached at E. With further loading (EF), the yield surface continues to harden.

To define the rate of hardening, a simple constant term may be used, and the yield function must be modified to take hardening into account:

$$f_{VM} = q - (\sigma_y + H_{VM}\gamma^p) \quad (1.5)$$

where H_{VM} is the assigned hardening gradient, and γ^p is the plastic shear strain.

The von Mises model is more suited to the analysis of metals; for the analysis of soils, several constitutive models have been developed which are more appropriate. The behaviour of soil is very complex, this will be explored in the following section. Different constitutive models capture different aspects of soil behaviour. Examples of such constitutive models include the Mohr-Coulomb model (described by Owen and Hinton (1980)), the hyperbolic soil model (Duncan and Chang, 1970), the Mod-

ified Cam-Clay model (Roscoe and Burland, 1968), Lade's model (Lade, 1977), the Matsuoka-Nakai model (Matsuoka and Nakai, 1974), and the hardening soil model (Schanz et al., 1999; Benz et al., 2008). The latter of these models is discussed and improved on in this thesis. A review and description of this model is detailed in Chapter 2, and a reformulation of the model is documented in Chapter 3. The proposed model is then validated in Chapter 4.

1.4 Behaviour of soils

In order to model the behaviour of soils, it is first necessary gain an understanding of the behaviour of soils. Soil is typically composed of granular material, and water and air which fill the space between soil grains. Soils are classified according to their grain structures, and in particular, their particle size (BS 5930:2015). Boulders and cobbles are the soils with the largest particles, with diameters ranging from 63 mm to 630 mm; the particle size of gravel ranges between 2 mm and 63 mm; sand ranges from 63 μm to 2 mm; silt ranges from 2 μm to 63 μm ; and clay is defined as any soil with a particle size of 2 μm or less.

In the presence of water, clays and silts tend to be cohesive. The particle size of these soils are small enough that colloidal effects occur in the clay-water mixture, which act as a homogeneous material on the macro scale (Schofield and Wroth, 1968). Clays also exhibit some frictional shearing resistance; this is related to the arrangement of the clay particles. Clay particles are typically long and flat; clays with particles which are oriented in the same direction offer less shearing resistance than those which are randomly oriented (Lambe and Whitman, 1969). The small size of the clay particles means that water flows through clays very slowly. Therefore the rate of loading on clay can have a significant effect on the resulting displacements, as initially, the load may be supported by the water, increasing the pore water pressure. The load is transferred to the soil skeleton as the water dissipates (Cotecchia and Chandler, 2000). Clays also exhibit stress memory, where historical

loading of the clay results in different mechanical properties. This effect is one aspect of a behaviour known as over-consolidation, and can be a result of soil erosion above the clay layer, or melting of glaciers for example; i.e. the current stress in the clay may not be the highest stress the clay has undergone historically (Craig, 2004).

The shear strength of sand is almost purely the result of the frictional interaction between particles; the particle size of sand is much larger than clay, the surface area between the particles and water is much lower, and colloidal forces do not significantly contribute to the soil strength. Denser sands inherently have more interlocking between particles, which increases the shear strength. The shape of the particles also affects the sand strength. Rough sand particles have a higher inter-particle friction than a smooth, weathered sand. On the macro scale, both of these factors contribute to the increase in strength of sands. Additionally, the distribution of particle sizes influences the sand strength (Lambe and Whitman, 1969).

Figure 1.6 depicts typical shear stress responses from a drained triaxial compression test. The procedure for this type of test is outlined in BS 1377-8:1990; the essence of this test is a body of soil which is initially compressed equally in all directions. After this, a vertical load is applied to the soil and the resulting stress and strain are measured. A higher compressive stress allows the soil to reach a higher shear stress before failure. Failure is defined as the point when an increase in deviatoric strain causes no increase in shear stress.

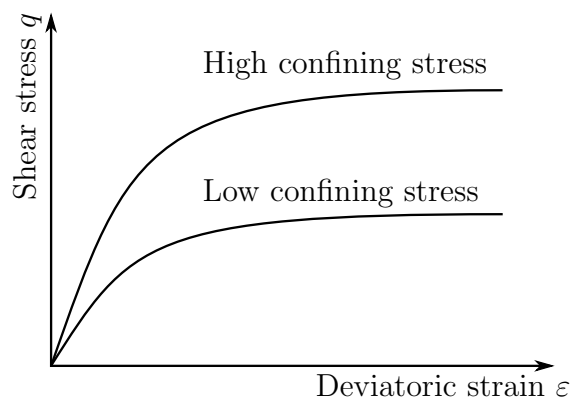


Figure 1.6: Typical triaxial shear stress results for soil under drained conditions

Shear strains in dense sands can lead to an overall increase in volume (Rowe, 1962; Wood, 1990). The cause of this is the rearrangement of sand particles as shear

planes are developed. Rowe (1962) described this behaviour in terms of a ‘saw tooth’ model (Figure 1.7). This model describes the relationship between compaction stress on the sand σ_n , the angle of dilatancy ψ , and the shear stress τ .

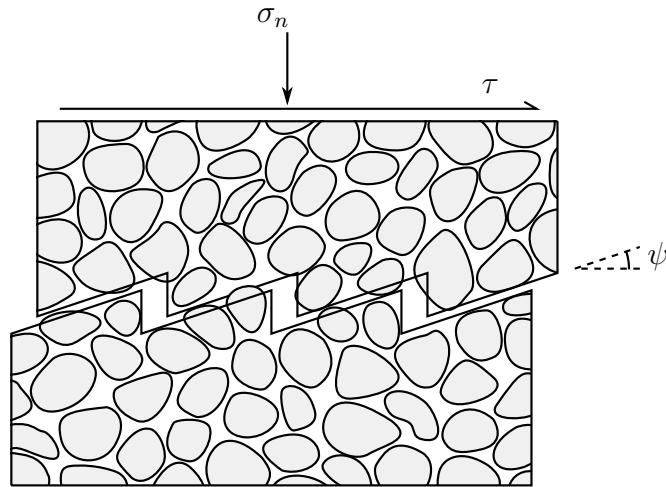


Figure 1.7: Saw tooth model for dilatancy, (after Rowe, 1962)

In terms of the macroscopic behaviour, sands typically compact initially under shearing. After extended shearing, loose sands continue to compact, whilst dense sands begin to dilate (Figure 1.8). A negative change in volumetric strain describes a reduction in soil void ratio, and a positive change describes dilatancy. Further shearing of dense sands can lead to an upper limit of dilation, where the void ratio reaches an equilibrium state. This is demonstrated in Figure 1.8, where the gradient of the volumetric strain for the dense sand reduces after the dilatant phase.

In this discussion, several key features of soil behaviour have been described. In the modelling of geotechnical structures, it is important to be able to capture as many features as possible which are appropriate to the soil being modelled. As discussed previously, several such models have been developed and implemented in various finite element software. Part of the work described in this thesis is to study an existing soil model, the hardening soil (HS) model, which captures many advanced soil features, and make improvements to its implementation including the reformulation of the model and a robust solution algorithm. A review of the current state of the HS model is conducted in Chapter 2, improvements are proposed in Chapter 3, and results from the new model are compared with the previous versions

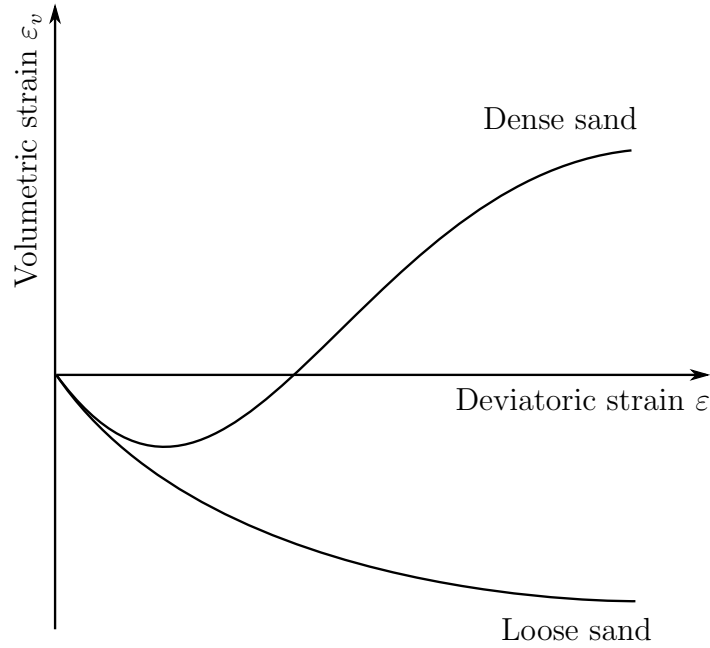


Figure 1.8: Typical triaxial volumetric response for dense and loose sand

of the HS model and experimental data in Chapter 4.

1.5 Reinforcement of soils

In the preparation of sites for civil engineering construction, it is common for some type of ground improvement work to be performed. The extent of ground improvement is typically determined from a site geotechnical survey; this may include techniques such as borehole analysis, shear vane tests, cone penetration tests (Das, 2011).

If it is determined that the soil is not strong enough to support the intended structure, then improvements must be made to the soil. One of the simplest methods is the compaction of the soil; this can be performed by methods such as vibration (Slocombe et al., 2000), drop hammer impact (Mayne et al., 1984), or kneading, which involves shearing the soil at surface level (Xanthakos et al., 1994). Each of these methods compacts different soils to varying extents, and combinations of the above methods may be used to create the desired soil properties.

Alteration of the drainage conditions of a soil can also affect the soil strength, as high pore water pressure can force soil grains to separate, thereby lowering the strength of the soil. Water flows very slowly through clays, and the presence of clay on a site can reduce the drainage through a soil. One remedy to this problem is the installation of sand wick drains (Xanthakos et al., 1994). The flow rate of water through sand is much faster than that of clay, therefore the addition of these channels can significantly reduce the distance needed for the water travel through low permeability material; thus, the drainage rate for the site is increased.

Another option for improving the strength of soil is the addition of cement. With this technique, the cement is mechanically mixed with the soil. Bergado et al. (1999) documented the experimental testing of clay-cement mixtures in relation to the use of the deep soil mixing method to produce vertical piles of clay, lime and cement, which reduce the long term settlement of an embankment. Spagnoli et al. (2016) documented the use of a similar technique used in the construction of offshore platforms. Several other authors have also contributed work relating to the testing of soil-cement mixtures (Amini and Hamidi, 2014; Khemissa and Mahamedi, 2014; Venkatarama Reddy and Latha, 2014). In a related line of study, Harbottle et al. (2014) demonstrated the benefits of cement producing bacteria embedded in soil. In this study, it was shown that the bacteria-soil mixture ‘self healed’ after induced failure.

Geosynthetics are a group of products covering a range of sheet materials. Generally, geosynthetics serve two purposes: the first is to bind with the soil particles (typically sand or gravel) and transfer shear stress in the soil to tensile stress in the fabric; the second is to control the movement of water. Geomembranes are used for the latter purpose and may consist of materials such as synthetic polymers or asphalt (Ingold, 1994). Geotextiles are sheets of woven material which provide some shearing resistance by bonding to the surrounding soil particles and are permeable to allow seepage (Khoury et al., 2010). Geogrids are sheets of material (typically polymer-based) which contain large apertures. The mechanism for reinforcement here is that soil particles fill the voids in the sheet, locking it in place and

allowing direct transfer of stress to the reinforcement material (Ingold, 1994). A comprehensive review of investigations using different types of sheet reinforcement was performed by Marto et al. (2013). Typical applications for such geosynthetics include slope reinforcement (Alamshahi and Hataf, 2009), improvement of bearing capacity (Latha and Somwanshi, 2009; Sireesh et al., 2009), and retaining walls (Yoo and Jung, 2004; Yang et al., 2009).

Fibres have been used previously in the reinforcement of concrete and in polymeric composites such as fibreglass and carbon fibre. Historically, this technique has been used in soils with the planting of vegetation where the roots provide the soil with additional stability near the surface. Waldron (1977) was one of the first to scientifically quantify the effect of fibre inclusion in soil where plant roots, mixed with soils, were subject to direct shear tests. Strength improvements were observed with use of the fibres.

Many materials are used in the manufacture of fibres. Randomly oriented natural fibres such as jute (Singh and Bagra, 2013) and coconut hair (Sivakumar Babu et al., 2008) have been investigated and shown to provide strength increases to soils. Polymer-based materials such as polypropylene (Tang et al., 2007; Diambra et al., 2010), polyamide (Estabragh et al., 2011), and polyethylene are also used and have the inherent advantage over natural fibres that they do not decompose or degrade. Recycled materials such as torn plastic bags (Muntohar, 2009) and shredded tyres (Hataf and Rahimi, 2006; Tafreshi and Norouzi, 2012) have also been shown to provide some strength increase to soils. A comprehensive literature review of studies using different fibre types was conducted by Hejazi et al. (2012), which goes into more detail about many fibre types.

Several methods for the reinforcement of soils have been presented in this section. The applicability of each method is heavily dependent on the requirements of each individual project and the nature of the soils on a given site. Environmental impact, cost of materials, and ease of construction all play an important role in the decision process for soil reinforcement. To prioritise environmental impact, methods such as

compaction will likely have the lowest long term effect as nothing is added to the soil. This method may not provide enough strength improvement for some applications, hence mechanical stabilisation may be necessary. Use of sheet geosynthetics has been shown to provide additional strength to soils, however the nature of this reinforcement is highly anisotropic, and may introduce planes of weakness (Koerner and Koerner, 2011). Randomly oriented fibres do not suffer from this limitation, and can reinforce the soil in all directions. If a strength increase in a particular orientation is desired, then the distribution of orientations can be controlled (Gray and Ohashi, 1983; Diambra et al., 2007).

The second focus of this thesis is the development of a constitutive model to describe the behaviour of fibre-reinforced soils. A thorough review of experimental studies and previous model developments is presented in Chapter 5. An experimental study was conducted, as described in Chapter 6; here the results of many experiments including triaxial tests, fibre pullout tests, and sample dissection are documented and discussed. A constitutive model based on the micro-mechanical relationship between fibre and soil particles, and on data obtained from the experimental study, is described in Chapter 7. This model is then used alongside the aforementioned HS-LC model and is tested against experimental data in Chapter 8.

1.6 Sign convention

This thesis adopts the standard sign convention in stress analysis where tension is taken as positive; this is opposite to the standard geotechnical sign convention. The reason for this choice in convention is to match the finite element software used in the development of the models proposed in later sections. Principal stresses are ordered $\sigma_1 \geq \sigma_2 \geq \sigma_3$; however, it is important to note that this work has a strong geotechnical theme; for the purpose of clarity, many of the standard soil tests are plotted on negative axes, such that they are directly comparable with geotechnical studies.

1.7 Tensor and invariant definitions

This work makes abundant use of stress tensors and invariants of stress tensors. It is therefore important to clearly define each term. The following section describes the stress and strain invariants in terms of the Cartesian tensors. The symmetrical shear terms in the 3-D stress tensor are replaced by the three independent shear terms and the tensors are arranged in vector form, suitable for use in computational stress analysis.

$$\boldsymbol{\sigma} = \begin{bmatrix} \sigma_x & \sigma_y & \sigma_z & \sigma_{xy} & \sigma_{yz} & \sigma_{xz} \end{bmatrix}^T \quad (1.6)$$

$$\boldsymbol{\epsilon} = \begin{bmatrix} \epsilon_x & \epsilon_y & \epsilon_z & \epsilon_{xy} & \epsilon_{yz} & \epsilon_{xz} \end{bmatrix}^T \quad (1.7)$$

The mean stress is defined as

$$p = \frac{\sigma_x + \sigma_y + \sigma_z}{3} \quad (1.8)$$

The shear stress is defined as

$$q = \sqrt{\frac{1}{2} [(\sigma_x - \sigma_y)^2 + (\sigma_y - \sigma_z)^2 + (\sigma_z - \sigma_x)^2] + 3(\sigma_{xy}^2 + \sigma_{yz}^2 + \sigma_{xz}^2)} \quad (1.9)$$

The Lode angle is defined as

$$\theta = \frac{1}{3} \arcsin \left(\frac{-27J_3}{2q^3} \right) \quad (1.10)$$

where

$$\begin{aligned}
J_3 = & (\sigma_x - p) \left[(\sigma_y - p)(\sigma_z - p) - \sigma_{yz}^2 \right] \\
& - \sigma_{xy} \left[\sigma_{xy}(\sigma_z - p) - \sigma_{yz}\sigma_{xz} \right] \\
& + \sigma_{xz} \left[\sigma_{xy}\sigma_{yz} - (\sigma_y - p)\sigma_{xz} \right]
\end{aligned} \tag{1.11}$$

The Lode angle defined in Equation 1.10 is equal to $\pi/3$ in triaxial compression and $-\pi/3$ in triaxial extension.

The volumetric strain is defined as

$$\varepsilon_v = \varepsilon_x + \varepsilon_y + \varepsilon_z \tag{1.12}$$

And finally, the shear strain is defined as

$$\gamma = \frac{1}{3} \sqrt{2 \left[(\varepsilon_x - \varepsilon_y)^2 + (\varepsilon_y - \varepsilon_z)^2 + (\varepsilon_z - \varepsilon_x)^2 \right] + 3 \left[\varepsilon_{xy}^2 + \varepsilon_{yz}^2 + \varepsilon_{xz}^2 \right]} \tag{1.13}$$

Chapter 2

The hardening soil model

The hardening soil model (hereinafter referred to as the HS model) is formulated to replicate the hyperbolic soil model (Duncan and Chang, 1970) in triaxial conditions. The main disadvantage of the hyperbolic soil model is its incremental formulation; this has been found to cause convergence problems, step size dependency, and an inability to capture path dependent behaviour (Bower and Duxbury, 2014). Many of these drawbacks are addressed in the HS model as it is formulated using plasticity theory which records plastic strains and state variables. Working in the plasticity domain also allows use of consistent tangent stiffness matrices; which lead to the quadratic convergence of global Newton-Raphson schemes.

The HS model is currently included in several finite element packages such as Plaxis (PLAXIS, 2016), ZSoil (Obrzud, 2010), and FLAC^{3D} (Jiang and Zhang, 2012).

The first version of the HS model developed by Schanz et al. (1999) is derived in principal stress space and uses a Mohr-Coulomb type shear yield surface which hardens from initial loading until the final Mohr-Coulomb failure limit is reached. The model uses concepts from earlier work by Vermeer (1978), as cited in (Vermeer, 1980). In addition, a cap surface (similar to that of the Modified Cam-Clay model) controls volumetric behaviour. A simple stress return procedure is discussed by Schanz et al. (1999) however, its full implementation is unclear.

The HS model was then modified by Benz (2007) as part of a larger project to introduce small-strain stiffness. This version of the model is derived in Cartesian stress space using the invariants p (mean stress), q (shear stress) and θ (Lode angle). Additional detail of this modification can be found in Benz et al. (2008). The model is implemented such that it is possible to change the failure criterion. For example, Benz (2007) compared the Mohr-Coulomb failure surface with the smooth failure surface by Matsuoka and Nakai (1974), this smooth formulation is more convenient from a numerical perspective, as the number of singularities (edges and corners) present in the yield surfaces in the HS model are reduced.

In this thesis, several versions of the hardening soil model are referred to. For the purpose of clarity, each version is named in Table 2.1. Note that the small strain stiffness version of the HS model is not included in this study. Instead, the smooth reformulation of the HS model is included (Benz, 2007; Benz et al., 2008).

Table 2.1: Different versions of the hardening soil model

Reference	Name	Short name
(Schanz et al., 1999)	Hardening Soil	HS
(Benz, 2007)	HS smooth shear surface	HS-smooth
Chapter 3	HS LUSAS-Cardiff	HS-LC

Both previous versions of the HS model (HS and HS-smooth) use a non-associated shear surface which hardens from initial loading. The first version (HS) uses associated gradients for the cap surface and the second (HS-smooth) uses similar but non-associated cap surface gradients. Both versions include stress dependent stiffness and stress dependent dilatancy. Triaxial compression test simulations give consistent results for both models in shear stress (q - ε_q) and volumetric strain (ε_v - ε_q), however, some of the material parameters must be adjusted to achieve this.

2.1 Model parameters

Most of the parameters used in the HS model can be calculated using standard triaxial compression and oedometer tests. This section briefly explains the meaning of each parameter and how they can be obtained.

2.1.1 Stiffness parameters

The HS model is based on the work of Duncan and Chang (1970), and is formulated to produce essentially the same response to this hyperbolic model under monotonic loading conditions. The hyperbola is defined in Equation 2.17 later in this chapter. A limit is placed on the shear stress (i.e. $q \leq q_f$), which is coincident with the Mohr-Coulomb failure envelope. A more detailed description of the hyperbolic model may be found in the literature (Kondner and Zelasko, 1963; Duncan and Chang, 1970; Schanz et al., 1999).

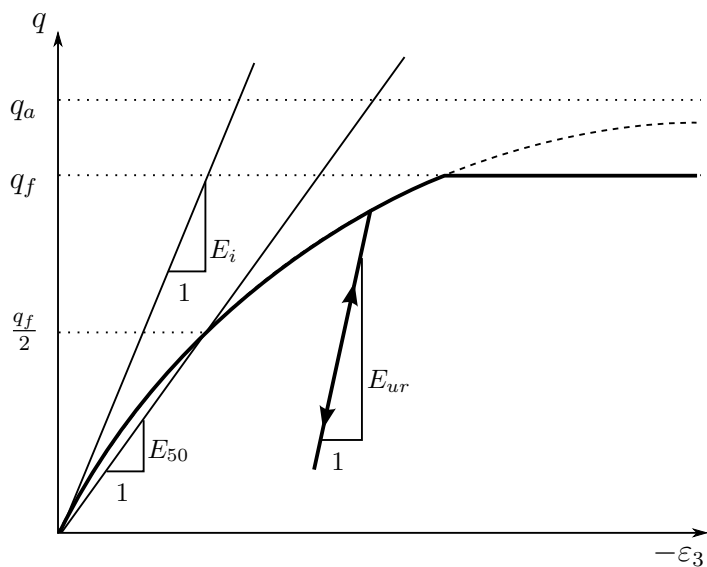


Figure 2.1: Triaxial hyperbola and key stiffness definitions

Reference stress σ^{ref}

Stress dependency is used throughout the HS model in areas such as the soil stiffness and dilatancy. The reference stress defines the level at which certain parameters have been calculated. With a scaling law, the stiffness for any stress level can be defined. For some stress dependent parameters, this stress level refers to the confining stress in a triaxial test, and for others it may represent one of the principal stresses.

50% strength reference modulus E_{50}^{ref}

The modulus E_{50} is defined by the secant stiffness at 50% of the failure shear stress in a triaxial test. The reference modulus E_{50}^{ref} is the value when the triaxial confining stress is equal to σ^{ref} . In the original HS model, this parameter is used directly, however the cap surface affects the steepness of this curve, therefore in the second approach by Benz (2007) it is used to calibrate other parameters such that the triaxial curve produced matches the provided E_{50}^{ref} .

Throughout analyses, the secant stiffness changes according to the minor principal stress, as shown in Equation 2.1; this is done according to a Janbu relationship (Janbu, 1963).

$$E_{50} = E_{50}^{ref} \left(\frac{-\sigma_1 + c \cot(\varphi)}{-\sigma^{ref} + c \cot(\varphi)} \right)^m \quad (2.1)$$

The angle of friction at failure φ , the cohesion c , and the stress dependency term m , are defined later in this section.

Unload-reload reference modulus E_{ur}^{ref}

The unload-reload modulus E_{ur}^{ref} is simply found by calculating the gradient of the unloaded portion of a triaxial curve, again at an effective confining stress of σ^{ref} .

Similarly to the secant stiffness, E_{ur} varies with the minor principal stress (Equa-

tion 2.2).

$$E_{ur} = E_{ur}^{ref} \left(\frac{-\sigma_1 + c \cot(\varphi)}{-\sigma^{ref} + c \cot(\varphi)} \right)^m \quad (2.2)$$

The unload-reload modulus E_{ur} is used in the assembly of the elastic stiffness matrix.

Initial reference modulus E_i^{ref}

The initial stiffness is used only in the second version of the HS model. It is used to calibrate E_{50} to the user supplied value. This parameter is not entered by the user, and acts as an auxiliary material parameter to ensure that the predicted E_{50} matches the user supplied value.

$$E_i = E_i^{ref} \left(\frac{-\sigma_1 + c \cot(\varphi)}{-\sigma^{ref} + c \cot(\varphi)} \right)^m \quad (2.3)$$

Oedometer reference modulus E_{oed}^{ref}

The oedometer stiffness is not used directly in the HS model, but other auxiliary parameters are calibrated to ensure that the simulated oedometer stiffness is the same as the one provided. This stiffness is calculated from a set of oedometer test results, and is the gradient of the stress-strain curve at an applied vertical load of σ^{ref} . Note the use of the major principal stress in Equation 2.4.

$$E_{oed} = E_{oed}^{ref} \left(\frac{-\sigma_3 + c \cot(\varphi)}{-\sigma^{ref} + c \cot(\varphi)} \right)^m \quad (2.4)$$

The stress dependent stiffness equations are not valid when the principal stress term falls below a critical value i.e. when the numerators in Equations 2.1 to 2.4 become negative. Hence a lower limit of $-c \cot(\varphi)$ is placed on the stress component.

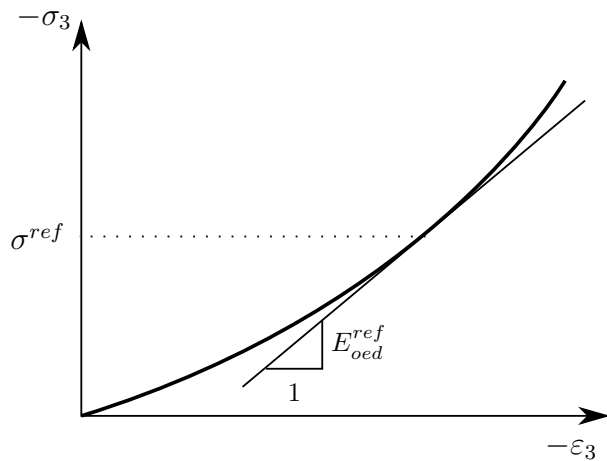


Figure 2.2: Oedometer curve and reference stiffness

Stress dependency exponent m

The stress dependency exponent is used in the calculation of the stress dependent Young's moduli. This can be calculated from a series of triaxial tests at different confining stresses. A simple method of calculating this parameter is to compare the secant stiffness E_{50} for three or more confining stresses, then adjusting the value of m in Equation 2.1 until it matches with the experimental values of E_{50} .

A value of $m = 0$ means that there is no stress dependent stiffness, and the stiffness remains constant, despite any changes in stress. A value of $m = 1$ means that the stiffness is directly proportional to the minor principal stress σ_1 .

2.1.2 Failure parameters

Friction angle φ

This is the angle of internal friction at failure; as the mean stress p increases, the soil grains compact, and the allowable shear stress q before failure also increases. The rate of increase is defined by the friction angle φ . This is the same friction angle which is used in many soil models such as Mohr-Coulomb. The friction angle

can be found by plotting several Mohr's circles to determine the failure envelope; the friction angle is related to the slope of this failure envelope.

Cohesion c

The failure envelope may intersect the shear stress axis when plotted. The cohesion defines where on the axis the intersect occurs. Typically, sands have very little cohesion and clays have a higher cohesion. Increasing the cohesion in the HS model has the effect of shifting the elastic domain along the mean stress axis, allowing tensile stresses to develop in the soil.

Failure ratio R_f

The failure ratio defines the ratio of the maximum asymptotic shear stress q_a to the failure ratio q_f (see Figure 2.1).

2.1.3 Dilatancy

The dilatancy characteristics of soil describe its volumetric behaviour. Loose sands tend to contract with shearing and reduce in volume as particles rearrange to fill voids. Dense sands tend to dilate with shearing (until a critical state is reached), and increase in volume as particles 'climb' over one-another during the formation of shear planes.

Dilatancy angle ψ

Using an associated flow rule over-predicts dilatancy in soils, therefore a non-associated flow rule is typically used where the dilatancy angle is lower than the friction angle ($\psi \approx \varphi - 30^\circ$). For loose sands, the dilatancy angle is close to zero which generates only contracting strains.

The hardening soil model uses Rowe's stress dilatancy theory (Rowe, 1962) in

its implementation (Equation 2.5) which relates the mobilised dilatancy angle ψ_m to the critical state friction angle φ_c and the mobilised friction angle φ_m .

$$\sin(\psi_m) = \frac{\sin(\varphi_m) - \sin(\varphi_c)}{1 - \sin(\varphi_m)\sin(\varphi_c)} \quad (2.5)$$

The mobilised friction angle may be calculated by several methods depending on the implementation. The original HS model uses a Mohr-Coulomb type approach for the calculation of the mobilised friction angle (2.6). The newer formulation by Benz uses the Matsuoka-Nakai failure criterion (2.7), and if using the Lode dependent formulation, mobilised friction angle is given by (2.8).

$$\sin(\varphi_m) = \frac{\sigma_1 - \sigma_3}{\sigma_1 + \sigma_3 + 2c \cot(\varphi)} \quad (2.6)$$

$$\sin(\varphi_m) = \sqrt{\frac{9I_3 - I_1I_2}{I_3 - I_1I_2}} \quad (2.7)$$

where I_1 , I_2 and I_3 are the first, second and third stress invariants given by the solution to the eigenvalue problem $|\sigma_{ij} - \lambda\delta_{ij}| = 0$

$$\sin(\varphi_m) = \frac{3q}{6\chi(p + c \cot(\varphi)) + q} \quad (2.8)$$

where $p = \sigma_{kk}/3$ is the mean stress, $q = \sqrt{3J_2}$ is the von Mises effective shear stress. χ is a Lode angle dependency which is discussed later. The critical state friction angle is given by

$$\sin(\varphi_c) = \frac{\sin(\varphi) - \sin(\psi)}{1 - \sin(\varphi)\sin(\psi)} \quad (2.9)$$

The definition of dilatancy angle used by Schanz et al. (1999) is that of Rowe

(1962) with a lower cutoff.

$$\sin(\psi_m) = \frac{\sin(\varphi_m) - \sin(\varphi_c)}{1 - \sin(\varphi_m)\sin(\varphi_c)} \geq 0 \quad (2.10)$$

Benz (2007) describes three additional methods which can be used to model the dilatancy cutoff. The first is that of Wehnert (2006) which imposes a non-zero limit to the dilatancy angle.

$$\sin(\psi_m) = \frac{\sin(\varphi_m) - \sin(\varphi_c)}{1 - \sin(\varphi_m)\sin(\varphi_c)} \geq 0.07 \quad (2.11)$$

Although as Benz (2007) notes, the lower limit in (2.11) effectively represents an additional material parameter.

A scaled approach (Søreide, 1990) is also mentioned by Benz (2.12). This provides a single non-linear function rather than a bilinear one.

$$\sin(\psi_m) = \left(\frac{\sin(\varphi_m) - \sin(\varphi_c)}{1 - \sin(\varphi_m)\sin(\varphi_c)} \right) \frac{\sin(\varphi_m)}{\sin(\varphi)} \quad (2.12)$$

The form of dilatancy relationship used in the HS small model is that of Li and Dafalias (2000). Here, dilatancy is defined as the ratio of plastic volumetric strain to plastic shear strain and is given by

$$\tan(\psi_m) = \left(M e^{\ln(p_p/p)/15} - \eta \right) / 10 \quad (2.13)$$

where

$$\frac{p_p}{p} = \frac{\eta \sin(\varphi_c(1 - \sin(\varphi_m)))}{M \sin(\varphi_m(1 - \sin(\varphi_c)))} \quad (2.14)$$

and $\eta = q/p$ is the stress ratio, M is the critical stress ratio, p_p is the cap hardening parameter which controls volumetric strain.

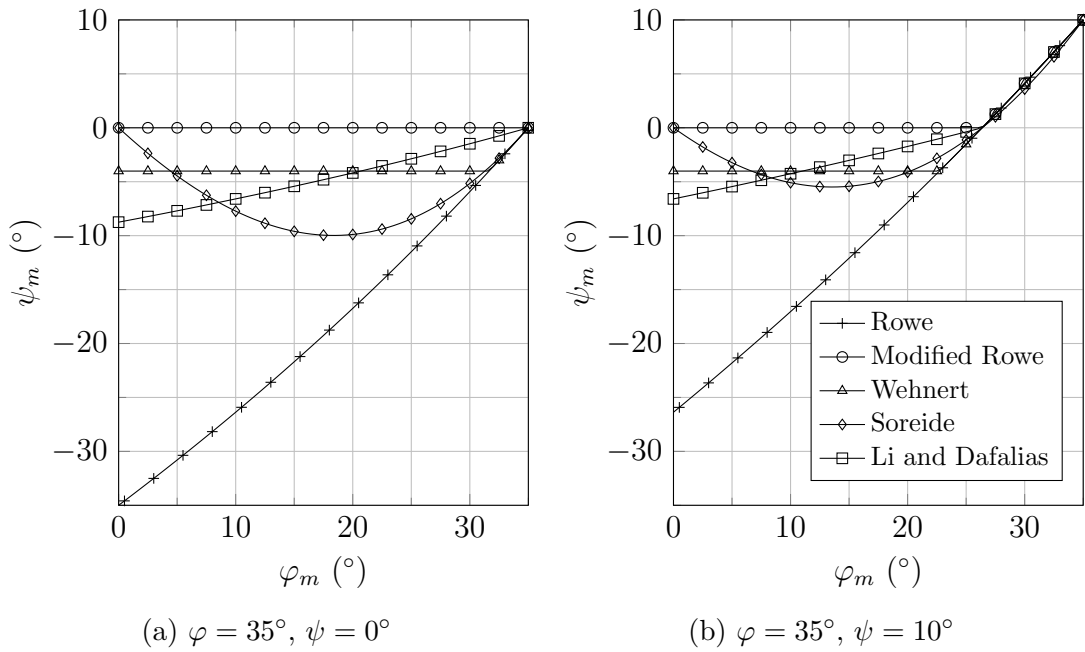


Figure 2.3: Mobilised dilatancy with mobilised friction for different theoretical models (redrawn from Benz, 2007)

This approach is a simplification of the original method by Li and Dafalias (2000); assumptions were made regarding the slope of the critical state line in $(e - \ln p)$ space. These assumptions have been made to avoid the addition of advanced soil parameters. These assumptions follow the full theory only for contracting states, and when dilation is detected, the original Rowe equation (2.5) is used.

Each method for calculating the mobilised dilatancy angle is represented in terms of the mobilised friction angle (Figure 2.3).

Initial void ratio e_0

This is the void ratio at the start of the analysis. This parameter is only required for the dilatancy cut-off, therefore is optional.

Limiting void ratio e_c

The void ratio varies throughout each analysis and is related to the volumetric strain. Dense sands increase in void ratio when sheared up to a limit where they cannot expand any more, this is known as the critical state. The original formulation of

the hardening soil model imposes a limit to the void ratio by a user defined critical void ratio e_c . If the void ratio (2.15) exceeds this value, then the dilatancy angle is set to zero.

$$e = (1 + e_0) \exp(\varepsilon_{v0} - \varepsilon_v) - 1 \quad (2.15)$$

where e_0 and ε_{v0} are the initial void ratio and volumetric strain, ε_v is the current void ratio.

$$\sin(\psi_m) = 0 \text{ if } e \geq e_c \quad (2.16)$$

2.2 Hardening shear yield surface

The main difference between versions of the HS model is the hardening shear yield surface. Essentially, this surface is designed to follow the hyperbola (2.17) in drained triaxial compression (Figure 2.1); described by Kondner and Zelasko (1963) as implemented by Duncan and Chang (1970).

$$\varepsilon_3 = \frac{q_a}{2E_{50}} \frac{\sigma_1 - \sigma_3}{(\sigma_1 - \sigma_3) - q_a} \quad (2.17)$$

where $q_a = q_f/R_f$ is the asymptotic shear stress. The failure stress q_f is given by

$$q_f = \frac{2c \cos(\varphi) - 2\sigma_1 \sin(\varphi)}{1 - \sin(\varphi)} \quad (2.18)$$

and R_f is a shear failure ratio and is typically taken as 0.9. Equation 2.18 is equivalent to the Mohr-Coulomb criterion for triaxial compression and extension.

This hyperbola gives reasonable approximations to triaxial results while using physical parameters, and the simplicity of the model makes it convenient for mod-

elling such tests. Duncan and Chang (1970) also used this model to simulate the load-displacement relationship of a circular footing in a finite element analysis. Results of this simulation were reasonable with 2% difference from experimental results in a serviceability range (displacements less than 10% of the footing width) and 15% difference at soil failure.

2.2.1 Shear surface in the original HS model

To reproduce the hyperbola in Figure 2.1 (page 21), Schanz et al. (1999) proposed a hardening yield function of the form

$$f_s = \frac{q_a}{E_{50}} \frac{q}{q_a - q} - \frac{2q}{E_{ur}} - \gamma^p \quad (2.19)$$

where the asymptotic shear stress q_a is calculated in terms of the mean stress instead of the minor principal stress. The plastic shear strain γ^p governs hardening in this surface, its evolution is described later in Equation 2.27.

$$q_a = \frac{1}{R_f} \frac{6 \sin(\varphi)}{3 - \sin(\varphi)} (-p + c \cot(\varphi)) \quad (2.20)$$

The model presented by Schanz et al. (1999) is formulated in principal stress space. The yield function may be expressed in terms of principal stresses as follows:

$$f_{s12} = \frac{q_a}{E_{50}} \frac{(\sigma_1 - \sigma_2)}{q_a - (\sigma_1 - \sigma_2)} - \frac{2(\sigma_1 - \sigma_2)}{E_{ur}} - \gamma^p \quad (2.21)$$

$$f_{s13} = \frac{q_a}{E_{50}} \frac{(\sigma_1 - \sigma_3)}{q_a - (\sigma_1 - \sigma_3)} - \frac{2(\sigma_1 - \sigma_3)}{E_{ur}} - \gamma^p \quad (2.22)$$

These yield functions may be visualised in principal stress space as in Figure 2.4.

For a sample which has undergone no shearing, the plastic shear strain γ^p is

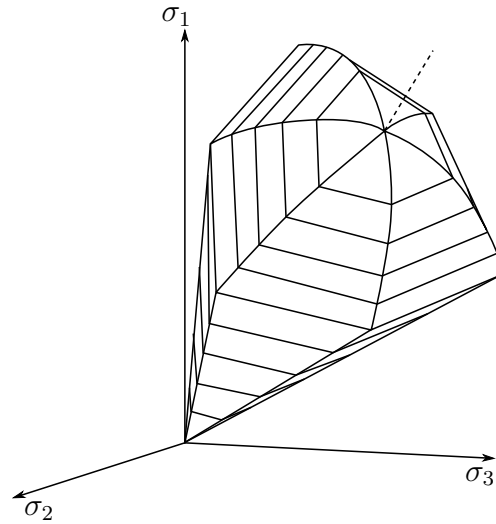


Figure 2.4: Representation of shear (cone) surface and cap surface in the HS model (redrawn from Schanz et al., 1999)

equal to zero. As shearing progresses, the shear surface hardens and the value of γ^p increases. Return mapping is discussed in more detail in Section 3.8. However, it is necessary in the definition of the evolution relationships to understand the role of plastic strains in return mapping.

During yielding of an elasto-plastic material the total strain vector is composed of an elastic component $\boldsymbol{\varepsilon}^e$ and plastic component $\boldsymbol{\varepsilon}^p$.

$$\Delta\boldsymbol{\varepsilon} = \Delta\boldsymbol{\varepsilon}^e + \Delta\boldsymbol{\varepsilon}^p \quad (2.23)$$

A trial stress state is calculated from the total strain increment $\Delta\boldsymbol{\varepsilon}$ and the elastic Hookean matrix (D matrix)

$$\boldsymbol{\sigma}_{tr} = \boldsymbol{\sigma}_0 + \mathbf{D}_e \Delta\boldsymbol{\varepsilon} \quad (2.24)$$

where $\boldsymbol{\sigma}_0$ is the converged stress at the start of the increment. If the trial stress $\boldsymbol{\sigma}_{tr}$ exceeds the yield criterion, the stress must be returned to the yield surface according to the flow rule. The amount of stress to be eliminated is summed during return mapping and is described by the plasticity multiplier $\Delta\lambda$.

$$\boldsymbol{\sigma} = \boldsymbol{\sigma}_{tr} - \Delta\lambda \mathbf{D}_{ep} \frac{\partial g}{\partial \boldsymbol{\sigma}} \quad (2.25)$$

where \mathbf{D}_{ep} is the consistent tangent matrix which relates infinitesimal stresses and strains. The formulation of this matrix is described in detail in Section 3.8.2.

For the shear yield surface and in this formulation of the HS model, the increment of plastic shear strain γ^p is equal to the plastic multiplier to the shear surface.

$$\Delta\gamma^p = h_s \Delta\lambda_s \quad (2.26)$$

where $h_s = 1$. For multiple surface stress return mapping, the plastic multiplier $\Delta\lambda_s$ is that of the shear surface only.

The plastic shear strain used in the shear yield surface can now be updated

$$\gamma^p = \gamma^p + \Delta\gamma^p \quad (2.27)$$

Plastic potential to the shear surface.

The Drucker-Prager surface (Drucker et al., 1952) is a conical surface (Figure 1.4b) which is circular in the π -plane. Plastic potential functions define the direction in stress space in which stress is returned to the yield surface. The Lode angle is constant in this function conveniently making stress returns radial in the π -plane. The plastic potential used in the HS model is given as

$$g_{s12} = \frac{\sigma_1 - \sigma_2}{2} - \frac{\sigma_1 + \sigma_2}{2} \sin(\psi_m) \quad (2.28)$$

$$g_{s13} = \frac{\sigma_1 - \sigma_3}{2} - \frac{\sigma_1 + \sigma_3}{2} \sin(\psi_m) \quad (2.29)$$

Similarly to the yield surface, the plastic potential function has two components

when written in terms of the principal stresses. The mobilised friction angle is calculated using Rowe's formula (2.5) with the dilatancy cutoff if necessary (Equation 2.15).

2.2.2 Shear surface in the HS-smooth model

The shear yield surface in the second version of the HS model (Benz, 2007) is somewhat more sophisticated than its predecessor. An asymptotic limit is placed on the mobilised friction angle instead of the shear stress.

$$f_s = \frac{3q}{2E_i} \frac{\left(\frac{1-\sin(\varphi_m)}{\sin(\varphi_m)}\right)}{\left(\frac{1-\sin(\varphi_m)}{\sin(\varphi_m)}\right) - R_f \left(\frac{1-\sin(\varphi)}{\sin(\varphi)}\right)} - \frac{3q}{2E_{ur}} - \gamma^p \quad (2.30)$$

where q is the von Mises shear stress, E_i and E_{ur} are the initial and unload-reload moduli as defined in Equations 2.3 and 2.2. φ_m is the mobilised friction angle; depending on the implementation, this may take the form of either Equations 2.6, 2.7 or 2.8. This surface is formulated in general stress space, avoiding the need for complex return mapping schemes which involve switching coordinate axes between principal and Cartesian. γ^p is the plastic shear strain and is used as a hardening parameter. Its hardening rule is slightly different from the original HS model (Equation 2.26) and can be expressed as:

$$\Delta\gamma^p = h_s \Delta\lambda_s \quad (2.31)$$

where $h_s = 1.5$

$$\gamma^p = \gamma^p + \Delta\gamma^p \quad (2.32)$$

$\Delta\lambda_s$ is the plasticity multiplier associated with the shear surface during a single or multi-surface stress return.

Plastic potential to the modified shear surface

The Drucker-Prager cone surface (Drucker et al., 1952) is used as a plastic potential in the HS model. Similarly to the original HS model, this version uses the mobilised dilatancy angle ψ_m to control the apex angle of the cone. As the model here is formulated in Cartesian stress space, the plastic potential takes the form:

$$g_s = q - (p + c \cot(\varphi)) \left(\frac{6 \sin(\psi_m)}{3 - \sin(\psi_m)} \right) \quad (2.33)$$

This cone has full rotational symmetry about the isotropic compression line $\sigma_1 = \sigma_2 = \sigma_3$.

2.3 Hardening cap surface

The cap yield surface limits the amount of volumetric strain and its influence dominates over the shear surface in oedometer loading. Again, different formulations are used in the two main versions of the model

2.3.1 Cap surface in original HS model

The cap yield surface, which can be seen represented in principal stress space in Figure 2.4 and in q - p space in Figure 2.5, limits the plastic volumetric strains in oedometer loading. The version proposed by Schanz et al. (1999) takes a similar form to the cap surface in the Modified Cam-Clay model. The equation for the cap surface is

$$f_c = \left(\frac{\tilde{q}}{\alpha} \right)^2 + p^2 - p_p^2 \quad (2.34)$$

where p is the mean stress, p_p is the mean stress associated with zero shear strain; i.e. the pre-consolidation pressure, α is an auxiliary material parameter controlling

the height of the ellipse and \tilde{q} is a special shear stress measure (2.35) and is used to ensure the cap and shear surfaces are the same shape at their intersection.

$$\tilde{q} = \sigma_1 + (\delta - 1)\sigma_2 - \delta\sigma \quad (2.35)$$

where

$$\delta = \frac{3 + \sin(\varphi)}{3 - \sin(\varphi)} \quad (2.36)$$

The hardening law of the cap surface is as follows

$$\Delta p_p = h_c \Delta \lambda_c \quad (2.37)$$

where

$$h_c = 2H \left(\frac{\sigma_3 + c \cot(\varphi)}{\sigma^{ref} + c \cot(\varphi)} \right)^m p \quad (2.38)$$

H is a function of the bulk stiffness in primary loading K_c and the unload-reload bulk modulus K_s

$$H = \frac{K_s K_c}{K_s - K_c} \quad (2.39)$$

The unload-reload bulk stiffness is calculated from the unload-reload reference modulus and Poisson's ratio

$$K_s = \frac{E_{ur}^{ref}}{3(1 - 2\nu_{ur})} \quad (2.40)$$

The ratio K_s/K_c is an auxiliary model parameter and is calibrated to known values of K_0 and E_{oed} . The stress dependency term in brackets in (2.38) is present

due to the definition of the elastic swelling modulus (2.40), which uses a reference value for Young's modulus. It is possible to instead use the current value of the unload reload modulus E_{ur} defined in (2.2) in place of the reference value E_{ur}^{ref} , and remove the stress dependency terms in (2.38).

Plastic potential to the cap surface

The cap surface in the HS model is associated, meaning that the plastic potential is the same as the yield function, i.e.

$$g_c = \left(\frac{\tilde{q}}{\alpha}\right)^2 + p^2 - p_p^2 \quad (2.41)$$

2.3.2 Cap surface in the HS-smooth model

The cap surface for the second version of the HS model is very similar to that of Schanz et al. (1999). A modification is made to allow for the new shear surface. The new cap yield function is given as

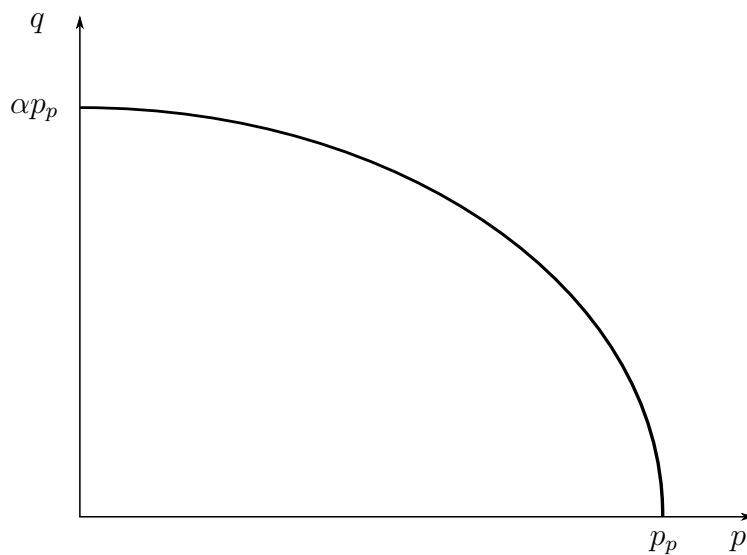


Figure 2.5: Cap surface in q - p space

$$f_c = \left(\frac{q}{\chi\alpha} \right)^2 + p^2 - p_p^2 \quad (2.42)$$

Note the change from the special stress measure \tilde{q} to the standard deviatoric stress q . The Lode dependency χ is used instead of \tilde{q} to alter the shape of the cap surface. The maximum value of χ is 1 for triaxial compression, meaning that this yield function is identical to (2.34) for triaxial compression. The Lode angle dependency in the Matsuoka-Nakai (LMN) model is as defined by Bardet (1990):

$$\chi = \frac{\sqrt{3}\varpi}{2\sqrt{\varpi^2 - \varpi + 1}} \frac{1}{\cos(\vartheta)} \quad (2.43)$$

where

$$\vartheta = \begin{cases} \frac{1}{6} \arccos \left(-1 + \frac{27\varpi^2(1-\varpi)^2}{2(\varpi^2 - \varpi + 1)^3} \sin^2(3\theta) \right), & \text{if } \theta \leq 0 \\ \frac{\pi}{3} - \frac{1}{6} \arccos \left(-1 + \frac{27\varpi^2(1-\varpi)^2}{2(\varpi^2 - \varpi + 1)^3} \sin^2(3\theta) \right), & \text{otherwise} \end{cases} \quad (2.44)$$

and

$$\varpi = \frac{3 - \sin(\varphi)}{3 + \sin(\varphi)} \quad (2.45)$$

Hardening law of modified cap surface

The evolution of the hardening variable p_p is identical to that of Schanz et al. (1999) in Equation 2.37.

Plastic potential to the modified cap surface

The cap surface used in the HS-smooth model is non-associated, meaning that the plastic potential function is different to the yield function. The only difference is that the Lode angle is frozen during return mapping (2.46), this is done to ensure volumetric returns are radial in the π -plane. The importance of this is most relevant

when stresses are returned to both the shear and cap surfaces simultaneously, as the plastic potential to the shear surface (and failure surface) is also radial in the π -plane. This case is of particular importance because loading conditions in most of the basic laboratory tests activate the shear and cap surfaces for primary loading. This is also a common occurrence in many boundary value problems.

$$g_c = \left(\frac{q}{\chi_{tr} M} \right)^2 + p^2 - p_p^2 \quad (2.46)$$

2.4 Failure criteria

2.4.1 Mohr-Coulomb criterion

The Mohr-Coulomb soil model is often used in geotechnical engineering practice. Its simplicity combined with its accurate prediction of soil failure have made it a commonly used tool for soil design problems. Only two parameters are required by this model: the friction angle at failure φ and the internal cohesion c . The concept of the failure model is based on that of limiting shear stress.

$$\tau = c + \sigma_n \tan(\varphi) \quad (2.47)$$

where τ is the limiting shear stress and σ_n is the normal stress applied to the soil, as shown in Figure 2.6.

The yield criterion in principal stress space may be expressed as follows (Owen and Hinton, 1980)

$$f_{MC} = (\sigma_1 - \sigma_3) - 2c \cos \varphi - (\sigma_1 + \sigma_3) \sin \varphi \quad (2.48)$$

Along with the ordering of principal stresses $\sigma_1 \geq \sigma_2 \geq \sigma_3$, Equation (2.48) fully represents the cone in principal stress space (Figure 2.7). In the π -plane (Figure

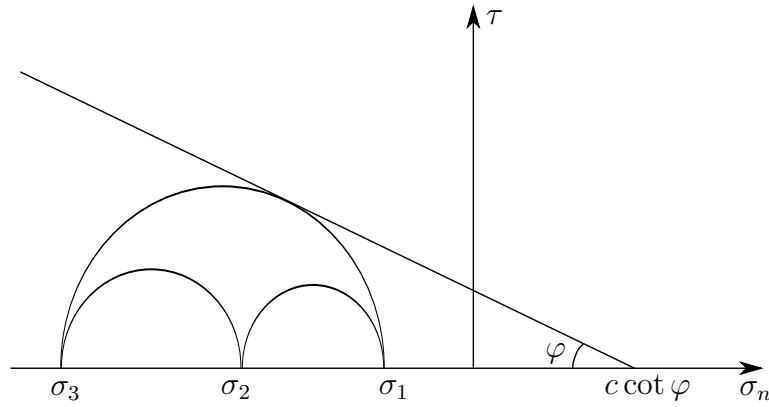


Figure 2.6: Mohr-Coulomb yield criterion and principal stresses

2.8) the Mohr-Coulomb surface is an irregular hexagon with the maximum strength occurring at each principal stress axis.

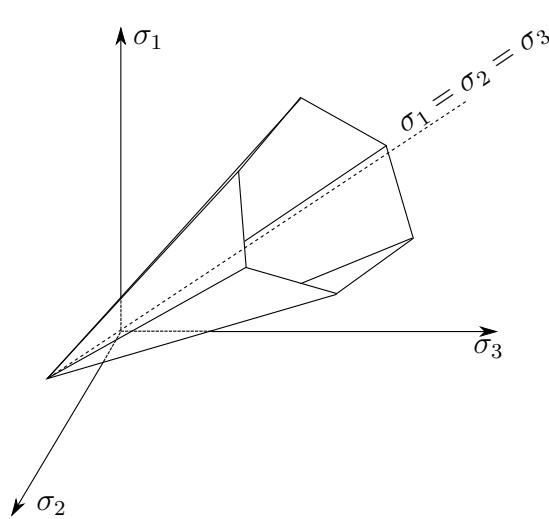


Figure 2.7: Mohr-Coulomb failure surface in principal stress space

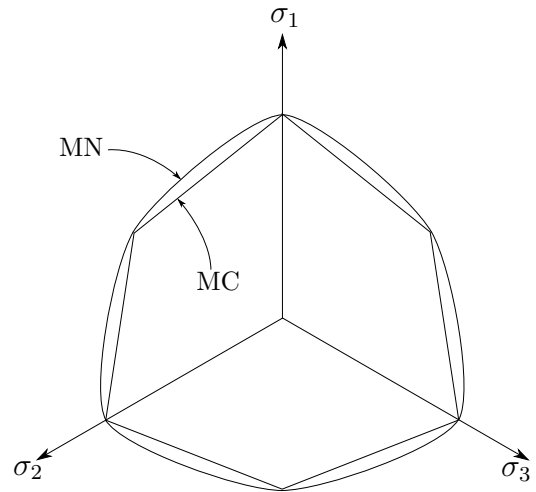


Figure 2.8: π -plane projection of Mohr-Coulomb criterion and Matsuoka-Nakai criterion

When working in Cartesian stress space, it is necessary to reformulate (2.48) into stress invariants. Owen and Hinton (1980) substitute the invariants I_1 , $\sqrt{J_2}$ and θ into (2.48) using the following relationship:

$$\begin{bmatrix} \sigma_1 \\ \sigma_2 \\ \sigma_3 \end{bmatrix} = \frac{2\sqrt{J_2}}{\sqrt{3}} \begin{bmatrix} \sin(\theta + \frac{2\pi}{3}) \\ \sin(\theta) \\ \sin(\theta + \frac{4\pi}{3}) \end{bmatrix} + \frac{I_1}{3} \begin{bmatrix} 1 \\ 1 \\ 1 \end{bmatrix} \quad (2.49)$$

Substituting the principal stresses from (2.49) into (2.48) gives a form of the Mohr-Coulomb criterion in terms of the computationally convenient stress invariants I_1 , $\sqrt{J_2}$ and θ . Owen and Hinton (1980) give the Mohr-Coulomb failure criterion in terms of these invariants:

$$\frac{I_1}{3} \sin(\varphi) + \sqrt{J_2} \left(\cos(\theta) - \frac{1}{\sqrt{3}} \sin(\theta) \sin(\varphi) \right) = c \cos(\varphi) \quad (2.50)$$

where I_1 is the first invariant of the stress tensor and J_2 is the second invariant of the stress deviator tensor. In terms of the invariants used in this thesis, the Mohr-Coulomb criterion may be expressed as:

$$f_{MC} = p \sin(\varphi) + \frac{q}{\sqrt{3}} \left(\cos(\theta) - \frac{1}{\sqrt{3}} \sin(\theta) \sin(\varphi) \right) - c \cos(\varphi) \quad (2.51)$$

2.4.2 Matsuoka-Nakai criterion

A major limitation of the Mohr-Coulomb criterion is that it does not consider the intermediate principal stress σ_2 . This causes strength predictions to be overly conservative with intermediate stress states. The Matsuoka-Nakai criterion (Matsuoka and Nakai, 1974) overcomes this limitation by utilising the concept of the spatially mobilised plane (see Figure 2.9, in which each combination of shear stresses are considered).

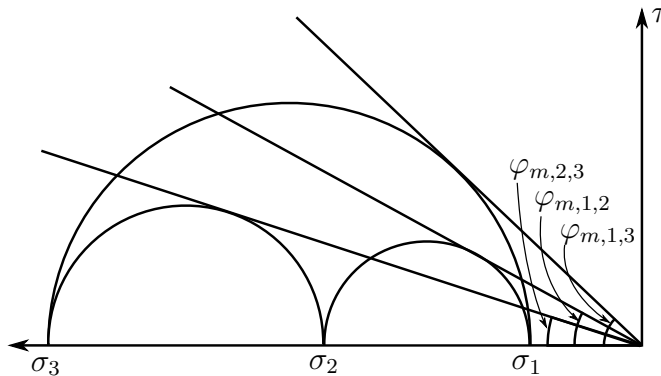


Figure 2.9: Spatially mobilised plane concept; each principal stress envelope is considered (Nakai and Matsuoka, 1983)

The equation for the spatially mobilised plane is given as

$$\tan\left(45^\circ + \frac{\varphi_{m,i,j}}{2}\right) = \sqrt{\frac{1 + \sin(\varphi_{m,i,j})}{1 - \sin(\varphi_{m,i,j})}} \quad (2.52)$$

Each mobilised friction angle $\varphi_{m,i,j}$ is limited to the friction angle at failure φ . Expressing (2.52) as a failure criterion gives the Matsuoka-Nakai (MN) stress envelope.

$$f_{MN} = \sqrt{\frac{9I_3 - I_1I_2}{I_3 - I_1I_2}} \quad (2.53)$$

When plotted in 3-D stress space, the MN criterion circumscribes each edge of the Mohr-Coulomb failure envelope, or the corners of the envelope in the π -plane (Figure 2.8).

2.5 Tension limit

Only the modified HS model by Benz employs a tension yield surface, however one could easily be implemented in the original HS model. The tension yield surface is associated and non-hardening; and limits each stress direction to a maximum tensile stress σ_t .

$$f_t = \sigma_i - \sigma_t \quad (2.54)$$

where $i = 1, 2, 3$.

2.6 Other contributions to the HS model

Although the development of the HS model is mostly attributed to two particular works (Schanz et al., 1999; Benz, 2007), with additional documentation by

Benz et al. (2008), other authors have also suggested and implemented changes and improvements. Marcher and Vermeer (2001) implemented a void ratio dependent friction angle with the HS model, which is able to model softening in soils. Further work was conducted on this line of work by Möller et al. (2004) where softening was instead implemented by applying a softening rule to the cohesion term used in the HS model. Results from this model appear to be promising in the analysis of tunnels in clay.

The modelling of undrained behaviour predicted by the HS model was addressed by Truty and Obrzud (2015), who implemented a mechanism for including the effects of pore pressure, and applied coupling mechanism between the hardening of the shear and cap surfaces. This model also used the small-strain stiffness feature by Benz (2007), and was able to predict the surface settlements above two tunnels in London clay with reasonably good accuracy.

Concluding remarks

In conclusion, a description of the hardening soil model in its current state has been given in this chapter. It is worth noting that each of the main contributors to the development of this model (Schanz et al., 1999; Benz, 2007; Benz et al., 2008) have performed validation analyses to compare against data from experiments, either performed by themselves, or extracted from case studies. The performance of the model in these analyses is discussed later in Chapter 4, where a new version of the HS model is compared to the current version and against existing and new experimental data.

Chapter 3

A robust implementation of the HS model

3.1 Motivation

In preliminary work for this thesis, several attempts were made at implementing the HS model as described in the literature (Schanz et al., 1999; Benz, 2007). On each occasion, it was found that although the models produced accurate results, their implementations lead to analyses which could converge poorly.

The main area of concern is the formulation of the shear yield surface f_s (Equations 2.19 and 2.30). Both versions of the yield surface suffer from the same problem which occurs whenever the trial shear stress $q_{tr} = q(\sigma_{tr})$ exceeds the asymptotic shear stress q_a , and the yield function f_s becomes negative (Figure 3.1). Considering the denominator in the first parts of Equations (2.19) and (2.30); as q approaches q_a , or as $\sin(\varphi_m)$ approaches the failure friction angle $\sin(\varphi)$, the yield function tends to infinity. Exceeding these values switches the sign of the denominator, and as a result the yield function becomes negative.

The converged stresses should be limited to the failure shear stress q_f (which is less than or equal to q_a). However, during the stress return procedure, the stress may

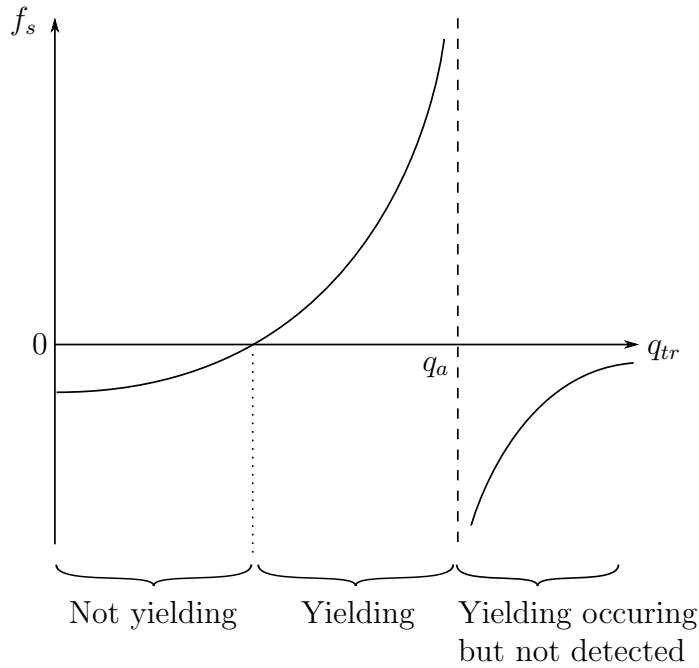


Figure 3.1: Asymptote in shear yield function for high trial stresses

exceed the valid range of the yield function and produce invalid results or numerical errors.

It is therefore essential with this model to limit the step sizes as the soil approaches failure. This approach is not ideal for a robust commercial implementation where users may apply any step size. It is for this reason that the shear yield function is modified here.

The second area of improvement is the hardening rule for the shear surface. In both formulations of the HS model (Schanz et al., 1999; Benz, 2007), the hardening rule for the shear surface is incremental in form; where the plastic shear strain term γ^p is accumulated with an incremental hardening rule (Equation 2.26). This incrementation is performed in an unchecked manner, and causes the solution to drift. Improved convergence is observed when γ^p is calculated directly from the total plastic strains using a non cumulative relationship.

Additionally, the return mapping scheme has been improved from the implementation by Benz (2007), which uses the closest point projection method with reductions on the residuals for the stress only. The proposed scheme also reduces

the residuals of the plastic strains and the state variables, resulting in a robust algorithm which can return from very large strain steps.

The modifications to the HS model are detailed in Section 3.2. Much of the formulation is akin to the original formulations, these are described in detail in Chapter 2, and a summary of the full model is included at the end of this chapter.

3.2 Changes to the shear yield surface

To address the asymptote in the shear yield function, the hyperbola by Duncan and Chang (1970), as shown in Figure 2.1 (page 21) is considered

$$\varepsilon_3 = \frac{q_a}{2E_{50}} \frac{q}{q - q_a} \quad (3.1)$$

Due to the influence of the cap surface, the predicted secant stiffness E_{50} can differ from the supplied value, therefore the substitution $E_i \approx 2E_{50}$ is made. The initial stiffness E_i can be adjusted such that the predicted value of E_{50} matches the supplied value.

$$\varepsilon_3 = \frac{q_a}{E_i} \frac{q}{q - q_a} \quad (3.2)$$

Unloading from any point on the hyperbola using the elastic stiffness gives the current plastic shear strain

$$\varepsilon_3^p = \frac{q_a}{E_i} \frac{q}{q - q_a} + \frac{q}{E_{ur}} \quad (3.3)$$

To obtain an equation relating the plastic shear strain γ^p to the current shear stress, from Equation 1.13, the definition of the plastic shear strain in triaxial stress space ($\sigma_1 = \sigma_2$) is

$$\gamma^p = \frac{2}{3} (\varepsilon_1^p - \varepsilon_3^p) \quad (3.4)$$

Considering a state of pure shear ($\varepsilon_v^p = \varepsilon_1^p + \varepsilon_2^p + \varepsilon_3^p = 0$) leads to the simple relation

$$\varepsilon_1^p = -\frac{1}{2}\varepsilon_3^p \quad (3.5)$$

Substituting the pure shear version of the plastic strains (3.5) into the triaxial definition of the plastic shear strain (3.4) gives

$$\gamma^p = -\varepsilon_3^p \quad (3.6)$$

Finally, substituting (3.6) into the hyperbolic plastic strain (3.3) and rearranging gives a relation very similar in form to the yield surface in the original HS model

$$0 = \frac{q_a}{E_i} \frac{q}{q_a - q} - \frac{q}{E_{ur}} - \gamma^p \quad (3.7)$$

The aim of this section is to reformulate the shear yield surface in a similar fashion to classical plasticity models such as the Mohr-Coulomb or Drucker-Prager models. The yield function should take a form similar to the Mohr-Coulomb cone, however the hardening rule should control the steepness of the cone. To remain equivalent to the original HS models, the new criterion must:

- Harden from initial loading
- Produce triaxial compression shear curves which follow Kondner's hyperbola (Equation 3.1)
- Have a limiting shear stress which is below the asymptotic shear stress q_a of Kondner's hyperbola. The final position of the yield surface should also

coincide with the standard failure criterion (Mohr-Coulomb, or Matsuoka-Nakai)

To meet the first criterion, the hardening function should start from zero. To meet the third criterion, the hardening function should be limited to R_f . To match Kondner's hyperbola, the hardening function should be based on the plastic strain equilibrium in Equation 3.7. Basic manipulation of Equation 3.7 leads to the following relationship

$$\frac{q}{q_a - q} - \frac{qE_i}{q_a E_{ur}} - \frac{\gamma^p E_i}{q_a} = 0 \quad (3.8)$$

The following substitutions can be made:

$$r_q = \frac{q}{q_a} \quad (3.9)$$

$$r_u = \frac{E_{ur}}{E_i} \quad (3.10)$$

Leading to the quadratic equation

$$r_q - \frac{r_q}{r_u} (1 - r_q) - \frac{\gamma^p E_i}{q_a} (1 - r_q) = 0 \quad (3.11)$$

Solving for r_q in Equation 3.11 gives

$$r_q = \frac{1}{2} \left(1 - r_u + \frac{\gamma^p E_i r_u}{q_a} \right) + \frac{1}{2} \sqrt{\left(r_u - 1 - \frac{\gamma^p E_i r_u}{q_a} \right)^2 + \frac{4\gamma^p E_i r_u}{q_a}} \quad (3.12)$$

where r_q is also limited to an upper value of R_f . The hardening function is plotted in Figure 3.2 for different values of q_a to demonstrate that it is used to scale a failure criterion and is dimensionless. The hardening function has an abrupt limit

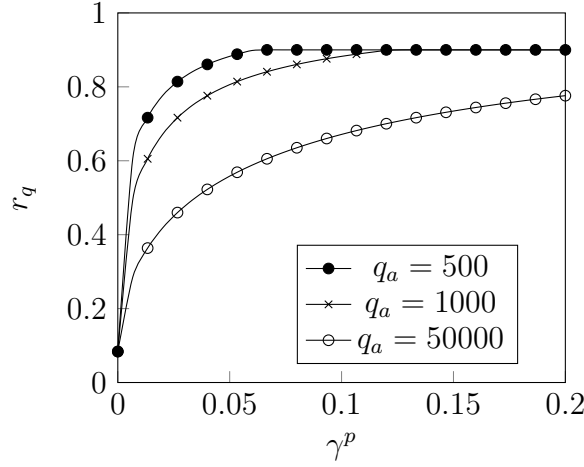


Figure 3.2: Shear surface hardening function with plastic shear strain ($R_f = 0.9$)

at $R_f = 0.9$ and increasing the asymptotic shear stress q_a effectively delays the reaching of this limit, and therefore soil failure when applied to the yield surface. To aid with convergence in load controlled tests, a small gradient G_f is given to r_q after reaching R_f . A value in the order $G_f = 10^{-6}$ would be suitable, depending on the convergence criteria adopted.

The yield function proposed by Panteghini and Lagioia (2013) is based on the Matsuoka-Nakai yield criterion (Equation 2.53), and formulated in terms of the more convenient stress invariants p , q and θ . The hardening function r_q is multiplied by the mean stress term.

$$f_s = q + \frac{Mr_q}{\rho R_f} (p - c \cot \varphi) \quad (3.13)$$

Including R_f in the denominator scales the hardening function to between 0 and 1, such that the final position of the yield surface is identical to the original failure criterion. ρ is the scaled Lode angle dependency function.

$$\rho = \frac{\Theta(\theta)}{\Theta(\pi/6)} \quad (3.14)$$

where Θ is the unscaled Lode angle dependency. ρ is scaled by dividing by the Lode dependency case for triaxial compression.

$$\Theta(\theta) = 2\sqrt{3} \cos \left[\frac{1}{3} \arccos(\xi \sin(-3\theta)) \right] \quad (3.15)$$

The parameter ξ is related to the friction angle at failure φ

$$\xi = \frac{\sin \varphi (9 - \sin^2 \varphi)}{(3 + \sin^2 \varphi)^{1.5}} \quad (3.16)$$

The parameter M from Equation 3.13 is defined as

$$M = \frac{3\sqrt{3}\eta}{\Theta(\pi/6)} \quad (3.17)$$

where

$$\eta = \frac{2 \sin \varphi}{\sqrt{3 + \sin^2 \varphi}} \quad (3.18)$$

This concludes the definition of the updated shear yield surface. As an alternative, the Mohr-Coulomb yield criterion can be used with the same hardening rule.

$$f_{s,MC} = \frac{r_q}{R_f} (p \sin(\varphi) - c \cos(\varphi)) + \frac{q}{\sqrt{3}} \left(\cos(\theta) - \frac{1}{\sqrt{3}} \sin(\theta) \sin(\varphi) \right) \quad (3.19)$$

Both yield functions are plotted in the π -plane (Figure 3.3), with different values of the hardening function for the smooth criterion. Both functions are also plotted in q - p stress space (Figure 3.4); the shape of both yield function plots are identical (in triaxial space) for all values of the hardening function r_q . In these examples, the friction angle is taken as $\varphi = 30^\circ$, the cohesion as $c = 10 \text{ kN/m}^2$, and the failure ratio $R_f = 0.9$.

It is also important to note that the yield loci in Figure 3.4 are straight. The original HS model produces curved lines for each given value of the hardening parameter

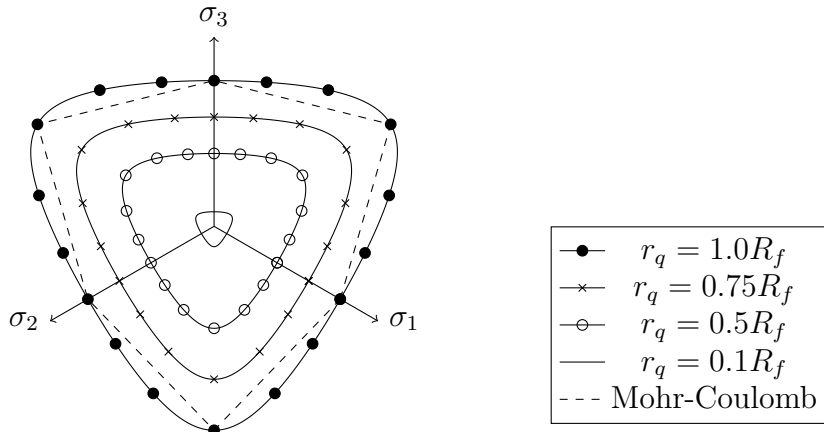


Figure 3.3: π -plane projection of the proposed yield surface with different values of hardening function r_q ; comparison with Mohr-Coulomb failure criterion

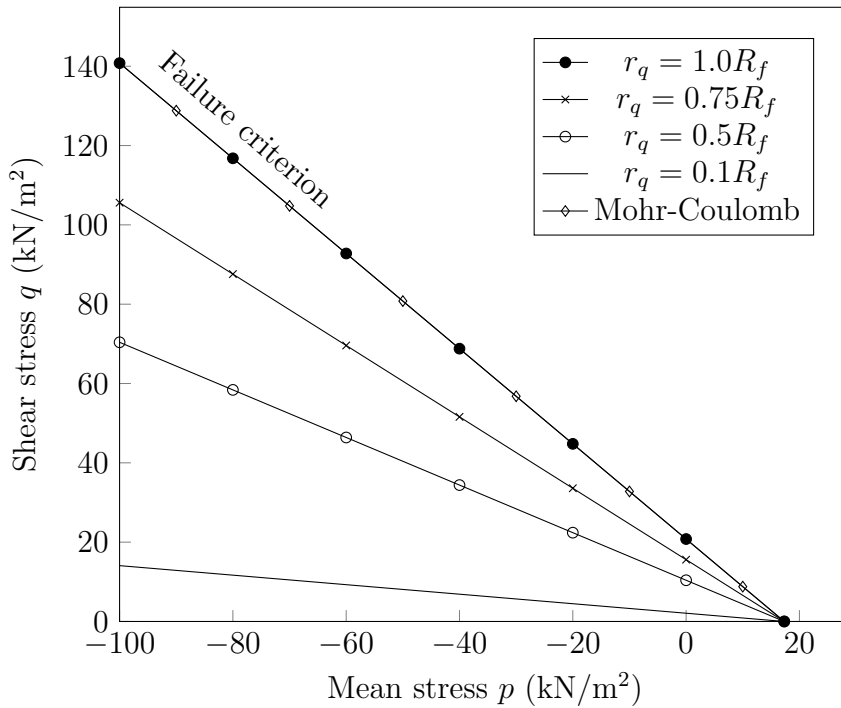


Figure 3.4: Yield surface for the proposed model (Equation 3.13) in q - p triaxial compression stress space, with different values of the hardening function r_q ; comparison with Mohr-Coulomb failure criterion

(see Benz, (2007) page 78).

The plastic potential function to the shear yield surface is the same as its yield function, except that the friction angle φ is replaced by the mobilised dilatancy angle ψ_m .

$$g_s = q + \frac{M_\psi r_q}{\rho_\psi R_f} (p - c \cot \varphi) \quad (3.20)$$

where

$$\rho_\psi = \frac{\Theta_\psi(\theta)}{\Theta_\psi(\pi/6)} \quad (3.21)$$

$$\Theta_\psi(\theta) = 2\sqrt{3} \cos \left[\frac{1}{3} \arccos (\xi_\psi \sin(-3\theta)) \right] \quad (3.22)$$

$$\xi_\psi = \frac{\sin \psi_m (9 - \sin^2 \psi_m)}{(3 + \sin^2 \psi_m)^{1.5}} \quad (3.23)$$

$$M_\psi = \frac{3\sqrt{3}\eta_\psi}{\Theta_\psi(\pi/6)} \quad (3.24)$$

$$\eta_\psi = \frac{2 \sin \psi_m}{\sqrt{3 + \sin^2 \psi_m}} \quad (3.25)$$

Alternatively, the approach used in the original HS implementation (Schanz et al., 1999) may be used; which is the Drucker-Prager cone surface, sized according to the mobilised dilatancy angle, as described in Equation 2.33.

3.3 Changes to the cap yield surface

The yield surface function of the cap surface remains identical to that proposed by Schanz et al. (1999), as shown in Equation 2.42. The shaping parameter χ relates to the terms used in the derivation of the shear yield surface in the HS-LC model by

$$\chi = \frac{M}{\rho} \left(\frac{3 - \sin \varphi}{6 \sin \varphi} \right) \quad (3.26)$$

The hardening of the cap surface remains in its incremental form as it was found that using a rule based on the total volumetric strain created a coupling effect with the shear yield surface, generating undesired behaviour. The following incremental form for the evolution of the cap surface is used

$$\frac{\partial p_p}{\partial \varepsilon_v^p} = \frac{K_s}{\frac{K_s}{K_c} - 1} \quad (3.27)$$

where K_s/K_c is an auxiliary parameter. In the HS-LC model, the value of K_s is dependent on the current unload-reload Young modulus E_{ur} instead of the reference modulus E_{ur}^{ref} used in the previous versions of the HS model.

$$K_s = \frac{E_{ur}}{3(1 - 2\nu_{ur})} \quad (3.28)$$

3.4 Tension yield surface

The previous versions of the HS model were formulated in principal stress space, and make use of a three-surface Rankine tension yield criterion (Equation 2.54). As the HS-LC model is formulated in general Cartesian stress space, it is more convenient to place a tensile limit on the mean stress:

$$f_t = p - \sigma_t \tag{3.29}$$

Similarly to the previous versions of the HS model, this tension surface is associated ($g_t \equiv f_t$) and does not harden.

3.5 Summary of the proposed model

Stiffness parameters

$$\text{Initial modulus: } E_i = E_i^{ref} \left(\frac{-\sigma_1 + c \cot(\varphi)}{-\sigma^{ref} + c \cot(\varphi)} \right)^m$$

$$\text{Unload-reload modulus: } E_{ur} = E_{ur}^{ref} \left(\frac{-\sigma_1 + c \cot(\varphi)}{-\sigma^{ref} + c \cot(\varphi)} \right)^m$$

Mobilised dilatancy

$$\text{Mobilised friction angle: } \sin(\varphi_m) = \frac{3q}{6\chi(p + c \cot(\varphi)) + q}$$

$$\text{Critical friction angle: } \sin(\varphi_c) = \frac{\sin(\varphi) - \sin(\psi)}{1 - \sin(\varphi) \sin(\psi)}$$

$$\text{Mobilised dilatancy angle: } \sin(\psi_m) = \frac{\sin(\varphi_m) - \sin(\varphi_c)}{1 - \sin(\varphi_m) \sin(\varphi_c)} \geq 0$$

Yield surfaces

$$\text{Shear: } f_s = q + \frac{Mr_q}{\rho R_f} (p - c \cot \varphi)$$

$$\text{Cap: } f_c = p^2 + \left(\frac{q}{\chi \alpha} \right)^2 - p_p^2$$

$$\text{Tension: } f_t = p - \sigma_t$$

Plastic potential surfaces

$$\text{Shear: } g_s = q + \frac{M_\psi r_q}{\rho_\psi R_f} (p - c \cot \varphi)$$

$$\text{Cap: } g_c = p^2 + \left(\frac{q}{\chi \alpha} \right)^2 - p_p^2$$

$$\text{Tension: } g_t = p - \sigma_t$$

Hardening rules

Shear: Related directly to plastic strains

$$\text{Cap: } \frac{\partial p_p}{\partial \varepsilon_v^p} = \frac{K_s}{\frac{K_s}{K_c} - 1}$$

Tension: No hardening

3.6 Auxiliary parameters

All versions of the HS model require calibration to a set of given parameters. These given parameters are:

- Oedometer modulus E_{oed}^{ref}
- Lateral earth pressure coefficient K_0
- Secant modulus E_{50}^{ref}

The auxiliary parameters used to calibrate the model are:

- Bulk stiffness ratio K_s/K_c
- Cap steepness α
- Initial stiffness E_i^{ref}

Each auxiliary parameter affects the calculated values of all three given parameters, therefore calculation of these parameters is non-trivial. However, the initial stiffness E_i^{ref} primarily affects the secant stiffness E_{50}^{ref} , and the other two parameters both affect K_0 and E_{oed}^{ref} similarly.

The reason for including the secant modulus calibration is that the influence of the cap in the model changes the predicted value of E_{50} throughout the simulation. The initial stiffness can be used to modify the initial gradients of a triaxial curve, in order to achieve the desired secant modulus.

The auxiliary parameters are also dependent on the other material parameters, therefore the relationship between the calibration parameters and auxiliary parameters is difficult to define for all possible sets of material properties.

A procedure has been adopted to calculate these parameters. First, the auxiliary parameters are given nominal values, an oedometer simulation is run up to the

reference stress σ^{ref} , and a triaxial simulation with a confining stress of σ^{ref} is run. The secant modulus is calculated from the triaxial results using $E_{50}^{ref} = q_{50}/\varepsilon_{50}$. The lateral earth pressure coefficient K_0 is calculated from the ratio between the horizontal and vertical stresses generated in the oedometer simulation $K_0 = \sigma_x/\sigma_y$. The calculated value of K_0 may vary slightly throughout the test and the average value is taken. The oedometer modulus E_{oed}^{ref} is also calculated from the oedometer simulation by calculating the gradient of the stress-strain curve at the reference stress $E_{oed}^{ref} = \sigma^{ref}/\varepsilon^{ref}$.

The values are varied using trial and improvement until the calculated values of E_{oed}^{ref} , E_{50}^{ref} , and K_0 match those supplied by the user. The HS model is quite sensitive to these parameters, therefore adequate calibration is crucial. Benz (2007) published auxiliary parameters used in simulations. As the model described here differs from the original formulations, the auxiliary parameters will also differ; however, they are calibrated to the same set of given parameters.

3.7 Summary of parameters in the HS-LC model

Each of the parameters discussed in this section are summarised in Table 3.1. Calibration parameters are not used directly in the model, however, the auxiliary parameters are adjusted to match predicted results with the calibration parameters.

Table 3.1: Material parameters used in the different versions of the HS model

Symbol	Name	Units / Notes	HS	HS-smooth	HS-LC
E_{ur}^{ref}	Unload-reload reference modulus	kN/m ²	✓	✓	✓
E_i^{ref}	Initial reference modulus	kN/m ² <i>auxiliary</i>		✓	✓
E_{50}^{ref}	Secant reference modulus	kN/m ² <i>calibration</i>	✓	✓	✓
E_{oed}^{ref}	Oedometer reference modulus	kN/m ² <i>calibration</i>	✓	✓	✓
σ^{ref}	Reference stress	kN/m ²	✓	✓	✓
m	Stress dependency exponent		✓	✓	✓
c	Cohesion	kN/m ²	✓	✓	✓
φ	Friction angle at failure	°	✓	✓	✓
ψ	Dilatancy angle	°	✓	✓	✓
ν	Poisson ratio		✓	✓	✓
K_0	Lateral earth pressure coefficient	<i>calibration</i>	✓	✓	✓
R_f	Asymptote failure ratio		✓	✓	✓
σ_t	Tensile limit	kN/m ²		✓	✓
α	Cap shape parameter	<i>auxiliary</i>	✓	✓	✓
K_s/K_c	Cap hardening parameter	<i>auxiliary</i>	✓	✓	✓
e_0	Initial void ratio		✓		✓
e_c	Critical void ratio		✓		✓

3.8 The closest point projection method

The HS-LC model has now been fully defined, and several options are available for the management of stress equilibrium during plastic loading. The purpose of stress return algorithms is to calculate the portion of the given strain step which

is plastic, two main categories of stress return algorithms are described below. It is worth noting that the following descriptions are based on a pre-calculation of a trial stress state, for which a stress state is assumed based on pure elastic loading. Other options are available (such as sub-stepping or step size control) but are not considered here.

Explicit algorithms: A strain step here works from the current step; the gradients of the yield surface(s) and plastic potential(s) are calculated from the current position. An example of this method is the cutting plane algorithm. This algorithm is described in detail by Simo and Hughes (2006) and Huang and Griffiths (2009). The main advantage of this method is its simplicity and the use of first order gradients only. However, as the gradients are calculated at the current state, the mapped return path may diverge from the yield surface if the step size is too large.

Implicit algorithms: The key difference with implicit algorithms is that the yield function and plastic potential gradients are always calculated at the subsequent step. This way, the solution will always be returned to the yield surface, regardless of the step size (subject to no numerical errors). Simo and Hughes (2006) and Huang and Griffiths (2009) describe this method, which is also employed by Benz (2007) in his formulation of the HS model.

The closest point projection (CPP) method, which is classed as a backward Euler method, is an implicit stress return mapping scheme. The returned stress path is based on the gradients at the final stress state (Figure 3.5).

A trial stress is calculated using the elastic stiffness matrix, the last converged stress and the strain increment.

$$\boldsymbol{\sigma}_{tr} = \boldsymbol{\sigma}_{LC} + \boldsymbol{D}_e \Delta \boldsymbol{\varepsilon} \quad (3.30)$$

As the functions governing the size and shape of the yield surfaces are non-linear,

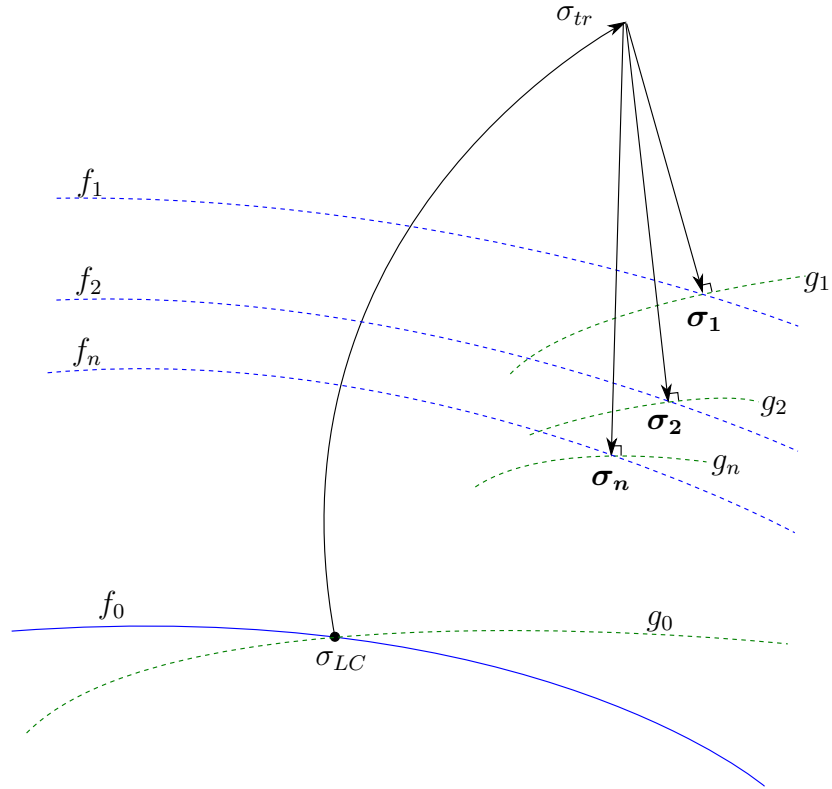


Figure 3.5: The closest point projection method

and hardening is active, an iterative process is used. The aim of the CPP method is to satisfy the equilibrium conditions:

$$f(\boldsymbol{\sigma}, \boldsymbol{\mu}) \leq 0 \quad (3.31)$$

$$\Delta\lambda \geq 0 \quad (3.32)$$

$$\Delta\lambda f(\boldsymbol{\sigma}, \boldsymbol{\mu}) = 0 \quad (3.33)$$

where $f(\boldsymbol{\sigma}, \boldsymbol{\mu})$ is the yield function which forms a surface in 3-D stress space, $\boldsymbol{\sigma}$ is the converged stress state, $\boldsymbol{\mu}$ represents one or more state variables which define the position of the yield surface and $\Delta\lambda$ is the plasticity multiplier which governs the size of the plastic strain steps.

As there are several yield surfaces present in the hardening soil model, and the evolution rules take different forms (Figure 3.6), a separate CPP algorithm is required for each yield surface and each possible combination of yield surfaces. The formulation of the CPP algorithms are documented in the following sections.

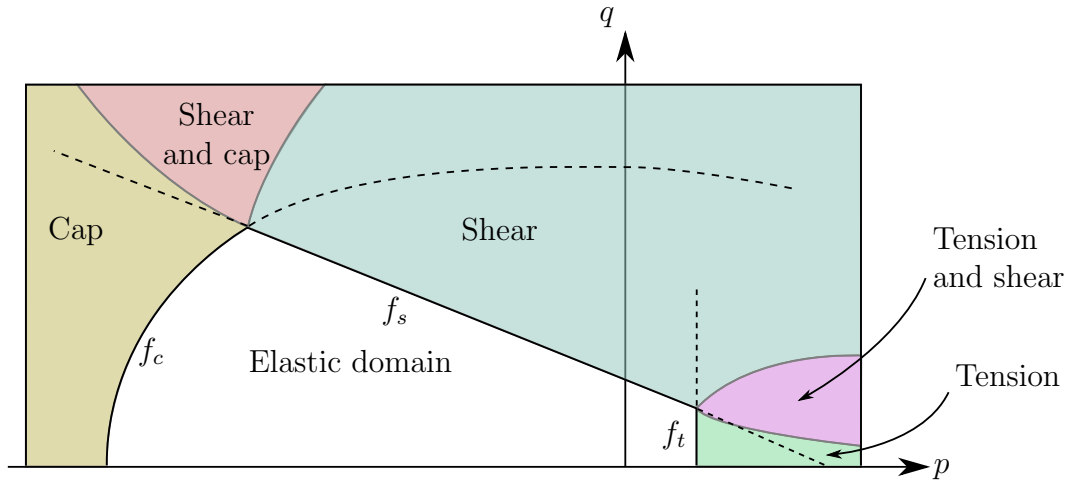


Figure 3.6: Yield surfaces in the HS model and their approximate stress return zones

3.8.1 CPP algorithms

The formulation of the CPP algorithms used in the HS-LC are described in this section. The full algorithms for each yield surface and each possible combination of yield surfaces are detailed in the Appendix (starting on page 239).

3.8.1.1 Shear surface return

The objective of the CPP algorithm for the shear surface is to satisfy the yield criterion. This yield function uses the plastic strains directly to drive the hardening rule.

$$f_s(\boldsymbol{\sigma}, \boldsymbol{\sigma}_{LC}, \boldsymbol{\varepsilon}^p) = 0 \quad (3.34)$$

The plastic strain residual is given by

$$\mathbf{R} = -\Delta\boldsymbol{\varepsilon}^p + \Delta\lambda \frac{\partial g_s}{\partial \boldsymbol{\sigma}} = \mathbf{0} \quad (3.35)$$

Expanding (3.35) as a Taylor's series, and substituting $d\Delta\lambda = \delta\lambda$ gives

$$\mathbf{R} + \delta\mathbf{R} = \mathbf{R} - \delta\varepsilon^p + \delta\lambda \frac{\partial g_s}{\partial \boldsymbol{\sigma}} + \Delta\lambda \frac{\partial^2 g_s}{\partial \boldsymbol{\sigma}^2} \delta\boldsymbol{\sigma} = \mathbf{0} \quad (3.36)$$

Rearranging to obtain the plastic strain increment

$$\delta\varepsilon^p = \mathbf{R} + \delta\lambda \frac{\partial g_s}{\partial \boldsymbol{\sigma}} + \Delta\lambda \frac{\partial^2 g_s}{\partial \boldsymbol{\sigma}^2} \delta\boldsymbol{\sigma} \quad (3.37)$$

Expanding (3.34) as a Taylor's series

$$f_s + \frac{\partial f_s^T}{\partial \boldsymbol{\sigma}} \delta\boldsymbol{\sigma} + \frac{\partial f_s^T}{\partial \varepsilon^p} \delta\varepsilon^p = 0 \quad (3.38)$$

Substituting the plastic strain increment (3.37) into (3.38)

$$f_s + \frac{\partial f_s^T}{\partial \boldsymbol{\sigma}} \delta\boldsymbol{\sigma} + \frac{\partial f_s^T}{\partial \varepsilon^p} \left(\mathbf{R} + \delta\lambda \frac{\partial g_s}{\partial \boldsymbol{\sigma}} + \Delta\lambda \frac{\partial^2 g_s}{\partial \boldsymbol{\sigma}^2} \delta\boldsymbol{\sigma} \right) = 0 \quad (3.39)$$

Grouping the $\delta\boldsymbol{\sigma}$ gives

$$f_s + \mathbf{F}_s^T \delta\boldsymbol{\sigma} + \frac{\partial f_s^T}{\partial \varepsilon^p} \left(\mathbf{R} + \delta\lambda \frac{\partial g_s}{\partial \boldsymbol{\sigma}} \right) = 0 \quad (3.40)$$

where

$$\mathbf{F}_s^T = \frac{\partial f_s^T}{\partial \boldsymbol{\sigma}} + \Delta\lambda \frac{\partial f_s^T}{\partial \varepsilon^p} \frac{\partial^2 g_s}{\partial \boldsymbol{\sigma}^2} \quad (3.41)$$

During the CPP iterations, the change in stress between iterations is

$$\delta\boldsymbol{\sigma} = -\mathbf{D}_e \delta\varepsilon^p \quad (3.42)$$

Substituting the plastic strain increment (3.37) into (3.42)

$$\delta\boldsymbol{\sigma} = -\mathbf{D}_e \left(\mathbf{R} + \delta\lambda \frac{\partial g_s}{\partial \boldsymbol{\sigma}} + \Delta\lambda \frac{\partial^2 g_s}{\partial \boldsymbol{\sigma}^2} \delta\boldsymbol{\sigma} \right) \quad (3.43)$$

Rearranging (3.43) gives

$$\delta\boldsymbol{\sigma} = -\mathbf{A}_e \left(\mathbf{R} + \delta\lambda \frac{\partial g_s}{\partial \boldsymbol{\sigma}} \right) \quad (3.44)$$

where

$$\mathbf{A}_e = \left(\mathbf{I} + \Delta\lambda \mathbf{D}_e \frac{\partial^2 g_s}{\partial \boldsymbol{\sigma}^2} \right)^{-1} \mathbf{D}_e \quad (3.45)$$

and \mathbf{I} is the identity matrix. Finally, the plasticity multiplier is calculated through substitution of (3.44) into (3.40) and rearranging for $\delta\lambda$.

$$\delta\lambda = \frac{f_s - \mathbf{F}_s^T \mathbf{A}_e \mathbf{R} + \frac{\partial f_s}{\partial \boldsymbol{\varepsilon}^p}{}^T \mathbf{R}}{\mathbf{F}_s^T \mathbf{A}_e \frac{\partial g_s}{\partial \boldsymbol{\sigma}} - \frac{\partial f_s}{\partial \boldsymbol{\varepsilon}^p}{}^T \frac{\partial g_s}{\partial \boldsymbol{\sigma}}} \quad (3.46)$$

The consistent tangent matrix is found by determining the relationship between incremental stresses and strains for a particular state.

$$d\boldsymbol{\sigma} = \mathbf{D}_e (d\boldsymbol{\varepsilon} - d\boldsymbol{\varepsilon}^p) \quad (3.47)$$

During the formulation of the consistent tangent, it is assumed that the stress state is on the yield surface ($f = 0$) and the residuals \mathbf{R} are equal to zero. Substitution of the previously defined relationships leads to the consistent tangent matrix in the form:

$$\mathbf{D}^{ep} = \frac{d\boldsymbol{\sigma}}{d\boldsymbol{\varepsilon}} = \mathbf{A}_e - \frac{\mathbf{A}_e \frac{\partial g_s}{\partial \boldsymbol{\sigma}} \mathbf{F}_s^T \mathbf{A}_e}{\mathbf{F}_s^T \mathbf{A}_e \frac{\partial g_s}{\partial \boldsymbol{\sigma}} - \frac{\partial f_s}{\partial \boldsymbol{\varepsilon}^p}{}^T \frac{\partial g_s}{\partial \boldsymbol{\sigma}}} \quad (3.48)$$

3.8.1.2 Cap surface return

Due to the incremental form of the cap surface hardening rule, the CPP algorithm to the cap surface is slightly different to that of the shear surface. Many of the terms in the cap CPP algorithm are identical to the shear surface; only with the subscript changing from f_s to f_c , for example. An additional residual is required for the hardening parameter, the CPP algorithm for the cap surface must also reduce this to zero

$$R_h = -\Delta p_p + \Delta\lambda \frac{\partial p_p}{\partial \varepsilon_v^p} \frac{\partial \varepsilon_v^p}{\partial \boldsymbol{\varepsilon}^p} \frac{\partial g_c}{\partial \boldsymbol{\sigma}} = 0 \quad (3.49)$$

The Taylor series expansion of (3.49) leads to the definition of the hardening parameter increment

$$\delta p_p = R_h + \frac{\partial p_p}{\partial \varepsilon_v^p} \frac{\partial \varepsilon_v^p}{\partial \boldsymbol{\varepsilon}^p} \left(\delta\lambda \frac{\partial g_c}{\partial \boldsymbol{\sigma}} + \Delta\lambda \frac{\partial^2 g_c}{\partial \boldsymbol{\sigma}^2} \boldsymbol{\delta\sigma} \right) \quad (3.50)$$

The expansion of the yield function is also different to accommodate the inclusion of only the hardening parameter instead of the plastic strains.

$$f_c + \frac{\partial f_c}{\partial \boldsymbol{\sigma}} \boldsymbol{\delta\sigma} + \frac{\partial f_c}{\partial p_p} \delta p_p = 0 \quad (3.51)$$

Substituting (3.50) into (3.51) and grouping the $\boldsymbol{\delta\sigma}$ terms gives

$$f_c + \mathbf{F}_c^T \boldsymbol{\delta\sigma} + \frac{\partial f_c}{\partial p_p} \left(R_h + \delta\lambda \frac{\partial p_p}{\partial \varepsilon_v^p} \frac{\partial \varepsilon_v^p}{\partial \boldsymbol{\varepsilon}^p} \frac{\partial g_c}{\partial \boldsymbol{\sigma}} \right) = 0 \quad (3.52)$$

where

$$\mathbf{F}_c^T = \frac{\partial f_c}{\partial \boldsymbol{\sigma}} + \Delta\lambda \frac{\partial f_c}{\partial p_p} \frac{\partial p_p}{\partial \varepsilon_v^p} \frac{\partial \varepsilon_v^p}{\partial \boldsymbol{\varepsilon}^p} \frac{\partial^2 g_c}{\partial \boldsymbol{\sigma}^2} \quad (3.53)$$

Substituting the stress increment relation in Equation 3.44 (with the cap surface

subscript) and rearranging gives the increment of the plasticity multiplier.

$$\delta\lambda = \frac{f_c - \mathbf{F}_c^T \mathbf{A}_e \mathbf{R} + \frac{\partial f_c}{\partial p_p} R_h}{\mathbf{F}_c^T \mathbf{A}_e \frac{\partial g_c}{\partial \boldsymbol{\sigma}} - \frac{\partial f_c}{\partial p_p} \frac{\partial p_p}{\partial \varepsilon_v^p} \frac{\partial \varepsilon_v^p}{\partial \boldsymbol{\varepsilon}^p} \frac{\partial g_c}{\partial \boldsymbol{\sigma}}} \quad (3.54)$$

The consistent tangent matrix for the cap surface is as follows

$$\mathbf{D}^{ep} = \mathbf{A}_e - \frac{\mathbf{A}_e \frac{\partial g_c}{\partial \boldsymbol{\sigma}} \mathbf{F}_c^T \mathbf{A}_e}{\mathbf{F}_c^T \mathbf{A}_e \frac{\partial g_c}{\partial \boldsymbol{\sigma}} - \frac{\partial f_c}{\partial p_p} \frac{\partial p_p}{\partial \varepsilon_v^p} \frac{\partial \varepsilon_v^p}{\partial \boldsymbol{\varepsilon}^p} \frac{\partial g_c}{\partial \boldsymbol{\sigma}}} \quad (3.55)$$

3.8.1.3 Tension surface return

The CPP algorithm for the tension surface is very similar to the shear surface algorithm, however as there is no hardening in this surface therefore some of the terms used in the algorithm reduce to zero. As previously, only significant changes from the shear surface formulation will be described here. The second derivatives of the plastic potential are also zero, however they have been included here in case of future change. One significant difference from the shear surface algorithm is that the Taylor series expansion of the yield criterion does not include a hardening term

$$f_t + \frac{\partial f_t}{\partial \boldsymbol{\sigma}} \boldsymbol{\delta} \boldsymbol{\sigma} = 0 \quad (3.56)$$

The $\boldsymbol{\delta} \boldsymbol{\sigma}$ terms do not need to be grouped in this case, however, this is done here to provide consistency between each surface formulation.

$$\mathbf{F}_t^T = \frac{\partial f_t}{\partial \boldsymbol{\sigma}} \quad (3.57)$$

The plasticity multiplier does not contain any hardening terms

$$\delta\lambda = \frac{f_t - \mathbf{F}_t^T \mathbf{A}_e \mathbf{R}}{\mathbf{F}_t^T \mathbf{A}_e \frac{\partial g_t}{\partial \boldsymbol{\sigma}}} \quad (3.58)$$

Similarly with the consistent tangent matrix

$$\mathbf{D}^{ep} = \mathbf{A}_e - \frac{\mathbf{A}_e \frac{\partial g_t}{\partial \boldsymbol{\sigma}} \mathbf{F}_t^T \mathbf{A}_e}{\mathbf{F}_t^T \mathbf{A}_e \frac{\partial g_t}{\partial \boldsymbol{\sigma}}} \quad (3.59)$$

3.8.1.4 Shear and cap surface return

When the shear and cap surfaces are both active, the stress state must return to the line which is the intersection of both surfaces. As the cap surface is uncoupled from the shear surface, its formulation remains identical to before. The terms relating to the shear surface must change to take into account the modified plastic strain increment. The calculation of the plasticity multipliers also changes to take into account the double return strategy. The total plastic strain residual now incorporates hardening from both surfaces

$$\mathbf{R} = -\Delta \boldsymbol{\varepsilon}^p + \Delta \lambda_s \frac{\partial g_s}{\partial \boldsymbol{\sigma}} + \Delta \lambda_c \frac{\partial g_c}{\partial \boldsymbol{\sigma}} = \mathbf{0} \quad (3.60)$$

Expanding (3.60) as a Taylor series and simplifying leads to a form of the plastic strain increment which involves both surfaces.

$$\delta \boldsymbol{\varepsilon}^p = \mathbf{R} + \delta \lambda_s \frac{\partial g_s}{\partial \boldsymbol{\sigma}} + \delta \lambda_c \frac{\partial g_c}{\partial \boldsymbol{\sigma}} + \left(\Delta \lambda_s \frac{\partial^2 g_s}{\partial \boldsymbol{\sigma}^2} + \Delta \lambda_c \frac{\partial^2 g_c}{\partial \boldsymbol{\sigma}^2} \right) \delta \boldsymbol{\sigma} \quad (3.61)$$

The expansion of the shear and cap yield surfaces remains identical to (3.38) and (3.51) respectively, however the new definition of the plastic strain increment (3.61) must be substituted into (3.38). Grouping the $\delta \boldsymbol{\sigma}$ after this substitution leads to

$$f_s + \mathbf{F}_s^T \delta \boldsymbol{\sigma} + \frac{\partial f_s}{\partial \boldsymbol{\varepsilon}^p} \left(\mathbf{R} + \delta \lambda_s \frac{\partial g_s}{\partial \boldsymbol{\sigma}} + \delta \lambda_c \frac{\partial g_c}{\partial \boldsymbol{\sigma}} \right) = 0 \quad (3.62)$$

where

$$\mathbf{F}_s^T = \frac{\partial f_s^T}{\partial \boldsymbol{\sigma}} + \frac{\partial f_s^T}{\partial \boldsymbol{\varepsilon}^p} \left(\Delta \lambda_s \frac{\partial^2 g_s}{\partial \boldsymbol{\sigma}^2} + \Delta \lambda_c \frac{\partial^2 g_c}{\partial \boldsymbol{\sigma}^2} \right) \quad (3.63)$$

The 2-surface form of the plastic strain increment (3.61) is now substituted into the incremental stress relationship (3.42).

$$\delta \boldsymbol{\sigma} = -\mathbf{D}_e \left[\mathbf{R} + \delta \lambda_s \frac{\partial g_s}{\partial \boldsymbol{\sigma}} + \delta \lambda_c \frac{\partial g_c}{\partial \boldsymbol{\sigma}} + \left(\Delta \lambda_s \frac{\partial^2 g_s}{\partial \boldsymbol{\sigma}^2} + \Delta \lambda_c \frac{\partial^2 g_c}{\partial \boldsymbol{\sigma}^2} \right) \delta \boldsymbol{\sigma} \right] \quad (3.64)$$

The stress increment is simplified to

$$\delta \boldsymbol{\sigma} = -\mathbf{A}_e \left(\mathbf{R} + \delta \lambda_s \frac{\partial g_s}{\partial \boldsymbol{\sigma}} + \delta \lambda_c \frac{\partial g_c}{\partial \boldsymbol{\sigma}} \right) \quad (3.65)$$

where

$$\mathbf{A}_e = \left(\mathbf{I} + \Delta \lambda_s \mathbf{D}_e \frac{\partial^2 g_s}{\partial \boldsymbol{\sigma}^2} + \Delta \lambda_c \mathbf{D}_e \frac{\partial^2 g_c}{\partial \boldsymbol{\sigma}^2} \right)^{-1} \mathbf{D}_e \quad (3.66)$$

Substituting (3.65) into (3.62) and (3.52), then rearranging into matrix form gives an expression for the plasticity multipliers to be solved.

$$\begin{bmatrix} f_s - \mathbf{F}_s^T \mathbf{A}_e \mathbf{R} + \frac{\partial f_s}{\partial \boldsymbol{\varepsilon}^p} \mathbf{R} \\ f_c - \mathbf{F}_c^T \mathbf{A}_e \mathbf{R} + \frac{\partial f_c}{\partial p_p} R_h \end{bmatrix} = \begin{bmatrix} \mathbf{F}_s^T \mathbf{A}_e \frac{\partial g_s}{\partial \boldsymbol{\sigma}} - \frac{\partial f_s^T}{\partial \boldsymbol{\varepsilon}^p} \frac{\partial g_s}{\partial \boldsymbol{\sigma}} & \mathbf{F}_s^T \mathbf{A}_e \frac{\partial g_c}{\partial \boldsymbol{\sigma}} - \frac{\partial f_s^T}{\partial \boldsymbol{\varepsilon}^p} \frac{\partial g_c}{\partial \boldsymbol{\sigma}} \\ \mathbf{F}_c^T \mathbf{A}_e \frac{\partial g_s}{\partial \boldsymbol{\sigma}} & \mathbf{F}_c^T \mathbf{A}_e \frac{\partial g_c}{\partial \boldsymbol{\sigma}} - \frac{\partial f_c}{\partial p_p} \frac{\partial p_p}{\partial \boldsymbol{\varepsilon}_v^p} \frac{\partial \boldsymbol{\varepsilon}_v^p}{\partial \boldsymbol{\varepsilon}^p} \frac{\partial g_c}{\partial \boldsymbol{\sigma}} \end{bmatrix} \begin{bmatrix} \delta \lambda_s \\ \delta \lambda_c \end{bmatrix} \quad (3.67)$$

The following substitution can be used:

$$\mathbf{\Omega}_f = \mathbf{\Omega} \begin{bmatrix} \delta\lambda_s \\ \delta\lambda_c \end{bmatrix} \quad (3.68)$$

3.8.1.5 Shear and tension surface return

The implementation of the shear and tension CPP algorithm is very similar to the shear and cap algorithm, however, as the tension surface does not exhibit any hardening, some of the expressions are simplified. There is also no hardening parameter residual to consider.

The Taylor series expansion of the tension yield criteria is identical to the single surface version (3.56). The plastic strain increment is similar to that of the shear and cap algorithm (3.61) and substitution into the incremental stress relation (3.42) gives

$$\delta\boldsymbol{\sigma} = -\mathbf{D}_e \left[\mathbf{R} + \delta\lambda_s \frac{\partial g_s}{\partial \boldsymbol{\sigma}} + \delta\lambda_t \frac{\partial g_t}{\partial \boldsymbol{\sigma}} + \left(\Delta\lambda_s \frac{\partial^2 g_s}{\partial \boldsymbol{\sigma}^2} + \Delta\lambda_t \frac{\partial^2 g_t}{\partial \boldsymbol{\sigma}^2} \right) \delta\boldsymbol{\sigma} \right] \quad (3.69)$$

Simplifying leads to

$$\delta\boldsymbol{\sigma} = -\mathbf{A}_e \left(\mathbf{R} + \delta\lambda_s \frac{\partial g_s}{\partial \boldsymbol{\sigma}} + \delta\lambda_t \frac{\partial g_t}{\partial \boldsymbol{\sigma}} \right) \quad (3.70)$$

where

$$\mathbf{A}_e = \left(\mathbf{I} + \Delta\lambda_s \mathbf{D}_e \frac{\partial^2 g_s}{\partial \boldsymbol{\sigma}^2} + \Delta\lambda_t \mathbf{D}_e \frac{\partial^2 g_t}{\partial \boldsymbol{\sigma}^2} \right)^{-1} \mathbf{D}_e \quad (3.71)$$

Substituting (3.70) into the previous expansions for each surface (3.40) and (3.56) (with the modified subscripts), then rearranging into matrix form gives the expression for the plasticity multipliers.

$$\begin{bmatrix} f_s - \mathbf{F}_s^T \mathbf{A}_e \mathbf{R} + \frac{\partial f_s}{\partial \varepsilon^p} \mathbf{R} \\ f_t - \mathbf{F}_t^T \mathbf{A}_e \mathbf{R} \end{bmatrix} = \begin{bmatrix} \mathbf{F}_s^T \mathbf{A}_e \frac{\partial g_s}{\partial \sigma} - \frac{\partial f_s}{\partial \varepsilon^p} \frac{\partial g_s}{\partial \sigma} & \mathbf{F}_s^T \mathbf{A}_e \frac{\partial g_t}{\partial \sigma} - \frac{\partial f_s}{\partial \varepsilon^p} \frac{\partial g_t}{\partial \sigma} \\ \mathbf{F}_t^T \mathbf{A}_e \frac{\partial g_s}{\partial \sigma} & \mathbf{F}_t^T \mathbf{A}_e \frac{\partial g_t}{\partial \sigma} \end{bmatrix} \begin{bmatrix} \delta \lambda_s \\ \delta \lambda_t \end{bmatrix} \quad (3.72)$$

The selection of which surface(s) to return is complex, as a simple zoning method (Figure 3.6) cannot be used. Section 3.8.3 describes the algorithm used in the HS-LC model which selects the active yield surface(s) based on a trial and error approach. This method is very similar to that described by Benz (2007).

3.8.2 Consistent tangent matrix

The consistent tangent matrix (CTM) relates infinitesimal stresses and strains (3.73). It is used to calculate the stress gradients when one or more yield surfaces are active. An important benefit of using the CTM is the preservation of the quadratic rate of convergence in the global Newton-Raphson iterative scheme.

Much of the theory for defining the consistent tangent matrix is discussed already, however it is worth noting that in the formulation of the CTM, the stress state is assumed to already be on one or more yield surfaces and the residuals relating to the active surface(s) are zero. The plasticity multiplier(s) $\Delta\lambda$ from the previous iteration are also required. The consistent tangent is defined as:

$$\mathbf{D}_{ep} = \frac{d\sigma}{d\varepsilon} \quad (3.73)$$

If the stress state lies on a single yield surface, then the consistent tangent is given as

$$\mathbf{D}_{ep} = \mathbf{A}_e - \frac{\mathbf{A}_e \frac{\partial g}{\partial \boldsymbol{\sigma}} \mathbf{F}^T \mathbf{A}_e}{\mathbf{F}^T \mathbf{A}_e \frac{\partial g}{\partial \boldsymbol{\sigma}} - \frac{\partial f}{\partial \boldsymbol{\varepsilon}_p}^T \frac{\partial g}{\partial \boldsymbol{\sigma}}} \quad (3.74)$$

When two surfaces are active, a more complex approach is used which takes into account the gradients and hardening rules from both surfaces.

$$\begin{aligned} \mathbf{D}_{ep} = \mathbf{A}_e &- (\Omega^{-1})_{1,1} \mathbf{A}_e \frac{\partial g_1}{\partial \boldsymbol{\sigma}} \mathbf{F}_1^T \mathbf{A}_e - (\Omega^{-1})_{1,2} \mathbf{A}_e \frac{\partial g_1}{\partial \boldsymbol{\sigma}} \mathbf{F}_2^T \mathbf{A}_e \\ &- (\Omega^{-1})_{2,1} \mathbf{A}_e \frac{\partial g_2}{\partial \boldsymbol{\sigma}} \mathbf{F}_1^T \mathbf{A}_e - (\Omega^{-1})_{2,2} \mathbf{A}_e \frac{\partial g_2}{\partial \boldsymbol{\sigma}} \mathbf{F}_2^T \mathbf{A}_e \end{aligned} \quad (3.75)$$

Single vector subscripts 1 and 2 may be replaced by s , c , or t , depending on which surfaces are currently active. The subscripts in Ω remain as 1 and 2.

The CTM is non-symmetric in the HS model whenever the shear surface is active, this is because the shear surface uses a non-associated flow rule. The CTM for the cap and tension surfaces are symmetric. The terms in Ω are also non-symmetric when returning to the shear and cap surfaces, as their hardening rules are based on total plastic strains, and incremental plastic strains respectively.

3.8.3 Return strategy

Due to the nature of the hardening rules in the HS model, a simple zoning approach cannot be used. Figure 3.6 indicates the problem with using a zoning method; the actual zones do not necessarily correspond to the gradients of each yield surface. Therefore, a trial and error approach is adopted. The full return strategy is described in Figure 3.7.

The most dominant surface in the HS model is the shear surface. For example, when a trial stress state yields both the shear and cap surface, after returning to the shear yield surface, the cap surface is often no longer active.

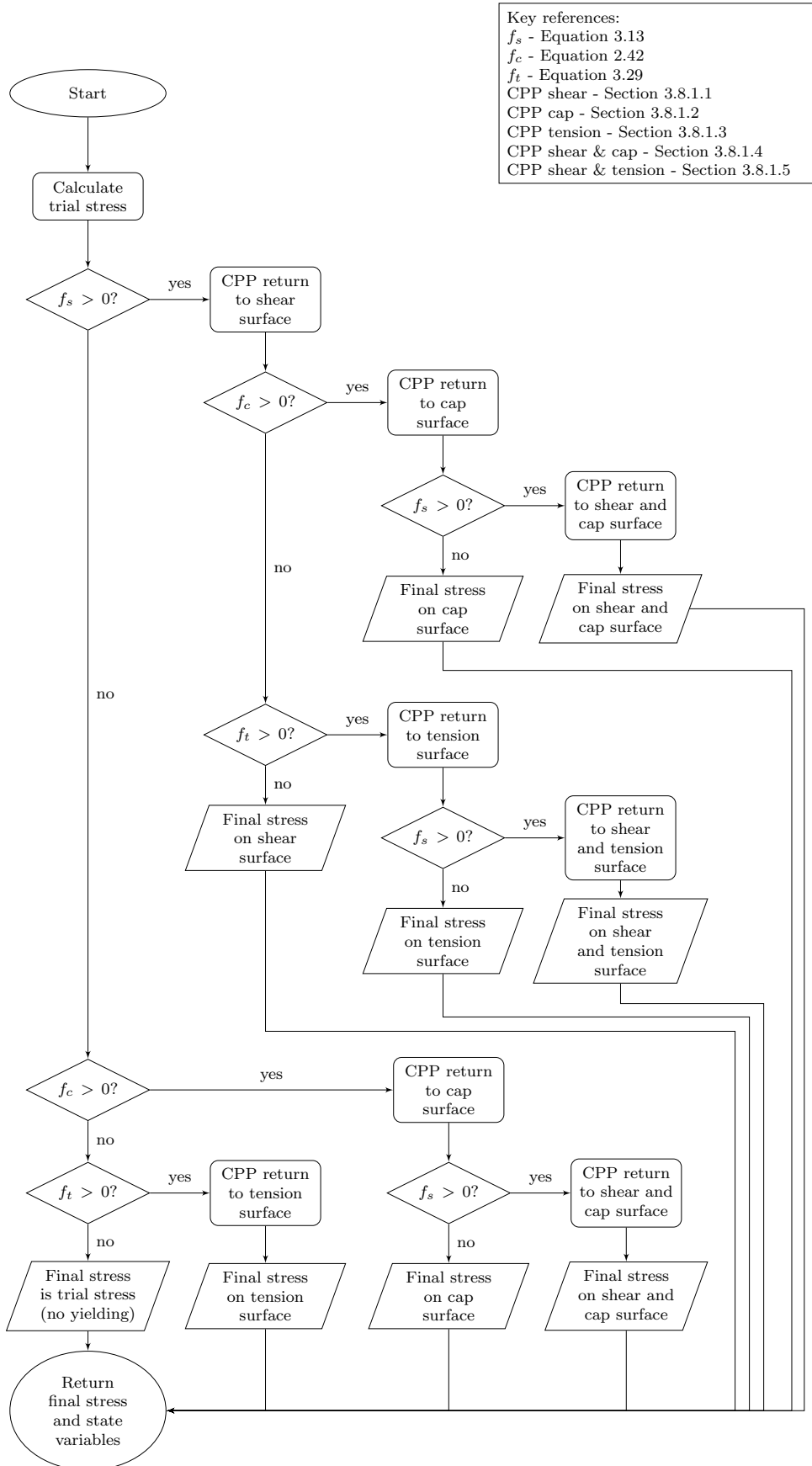


Figure 3.7: Return mapping algorithm used in the HS-LC model

3.9 Stiffness update

The Young modulus used in the elastic stiffness matrix and shear yield function is dependent on the minor principal stress σ_1 . A stress of zero in the standard HS formulation leads to a stiffness of zero. This presents a numerical difficulty which can be solved by imposing a lower limit to the soil stiffness.

In the proposed formulation of the HS model, this limit is applied by using the atmospheric pressure p_a as an input parameter, and minimising the stress used in the Young modulus calculation to a factor of the atmospheric pressure. With this new model, Equation 2.1 becomes:

$$E_{50} = E_{50}^{ref} \left(\frac{-\min(\sigma_1, Y_f p_a) + c \cot(\varphi)}{-\sigma^{ref} + c \cot(\varphi)} \right)^m \quad (3.76)$$

and similarly for the other Young moduli. By default, $p_a = -100 \text{ kN/m}^2$ is a reasonable approximation of the atmospheric pressure, and $Y_f = 0.001$ is a suitable value for the minimum factor which does not significantly affect results after the stress increases above this level.

During testing of the HS-LC model (discussed later in Chapter 4), it was found that some step size dependency occurred in certain simulations, namely oedometer tests where a soil is subject to confined vertical loading. In the basic model, the Young moduli are based on the stresses from the last converged state, and are frozen throughout a given increment. For tests where the minor principal stress σ_1 remains constant, this is ideal, as the Young moduli remain constant throughout the shearing phase. However, in oedometer simulations and more complex boundary value problems, the stiffness changes in each load increment.

Using the last converged stress for the soil stiffness causes the solution to drift. This is most prominent in Figure 4.4 which is discussed later in Chapter 4.

To overcome this issue, it is proposed that a modified Newton-Raphson type method is adopted. In the Modified Newton-Raphson (MNR) method, the stiff-

ness for the first two or more iterations is updated. The standard Newton-Raphson method updates the stiffness on every iteration, and an explicit method only calculates the stiffness for the first iteration.

The standard Newton-Raphson method converges the fastest but requires calculation of the tangent stiffness matrix on every iteration. The explicit method only requires the calculation of the tangent matrix to be performed once, however is slower to converge. The MNR method is a compromise of both methods, where a tangent stiffness which is more accurate than that used in the explicit method, is used throughout the increment.

In this application, the MNR method is not used to improve convergence or speed, but to reduce step size dependency. The yield function and plastic potential gradients (and hence the tangent stiffness matrix) are updated on each iteration, making this method more akin to the standard Newton-Raphson method. However, in this implementation of the HS model, Young moduli are updated for a controlled number of iterations, then frozen for the remainder of the increment.

Additionally, the level of which the stiffness is modified can be controlled by a weight factor r . Some portion of the last converged stress can be used to calculate the Young moduli, this should provide some additional stability in the model whilst removing some or all of the step size dependency. Application of this factoring can be applied as follows:

$$E_{50} \left(\boldsymbol{\sigma}^{LC} (1 - r) + \boldsymbol{\sigma}^{LI} r \right) \quad (3.77)$$

where $\boldsymbol{\sigma}^{LC}$ is the last converged stress, $\boldsymbol{\sigma}^{LI}$ is the stress at the end of the previous iteration, and r is the stiffness update weight factor, which ranges from 0 to 1. A value of $r = 0$ gives the original explicit method, and a value of $r = 1$ makes the model use purely the updated stress. Any values in-between use a combination of both.

This updated procedure is performed until the absolute relative change in Young

modulus between iterations E_{change} reduces below a pre-set tolerance E_{tol} :

$$E_{change} = \frac{|E_{50} - (E_{50})_{LI}|}{E_{50}} \leq E_{tol} \quad (3.78)$$

It is the responsibility of the user to determine if their model is step size converged. This is done simply by running simulations with different step sizes and determining at what size of step when adjusted slightly does not significantly affect the results. There can be significant computational cost in decreasing step size, and the methods described in this section should allow the user to lower these costs by reducing the number of steps required. However, it is still vital that step size dependency is checked to ensure accurate results.

The proposed model as described in this chapter will hereinafter be referred to as the HS-LC model. By default, the dilatancy model by Rowe with the zero cutoff is used (Equation 2.10). The failure criterion used in this study is that proposed by Panteghini and Lagioia (2013). Use of the model may or may not include the stiffness update procedure described in Section 3.9; by default, it is not used and the stiffness is based on the last converged state. Some of the model verifications use the stiffness update procedure, and details of the parameters used are noted.

Chapter 4

HS-LC model validation

This chapter describes a series of validations of the improved hardening soil model formulated in Chapter 3. It is important to assess the performance of the soil model before it is applied to the composite model described later, therefore a selection of case studies for unreinforced soils are described here.

The chosen scenarios are a combination of laboratory tests, and more complex boundary value problems. The work of Schanz et al. (1999) and Benz (2007) provide several case studies to compare against the new hardening soil model.

All simulations are performed in the finite element software LUSAS. Single elements are used for simpler simulations such as triaxial and oedometer tests. These simulations are symmetrical about the vertical axis, therefore axisymmetric quadrilateral elements are used. For the boundary value problems, more detailed descriptions are included in their respective sections.

Each set of results is discussed in full within this chapter; this includes the description of each problem, the results, and a discussion of the results. Later case studies will build on the discussions from previous analyses; hence this chapter forms a narrative, starting with very basic simulations, leading to more complex field simulations.

In addition, some of the material variables, namely the initial modulus E_i^{ref} ,

cap steepness α and the cap hardening K_s/K_c parameters, must be modified for the HS-LC model. These parameters however, are calibrated to the same values of oedometer modulus E_{oed} , stiffness ratio K_0 and secant modulus E_{50}^{ref} as the HS model. The material properties used in the HS-LC model are detailed in Table 4.1.

4.1 Oedometer tests

This first test is taken directly from the work of Schanz et al. (1999), and is based on a simple one dimensional loading of a dry sand. Normally this type of test is reserved for consolidation analysis of clays and silts; time is usually an important factor in an oedometer test because the clay must be allowed to consolidate. However, using a sand means that displacements may be assumed to occur instantaneously with applied loads, as the grain repacking is immediate due to the lack of cohesion.

The test consists of a cylinder of sand, packed to a certain density, and loaded vertically (Figure 4.1a). The cylinder, base and loading cap are made from stiff materials, such that the soil may be assumed to only deform vertically.

Domain: The domain of the oedometer problem was taken to be a 5×5 cm square (Figure 4.1b), with its left side coincident with the axis of symmetry; representing a cylinder. The actual size and proportions of the quadrilateral have no effect on the results, as this problem can equally be modelled with a single Gauss point.

Boundary conditions: The sand was subject to roller supports along its boundaries, this allows the mesh to slide along the boundaries, but not move through them. The axis of symmetry automatically enforces this boundary. The prescribed displacement on the top surface also forms a boundary and the mesh was free to move horizontally on the top surface. The load curve for the prescribed displacement is shown in Figure 4.3.

Table 4.1: Material parameters used in the hardening soil model simulations. For all materials; $\sigma^{ref} = -100 \text{ kN/m}^2$, $p_a = -100 \text{ kN/m}^2$, $\sigma_t = 0 \text{ kN/m}^2$, $Y_f = 10^{-3}$, $G_f = 10^{-4}$

ID	Name	D t/m ³	E_{50}^{ref} kN/m ²	E_{ur}^{ref} kN/m ²	E_i^{ref} kN/m ²	E_{oed}^{ref} kN/m ²	m	c kN/m ²	φ °	ψ °	ν	K_0^{NC}	R_f	α	K_s/K_c
LS1	Loose sand		23890	60000	68913	16500	0.65	0.0	34	0.8	0.20	0.44	0.9	0.959	1.650
DHS	Dense Hostun sand		30000	90000	109303	30000	0.55	0.0	42	16	0.25	0.40	0.9	1.140	1.761
LHS	Loose Hostun sand		12000	60000	37420	16000	0.75	0.0	34	0	0.25	0.44	0.9	1.049	1.875
C1	Clay		2150	11500	6685	1050	0.8	0.0	20	0	0.20	0.66	0.9	1.015	5.373
S1	Sand	2.0	25900	79189	45000	25900	0.5	0.0	35	0	0.45	0.426	0.85	1.504	8.817
L1	Very dense silt	1.161	100625	300000	333000	80000	0.65	23.94	35	0	0.45	0.50	0.85	1.38	11.80
L2	Dense silty sand	1.081	69000	172500	212000	63000	0.6	23.94	35	0	0.45	0.426	0.85	1.48	9.10
L3	Dense sand	0.705	52500	157500	160000	52500	0.6	0.0	35	0	0.45	0.426	0.85	1.52	8.40
DLS	Dense Leighton Buzzard sand	1.665	32700	98100	107241	32700	0.85	20.0	34.6	1.8	0.30	0.40	0.95	1.296	1.720
LLS	Loose Leighton Buzzard sand	1.608	15000	45000	39642	15000	0.55	5.0	14.5	0.0	0.30	0.75	0.95	0.564	2.439

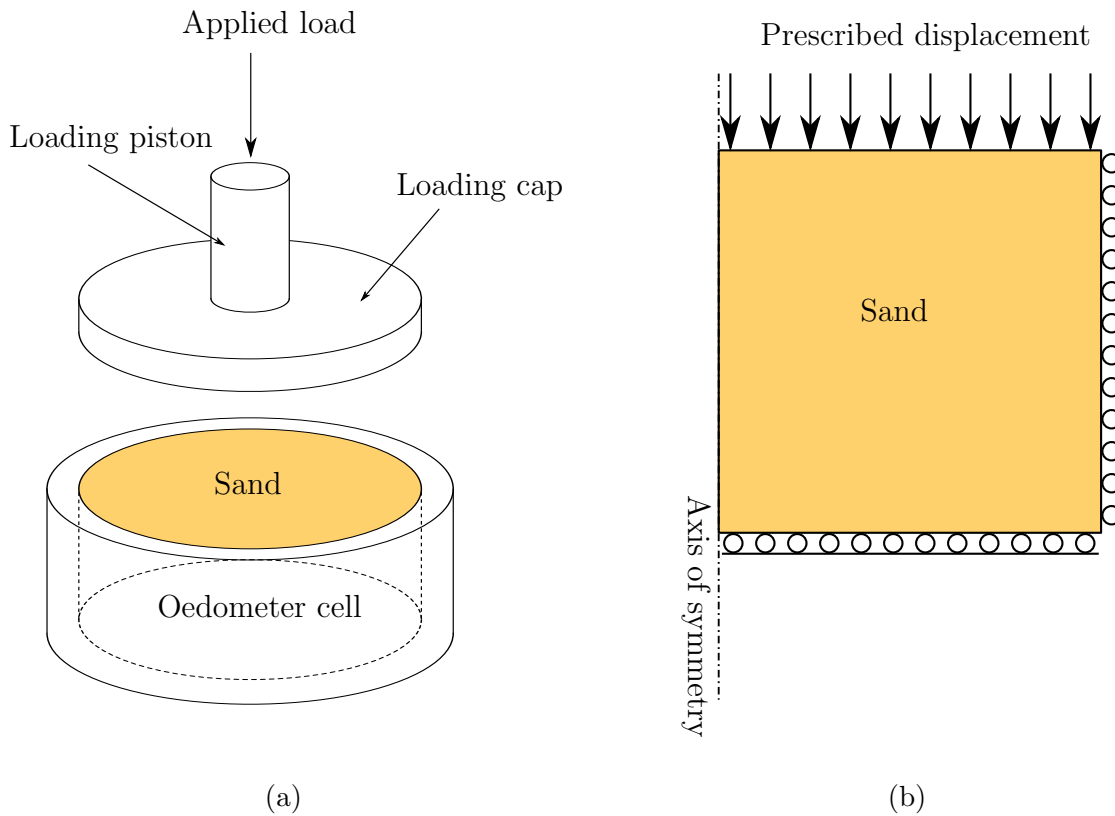


Figure 4.1: Oedometer test; (a) 3-D configuration and (b) axisymmetric model used with boundary conditions and loading

Mesh: Similarly to the domain, the actual mesh used is not significant in this analysis. The mesh used in this example was a single eight-noded quadrilateral. The results are obtained from the mid-side node on the left side of the square, as this represents the centre of the sand. This selection is arbitrary as the results are constant throughout the mesh.

Materials: The soil tested was a loose sand, the properties of the sand used in the HS-LC model are listed as LS1 in Table 4.1. Most of the parameters here are identical to those found in the original source paper by Schanz et al. (1999). Some of the values were not published and had to be calculated from the available experimental data. The auxiliary parameters α , K_s/K_c , and E_i^{ref} were also calibrated using a trial and error approach by running the model several times and varying these parameters until a suitable match with the experimental data (Schanz et al., 1999) was found.

From the experimental data, it was found that the secant modulus E_{50}^{ref} was

rounded to one significant figure; this suggests a minor inaccuracy. In this study, a revised value was used based on experimental triaxial test results on the same sand. Also, a small dilatancy angle was introduced to reflect observations in the experimental triaxial results, as the sand exhibited some increase in volume after extensive shearing.

Convergence criteria: The chosen residual force norm criterion was 0.001%, and the incremental displacement norm criterion was 0.01% for this test.

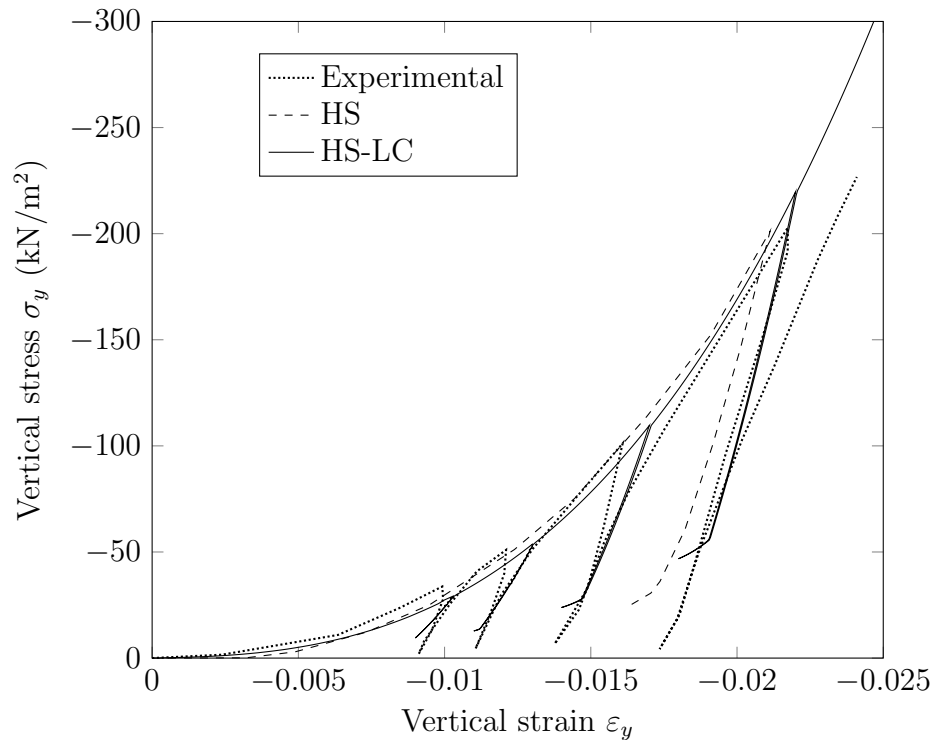


Figure 4.2: Single element oedometer simulation, comparison with experimental and predicted results from Schanz et al. (1999)

Discussion: Both versions of the HS model replicate the experimental data well, as shown in Figure 4.2. The primary loading curves are very similar for both predictions and experimental results.

The loading path for this simulation is shown in Figure 4.3 and includes several unloading and reloading cycles. Figure 4.3 also shows the required number of iterations for each increment. As can be expected for this heavily restrained, single element test; each increment converges in a single iteration.

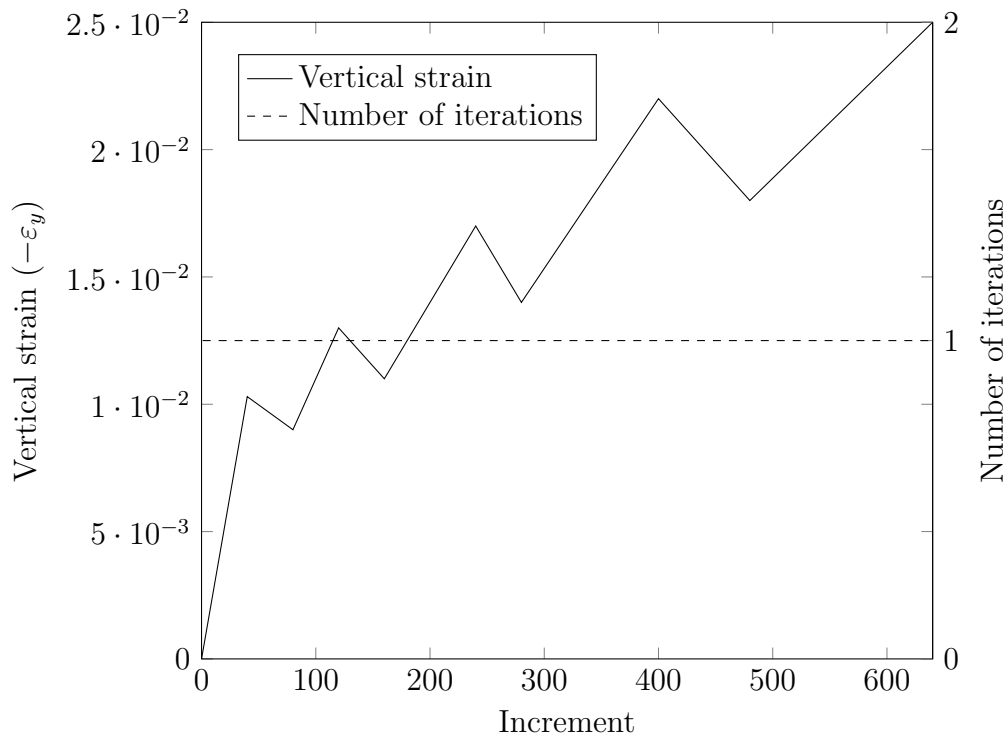


Figure 4.3: Load curve and converged iteration numbers for oedometer test

The published data from the original HS model prediction only includes one unloading cycle. The gradient of this unloading cycle matches the experimental results. The HS-LC model also predicts the unloading gradients well, however, the path for unloading is predicted to be identical to the reloading path. This does not reflect the observed behaviour where the unloading and reloading paths are different.

The reason for identical unloading and reloading paths is due to the assumed elastic behaviour when below the yield surfaces. Plasticity does not come into effect until the primary loading curve is reached again, and the yield surface(s) become active.

The experimental unloaded paths show some stress dependency, i.e. the gradient for the first unloaded path is less steep than the final unloaded path. The HS-LC model repeats this observation but to a greater degree. The mechanism which controls this in the model is the stress dependent unload-reload stiffness, which is based on the minor principal stress σ_1 . The curvature of the unloaded paths for the experimental and HS-LC predicted results are similar.

Another feature of the predicted results for both the HS and HS-LC models

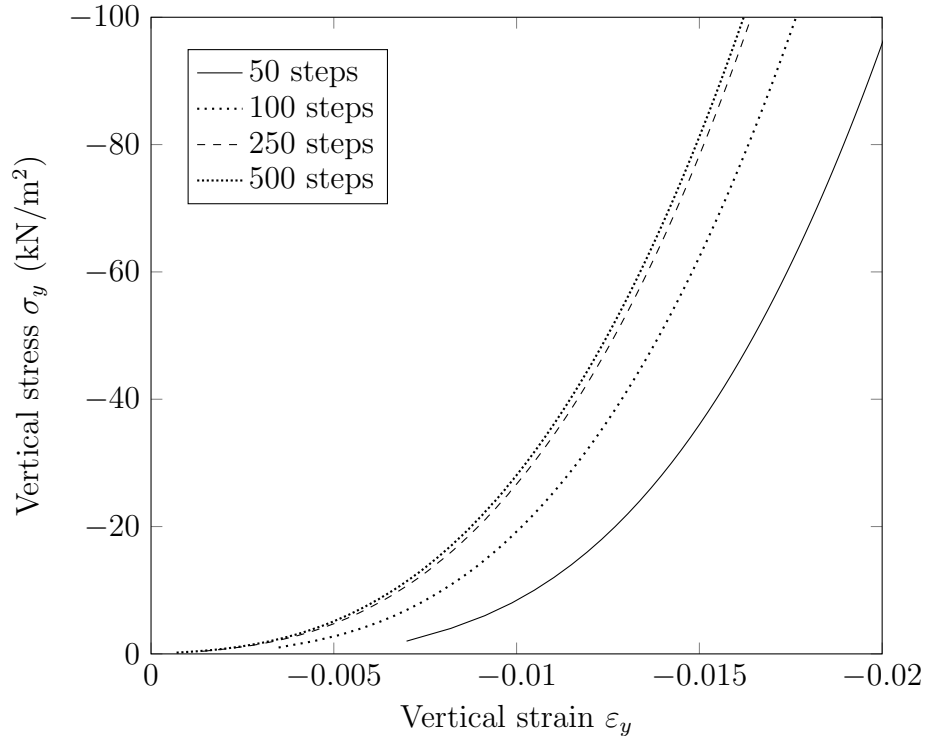


Figure 4.4: Oedometer loading paths for different step sizes (load controlled test, total vertical load $\sigma_3 = -100 \text{ kN/m}^2$)

is the distinct change in gradient towards the end of each unloading cycle. This occurs when the vertical stress falls below the radial stress in the soil, changing the orientation of the major principal stress. This feature is also present in the third and fourth unloading cycle of the experimental results, but to a lesser extent.

The calibrated auxiliary parameters α , K_s/K_c from this test are used in the simulation of a triaxial test using the same sand (see Section 4.2), this triaxial test was also used to calibrate the initial modulus E_i , which was used in this oedometer simulation.

The analysis of this oedometer test also includes an investigation of step size dependency in the HS-LC model. Figure 4.4 shows the oedometer loading response for the same soil and the same total load applied over different numbers of increments. This series of tests shows some significant step size dependency, where the 50 step test shows a much softer initial state than the smaller step size tests. The solution appears to converge between the 250 and 500 step results where the responses are very similar. It is important to note that these tests were performed with equal

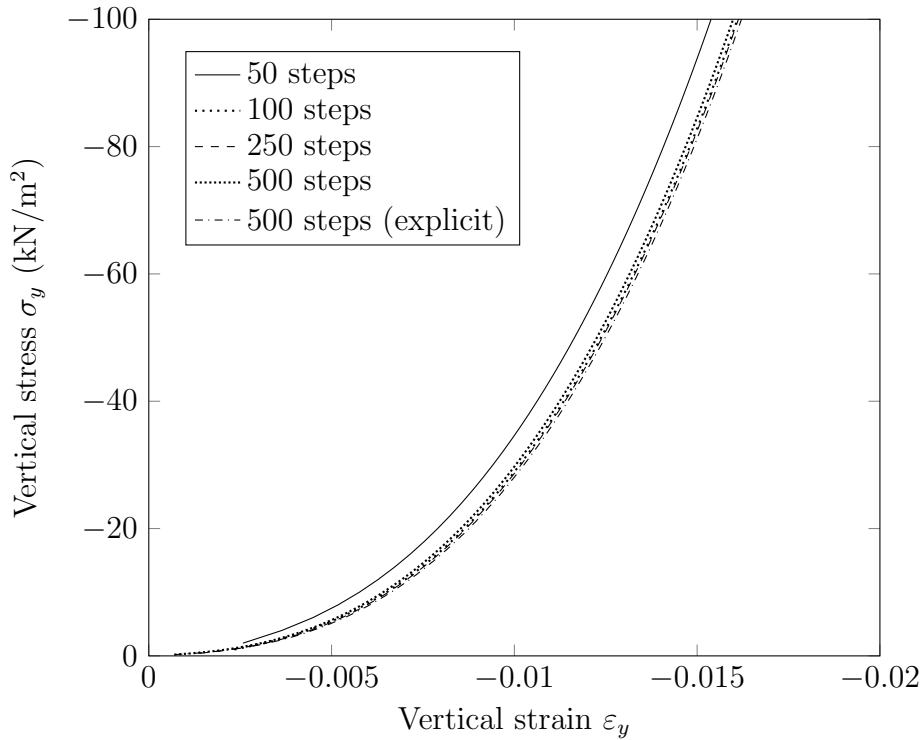


Figure 4.5: Oedometer loading paths for different step sizes using updated Young's moduli, $E_{tol} = 0.05$, and $r = 0.33$

stress increments. A more sensible approach for this type of test is to use smaller step sizes at the start of the test, however this approach was chosen to demonstrate the issue with step size dependency.

The paths of each test after approximately $\sigma_y < -20 \text{ kN/m}^2$ are very similar. A translation of each load curve horizontally produces a set of curves which are more similar than shown in Figure 4.4. This indicates that the model is most sensitive to step size at low stress levels.

The stiffness update method detailed in Section 3.9 is used to address the issue of step size dependency. In this method, the Young moduli, used in the calculation of the elasticity matrix D_e and within the shear yield surface f_s , are updated for the first few increments, and frozen thereafter. A weighting factor is also applied to include some portion of the Young moduli from the last converged state (Equation 3.77). In this study, the stiffness is updated using a tolerance of $E_{tol} = 0.05$, and a weighting factor of $r = 0.33$ is used.

The results obtained using these parameters are shown in Figure 4.5. The 500

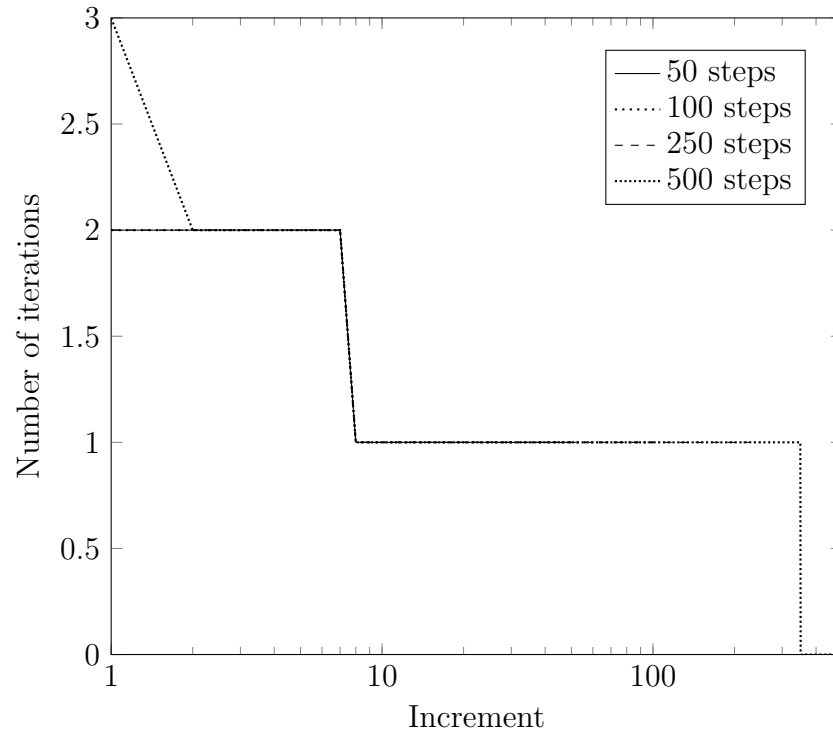


Figure 4.6: Converged iteration numbers for oedometer step size study

step results from the previous study (Figure 4.4) are included in this figure for comparison. The stiffness update has significantly reduced the step size dependency for this problem, requiring only 100 steps to achieve the same results as the 500 step analysis using the fully explicit method. In the prior example (Figure 4.4), the 50 step test load curve is below the converged solution. With the updated stiffness results (Figure 4.5), the 50 step simulation produces a curve which is higher. The reason for this is that the stresses are not fully converged when the stiffness updates and subsequently freezes. This can cause the minor principal stress σ_1 used in the modulus calculation to be higher than the final converged result, resulting in a higher stiffness.

The first oedometer simulation (Figure 4.3) converges in only 1 iteration for each increment. This is a strain controlled simulation, with restrained boundaries, therefore the problem has zero degrees of freedom. Step size dependency is less of an issue in this analysis as the vertical strain is not allowed to drift.

The analyses in the step size study are stress controlled tests, where the vertical strain is the unknown variable. For the first step size tests using the explicit method

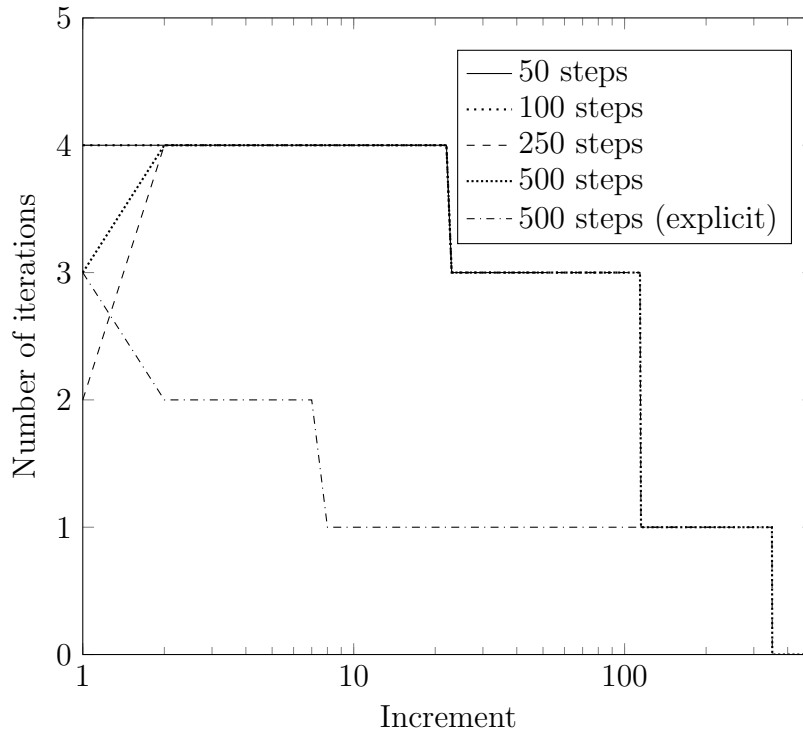


Figure 4.7: Converged iteration numbers for oedometer step size study using updated Young moduli, $E_{tol} = 0.05$, and $r = 0.33$

(Figure 4.6), most increments converged in 2 iterations or fewer. The first step in the 500 step analysis required 3 iterations, the most likely cause of this is that the stress level is close to the minimum factor for stress dependency Y_f as described in Equation 3.76, which does introduce a change in gradient of the stiffness. The final few iterations of the 500 step analysis required 0 iterations for convergence, this is because the soil stress is very close to the reference stress σ^{ref} , and the elastic trial solution σ_{tr} is effectively equal to the converged solution, and the trial state is deemed to be converged.

Use of the stiffness update increases the number of iterations required for convergence (Figure 4.7). The iterations from the 500 step analysis using the fully explicit method from Figure 4.6 are also included for comparison. For these analyses, increments required 4 or fewer iterations to converge. This is to be expected as the stiffness is changing within the increment, and an additional layer of non-linearity is present in the model.

To obtain a step size converged solution, two approaches have been explored. One approach is to decrease the step size, this comes at a cost of requiring more

load steps. The second approach is to use the stiffness update method as described in Section 3.9, however this comes at a cost of having to deduce the optimal parameters, and also requiring more iterations for each increment. In any case, it is clear that it should be established as to whether or not the solution is step size converged.

4.2 Triaxial tests

The triaxial test uses standardised apparatus and procedure to determine the shearing properties of soils. Further details of the steps involved in a triaxial test can be found in Section 6.2.1. Essentially, the test consists of two main stages; an initial compression (or consolidation), followed by an unconfined vertical compressive load.

Schanz et al. (1999) provided triaxial experimental data of a loose sand, along with predictions using the HS model. Benz (2007) also provided experimental data and predictions using the HS-smooth model of three more soils. This data is used as a comparison for the new HS-LC model.

Domain: Similarly to the oedometer tests, the actual geometry of the problem is not important. In LUSAS, the triaxial test was modelled as a square in axisymmetric space, and therefore represents a cylinder. The height and width of the square used in this example were modelled as 5 cm.

Boundary conditions: The bottom surface of the soil was supported in the vertical direction and free to move horizontally, this allows for volumetric contraction and expansion. The axis of symmetry inherently suppresses any movement through the axis, therefore is equivalent to a horizontal support, with free vertical movement.

Mesh: A single eight-noded quadrilateral element was used to model the triaxial test. Results are extracted from the left mid-side node.

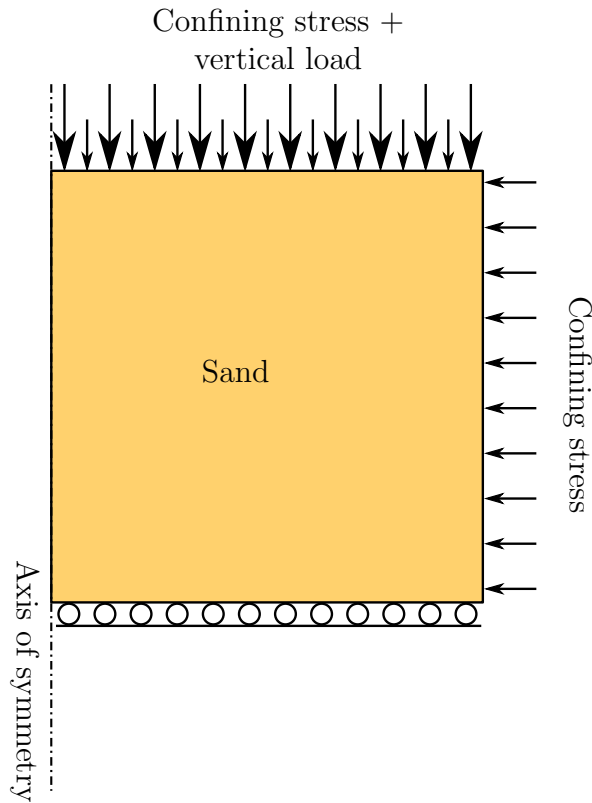


Figure 4.8: Triaxial test; axisymmetric model used with boundary conditions and loading

Materials: A selection of materials are used in this series of tests. The first material was the same as the previous oedometer test (LS1), the purpose of including this simulation is to verify that the same set of parameters can reproduce results from the original HS model (Schanz et al., 1999) for both oedometer and triaxial loading conditions.

Three more materials are included in the triaxial compression study. The material parameters are taken from the second development of the HS model (Benz, 2007); namely dense Hostun sand (DHS), loose Hostun sand (LHS) and a kaolin clay (C1). Only the auxiliary parameters are modified from the original work such that the calibration parameters E_{50}^{ref} , E_{oed}^{ref} , K_0 , are equivalent between the two models.

Throughout the analyses, the modified Rowe dilatancy relationship (Equation 2.10) was used.

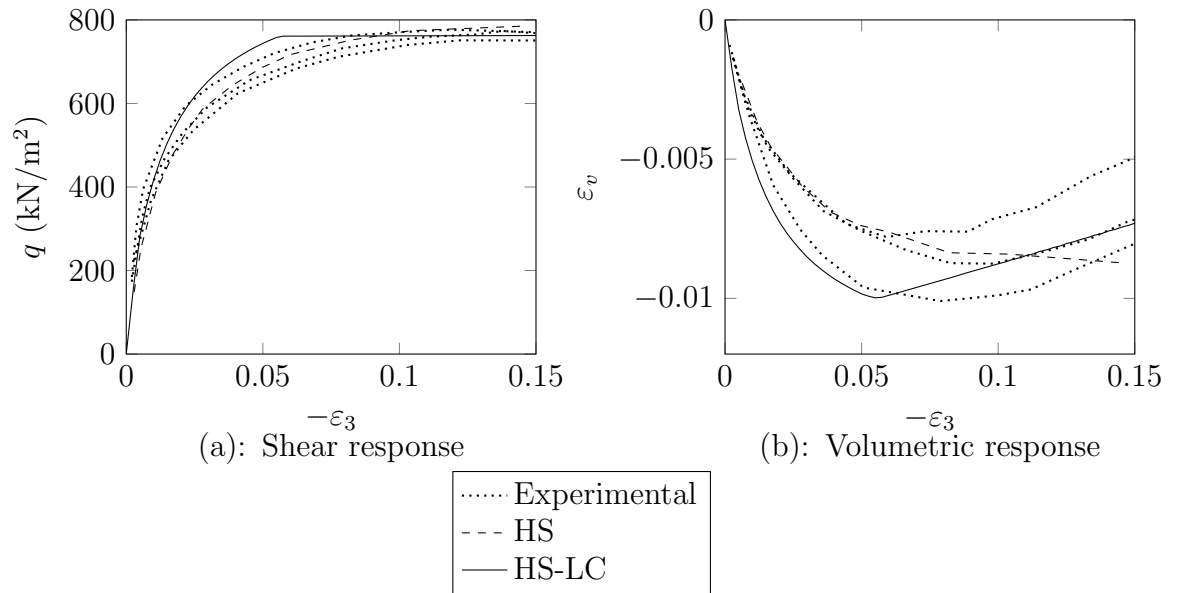


Figure 4.9: Triaxial test results (experimental and predicted) of a loose sand (LS1)

Loading: For the first analysis, the soil was given an initial residual compressive stress of 300 kN/m^2 . A vertical displacement was prescribed to the top surface at a rate of 0.0125 cm per increment for 80 increments, giving a total axial strain of 20% at the end of the test.

For the remaining triaxial analyses, the soil was given an initial residual compressive stress of either 100 , 300 , or 600 kN/m^2 . The vertical displacement was applied over 50 increments, at a rate of 0.01 cm per step, giving a total axial strain of 20% by the end of the test.

Convergence criteria: The residual force norm criterion used in this simulation was 0.001% , and the incremental displacement norm criterion was 0.01% .

Discussion: In reference to the first simulation (Figure 4.9), The shear response for both the HS and HS-LC models match the experimental data very well (Figure 4.9a); the failure point on the HS-LC model clearly becomes active at a strain of $\varepsilon_3 = -0.08$ where no shear increase is observed, however, the initial gradient is very slightly under-predicted.

The volumetric response (Figure 4.9b) using the HS-LC model is somewhat dif-

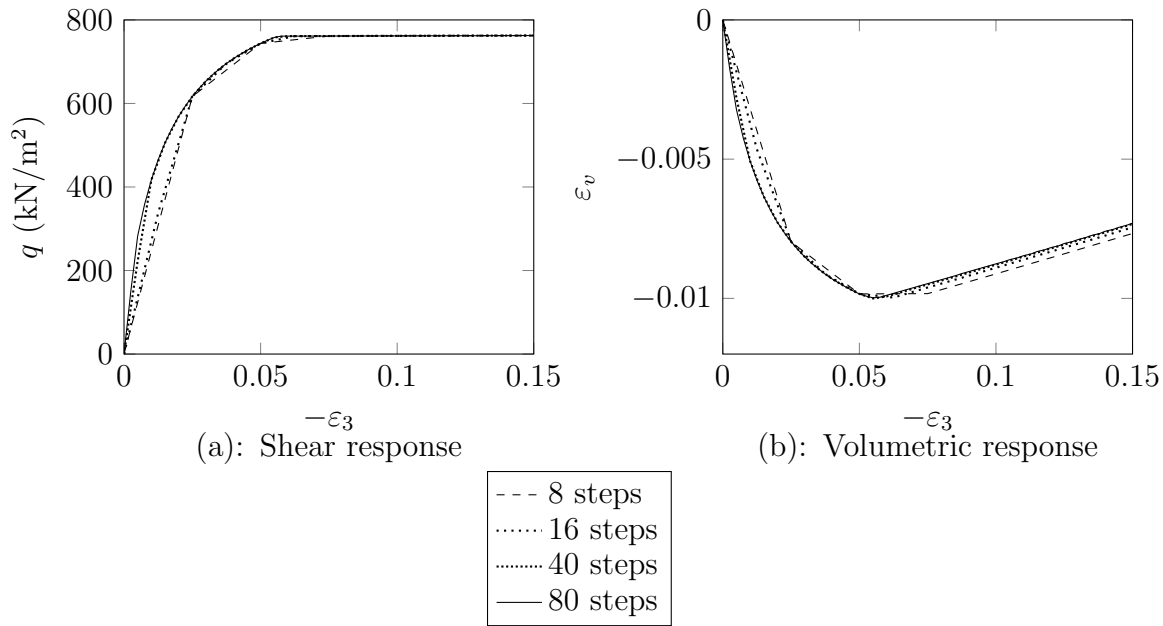


Figure 4.10: Triaxial test results with different step sizes (L1)

ferent to the original HS prediction. The initial gradient is steeper, which would indicate that the HS-LC model exhibits more contractive behaviour than the HS model initially, however both results are within the range of experimental variation. The post-failure gradient of the experimental results is slightly dilative, this is not captured in the original HS model because a dilatancy angle of $\psi = 0^\circ$ was used, but it is captured in the HS-LC model using $\psi = 0.8^\circ$. This is not a reflection of the capability of the HS model, but a minor issue with the selection of parameters.

A step size dependency study is included in Figure 4.10, where the same triaxial test is repeated with different numbers of steps to achieve the same total strain. The 80 step simulation produces a smooth curve, then a change in gradient when failure is initialised. The larger step size tests appear to meet the 80 step shear curve at the end of each load step. For the volumetric curve, the results match until the curve changes at a strain of $\varepsilon_3 = -0.05$. After this point, the larger step results project past the 80 step results until the next increment begins, where the gradients match thereafter.

The convergence for each of the different step sizes (Figure 4.11) is similar. Most increments converged in 2 iterations or fewer; however, the 8 step test required 12 iterations for the first increment.

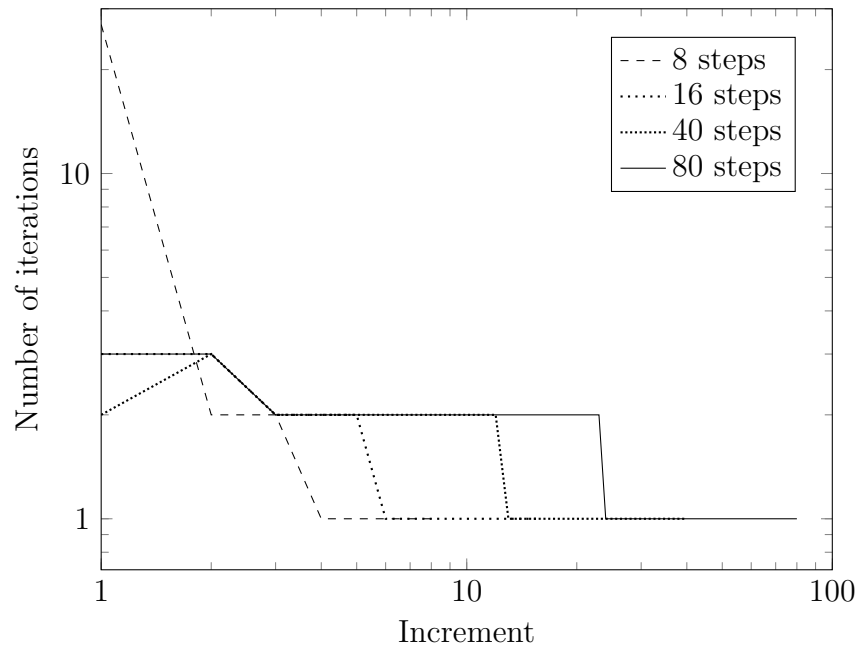


Figure 4.11: Converged iteration numbers for triaxial step size study using HS-LC model

Referring to the second series of triaxial tests (Figures 4.12, 4.13, 4.14), it appears that the HS-LC model has replicated the results produced by the HS-smooth model excellently in both the shear and volumetric responses.

The HS-LC simulations predict the initial shear response very similarly to the HS-smooth model. There is a slight difference in predicted shear responses towards soil failure such that the HS-LC model produces curves which are steeper than the HS-smooth model when approaching failure. This effect is most prominent in the $\sigma_1 = -600 \text{ kN/m}^2$ dense Hostun sand simulation (Figure 4.12).

The experimental volumetric results for the loose sand and the clay are replicated near-perfectly using the HS-LC model. The volumetric results from the dense sand differ slightly: the HS-LC model exhibits a more prolonged compression phase than the HS-smooth model, i.e. dilatancy occurs later. This difference is most obvious in the 600 kN/m^2 simulation in Figure 4.12. It is likely that the difference in dilatancy relationship used in each simulation is the cause of this difference; the HS-smooth model uses the dilatancy model by Li and Dafalias (2000) shown in Equation 2.13, and the HS-LC model uses the modified dilatancy model by Rowe (1962) shown in Equation 2.10.

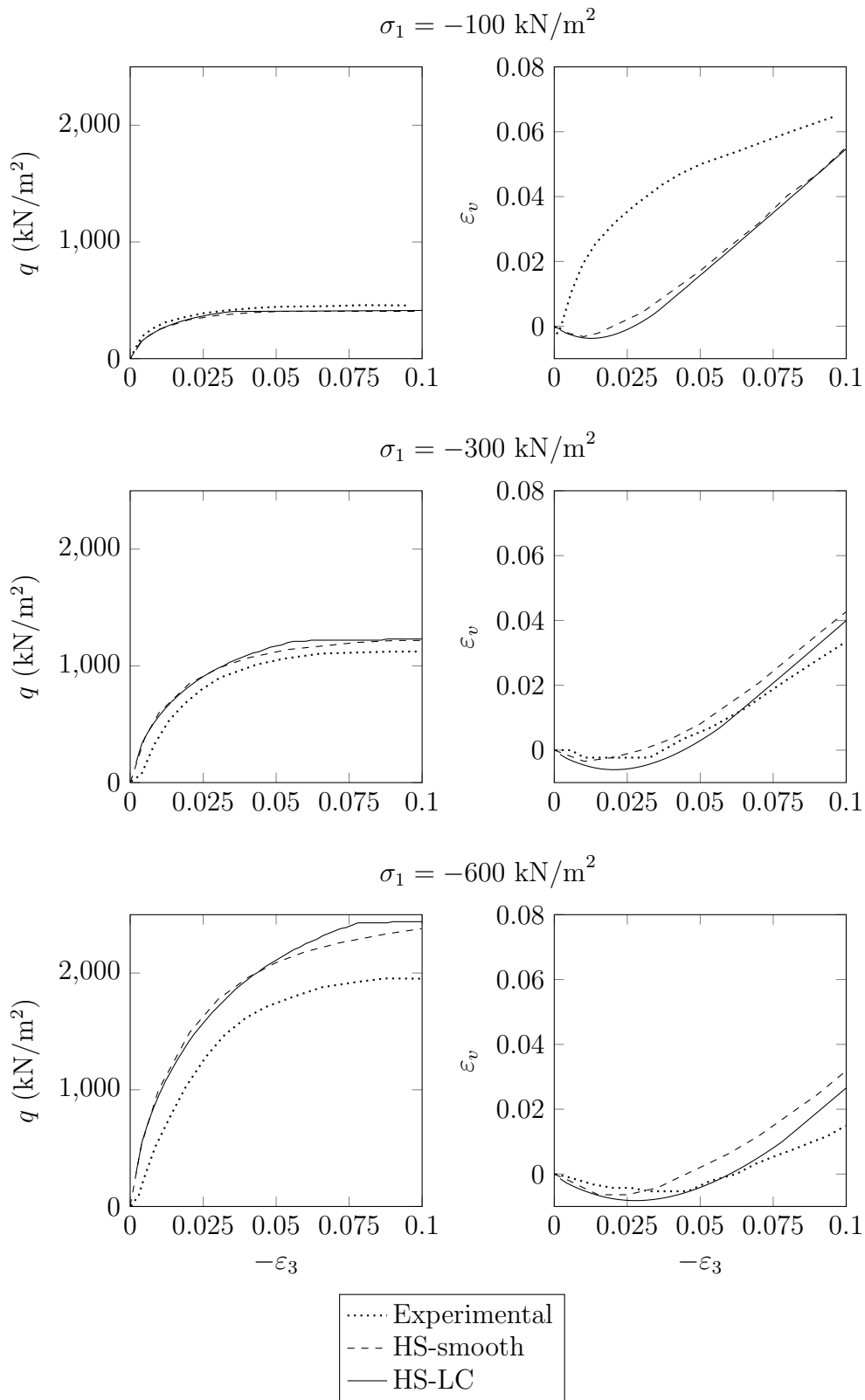


Figure 4.12: Experimental and predicted triaxial test results on dense Hostun sand (DHS), experimental and HS predictions from Benz (2007), and predictions with the HS-LC model

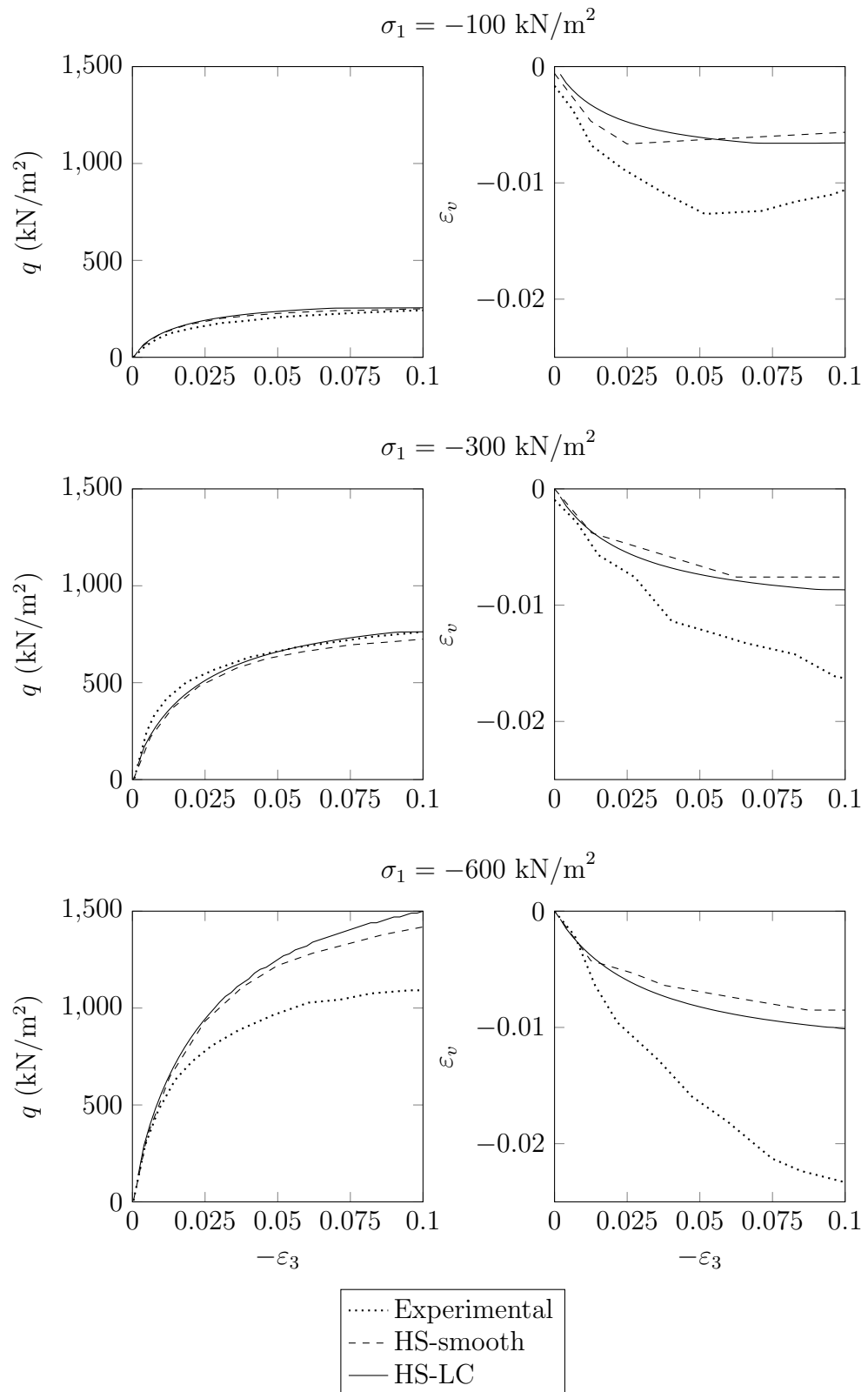


Figure 4.13: Experimental and predicted triaxial test results on loose Hostun sand (LHS), experimental and HS predictions from Benz (2007), and predictions with the HS-LC model

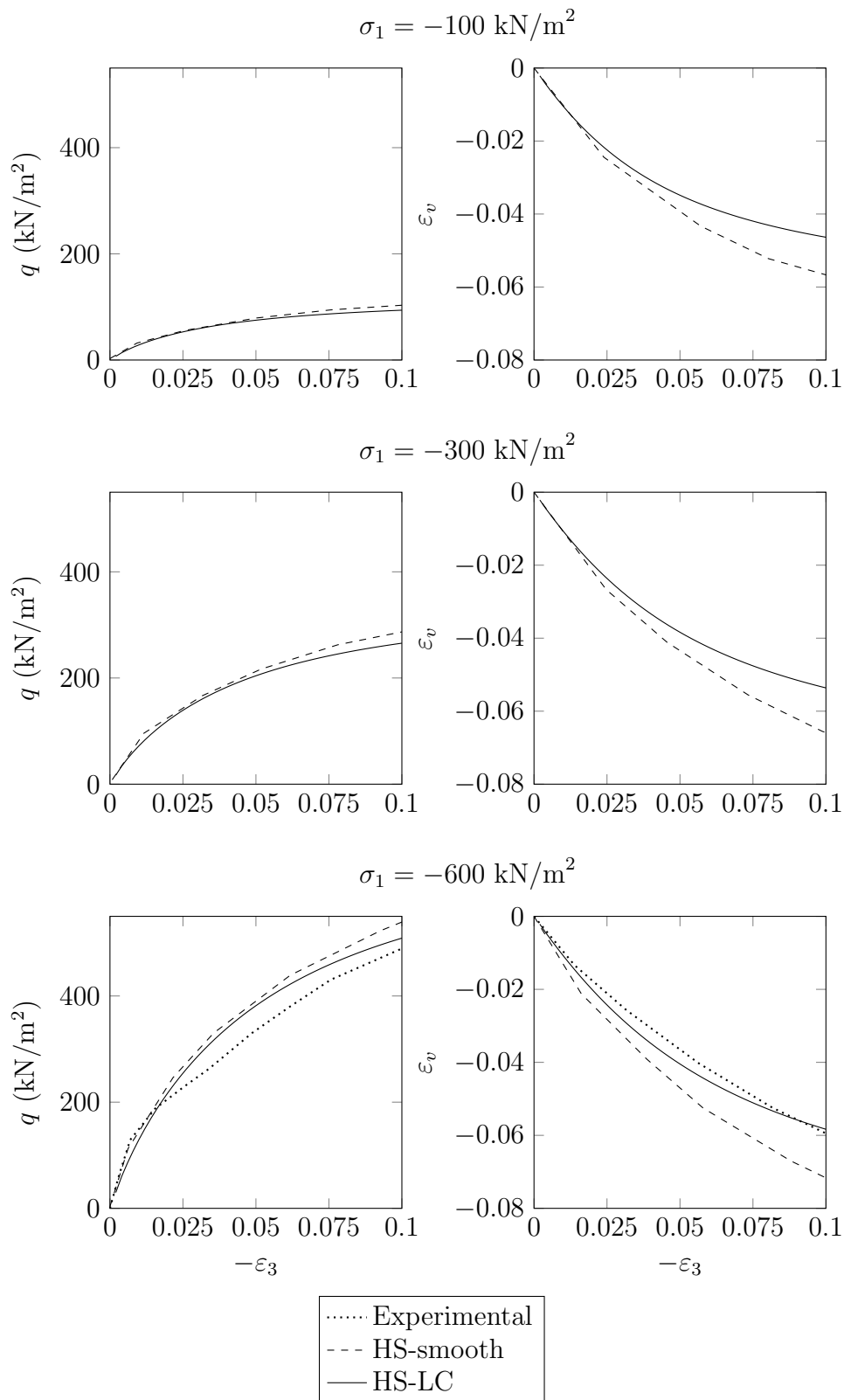


Figure 4.14: Experimental and predicted triaxial test results on clay (C1), experimental and HS predictions from Benz (2007), and predictions with the HS-LC model

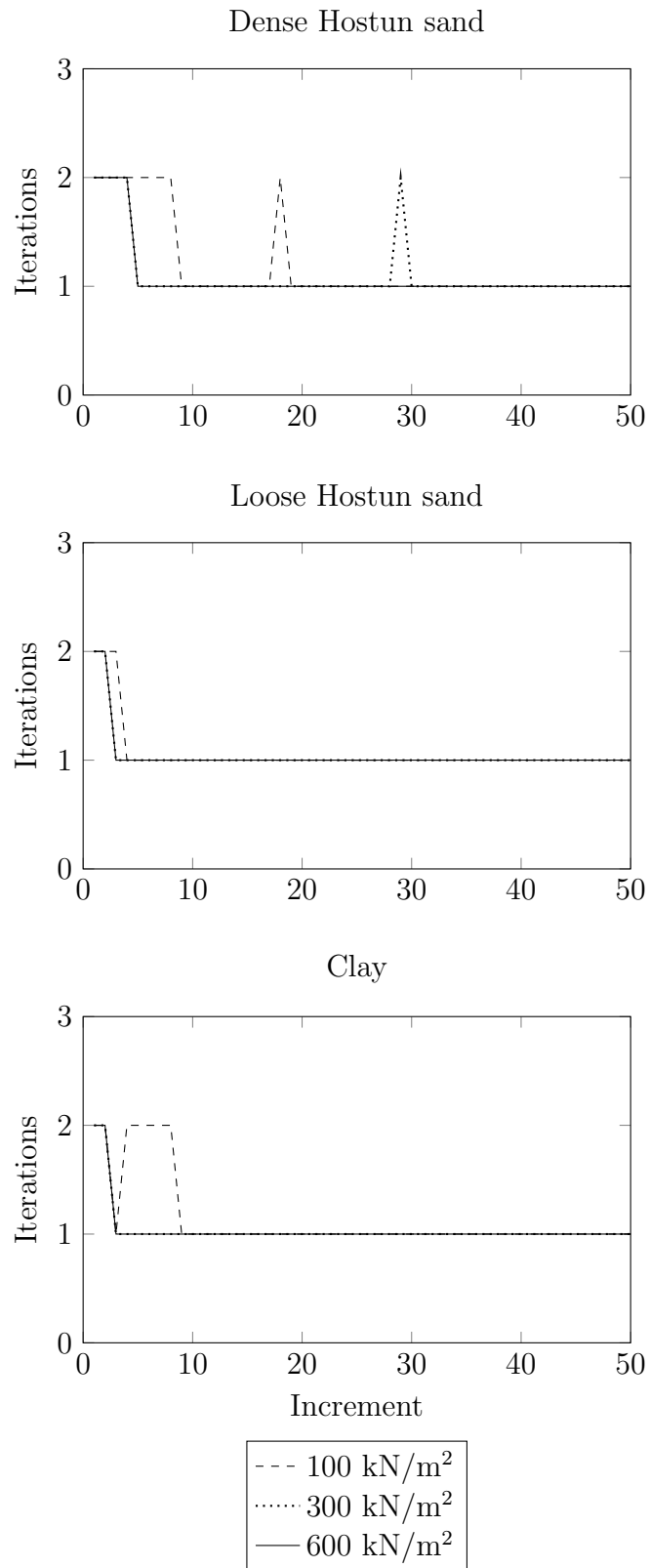


Figure 4.15: Converged iteration numbers for triaxial tests using the HS-LC model

Overall, the experimental results are captured well by both models. The shear response of the dense sand is predicted very well for the 100 and 300 kN/m² tests, however the strength of the 600 kN/m² soil is over-predicted. The volumetric response of the 100 kN/m² dense sand is also predicted incorrectly for both models, in the experimental test, the soil shows dilatant behaviour immediately. However, the validity of this response (and other experimental results) in this series are questionable because no repeat experiments are shown.

The volumetric contraction of the loose Hostun sand (Figure 4.13) is under-predicted by both the HS-smooth and HS-LC models. With these models, there is very little control for this type of behaviour. It is believed that using the dilatancy model by Wehnert (2006) in Equation 2.11 could improve this prediction, as the non-zero dilatancy encourages contractive behaviour at a low shear stress. The shear response of the loose Hostun sand is also predicted very closely, however, the 600 kN/m² strength is over-predicted.

Experimental results are not available for the 100 and 300 kN/m² clay tests (Figure 4.14), however, both the shear and volumetric predictions for the 600 kN/m² clay match the experimental results very well.

Convergence for the triaxial tests was very good (Figure 4.15); every increment converged in 3 iterations or fewer for all materials. Most increments converged in 1 increment, and peaks in required iterations occurred during changes in the model. For example, the transition into the dilatant mode of the modified Rowe stress dilatancy relationship (Equation 2.10) and initiation of soil failure ($r_q \geq R_f$).

4.3 Circular footing

A 1.22 m (4 ft) radius circular footing on a sand was analysed. Predictions from using the Duncan-Chang (DC) model are available (Mitchell and Gardner, 1971) and can be directly compared with the HS model, as it shares many common parameters with the DC model; additional parameters were obtained by simulating triaxial and

oedometer tests and calibrating to given parameters. Mitchell and Gardner (1971) also performed a linear elastic analysis of this footing problem using an analytical method by Huang (1967), this has been included in comparisons.

Domain: The problem domain is shown in Figure 4.16. The footing radius is 1.22 m, and the soil domain extends 9.14 m horizontally and vertically from the centre of the footing base.

Boundary conditions: The base of the soil was fully fixed, and the vertical boundaries are supported horizontally, with the axis of symmetry, the horizontal restraint is inherently included.

Mesh: The problem is initially modelled using a fairly coarse axisymmetric mesh with 170 quadratic, quadrilateral elements. The footing and the soil are modelled using the same continuous mesh. The mesh was refined near the footing, and made increasingly coarse further away from the footing.

A mesh convergence study was also performed here, which compares three different meshes of 170, 576, and 2115 elements, as shown in Figures 4.16, 4.17, and 4.18 respectively.

Materials: The footing was modelled as concrete with Young's modulus 30 GN/m² and Poisson's ratio 0.2. The sand material properties can be found in Table 4.1 and are denoted S1.

Loading: Loading was performed in four stages: First, a nominal isotropic compressive stress of 5 kN/m² was applied to resolve convergence issues from starting at zero stress. Second, the self weight of the soil was taken into account by applying a gravity body force acceleration ($g = 9.807 \text{ m/s}^2$). Third, the overburden pressure was applied; this is equivalent to 0.914 m (3 ft) of soil above the base of the footing.

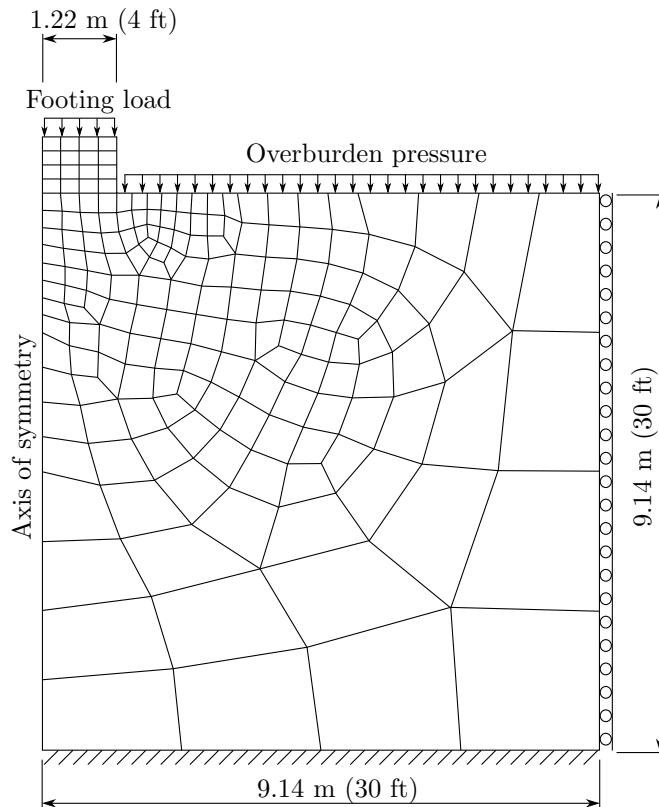


Figure 4.16: Footing analysis mesh and geometry (coarse 170 element mesh)

Finally, the footing load was applied as a constant pressure on the footing only at a rate of 1 kN/m^2 per step, taking a total of 240 steps.

Convergence criteria: The residual force norm criterion was 0.1%, and the incremental displacement norm criterion was 1.0%. The stiffness update procedure was used with a modulus change tolerance of $E_{tol} = 0.05$, and a weighting factor of $r = 0.33$.

Discussion: The results from the numerical simulation of the footing (Figure 4.19) are in close agreement with previous results from Mitchell and Gardner (1971) in both the linear elastic simulation, and the non-linear DC simulation. This is to be expected as the HS model is formed from the same basis as the DC model, also many of the main material parameters are identical. The major difference between the models is the implementation: the DC model is based on an incremental relationship, and the HS model is based around plasticity.

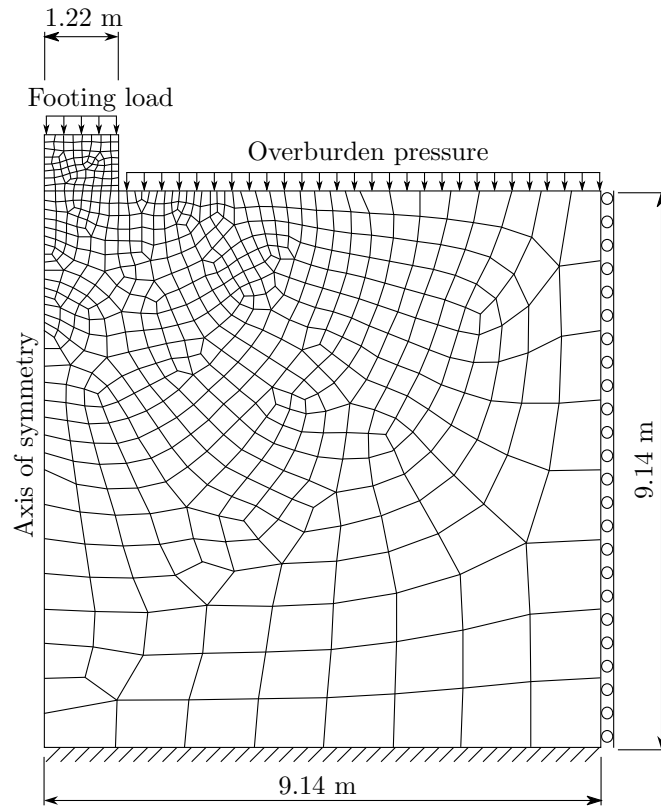


Figure 4.17: Footing analysis mesh and geometry (medium 576 element mesh)

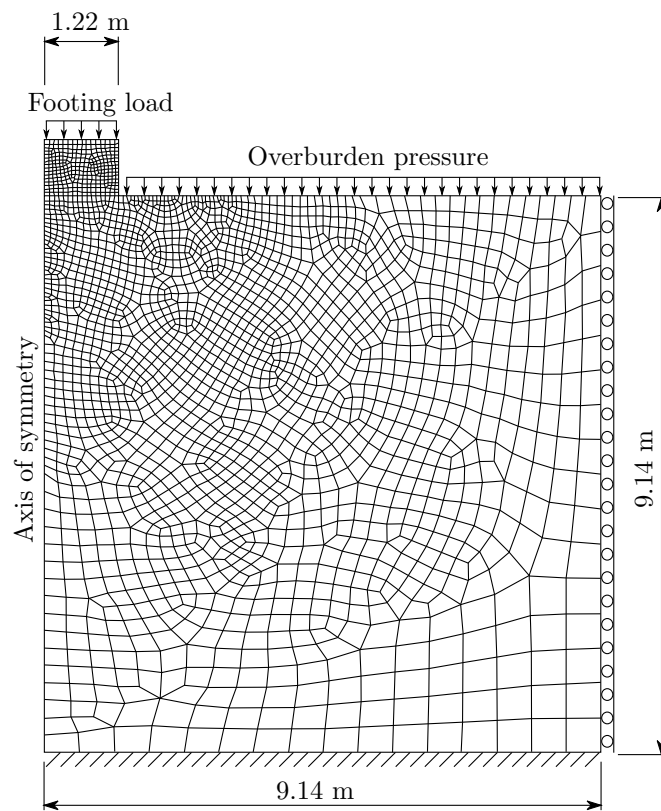


Figure 4.18: Footing analysis mesh and geometry (fine 2115 element mesh)

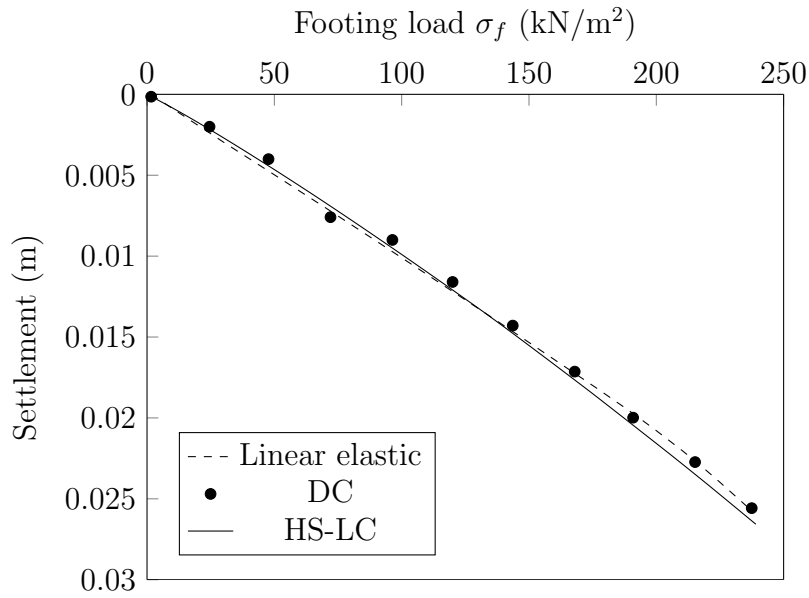


Figure 4.19: Circular footing settlements with linear elastic, Duncan-Chang, and HS-LC model

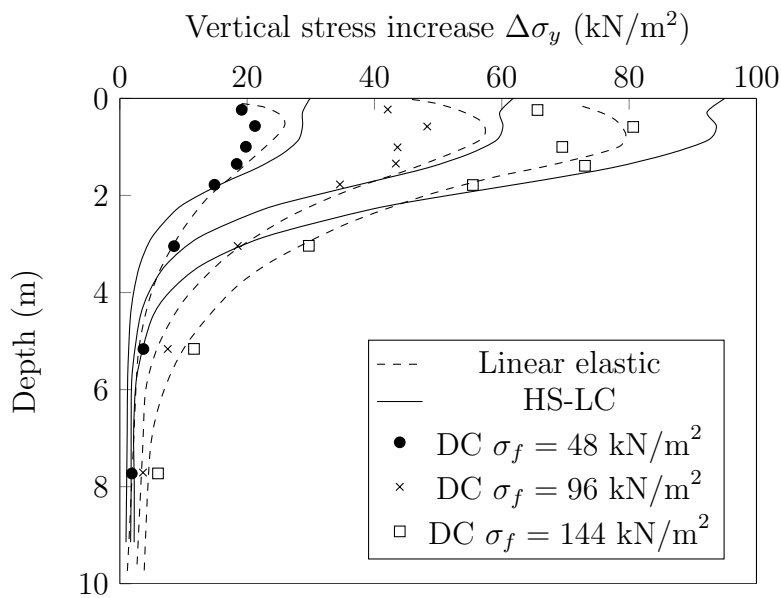


Figure 4.20: Circular footing stress profile beneath centreline with linear elastic, Duncan-Chang, and HS-LC model

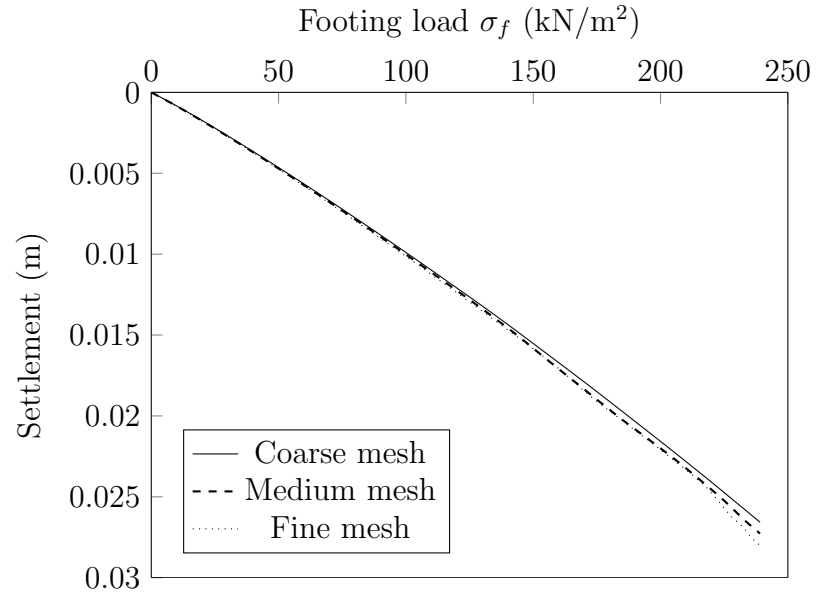


Figure 4.21: Circular footing predicted settlements using the HS-LC model with different mesh densities

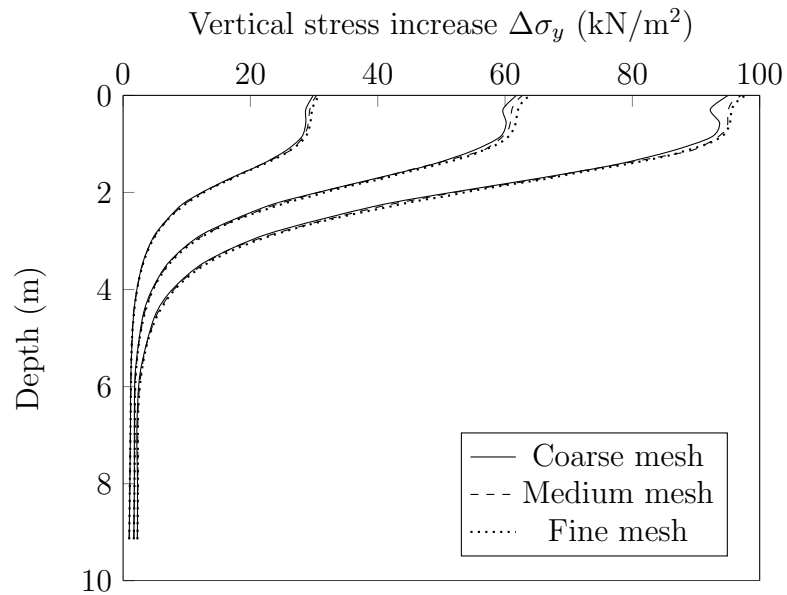


Figure 4.22: Circular footing stress profile beneath centreline using HS-LC model with different mesh densities

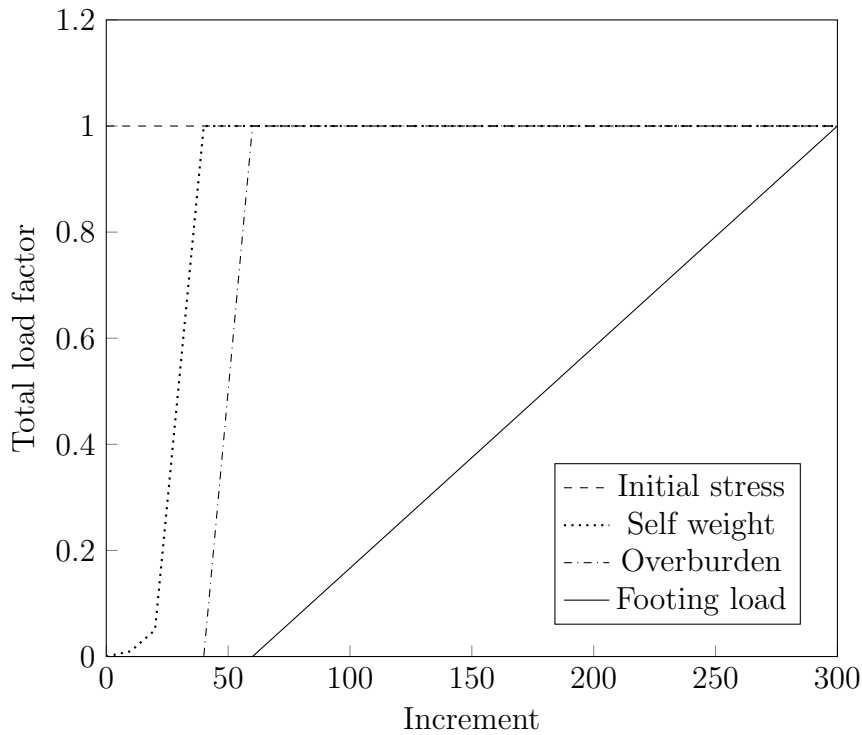


Figure 4.23: Load curves circular footing tests

The DC model does not use any total strain relationships or residuals to check if the internal stresses are balanced. Therefore, convergence to the true solution cannot be guaranteed (Bower and Duxbury, 2014). This may be the reason for the apparent scattering of the DC results in Figure 4.19. The DC model is also somewhat sensitive to the step size (Bower and Duxbury, 2014); the load in the DC simulation was applied in steps of 24 kN/m^2 (500 psf). It may be possible to reduce this apparent randomness in the DC model by reducing the step size, utilizing a sub-stepping scheme, or by refining the mesh.

Similarly with the vertical stress profile (Figure 4.20), the DC model produces profiles which oscillate near the top surface of the soil, particularly for the higher applied loads. The HS model also produces results which oscillate to a lesser degree near the surface. It is believed that this is due to the coarse mesh used in both simulations.

The mesh convergence study analysed compared results for the load-settlement curve (Figure 4.21) and the vertical stress profile (Figure 4.22) for meshes of three different densities. The predicted load-settlement curves for each mesh are visually

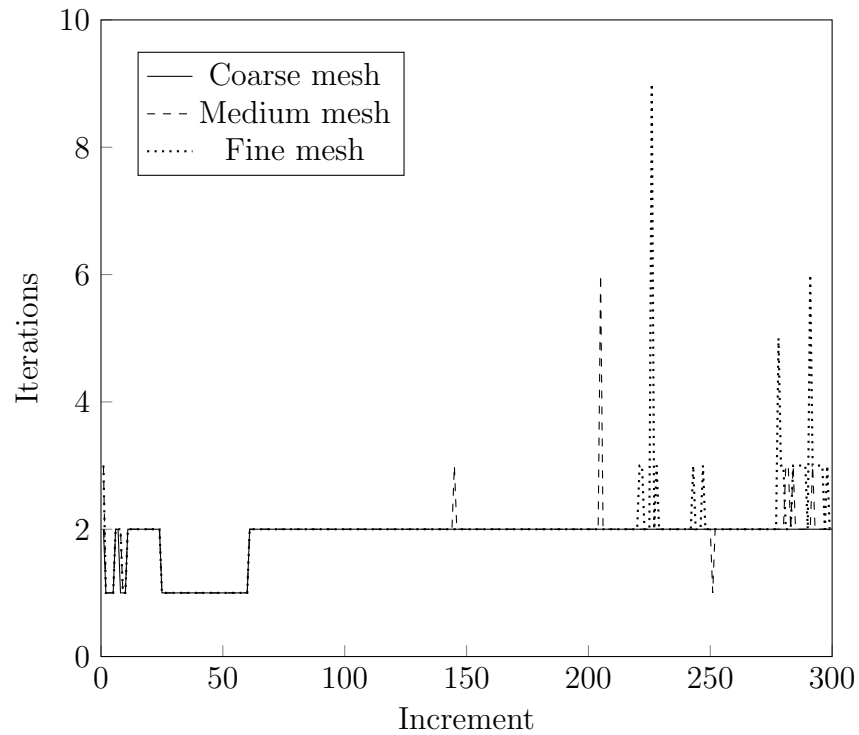


Figure 4.24: Converged iteration numbers for circular footing tests

very similar, indicating that the problem is not dependent on the mesh density. The vertical stress profile is, in general, very similar for each mesh. The most significant difference here is the prediction of vertical stress near the soil surface. The coarse mesh appears to provide a slightly unstable solution, where the results oscillate slightly. However, the medium and fine meshes both produce very similar curves which do not oscillate.

The DC model tends to exhibit lower stresses than the linear elastic model near the soil surface and matches the elastic results well when deeper into the soil. The HS model predicts higher stresses than the elastic model near the soil surface, and lower stresses deeper into the soil. The reason for the lack of vertical stress increase in the deep soil when using the HS model is that a higher portion of the stress is transferred horizontally. As no experimental are data available for this problem, it is difficult to comment on the accuracy of each model.

4.4 Leesburg footing

A second footing was analysed, which is a square footing located in the town of Leesburg, New Jersey, USA. The footing rests on several layers of soil, each with different material properties. Experimental data and predictions using the DC model are provided by Mitchell and Gardner (1971).

Domain: The footing used in the experimental study was a 1.524 m (5 ft) square, however it was analysed as a circular footing with an equivalent area such that the analysed footing diameter is 1.72 m. This is the same method used to analyse the footing in the work of Mitchell and Gardner (1971). The total depth of the soil was modelled as 7.312 m and the width of the axisymmetric domain was 15.0 m. The full geometry of the problem, including the depth of each layer is shown in Figure 4.25.

A second analysis was conducted which models the full three-dimensional geometry of the footing. In this model, a cuboid which represents the footing was placed in the centre of a larger cuboid which represents the soil. The symmetry of the geometry is exploited such that the domain is reduced to a quarter of the full geometry.

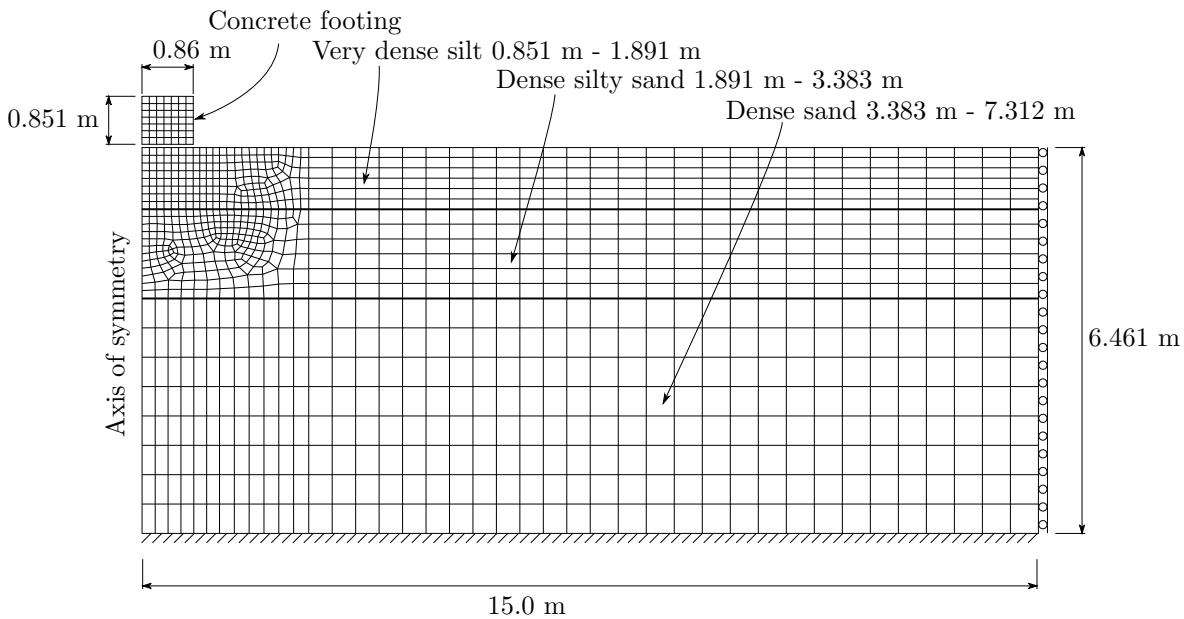


Figure 4.25: Leesburg footing geometry and mesh

Boundary conditions: The base of the soil was fully fixed, and the far field boundary was supported in the horizontal direction only. The axis of symmetry is inherently supported horizontally.

For the three-dimensional analysis, the planes where the symmetry are cut were restrained from moving perpendicularly to each plane, making the ‘cut’ model equivalent to the full geometry. The base of the soil was fixed in all directions, and the vertical faces opposite the footing were restrained in all directions except for vertically.

Mesh: For the axisymmetric analysis, the soil and footing were modelled using 1089 linear, quadrilateral, axisymmetric elements. For the three-dimensional analysis, 22197 quadratic, tetrahedral elements were used to model the soil and footing.

Contact spring elements were used in the joint between the footing and the soil. These are special joint elements in LUSAS which do not activate until the two designated contact surfaces meet. The perpendicular spring stiffness is set very high (100 GN/m^2), to simulate a rigid contact surface. The sliding spring stiffness was set to 1 MN/m^2 to simulate some sliding friction. It was found that adjustment of the spring stiffness had little influence of the footing displacement results. A total of 8 linear joint elements were used in the axisymmetric model, and 81 joint elements were used in the three-dimensional analysis.

A mesh convergence study was also performed on both the axisymmetric and 3-D analysis. The results were found to not differ significantly when using 275, 1089, or 4497 axisymmetric elements. Similarly for the 3-D analysis, using meshes of 8688, 22197 or 41204 tetrahedral elements did not significantly alter the results.

Materials: There are four soil layers considered in this analysis; a sandy topsoil, a very dense silt (L1), a dense silty sand (L2), and a dense sand (L3). Full material properties used in this analysis are shown in Table 4.1. The sandy topsoil layer was not modelled as part of the domain, but was applied as a vertical distributed load

representing the self weight of this layer which is 1.762 t/m^3 . The thickness of this layer was 0.851 m .

Loading: An initial compressive stress of 10 kN/m^2 was first applied to the soil, this is to avoid having invalid initial conditions of zero stress. This was of a low enough magnitude as to be negligible compared to the other applied loads. The self weight of the soil was modelled using a gravity body force applied to the entire soil. The different densities of each soil were automatically taken into account. The next loading phase was the overburden pressure from the ‘sandy topsoil’ layer, which was modelled as a uniformly distributed load of 14.71 kN/m^2 applied to the top of the ‘very dense silt’ layer. The final stage was the loading of the footing, which was a 600 kN/m^2 face load applied to the top of the footing.

The initial compressive stress was an assumed residual stress state for the soil, each subsequent loading phase was applied over 10 increments, giving a total of 30 increments for the analysis.

Convergence criteria: The residual force norm criterion used was 0.1% , and the incremental displacement norm criterion was 1.0% . The stiffness update procedure was used with a modulus change tolerance of $E_{tol} = 0.05$, and a weighting factor of $r = 0.33$.

Discussion: The axisymmetric predictions for the HS and the DC model are in close agreement (Figure 4.26). There is some deviation towards the end of the simulation ($\sigma_f > 500 \text{ kN/m}^2$) where the gradient predicted with the HS-LC model is slightly less steep than that of the DC model. It was found that adjustment of the post-shear-failure gradient in r_q (Equation 3.12) did alter this effect slightly. Modification of the arbitrarily assigned spring stiffness also had very little impact on the results in Figure 4.26.

The load-displacement curve for the three-dimensional analysis initially follows

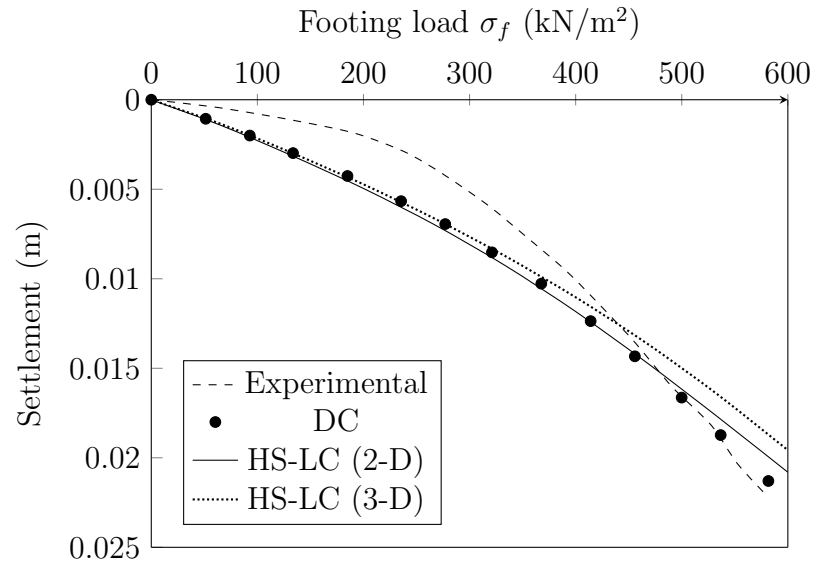


Figure 4.26: Leesburg footing settlements with experimental, DC, and HS-LC model results, experimental and DC results from Mitchell and Gardner (1971)

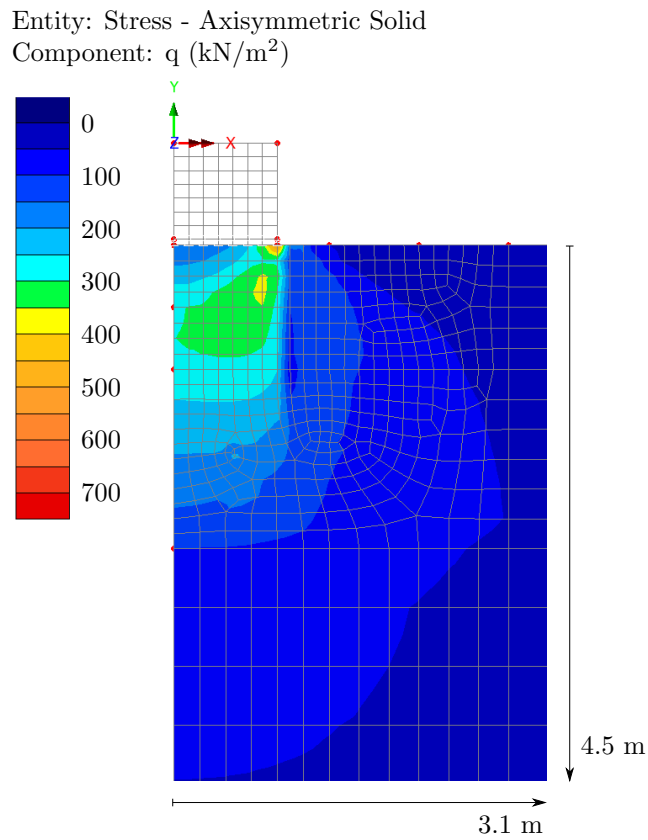


Figure 4.27: Cropped shear stress contour plot from the fully loaded Leesburg footing in the axisymmetric analysis

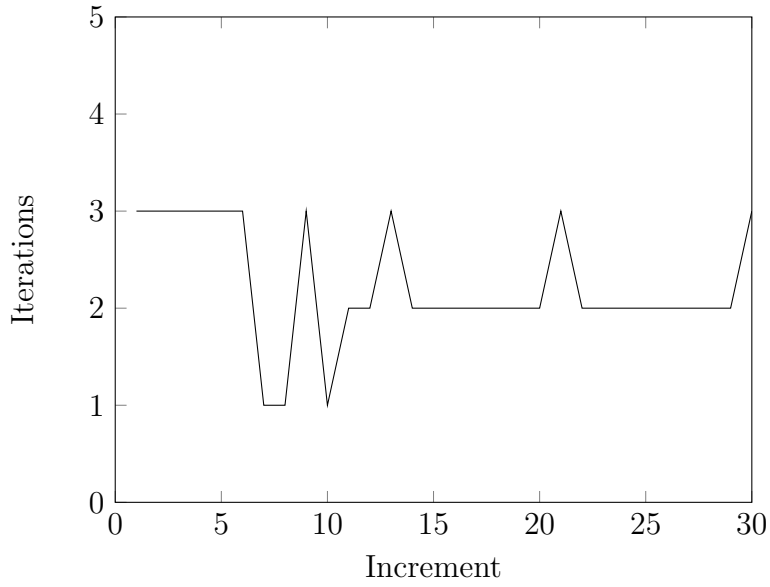


Figure 4.28: Converged iteration numbers for the axisymmetric Leesburg footing test

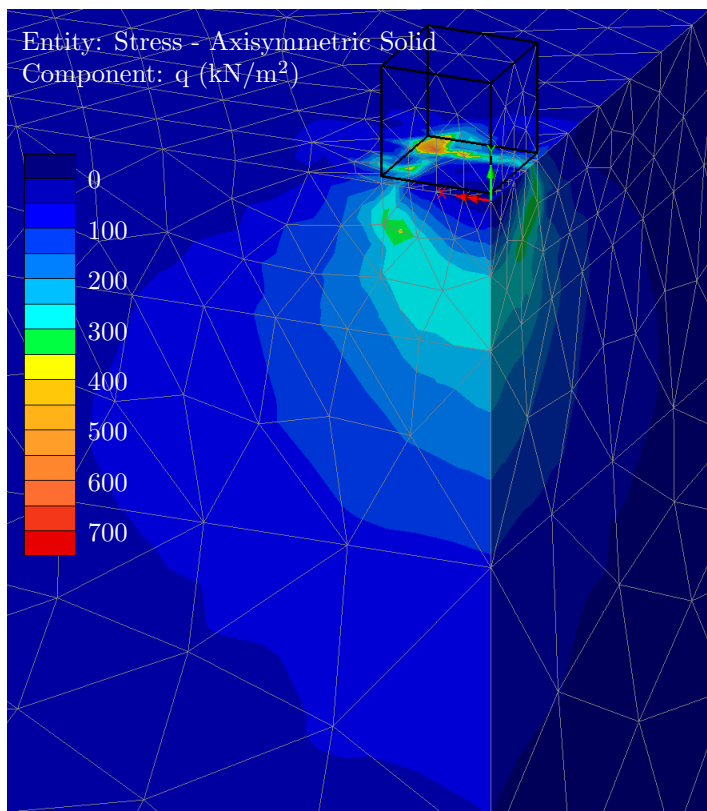


Figure 4.29: Shear stress contour plot from the fully loaded Leesburg footing in the three-dimensional analysis

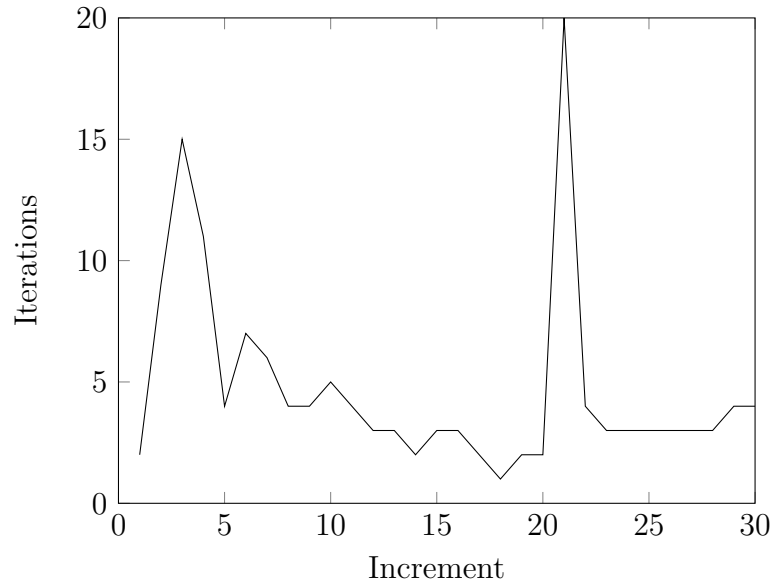


Figure 4.30: Converged iteration numbers for the three-dimensional Leesburg footing test

the axisymmetric results closely. However, the two solutions diverge slightly after a footing load of $\sigma_f = 300 \text{ kN/m}^2$, at this stage, the 3-D solution becomes slightly stiffer.

The shear stress plot of the axisymmetric results (Figure 4.27) show the distribution of shear stress around the footing. The area immediately under the centre of the footing undergoes less shear stress than the surrounding soil. This is because the loading conditions at this point are predominantly isotropic. A stress concentration develops at the edge of the footing, this is to be expected as the vertical load applied to the soil is discontinuous, and stops when outside the range of the footing.

Similar behaviour is observed for the 3-D analysis shear stress plot (Figure 4.29). The region under the centre of the footing undergoes very little shearing. The shear stress in this model is highly concentrated at the corner of the footing, and a lower shear stress concentration is located along the edges of the footing. This is because the discontinuity of loading is high at the footing edge, and highest at the footing corner.

Neither model is able to recreate the experimental results exactly with the given parameters; the stiffness at the start of the simulations is under-predicted, resulting

in the footing settlement being over-predicted. It may be possible to further improve this prediction by using the HS-LC model with altered parameters. The dilatancy is not modelled appropriately here therefore the method most likely to improve these results would be to use a more realistic set of Poisson's ratios and dilatancy angles.

This simulation has indicated the robustness of the proposed model by only requiring ten increments for each loading stage (as shown in Figure 4.28). The convergence criteria were a residual force norm of 0.1%, and an incremental displacement norm of 1.0%. Each increment in the axisymmetric analysis (Figure 4.28) converged in 3 iterations or fewer; peaks in loading are observed when a new load stage starts. The increments in the 3-D analysis (Figure 4.30) typically converged in 5 iterations or fewer, with peaks of 15 and 20 iterations at the start of the gravity and footing load stages respectively. It was found that lowering the density of the 3-D mesh significantly reduced the required number of iterations at these stages. The higher mesh density around the loading discontinuity created a steeper gradient and a higher shear stress at this point. It is likely that this increase in shear stress caused the solution to become less stable.

Ideally, the mesh used should be dense enough to capture behaviours around points of interest, such as the edge and corners of footings. However, in problems such as this, using too fine a mesh may create instabilities in the global solution. If a dense mesh were to be used for a problem such as this, then the problem can be stabilised using smaller step sizes. This is not a problem unique to the HS-LC model, as it can occur with many other material models and can also be resolved by modifying the geometry at the singularity (Huebner et al., 2001).

Concluding remarks

In this chapter, the performance of the HS-LC model was evaluated by comparing results from the previous versions of the HS model (Schanz et al., 1999; Benz, 2007), and from published experimental results. These comparisons consisted of both lab-

oratory based tests, and more complex problems; namely, footings on soil. For each case, the HS-LC model produced results which were in good agreement with the published results.

Alongside these results, a study on the influence of step size was also performed. For simulations of triaxial tests, it was found that the step size did not influence the results. However, for oedometer simulations, some step size dependency was observed. A method to resolve this issue was described Section 3.9 and is tested in this chapter. Use of this method significantly reduced the influence of the step size.

A mesh convergence study was also performed on the simulation of a circular footing. Here, three meshes were studied and it was found that each of them produced very similar results.

The performance of the HS-LC model was also evaluated by investigating the required number of iterations for each load increment to converge. For the basic laboratory simulations, the convergence rate was very good, with increments typically converging in 3 or fewer iterations. The more complex, boundary value problems also typically converged in less than 3 iterations per increment, however, some peaks in required iterations were observed, particularly during changes to load conditions; e.g. when the load on a footing initiates.

Chapter 5

A literature review on fibre-reinforced soils

The requirements for engineering soils are becoming increasingly demanding; with larger structures being built and less choice in where to put them, engineers cannot always be selective with site choice and soils often need to be improved. Such improvements can be achieved by methods such as vibro-compaction and drop weight compaction to increase the soil friction angle, or by importing stronger soils. Use of geosynthetics is another option to improve soil strength which can be applied in conjunction with other methods. These include geogrids, geomats, gemembranes for applications such as retaining walls (Yang et al., 2009; Yoo and Jung, 2004), embankments (Alamshahi and Hataf, 2009) and footings (Latha and Somwanshi, 2009; Sireesh et al., 2009).

Adding short manufactured fibres to the soil is a relatively new soil strengthening technique. The idea of this came from the well used concept of plant roots for slope stability (Waldron, 1977). The network of roots embeds into the surface of the soil, crossing potential shear failure surfaces and preventing the movement of soil particles.

Manufactured short fibres come in many forms. Common materials include polypropylene (Yetimoglu and Salbas, 2003; Cai et al., 2006; Tang et al., 2007; Di-

Diambra et al., 2010; Tang et al., 2010; Ibraim et al., 2012), polyethylene (Estabragh et al., 2014), polyamide (Michalowski and Čermák, 2003), steel (Michalowski and Zhao, 1996) and natural fibres such as coir (Sivakumar Babu et al., 2008; Maliakal and Thiyyakkandi, 2013) and oil palm empty fruit bunch (Ahmad et al., 2009). Different geometries are also available and all affect the strength of the composite material. Variations in fibre characteristics include:

- length (typically 6 mm to 50 mm)
- diameter / thickness (typically 30 μm to 1 mm)
- crimped or straight
- textured or smooth.

5.1 Experimental studies

Experimental evidence using several types of fibre and different soils typically show a significant improvement of shear strength in triaxial compression tests (Diambra et al., 2010; Consoli et al., 1998; Maher and Gray, 1990; Li and Zornberg, 2013; Michalowski and Čermák, 2003; Michalowski and Zhao, 1996; Sadek et al., 2010) along with a decrease in dilatancy for dense sands (Diambra et al., 2010; Consoli et al., 1998; Michalowski and Čermák, 2003; Michalowski and Zhao, 1996; Sadek et al., 2010). The strength of the composite is also heavily dependent on the distribution of fibre orientations (Michalowski and Čermák, 2002) such that the fibres aligned with the direction of the largest extension have the largest effect on the strength. Ibraim et al. (2012) also compared different sample preparation methods, producing distribution functions of fibre orientation for the moist-tamping technique and several variations with different fibre types.

Diambra et al. (2013) conducted a series of triaxial tests on three fibre types and at different concentrations. 35 mm length, 0.1 mm diameter, crimped fibres; 20 mm length, 0.03 mm diameter, monofilament fibres; and 40 mm length, 0.12×1.45 mm

rectangular, platy fibres were included in the testing program. Each fibre was made from polypropylene, however the Young moduli for each fibre was found to differ, with $E_f = 900, 2600, 4000 \text{ MN/m}^2$ for the crimped, monofilament and platy fibres respectively. Increasing the fibre content was found to increase the soil strength and increase dilatancy in triaxial compression (the soil was defined as a loose sand). In triaxial extension, the shear strength was largely unaffected by the presence of fibres, however the dilatancy was again increased. This increase in dilatancy is attributed to the increased occupation of voids in the composite.

For the same given fibre content and at the same confining stress, Diambra et al. (2013) found that the larger, rectangular fibres gave the least strength increase; the 20 mm monofilament fibres gave the largest strength increase, however the composite was observed to reach a distinct peak shear stress; the 35 mm crimped fibres contributed slightly less to the strength. However no peak shear stress was observed in the measured strain range of 30%.

Use of organic fibres may be limited for many engineering applications. One of the biggest concerns with their use is their degradation, particularly as they tend to be hydrophilic. Rahman et al. (2007) investigated the effects of coating oil palm empty fruit bunch (OPEFB) fibres with allyl methacrylate and methanol (after de-waxing). Accelerated weathering tests subjected the wetted soil-fibre composites to repeated cycles of light and temperature. It was found that the untreated fibres degraded at a faster rate than the polymer coated fibres. For 100 hours of accelerated weathering, the untreated fibre lost 3% of its weight, 21% of its tensile strength and 24% of its length; whereas the polymer treated fibre lost 2% of its weight, 8% of its tensile strength and 10% of its length. Urea coating was also tested with similar improvements to degradation properties.

Triaxial testing of OPEFB fibres (both treated and untreated) was performed by Ahmad et al. (2009) for a selection of fibre concentrations and lengths. Strength improvements were observed with the OPEFB fibres and additional strength was obtained from treatment of the fibres. The greatest strength improvement was seen

from 30 mm length fibres at a concentration of 0.5%, where the friction angle was increased by 25% and the cohesion was increased by 35%. Fibre concentration of 0.25% was also investigated and was also found to improve the soil strength, albeit to a lesser extent. Three lengths of fibre were also tested; 15, 30, and 45 mm; it was found that the 30 mm fibre provided the greatest strength improvement, followed by the 45 mm fibre. A reduction in dilatancy was also observed with fibre inclusion. Finally, it was found that the polymer coating on the fibres improved the strength properties of the composite, this was attributed to a larger fibre diameter and increased fibre tensile strength.

Maliakal and Thiyyakkandi (2013) investigated the influence of coir fibres (coconut husk) on clayey soil. The average diameter of these fibres was 0.24 mm, and the average tensile strength was reported to be 10100 kN/m². Similarly to the aforementioned studies, use of fibres increased the shear strength of the soil. Different fibre concentrations of 0%, 0.5%, 1% and 2% (by mass) were studied and it was found that within this range, increasing the fibre content increased the shear strength of the soil by 200% for the fibre concentration of 0.5%, and 280% for the concentration of 2%. Fibre lengths of 12, 24, and 36 mm were also studied at a concentration of 1%, with the longest fibre length increasing the shear strength of the soil by 220%, and the shortest by 200%.

A body of knowledge regarding the behaviour of fibre-reinforced soil is well established in the literature. Due to the lack of case studies on field projects using fibre-reinforced soils, it can be concluded that use of this technology is not yet widely applied in routine design. Development of accurate models to predict the behaviour of soil-fibre composites is one step which can contribute to the widespread use of this technology. Several such models have been proposed, and are discussed in the following section. These models range in complexity, and later models are typically based on theory developed for prior models.

5.2 Previously proposed soil-fibre models

In this section, five different soil-fibre models are explored, and their main features are discussed. The first is proposed by Maher and Gray (1990), which is based on earlier work by Gray and Ohashi (1983), and takes a simplified model based on the behaviour of a single fibre, and then homogenises this model into a soil model through a statistical approach. This model is then used to predict the failure envelope of fibre-reinforced soils.

The second model discussed was proposed by Michalowski and Čermák (2003), and is based on a previous model by Michalowski and Zhao (1996). This model uses an energy approach to predict the failure envelope of fibre-reinforced soils. The next model by Diambra et al. (2010) uses a combination of mechanical and empirical relationships, along with the statistical integration approach used by Maher and Gray (1990), to predict the stress-strain paths of soil-fibre composites in triaxial tests. A number of modifications were then made to this model by Diambra and Ibrahim (2015), which replace some of the empirical relationships with micromechanical relationships. Additionally, a more advanced soil model was used to analyse the soil portion.

Another model, which only looks at the behaviour of a single fibre, was proposed by Zhu et al. (2014). This model is based on the observed behaviour of a fibre during a pullout test in clay, and uses a combination of mechanical relationships and calibrated parameters. Each of the aforementioned models are now discussed in the following section.

5.2.1 Statistical distribution model with shear strength increase

The strength increase for a particular shear plane can be identified for each orientation by the portion of fibres crossing the plane. Maher and Gray (1990) applied

a probability function to the strength increase model varying both the fibre orientation and the position of the shear plane along the fibre length. They base their model on the micromechanical model of Gray and Ohashi (1983).

The assumptions used in the micromechanical model (Gray and Ohashi, 1983) are as follows

- Fibres extend equal lengths over each side of the shear plane
- The fibres are elastic
- The fibres are oriented in a single direction
- The fibres are thin enough such that shear and bending stiffness is negligible

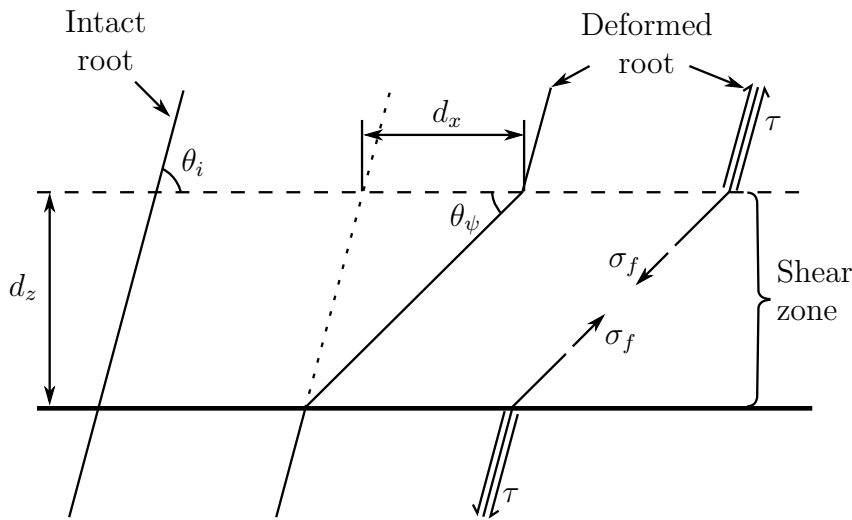


Figure 5.1: Fibre-reinforcement model: fibres obliquely crossing a shear zone (re-drawn from Gray and Ohashi, 1983)

In reference to Figure 5.1 the increase in shear strength is due to the pullout resistance of the embedded fibre length. This shear strength increase is given by

$$\Delta S_R = t_f \left[\sin(90 - \theta_\psi) + \cos(90 - \theta_\psi) \tan(\varphi) \right] \quad (5.1)$$

$$\tan(\theta_\psi) = \left[\frac{1}{k + (\tan^{-1} \theta_i)^{-1}} \right] \quad (5.2)$$

where θ_ψ is the orientation of the fibre relative to the shear plane (for fibres perpendicular to the shear plane, $\tan(\theta_\psi) = d_z/d_x$), φ is the internal angle of friction of the unreinforced sand, k is the shear distortion ratio ($k = d_x/d_z$), θ_i is the initial orientation of the fibre relative to the shear zone, d_x is shear displacement, d_z is the thickness of the shear zone. The mobilised tensile strength per unit area of soil is given by

$$t_f = \left(\frac{A_f}{A} \right) \sigma_f \quad (5.3)$$

where σ_f is the tensile stress carried by the fibre, A and A_f are the cross sectional areas of the soil and fibres respectively; the ratio of these is synonymous to the volume fraction.

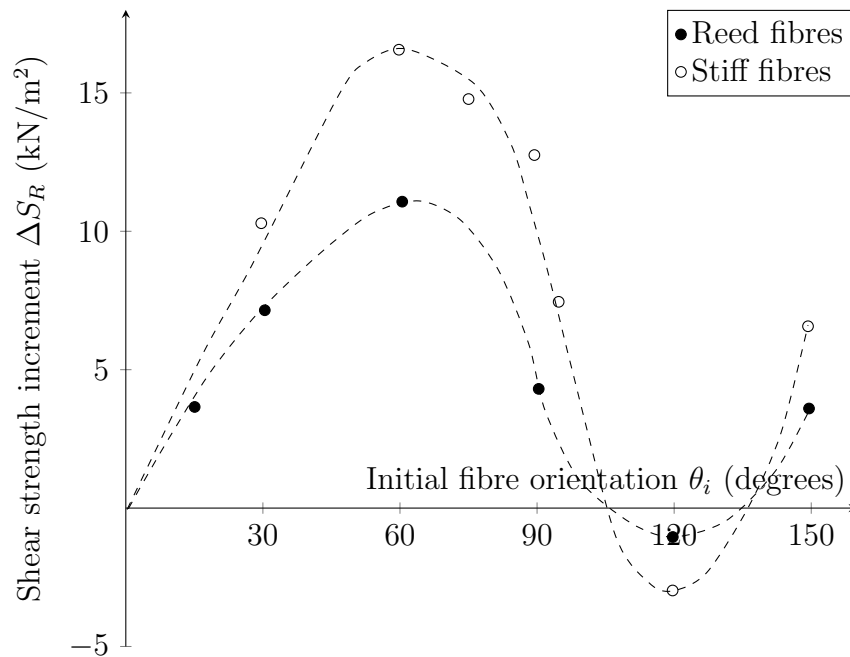


Figure 5.2: Influence of fibre orientation on shear strength in a reinforced shear box test (redrawn from Gray and Ohashi, 1983), soil is a dune sand with friction angle $\varphi = 39^\circ$, stiff fibre results from Jewell (1980)

Jewell (1980) showed experimentally and Gray and Ohashi (1983) with this model that varying the initial fibre orientation changed the composite strength (Figure 5.2) with the optimum orientation being approximately 60° to the shear plane. Maher and Gray (1990) made use of this feature to model randomly distributed short fibres. The orientation of the fibres on a horizontal axis (Equation 5.4) and vertical

inclination (Equation 5.5) is varied according to the probability density functions:

$$P_{\theta}(\theta_i) = \frac{1}{2\pi}d\theta_i \quad (5.4)$$

$$P_i(i) = \frac{1}{\pi}di \quad (5.5)$$

This corresponds to a fully random orientation distribution within a spherical coordinate system. The position of the failure plane along the fibre length is described statistically by

$$P_x(x) = \frac{2}{L}dx \quad (5.6)$$

which represents a uniform distribution of fibre positions relative to the shear plane.

Comparison with experimental results (Figure 5.3) shows reasonably good predictions of failure envelopes in principal stress space for different soil and fibre types. The principal stress envelopes are either linear, bi-linear or curved; this is also captured in the predictions.

The critical confining stress where the failure envelope changes shape is indicative of the fibre contribution. For most of the tests, the fibre content was kept constant at $w_f = 3\%$. The range of confining stresses studied was also constant between 50 kN/m^2 and 400 kN/m^2 . The change in gradient of the failure envelope indicates that the fibres contribute less to the strength of the composite. The gradient of this section is equal to the gradient of the failure envelope for an unreinforced soil.

The nature of the failure envelope was found to be dependent on many factors, including fibre modulus, fibre aspect ratio, soil particle size and particle shape.

It was also found that the increase in fibre content is approximately proportional to the shear strength increase. However an asymptotic upper limit of fibre content does exist where no increase in strength is observed (Maher and Gray, 1990).

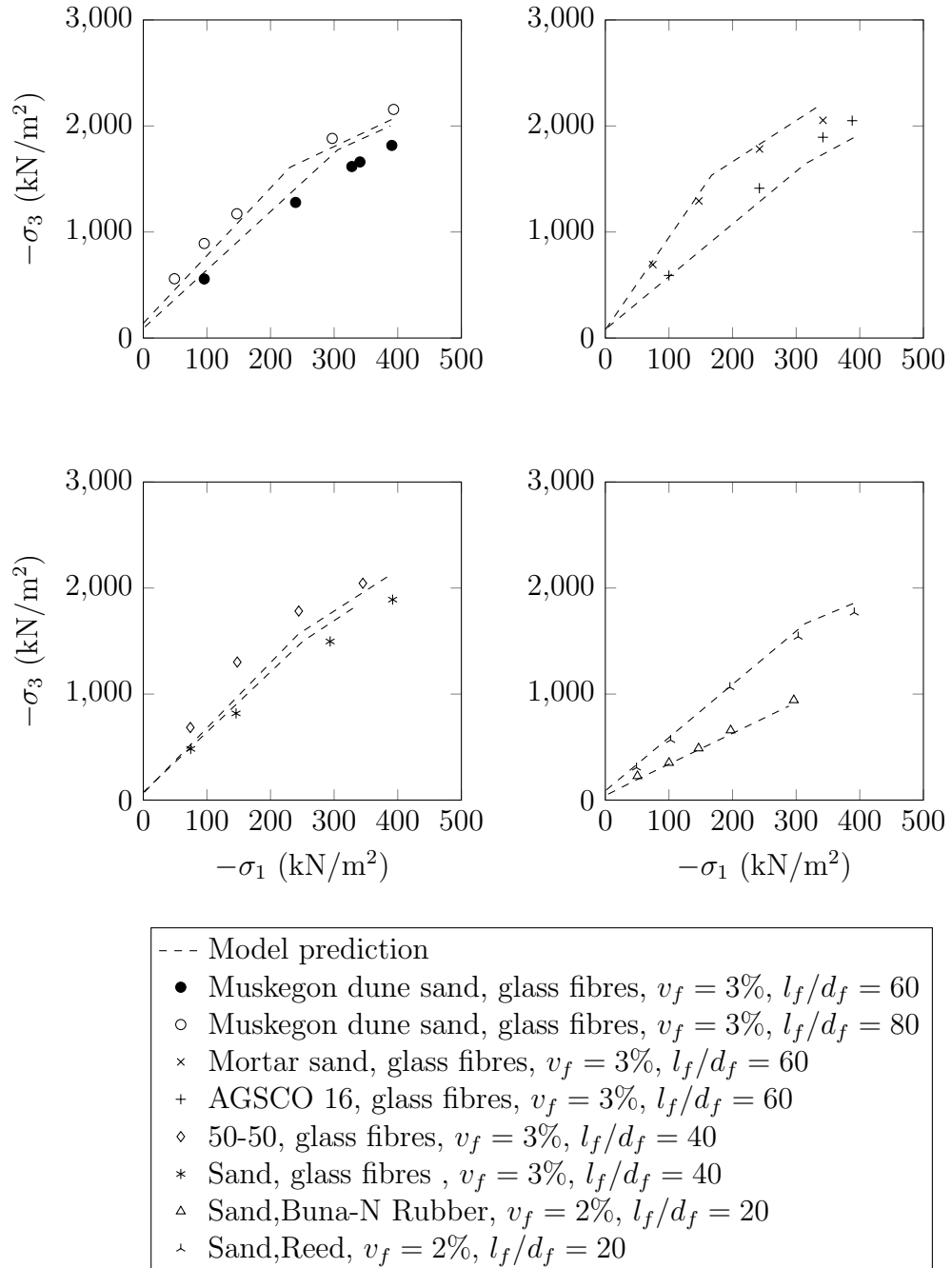


Figure 5.3: Experimental and predicted failure envelopes in principal stress space for soils reinforced with different fibres (redrawn from Maher and Gray, 1990)

5.2.2 Energy-based homogenisation method

A failure criterion describing the ultimate state of fibre-reinforced soils was developed by Michalowski and Čermák (2003) for axisymmetric conditions. The model is based on earlier work by Michalowski and Zhao (1996) which defines a failure criterion for fibre-reinforced soil in plane strain conditions. The formulation begins with the equation governing the dissipation rate of a single fibre with the strain rate $\dot{\epsilon}_\theta$ oriented in the direction of the fibre, which is presented as:

$$\dot{d} = \frac{1}{2} \pi r_f l_f^2 \langle \dot{\epsilon}_\theta \rangle \bar{\sigma}_r \tan \varphi_i \quad (5.7)$$

and is given for fibres in the elastic region where r_f is the fibre radius, l_f is the length of the fibres, φ_i is the frictional angle for the fibre-soil interface, and $\bar{\sigma}_r$ is the average radial stress acting on the fibre. For fibres which are yielding, the following relationship is used:

$$\dot{d} = \pi r_f^2 l_f \sigma_0 \left(1 - \frac{1}{4\eta} \frac{f_y}{\bar{\sigma}_n \tan \varphi_i} \right) \langle \dot{\epsilon}_\theta \rangle \quad (5.8)$$

Note the Macauley brackets around the strain term denoting fibre contributions for tensile strains only. η is the fibre aspect ratio l_f/r_f , and f_y is the fibre yield stress.

This expression is then integrated over a unit sphere to obtain the energy dissipation rate per unit volume. For an isotropic distribution of orientations, the dissipation rate in the composite when the fibres are not yielding is given by

$$\dot{D}_r = \frac{1}{3} w_f \eta M \bar{\sigma}_n \tan \varphi_i \dot{\epsilon}_3 \quad (5.9)$$

and when the fibres are yielding

$$\dot{D}_r = \frac{w_f f_y}{3} M \left(1 - \frac{1}{4\eta} \frac{f_y}{\bar{\sigma}_n \tan \varphi_i} \right) \dot{\epsilon}_3 \quad (5.10)$$

where M is a material constant related to the friction angle of the granular matrix.

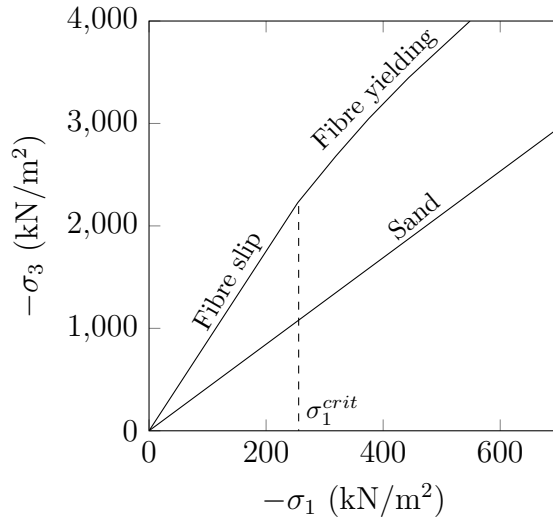


Figure 5.4: Failure criterion for fibre-reinforced soils (redrawn from Michalowski and Čermák, 2003), $w_f = 2\%$, $\eta = 150$, $\varphi = 38^\circ$, $\varphi_i = 15^\circ$, $f_y = 100 \text{ MN/m}^2$

The yield surface for this composite model shows two distinct surfaces (Figure 5.4). In three-dimensional stress space, the yield surface may be visualised as a cone; axisymmetric about the line $\sigma_1 = \sigma_2 = \sigma_3$. The yield surface for the unreinforced sand is linear, and the introduction of the fibres increases the angle of the cone. When the fibres begin to yield, the cone becomes non-linear. The transition into non-linearity is described as the critical confining stress σ_1^{crit} .

Predictions of the model capture the failure envelope for reinforced sands and is consistent with experimental data. Figure 5.5a with a 0.5% fibre content shows a small increase in the size of the failure envelope for higher confining stresses. At low confining stress ($-\sigma_1 \approx 100 \text{ kN/m}^2$) neither the experimental nor the prediction show any increase in maximum $-\sigma_3$ from the unreinforced sand.

At 1.5% fibre content (Figure 5.5) the failure envelope is expanded further, allowing a higher σ_3 before failure. At low confining stress there is now some strength increase; this is captured in the predictions.

Overall, it is evident that this model is able to predict the failure of fibre-reinforced sand with good accuracy. Figure 5.5, along with additional figures in the paper by Michalowski and Čermák (2003), show that the failure criterion proposed is a good match for the experimentally derived failure surface. The predictions

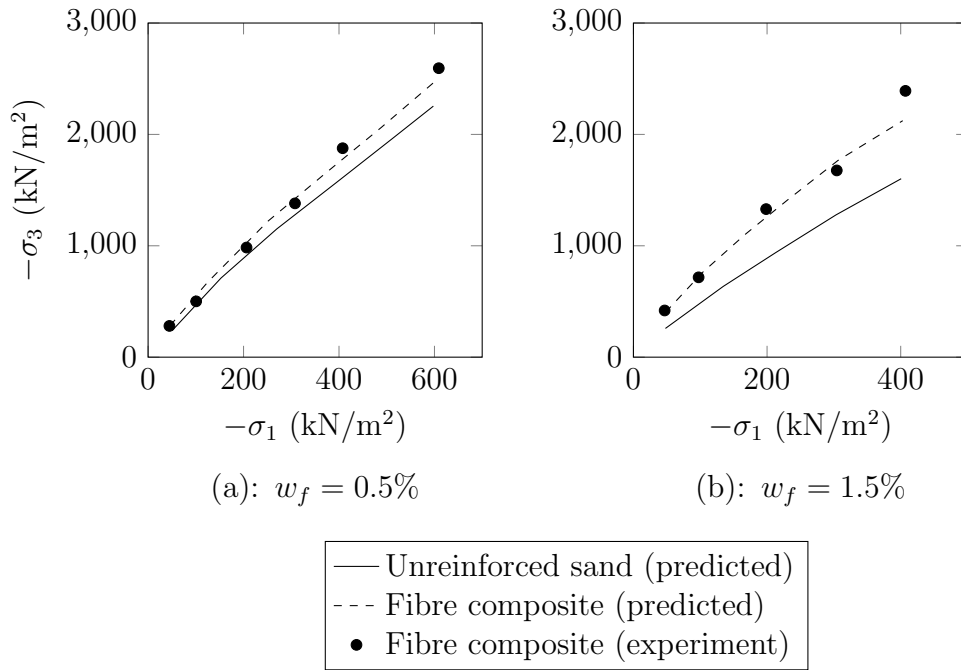


Figure 5.5: Experimental and predicted failure criteria for unreinforced and reinforced coarse sand with different concentrations of polyamide fibres (redrawn from Michalowski and Čermák, 2003)

with this model appear to be closer to the experimental data than shown with the model proposed by Maher and Gray (1990), however, fewer variations are tested, therefore it is not appropriate to directly compare the accuracy of both models.

5.2.3 Fibre contribution matrix with empirical debonding

A model based on the rule of mixtures was presented by Diambra et al. (2010), and calculates the strength contribution of the matrix (soil) and fibre separately, these contributions are summed according to their respective volume fractions as

$$\boldsymbol{\sigma} = \boldsymbol{\sigma}_m v_m + \boldsymbol{\sigma}_f v_f \quad (5.11)$$

With the rule of mixtures, the fibres are assumed to be distributed uniformly throughout the matrix. The fibres and matrix are governed by their own constitutive law, making this model ideal to apply to a variety of soil plasticity models (e.g. Mohr-Coulomb).

The stress state for a composite is considered as the sum of the contributions by the fibre and the matrix. $\boldsymbol{\sigma}_m$ and $\boldsymbol{\sigma}_f$ are the stresses carried by the matrix and fibre respectively, v_m and v_f are the volume fractions of the matrix and fibre respectively such that $v_m + v_f = 1$. Voigt's hypothesis holds for this model whereby the strains in the fibre and matrix are assumed to be identical.

$$\boldsymbol{\varepsilon} = \boldsymbol{\varepsilon}_m = \boldsymbol{\varepsilon}_f \quad (5.12)$$

A non-uniform distribution function is used to describe the variation of orientations with a particular sample preparation method.

$$\rho(\vartheta) = \frac{2ab|\cos(\theta)|}{\cos^2(\vartheta)(b^2 - a^2) + a^2} \quad (5.13)$$

where a and b are curve fitting parameters to match the given orientation distribution.

A probability function is inserted into the spherical integral. In the axial and radial coordinate system, the fibre stiffness matrix is

$$v_f \begin{bmatrix} d\sigma_{f,3} \\ d\sigma_{f,1} \end{bmatrix} = E_f f_b \begin{bmatrix} \int_{\vartheta_1}^{\vartheta_2} \rho(\vartheta) \cos(\vartheta) \sin^4(\vartheta) d\vartheta & \int_{\vartheta_1}^{\vartheta_2} \rho(\vartheta) \cos^3(\vartheta) \sin^2(\vartheta) d\vartheta \\ \frac{1}{2} \int_{\vartheta_1}^{\vartheta_2} \rho(\vartheta) \cos^3(\vartheta) \sin^2(\vartheta) d\vartheta & \frac{1}{2} \int_{\vartheta_1}^{\vartheta_2} \rho(\vartheta) \cos^5(\vartheta) d\vartheta \end{bmatrix} \begin{bmatrix} d\varepsilon_3 \\ d\varepsilon_1 \end{bmatrix} \quad (5.14)$$

The integral limits in (5.14) represent the range where the fibres are active, i.e. in tension, for triaxial states. In triaxial compression, the active fibres are predominantly closer to the horizontal plane, therefore $\vartheta_1 = 0$ and $\vartheta_2 = \vartheta_c$. In

triaxial extension, $\vartheta_1 = \vartheta_c$ and $\vartheta_2 = \pi/2$, where

$$\vartheta_c = \arctan\left(\sqrt{-\frac{d\varepsilon_1}{d\varepsilon_3}}\right) \quad (5.15)$$

This model does not take into account the position of the fibre relative to a shear plane, instead this effect becomes part of a fibre debonding function defined as

$$f_b = K_e \left(1 - \exp\left\{-c_s \frac{p'}{p^{ref}}\right\}\right) \quad (5.16)$$

where K_e is an fibre-particle bonding efficiency coefficient and c_s is a stress dependency coefficient. The fibre slip is related to the mean effective stress p' , and is normalised by a reference stress p^{ref} .

This function takes permanent fibre debonding into account with $f_b = 1$ for full length bonding and $f_b = 0$ for complete debonding of fibres. For the latter case, the fibres do not contribute to the composite strength.

Used alongside the Mohr-Coulomb soil model, Diambra et al. (2010) reported that this fibre model produces comparable results to triaxial compression tests (Figure 5.6) with predictions within around 5% of experimental results. Unreinforced specimens exhibit a limiting shear stress, with even low amounts of reinforcement (0.3%) the composite appears to undergo linear hardening indefinitely.

Experimental data show that an increase in fibre content increases the dilatancy during shearing. This trend is replicated in the model. However, the actual values of volumetric strain are not captured accurately with differences of up to 50% between experiments and predictions. This inaccuracy may be due to the chosen matrix material model. Diambra et al. (2013) applied the same fibre model to a more advanced soil model, known as the Severn-Trent model (Gajo and Muir Wood, 1999), shown in Figure 5.7. Here the non-linearity in the $q - \varepsilon_q$ and $\varepsilon_p - \varepsilon_q$ plots are captured by the model. Unreinforced simulations of the volumetric effects are within 10% of the experimental results and the reinforced sample simulations are

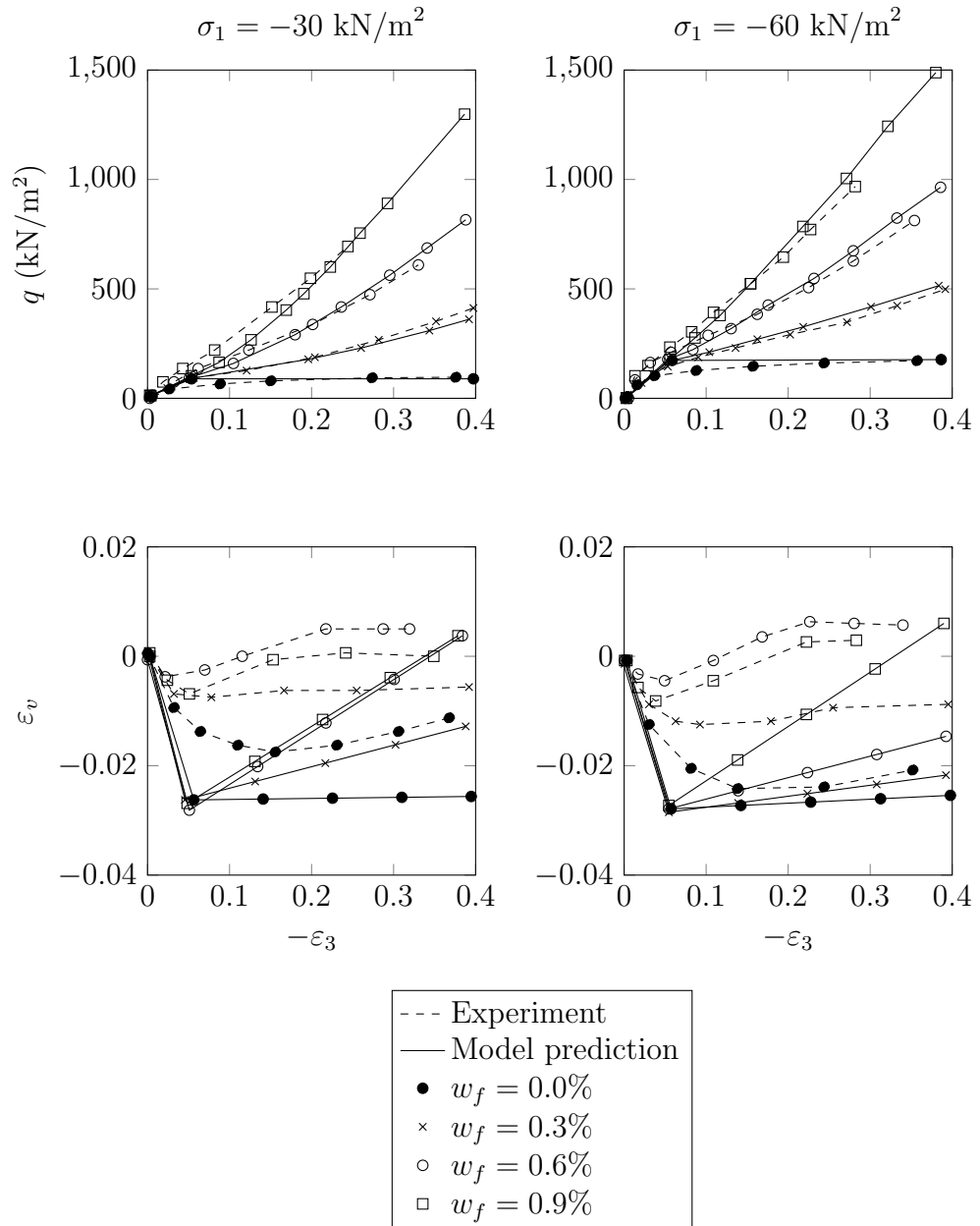


Figure 5.6: Experimental and predicted triaxial test results on loose sand-fibre composite at different fibre contents and confining stresses; the Mohr-Coulomb soil model is used here (redrawn from Diambra et al., 2010)

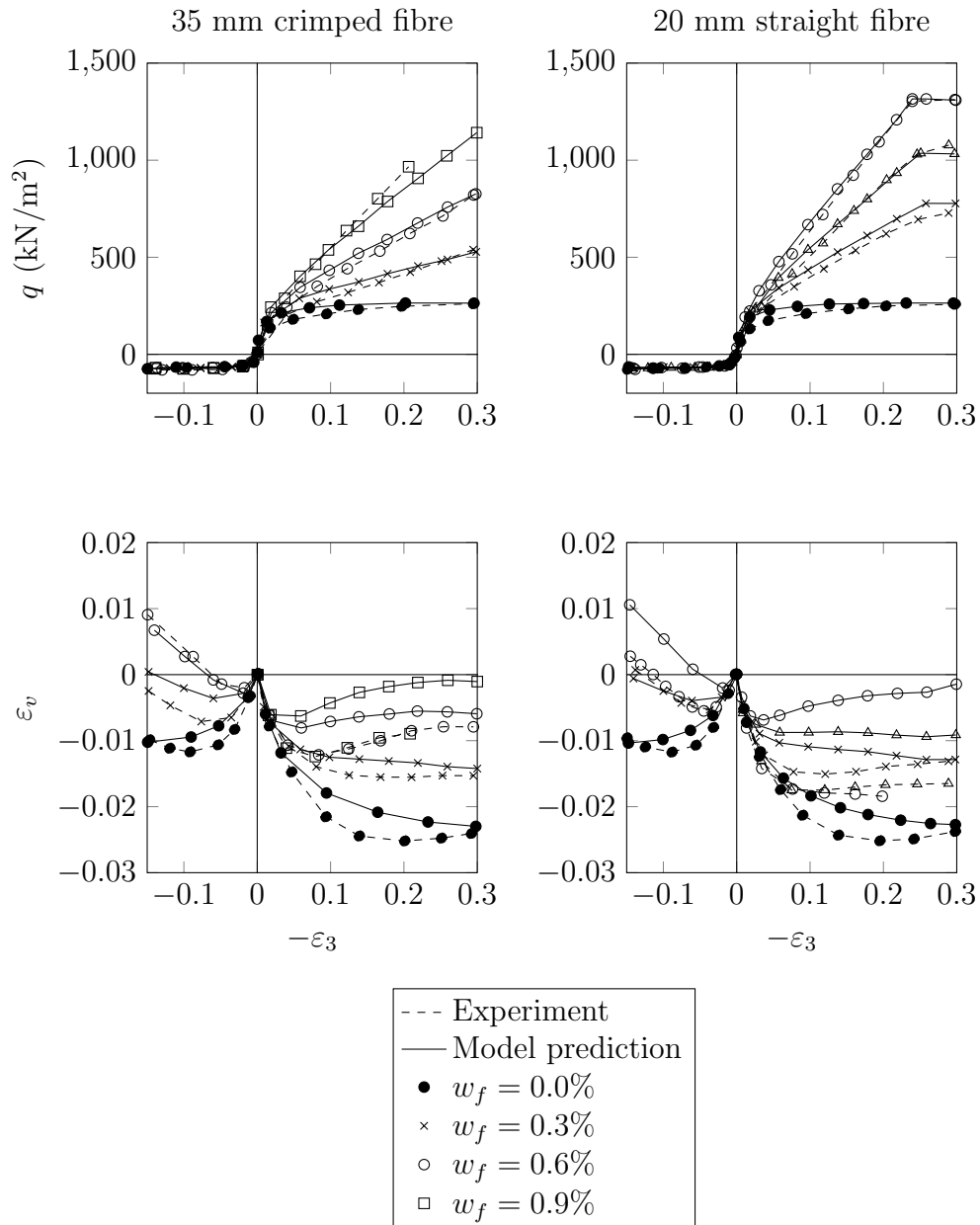


Figure 5.7: Experimental and predicted triaxial compression and extension test results on loose sand-fibre composite at different fibre contents and confining stresses, the Severn Trent soil model is used here (redrawn from Diambra et al., 2013)

within 20% for the fibre contents of 0.6% and 0.3% and less accurate for 0.9% fibre content.

These improvements in the predictions from Diambra et al. (2010) to Diambra et al. (2013) suggest that the accuracy of the soil-fibre composite models is heavily dependent on the chosen soil constitutive model. Therefore, advanced soil models should be used to predict unreinforced soil behaviour before attempting to introduce an overlaying fibre model.

5.2.4 Fibre pullout model in clay

A micromechanical model for the slip of a single fibre in a clay matrix was proposed by Zhu et al. (2014). The driving component of this model is the pullout force, where a single fibre is pulled through a fixed volume of soil. Zhu et al. (2014) make several observations regarding the different pullout stages. During the first stage, elastic slip occurs where the mobilised shear stress increases linearly with slip displacement and is fully recoverable until a critical interface shear stress is reached τ_{max} . A softening phase then occurs in clays where the interface shear stress reduces linearly with displacement, this effect first occurs at the fibre ends where the most slip occurs. The interface shear stress continues to soften until a residual stress is reached τ_{res} . At this stage; strength contribution of the fibres can no longer increase.

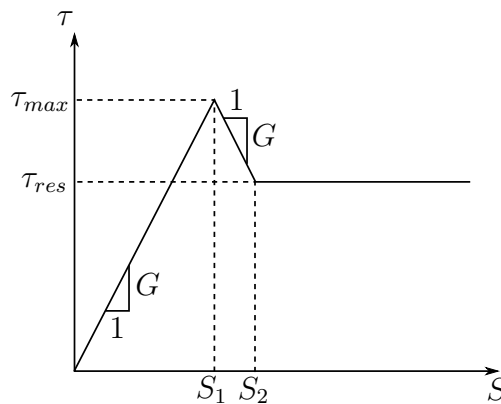


Figure 5.8: Proposed fibre slip model: interface shear stress against slip displacement (redrawn from Zhu et al., 2014)

A simple force equilibrium of a infinitesimal fibre slice is taken

$$dF(x) = -2\pi r_f \tau(x) dx \quad (5.17)$$

Substituting a mechanical relationship between $F(x)$ and $\tau(x)$, and differentiating, leads to the second order differential equation

$$\frac{d^2 F}{dx^2} - \beta^2 F = 0 \quad (5.18)$$

where

$$\beta = \sqrt{\frac{2G}{r_f E_f}} \quad (5.19)$$

and G is the shear modulus of the matrix.

Applying the boundary conditions $F(l_f) = 0$ and $F(0) = F_0$ where F_0 is the pullout force, the solution for the elastic stage becomes

$$F_e(x) = F_0 \frac{\sinh(\beta(l_f - x))}{\sinh(\beta l_f)} \quad (5.20)$$

The subsequent stages are formulated similarly, with varying boundary conditions. Simulations using this pullout model (Figure 5.9) produce results which closely match the experimental pullout data. Tang et al. (2010) performed a series of pullout tests on different water contents and dry densities, and this model was able to accurately reproduce results for dry densities of 1.4, 1.5, 1.6, 1.7 g/cm³ and water contents of 14.5, 16.5, 18.5, 20.5%, however, some non-linearity in the elastic stage is missed in most predictions.

Although this model produces accurate results, it is unclear if it is directly applicable to granular soils. However, as the formulation is based on the pullout force rather than the matrix displacement, it may not be possible to implement in a homogenised model in its current form.

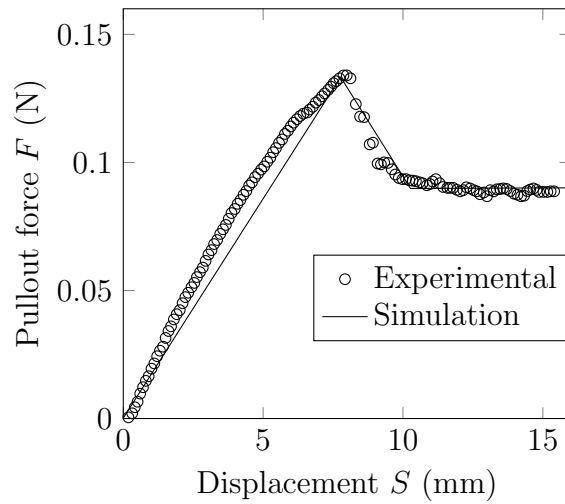


Figure 5.9: Simulated and experimental fibre pullout results (redrawn from Zhu et al., 2014)

5.2.5 Shear lag soil model

Following from previous work (Diambra et al., 2010, 2013), Diambra and Ibraim (2015) presented a further development of their soil-fibre model, which takes into account the non-uniform stress within a fibre during loading (Diambra and Ibraim, 2015). The shear lag model, first proposed by Cox (1952), is based on the transfer of strain from the matrix to the fibre, through a shear layer acting at the interface (Figure 5.10). At some distance R the shear stress in the soil is assumed to equal zero and the deformation contours remain straight.

To model a single fibre, a composite cylinder of radius R_c and length l_f containing matrix material and a single fibre in the centre is considered (Figure 5.11). The size of this influence cylinder is governed by the volume fraction of the fibres (assuming fully homogeneous, random fibre positions).

$$R_c = r_f \sqrt{\frac{1}{v_f}} \quad (5.21)$$

where r_f is the fibre radius and v_f is the volume fraction of fibres to soil. The radius of the shear stress carrying cylinder is given by the average of the fibre radius and the composite cylinder radius.

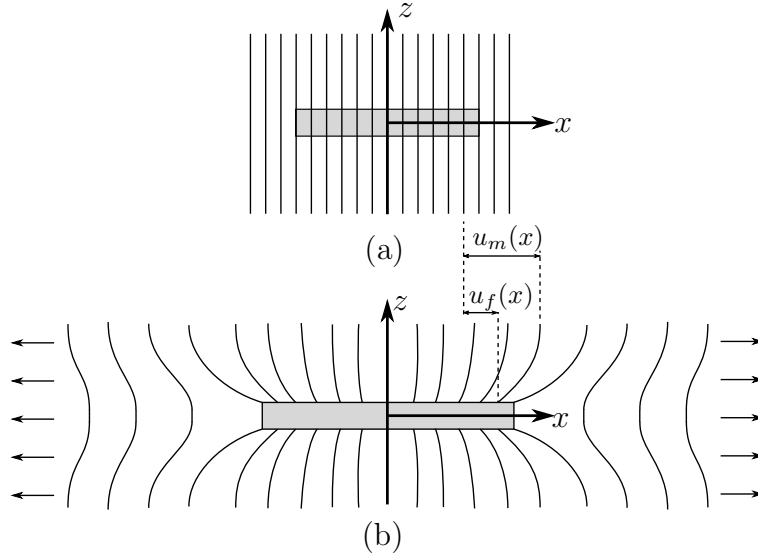


Figure 5.10: Shear lag concept, showing strain contours of (a) un-deformed state and (b) deformed state (Hull and Clyne, 1996) as cited in Diambra and Ibraim (2015) (redrawn)

$$R = \frac{R_c + r_f}{2} \quad (5.22)$$

Based on the approach by Aveston and Kelly (1973) the effects on the cylinder are governed by two behaviours. Firstly, an axial stress is applied to the outside surface of the cylinder σ_m . The volume of the cylinder then carries pure shear, with the maximum shear stress at the fibre-matrix interface τ_i .

To determine the stress in the fibre, a force equilibrium is taken on an infinitesimal length of fibre in a strained state.

$$\delta\sigma_f = -2\frac{\tau_i}{r_f}dx \quad (5.23)$$

Similarly to the model by Zhu et al. (2014), substituting a micro-mechanical relationship between the interface shear stress τ and the axial fibre stress σ_f , and differentiating, leads to

$$\frac{\delta^2\sigma_f}{\delta x^2} = \frac{n^2}{r_f^2}(\sigma_f - E_f\varepsilon) \quad (5.24)$$

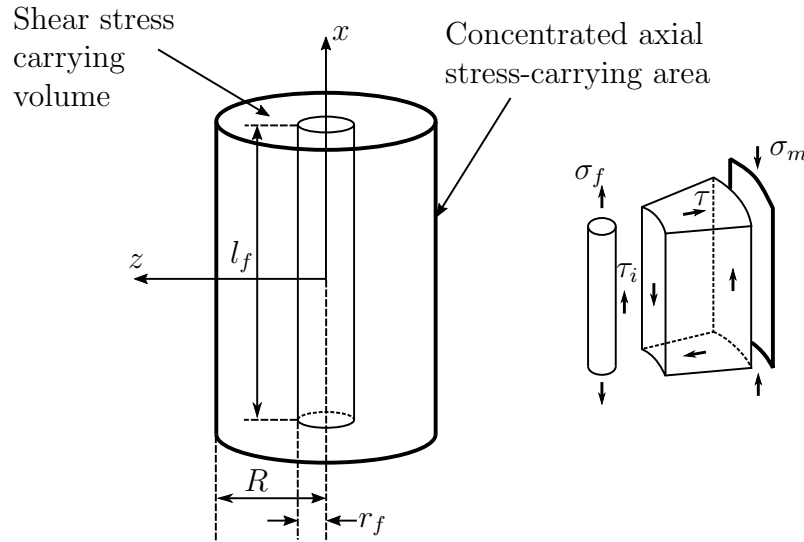


Figure 5.11: Geometry and stress transfer in idealised soil-fibre composite (redrawn from Diambra and Ibraim, 2015)

where n is a parameter related to the interface shear strength and fibre geometry, E_f is the axial Young modulus of the fibre, ε is the applied far field composite strain, i.e. the strain at a distance R from the fibre axis. Imposing the boundary conditions of zero end forces, the solution to (5.24) is

$$\sigma_f(x) = E_f \varepsilon \left(1 - \frac{\cosh\left(\frac{nx}{r_f}\right)}{\cosh\left(\frac{nl_f^*}{2r_f}\right)} \right) \quad (5.25)$$

where x is the position along the fibre ($-l_f/2 \leq x \leq l_f/2$) and l_f^* is the effective fibre length which is a reduction of the true fibre length. Discrete element modelling by Maeda and Ibraim (2008) indicated the full length of the fibre may not be fully mobilised, therefore the approach used here is to reduce the fibre length according to the grain size and fibre diameter.

To model debonding, a fibre debonding function is used. This is similar to the approach taken by Diambra et al. (2010), however the level of debonding is now governed by the effective aspect ratio; which is a given parameter.

$$f_b = \frac{s^*}{s} - \frac{\tanh(ns^*)}{ns} \quad (5.26)$$

where s is the true aspect ratio of the fibre $l_f/2r_f$ and s^* is the effective aspect

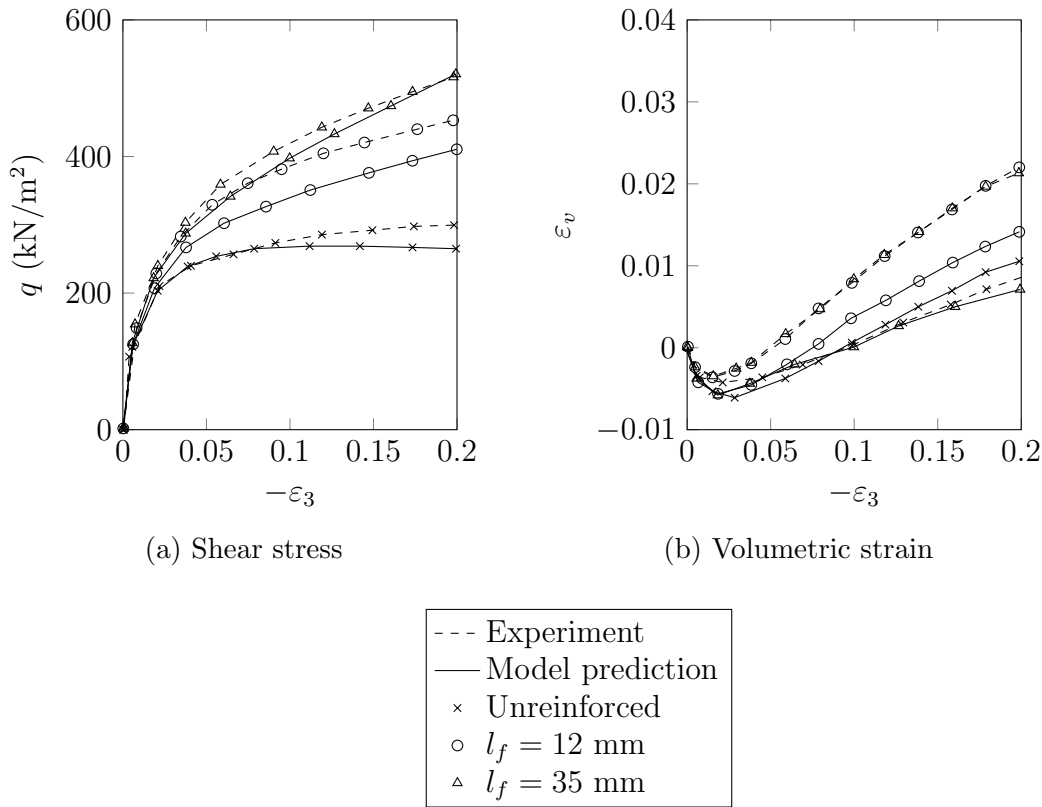


Figure 5.12: Experimental and predicted triaxial compression test results for different fibre lengths (Diambra and Ibraim, 2015)

ratio l_f^*/r_f . This debonding function is more advanced than that used previously (5.16), taking into account particle size, fibre aspect ratio, fibre and soil stiffness, fibre content and confining stress. From here, the implementation of this model is similar to that of Diambra et al. (2010), discussed in Section 5.2.3.

Predictions for this model follow the experimental results closely (Figure 5.12). The underlying soil model chosen here was the Severn Trent model. Increasing fibre length increases composite shear strength (for the same fibre content). Deviatoric q - ε_q paths predict the initial stiffness well, however composite stiffness after matrix yielding is somewhat under-predicted. Volumetric strain predictions give reasonable results, producing more dilatancy with added reinforcement. Experimental results suggest no particular correlation between fibre length and dilatancy, however the model exhibits decreasing dilatancy with increasing fibre length.

Table 5.1: Comparison of key features in several soil-fibre composite models

	(Maher and Gray, 1990)	(Michalowski and Čermák, 2003)	(Diambra et al., 2010)	(Zhu et al., 2014)	(Diambra and Ibraim, 2015)
Confining stress dependency	✓	✓	✓		✓
Fibre content	✓	✓	✓		✓
Fibre aspect ratio	✓	✓		✓	✓
Dilatancy effects		✓	✓		✓
Debonding			✓	✓	✓
Post peak slip softening				✓	
Variation of orientation	✓	✓	✓		✓
Variation of position	✓				
Fibre distribution function	✓		✓		✓
Fibre yielding	✓	✓			

5.2.6 Summary of soil-fibre models

The soil-fibre composite models available in the literature each make their own set of assumptions to model a limited number of features. These features are listed in Table 5.1. Key features include dependency on confining stress, fibre content, aspect ratio and orientation; these are included in most models. Advanced features include fibre-soil debonding, consideration for dilatancy and contraction, and fibre yielding; however the latter is not required as fibre yielding occurs beyond the strain/stress levels seen in practice (Michalowski and Čermák, 2003). Post peak softening is a feature necessary for fibres in a clay matrix; a drop in shear strength is observed after a peak, until a residual shear strength is reached (Zhu et al., 2014).

A convenient feature present in several models is the option to choose different orientation distribution functions. Some models initially assume an isotropic distribution and incorporate this into the formulation. Other models allow the distribution function to be changed. This is useful for analysing various preparation methods. The moist tamping technique (involving the layering of soil and fibres, then compacting each layer) leads to the fibres preferentially oriented near the horizontal plane (Ibraim et al., 2012). Whereas other preparation methods may lead to different distributions.

The current state of soil-fibre modelling is limited to single point representations of the behaviour of an assumed representative volume element (RVE). Ideally, a constitutive model should be applicable with generic analysis techniques such as the finite element method. The models by Michalowski and Čermák (2003), Diambra et al. (2010), and Diambra and Ibraim (2015) appear to be formulated in such a way that they could readily be coded into a full finite element analysis algorithm. The models by Maher and Gray (1990) and Zhu et al. (2014) would require further work to ensure that the model can be driven by stresses and strains in the soil.

Additionally, the prediction of soil-fibre composite failure has so far proved to be successful (Maher and Gray, 1990; Michalowski and Čermák, 2003), with models able to replicate the failure envelope of soil-fibre composites with reasonable accuracy. The shear stress-strain paths predicted by the models of Diambra et al. (2010) and Diambra and Ibraim (2015) were shown to also be reasonably accurate. However, the prediction of volumetric strains could be improved.

In the current study, based on previous work outlined in this chapter, a new model will be formulated to exploit the strengths of these existing models, whilst attempting to address their shortcomings. The model formulation, which makes use of experimental data detailed in Chapter 6, is described in Chapter 7. Using the rule of mixtures, this composite model is composed of the HS-LC model described in Chapter 3, and the proposed fibre model described in Chapter 7.

Chapter 6

Experimental program

In order to develop a new model to describe the behaviour of fibre-reinforced soils, it is important to have a detailed understanding of the effects of fibre inclusion for a variety of fibre types and soil conditions. Therefore a series of experimental tests were performed on unreinforced sand and fibre-reinforced sand. The first objective was to identify the characteristics of the sand alone, the second was to investigate the influence of fibres. The purpose of the unreinforced tests is to isolate the soil contribution to the composite strength. The laboratory testing was performed as part of two MSc projects, which the author co-supervised (Chatzopoulos, 2015; Wang, 2015). A summary of the test sets performed is listed below; these tests are a combination of standard laboratory soil tests and purpose-built tests.

- Fibre pullout tests for different confining stresses (100 kN/m², 200 kN/m², 300 kN/m², 400 kN/m², 500 kN/m²)
- Drained triaxial tests with different fibre contents (0.0, 0.3, 0.6, 0.9% by dry mass) at 300 kN/m² confining stress
- Drained triaxial tests with different confining stresses (100 kN/m², 300 kN/m², 500 kN/m²) for unreinforced sand and 0.3% reinforcement by dry weight
- Drained triaxial tests using three different fibre types at different confining stresses (200 kN/m², 400 kN/m², 600 kN/m²)

Table 6.1: Soil classification of the sand used in testing

min. void ratio	e_{min}	0.55
max. void ratio	e_{max}	0.83
avg. particle size	d_{50}	0.532 mm
coefficient of uniformity	C_u	2.16
particle density	ρ_s	2.814 g/cm ³

- Drained triaxial tests with samples prepared using three different methods
- Dissection of reinforced samples prepared using the same three methods

In Section 6.1 the materials used in testing are described, Section 6.2 details of the apparatus used for the tests listed above. The triaxial tests are described together however the sample preparation methods are described separately. The results from each set of tests are then compared and discussed in Section 6.3. It is the aim of this chapter to form the basis of a new model, which is proposed in the following chapter.

6.1 Material properties

6.1.1 Leighton Buzzard sand

A single sand type was used throughout the testing program; this is Leighton Buzzard sand and is compacted to different bulk densities for different tests. Further properties of the sand used in each test are described in the relevant sections. Using a proctor compaction test, sieve analysis, and a particle, density test the properties in Table 6.1 were determined (Chatzopoulos, 2015). In addition, the particle size distribution is shown in Figure 6.1.

The optimum water content was determined using the standard proctor test and was found to be 18%. A different void ratio was chosen for each test type, and each is detailed under the relevant sections.

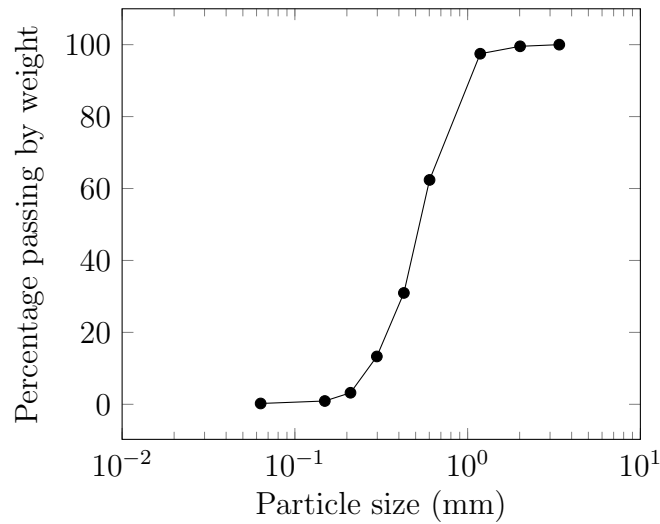


Figure 6.1: Particle size distribution of the sand used in testing

A sieve analysis of the soil determined the particle size distribution (Figure 6.1). The coefficient of uniformity of the soil was found to be $C_u = 2.16$ and the average particle size was found to be $d_{50} = 0.535$ mm. Less than 35% of the soil particles are smaller than 0.06 mm which puts the soil into the category of a ‘slightly clayey sand’ under the British Soil Classification System (Dumbleton, 1981).

6.1.2 Fibres

A selection of different fibres were tested in the experimental program. All fibres tested are made from polypropylene. Figure 6.2 shows a 2:1 scale sketch of each fibre and Table 6.2 details their geometric properties. The Conplus fibres (F2,F3,F4) are straight and cylindrical, they are monofilament, however, due to their small diameter, are prone to clumping. Hence, they normally require thorough mixing when adding to a soil for reinforcement. The diameter of the Conplus fibres is $18 \mu\text{m}$ and comes in three separate lengths of 6, 12, and 18 mm.

The Loksand fibres (F1) also have a cylindrical cross section, however they have been crimped along the fibre length, resulting in bending and kinking. The diameter of the Loksand fibres is $88 \mu\text{m}$ and the length is 35 mm.

The full length of the Durus S400 fibre (F5) is 45 mm and its diameter is 1 mm. The surface of the fibre is embossed on one side and has a rough texture, and has an

Table 6.2: Geometric properties of fibres used in testing

ID	Name	Type	Radius (mm)	length (mm)
F1	Loksand	crimped	0.044	35
F2	Conplus6	monofilament	0.009	6
F3	Conplus12	monofilament	0.009	12
F4	Conplus18	monofilament	0.009	18
F5	Durus S400	embossed	0.5	22.5 (45)

oval cross section. For triaxial tests using this fibre, the fibres were cut in half; this was because the largest available triaxial cell was 70 mm in diameter. It was thought that decreasing the fibre length would achieve a more homogeneous composite and would be easier to mix in the triaxial mould. The full fibre length was used in the fibre pullout tests, however only a limited portion of the fibre was exposed to the soil.

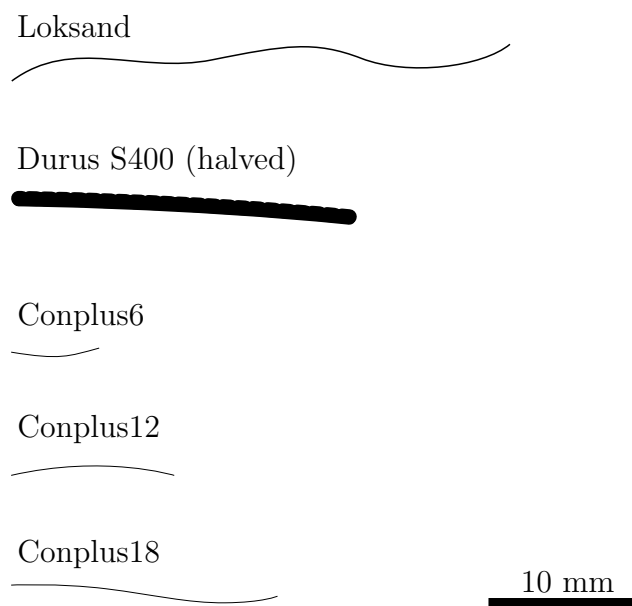


Figure 6.2: Fibres used in the experimental study

Although material testing of the polypropylene fibres was not performed in this study, similar studies using similar fibres (Ibraim et al., 2012; Diambra et al., 2010) report the material properties for polypropylene fibres shown in Table 6.3. The

Table 6.3: Properties of polypropylene

Young's modulus	E_f	900 N/mm ²
Tensile strength	σ_f^{max}	200 N/mm ²
Density	ρ_f	910 kg/m ³

reported fibre modulus is that of the initial stiffness in a tensile test. The density of polypropylene is taken from the data sheets provided with the fibres.

6.2 Testing setup and procedures

6.2.1 Triaxial tests

A series of consolidated drained triaxial tests (with volume change measurement) were performed in accordance with clause 7 of BS 1377-8:1990. The diameter of the soil samples is 70 mm and the height is 140 mm. The void ratio for each specimen before consolidation is 0.75 for the first documented tests using 35 mm Loksand fibres.

The rate of loading during the shearing stage was 2 mm per minute with a maximum displacement of 30 mm, which corresponds to 20% vertical strain in the specimen. Each test was repeated once or twice, depending on how similar the first two results were.

Several methods for preparing the triaxial samples were used and are listed below. It is known that the preparation method significantly affects the strength of the composite (Ibrahim et al., 2012; Michalowski, 1997), therefore the distribution method for each preparation must be characterised.

Layered stirring

The soil and fibres were split into six separate volumes and stirred separately. Each part was tipped into the mould, stirred again within the mould and tamped to

achieve the desired void ratio. This process was repeated for the remaining five layers.

Stirring

In this method, the entire sample was stirred with the fibres then tipped into the triaxial mould. Stirring was continued as the sample was tipped. The soil was then tamped to achieve the target void ratio.

Tumbling

The sand, water and fibres were placed into a sealed container and shaken vigorously. The mixture was then tipped into the mould and tamped from the top. This method and the stirring method are somewhat cruder than the layering methods, and a less uniform composite is produced. However, it would more likely reflect how a soil-fibre composite would be produced on a large scale in the field.

6.2.2 Fibre pullout tests

In order to test the frictional properties of a single fibre, a pullout testing apparatus (Figure 6.3) was devised (Chatzopoulos, 2015); taking inspiration from the arrangement used by Li and Zornberg (2013). The sand was compacted, to a void ratio of $e = 0.59$, in a 60 x 60 x 60 mm acrylic box which had an open top and two holes in opposite sides with stainless steel tubes glued into the holes. The size of this tube was large enough that the fibre could slide freely through, and small enough that sand particles would be unlikely to enter the gap between the fibre and tube. The gap between the tubes on the inside of the box was 20 mm, this is to ensure the exposed fibre surface remains constant throughout the test. A loading cap covered the entire top surface of the sand and was attached to a loading frame which applied the confining stress to the sand. A hand crank applied the pullout force which was measured by a load cell, and pullout displacement was measured

using linear variable differential transformers (LVDTs).

The strength of the knot was also tested by comparing the force-displacement curves for the knotted fibre-cable against cable only, no distinct ‘jump’ in the force displacement curves for the knotted test was observed (in the stress range beyond expected in the pullout tests), it was therefore concluded that the knot strength was sufficient (Chatzopoulos, 2015).

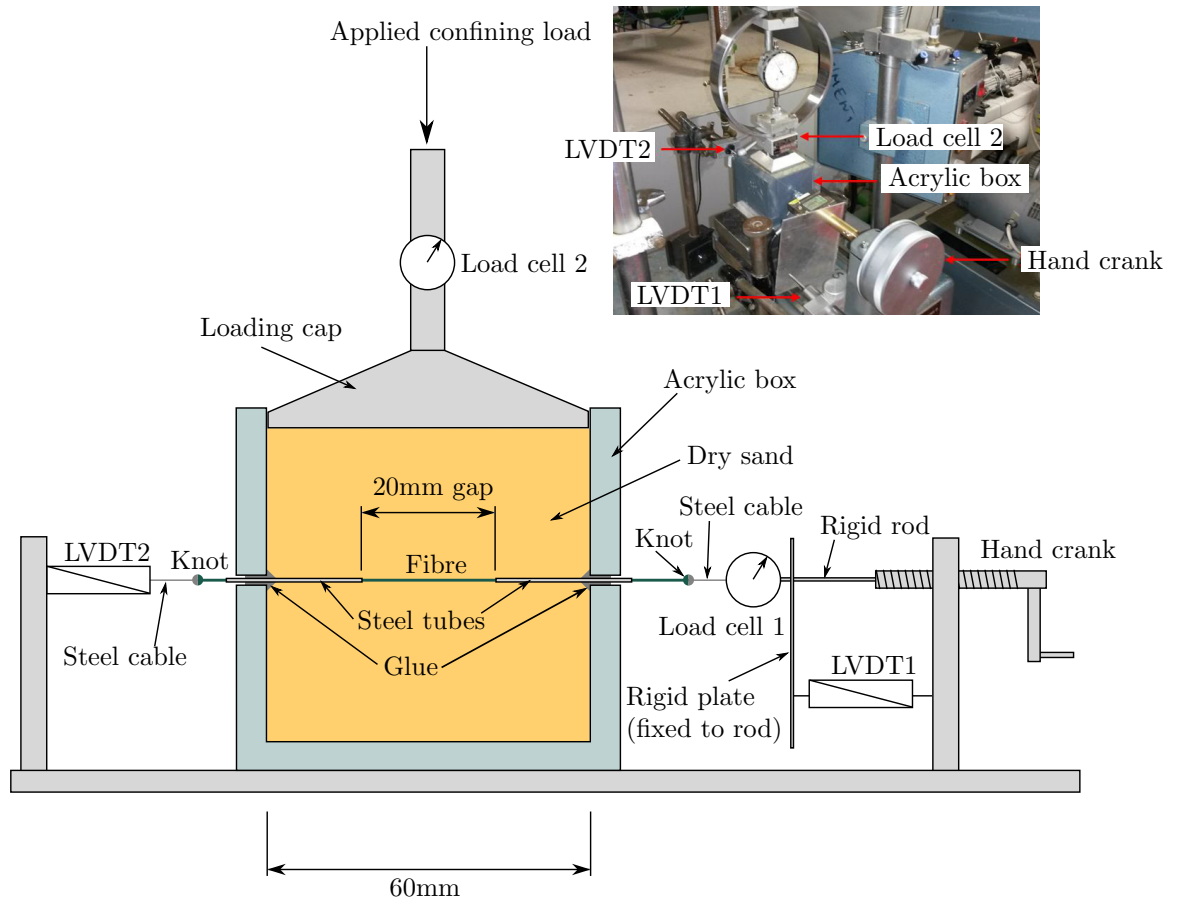


Figure 6.3: Schematic of fibre pullout test (Chatzopoulos, 2015)

The purpose of this test was to determine the friction characteristics of the fibre-soil interface. It was anticipated that only a negligible amount of fibre-cable extension would occur, and the fibre would travel through the soil as a rigid body. To confirm this assumption, a second LVDT recorded the tail displacement, if LVDT1 and LVDT2 recorded the same displacements, then it could be confirmed that this assumption is true.

The fibre-cable arrangement was threaded through the steel tubes and posi-

tioned such that the leading end of the fibre was just inside the leading plastic tube (rightmost tube in Figure 6.3).

The sand used in the pullout test was dry and packed in three equal layers while the fibre was in position. The fibre was held taught as to avoid sagging during sand packing. A target void ratio of $e = 0.59$ was chosen for this set of tests, which was achieved using vibro-compaction.

A loading cap (from standard shear box apparatus) of the same plan dimensions as the box was then placed onto the top of the sand. The load cap was fitted with a 2000 Newton analogue force gauge and connected to a loading frame which applied the vertical load. A 100 Newton digital force gauge (load cell 1) was attached to the fibre and the rigid rod to measure the pullout force. The rigid plate was required for the measurement of the frontal fibre displacement, one end of LVDT1 was attached to the crank support and the tip was resting against the rigid plate.

The gauges were synchronised with the recording computer and set to zero. The fibre was then loaded by rotating the hand crank. As the loading is effectively manual, a stopwatch was used to ensure the fibre was pulled at an approximate rate of 2 mm per minute.

6.2.3 Sample dissection

A series of tests to characterise the fibre distributions for each of the preparation methods used in triaxial testing was undertaken (Wang, 2015). The fibres used in this part of the study were the Durus S400 fibres (F5); the largest fibres were chosen for ease of observation.

First, the samples were prepared in accordance with the three methods described in Section 6.2.1, the samples were prepared in a latex tube within a cylindrical steel mould. Each sample was then fully saturated, frozen, then removed from the steel mould and placed back into the freezer. In order to allow enough time to examine the samples, each composite cylinder was quartered using a wet-cut chop saw. The

first cut was made half way along the height of the cylinder, producing two smaller cylinders, the second and third cuts were made along the length of each smaller cylinder to produce four semi-circular prisms. Each quarter sample was then placed back into the freezer such that each could be examined from its frozen state. It was observed during cutting that the fibres were cleanly cut by the saw, with no credence that fibres had been disturbed.

Each quarter sample was then placed upright into a tray and the sand was carefully scraped away from the top to reveal partially embedded fibres. The angle from the vertical axis of each protruding fibre was measured with a protractor and classified in 15° intervals. This fibre was then removed by gently pulling it axially and then discarded. This process was repeated until all the fibres from the quarter sample were exhumed and classified, half fibres from the cutting process were also taken into account. The remaining quarters of the sample were then examined in the same manner.

6.3 Experimental results

6.3.1 Triaxial tests

In this first series of triaxial tests (Chatzopoulos, 2015), both the shear and volumetric responses were recorded. The samples in Figures 6.4 to 6.7 were prepared using the layered stirring method as described in Section 6.2.1. In the volumetric strain plots, positive strains are dilative and negative strains are compressive. The axial compressive strains are negative by the current sign convention, however they are plotted on negative axes to allow comparison with other geotechnical works.

Firstly, the unreinforced sand exhibits typical triaxial behaviour. In Figure 6.4a, each curve has an initial steep region, then curves as the shear stress increases. A distinct limit in the shear stress is observed for each test, and increasing the confining stress on the sand increases the soil shear capacity. The repeatability of the shear

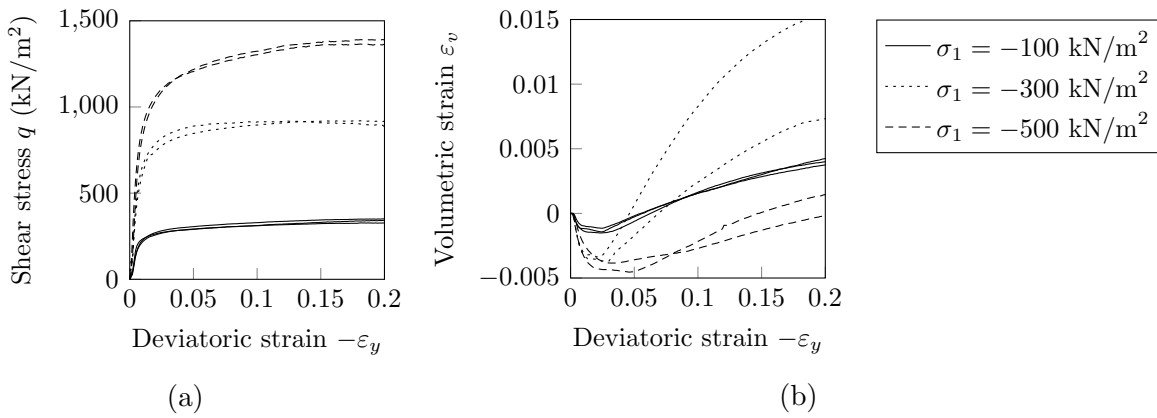


Figure 6.4: Drained triaxial test results for unreinforced sand at different effective confining stresses

response is very good.

In Figure 6.4b the deviatoric load first compresses the soil, however, at a certain point, the soil begins to dilate. The chosen void ratio has created a densely arranged packing structure of the sand grains. This causes the soil to dilate as the particles attempt to ‘climb over’ one another. Counter-intuitively, the sample with the highest degree of dilatancy is the one confined to 300 kN/m², and the lowest is the sample confined to 500 kN/m². It is suspected that the compaction of the samples in the consolidation phase of the triaxial test generates different void ratios at the start of the deviatoric loading phase, and that the relationship between the confining stress and the void ratio is non-linear. The repeatability of the volumetric results is, in general, reasonably good. However there is a great difference in the 300 kN/m² results, therefore the volumetric results should be treated with some scepticism.

Next, a similar set of triaxial tests were performed, but using sand reinforced with 0.3% (by mass) Loksand fibres (Figure 6.5). With regard to the shear plot (Figure 6.6a), the first observation to make is the increase in shear strength. The unreinforced sand reaches a distinct limit in shear stress, however the addition of fibres allows the shear stress to increase indefinitely (within the strain range investigated). Instead of the soil failing and tending towards a zero gradient, the composite reaches a constant, non-zero gradient. Again, the response in shear stress shows a good repeatability.

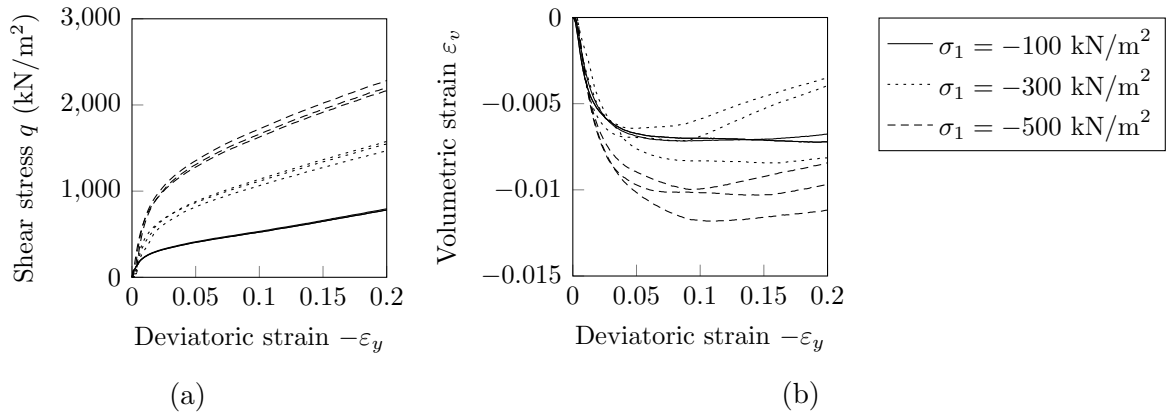


Figure 6.5: Drained triaxial test results of Loksand fibres (F1) at content $w_f = 0.3\%$ at different effective confining stresses

The volumetric response for the reinforced samples (Figure 6.6b) has changed significantly due to the addition of fibres. The composite now does not exhibit dilatancy, and is more characteristic of a loose sand. The degree of dilatancy reduction is still affected by the confining stress, and the 300 kN/m² is still the most dilatant. The repeatability of these volumetric results is better than the unreinforced specimens.

A comparison of the triaxial response of different fibre contents using Loksand fibres can be seen in Figure 6.6. The shear response (Figure 6.6a) intuitively shows that increasing the fibre content also increases the composite strength. However, the initial stiffness appears to have decreased; for example a deviatoric strain of $\varepsilon_y = -0.02$ gives a shear stress of $q = 800$ kN/m² for the unreinforced specimen, and a shear stress of $q = 400$ kN/m² for the 0.9% reinforced specimen.

The volumetric strains (Figure 6.6b) also reduce with increasing fibre content. The presence of fibres appears to inhibit soil dilation, and the reduction in volumetric strain at the end of the test is close to linearly proportional to the fibre content. On a global scale, dilatancy occurs when the horizontal strains exceed the vertical applied strain in a triaxial test. One possible explanation for the reduction in dilatancy is that the fibres on the horizontal plane are active, and preventing the specimen from expanding horizontally.

The Durus fibres (F5) are then compared with the Loksand fibres (F1) at a single

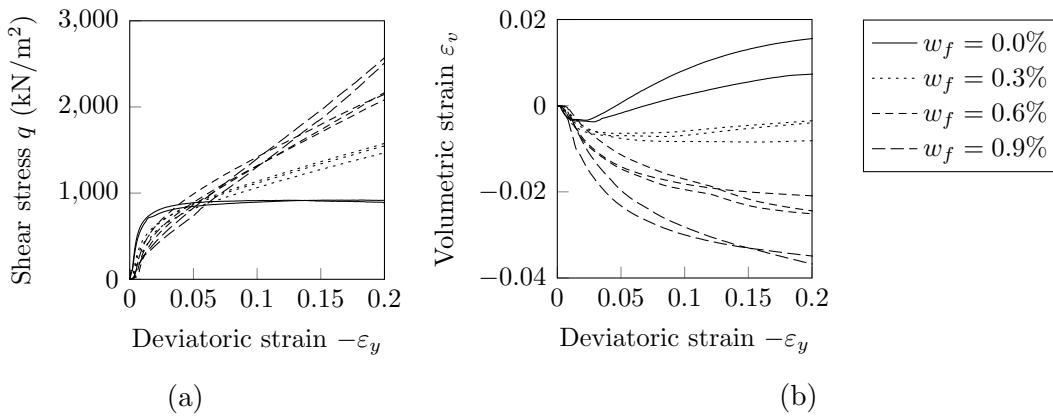


Figure 6.6: Drained triaxial test results at 300 kN/m² effective confining stress for sand reinforced with Loksand fibres (F1) with different fibre concentrations

fibre content of $w_f = 0.3\%$ and a single confining stress $\sigma_1 = -300$ kN/m² (Figure 6.7). From Figure 6.7a, it would appear that some nominal strength improvement over the unreinforced sand is developed with the use of the Durus S400 fibres. However, the composite still reaches a distinct shear stress limit. Similarly for the volumetric response (Figure 6.7b), some reduction in dilatancy is observed but not to the same magnitude as with the Loksand fibres.

There are two possible explanations for the difference in failure behaviour of the Durus S400 fibres and the Loksand fibres. The first being the ratio of exposed fibre surface area to fibre volume, with the Durus S400 fibres having a much lower ratio. The second reason may be due to the higher stiffness of the Durus S400 fibres; the Loksand fibres are very flexible and when compressed in sand, may bend and twist, tangling with the sand grains and increasing the bond strength; this aspect was also discussed by Diambra et al. (2013).

The second series of triaxial tests (Wang, 2015) investigates the effect of fibre length and fibre preparation method on the strength properties of the composites. In this part of the study, Conplus fibres are used which are available in lengths of 6, 12, and 18 mm. The preparation method used in the length study is the stirring method, as described in Section 6.2.1. Results of triaxial tests with sand reinforced with the Conplus fibres of different lengths are shown in Figures 6.8, 6.9 and 6.10.

The addition of any length of fibre appears to have affected the shear response

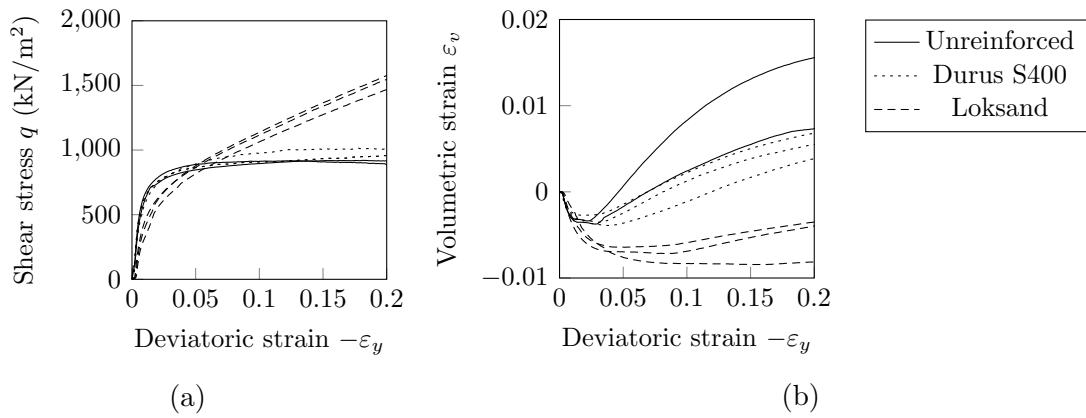


Figure 6.7: Drained triaxial test results at effective confining stress of -300 kN/m^2 with fibre content $w_f = 0.3\%$ for different fibre types (F5, F1)

very little when compared to the unreinforced response. Therefore it is impossible to comment on the effect of fibre length from this data. The reason for this lack of strength improvement is most likely due to the fibre geometry: The Loksand fibres have a diameter of $88 \mu\text{m}$, and the Conplus fibres have a diameter of $18 \mu\text{m}$. It is possible that the sand is not able to bond to the fibre surface. Another reason may be the fibre length; the Loksand fibres are 35 mm long and the largest Conplus fibres are 18 mm long. There may not be enough fibre surface available to develop a shear band, hence the fibre strength is not mobilised.

The third in the series of reinforced triaxial tests is the comparison of different preparation methods. Three different methods were used to mix the fibre and sand; these were the layered stirring, stirring, and tumbling methods, and are described in Section 6.2.1. Triaxial tests in this study are performed at confining stresses of 200 kN/m^2 , 400 kN/m^2 , and 600 kN/m^2 (Figures 6.11, 6.12, and 6.13).

The triaxial sample preparation study showed a poor repeatability of the stirring method for the 200 kN/m^2 , however the higher confining stress results show better repeatability. It was expected that a higher proportion of fibres near the horizontal orientation would produce a stronger composite. It is difficult to confirm this result from the preparation method study (Figures 6.11 to 6.13) because the level of variation between repeats appears to exceed the strength increase. This expected result can be seen for the 400 kN/m^2 test shown in Figure 6.12 and to a lesser extent for the 600 kN/m^2 test shown in Figure 6.13.

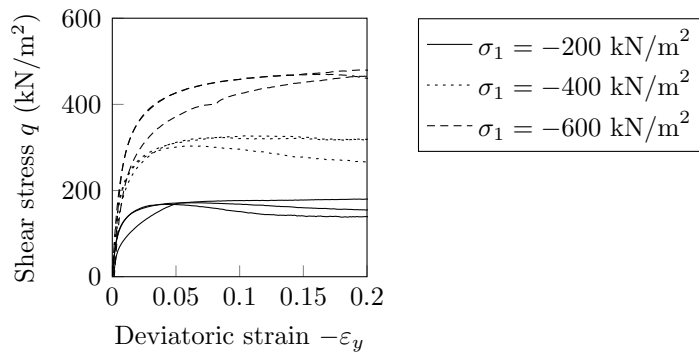


Figure 6.8: Drained triaxial test results with 6 mm Conplus fibres (F2) at fibre content $w_f = 0.3\%$ for different effective confining stresses

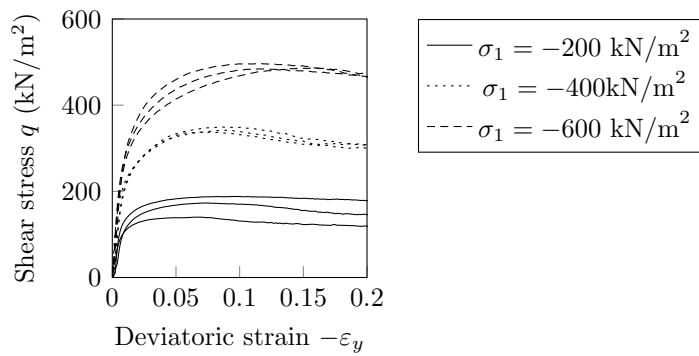


Figure 6.9: Drained triaxial test results with 12 mm Conplus (F3) fibres at fibre content $w_f = 0.3\%$ for different effective confining stresses

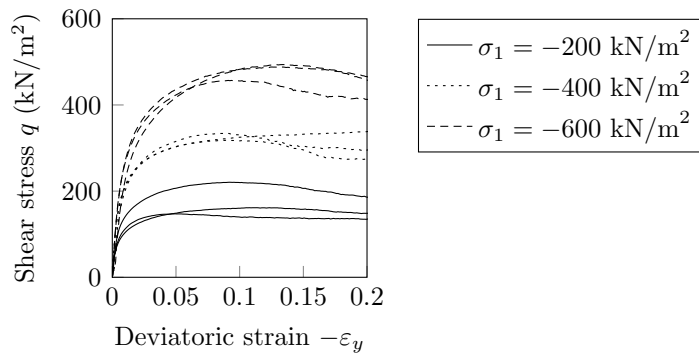


Figure 6.10: Drained triaxial test results with 18 mm Conplus fibres (F4) at fibre content $w_f = 0.3\%$ for different effective confining stresses

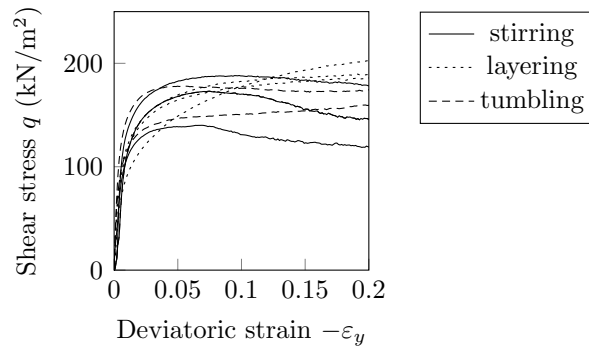


Figure 6.11: Drained triaxial test results at an effective confining stress of $\sigma_1 = -200 \text{ kN/m}^2$ with 12 mm Conplus fibres (F3) at fibre content $w_f = 0.3\%$ for different preparation methods

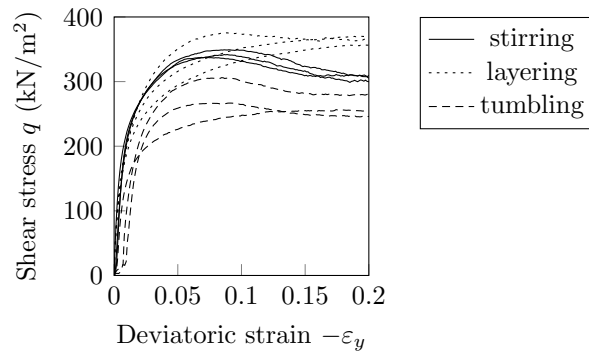


Figure 6.12: Drained triaxial test results at an effective confining stress of $\sigma_1 = -400 \text{ kN/m}^2$ with 12 mm Conplus fibres (F3) at fibre content $w_f = 0.3\%$ for different preparation methods

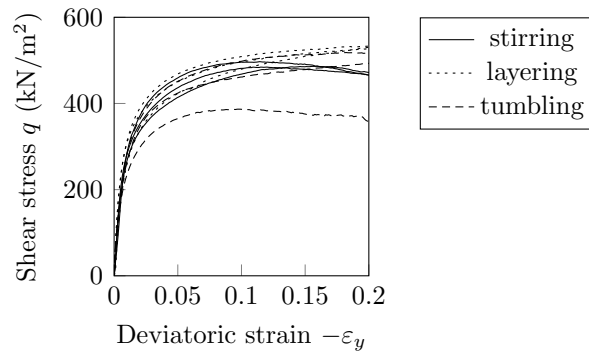


Figure 6.13: Drained triaxial test results at an effective confining stress of $\sigma_1 = -600 \text{ kN/m}^2$ with 12 mm Conplus fibres (F3) at fibre content $w_f = 0.3\%$ for different preparation methods

6.3.2 Fibre pullout tests

The fibre pullout tests as described in Section 6.2.2 used the full length Durus S400 fibres. The reason for this choice of fibre was the ease of mounting to a cable for loading and measurement. The other fibre types are manufactured by shaving from a plate which has the same width as the fibre length. They are not made by extrusion then cut to length; if this were the case then it would be possible to use a longer uncut fibre.

The pullout tests were performed at different vertical confining stresses and each test was repeated at least once. Referring to Figure 6.14, each load-displacement curve has a distinct peak load before dropping to a reasonably level residual load. The path to the peak load is linear in most cases as is the first drop to the residual load.

The residual section then appears to oscillate. These oscillations are most likely due to shear planes developing at the micro-scale; as the fibre is pulled, the grains climb over one-another. When this happens, the fibre slips under a reduced load until another set of shear planes are developed. The amplitude of the oscillations increases along with the confining stress; this suggests that the grains are more densely packed under the higher load, requiring more force to break each shear band.

Figure 6.15 shows a linear relationship between confining stress and the peak and residual loads. The gradient of these curves is important for characterising the interface for this particular choice of soil and fibre. It is expected that a different fibre or a different soil would produce different gradients.

The gradient of the peak pullout data is $F_p/\sigma_c = 0.044$ and the gradient of the residual data is $F_p/\sigma_c = 0.031$. The initial gradient of each the pullout curve is also important for the purpose of modelling this behaviour. The initial gradient was found not to be related to the confining stress, as no correlation was observed. The mean gradient for this particular fibre and soil was found to be $F_p/S = 33.5$ N/mm

(individual values vary between 26.7 and 38.6 for the different confining stresses).

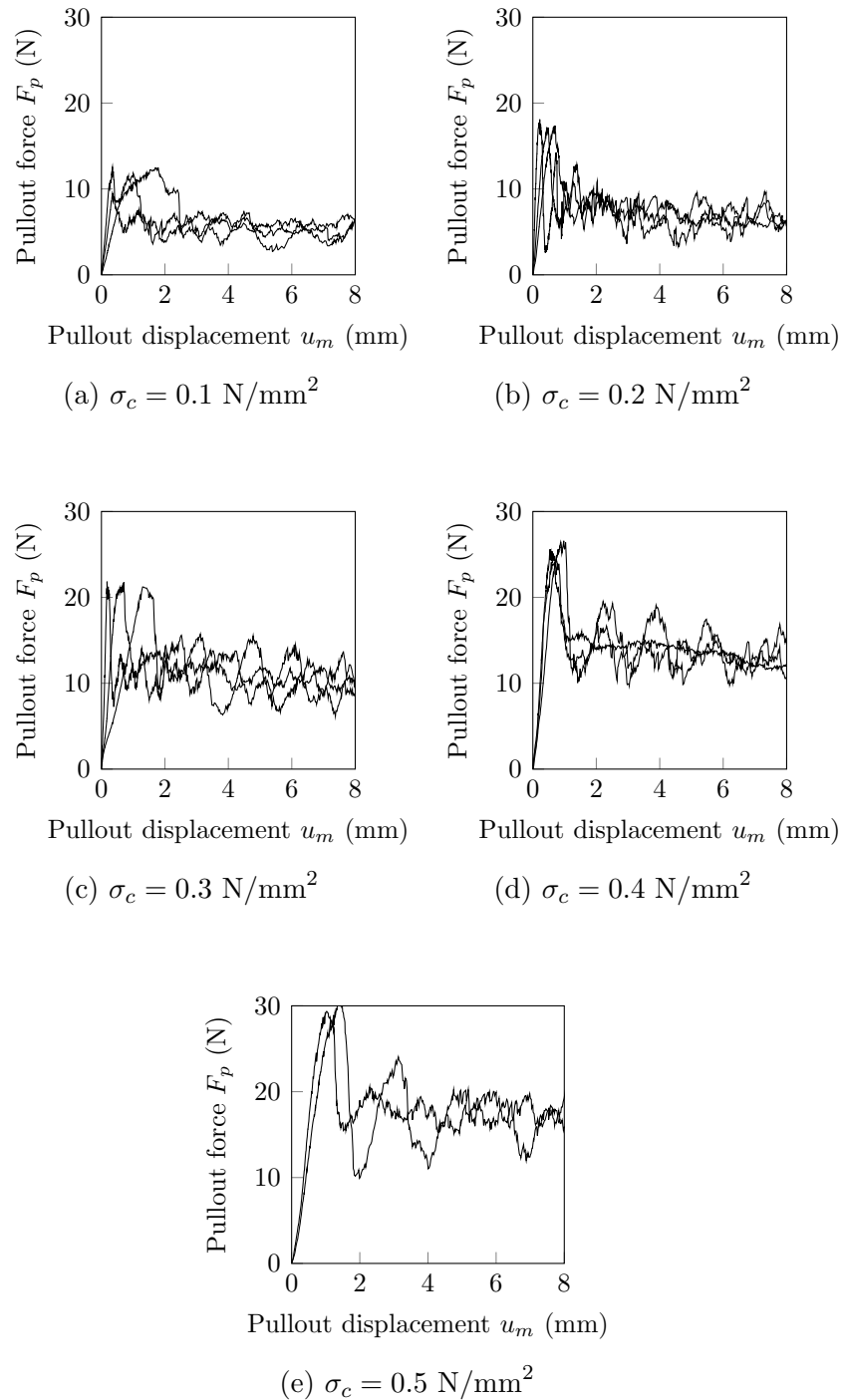


Figure 6.14: Fibre pullout results at different vertical stresses using 45 mm Durus S400 fibres, 20 mm fibre length is in contact with the soil

6.3.3 Sample dissection

A total of three prepared samples were analysed using the approach as outlined in Section 6.2.3; one for each preparation method. Figures 6.16, 6.17, and 6.18 show

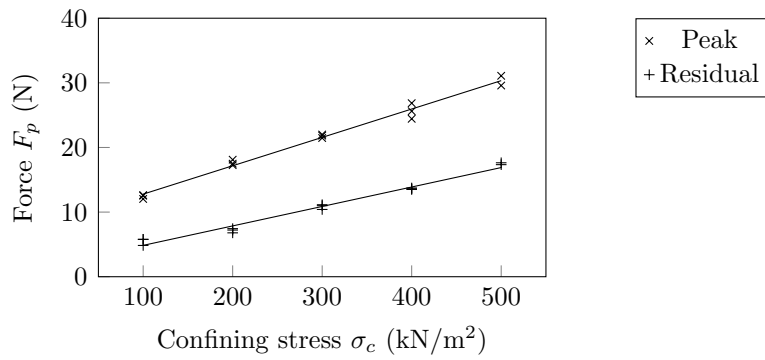


Figure 6.15: Peak and residual pullout forces for different confining stresses

the observed portion of fibre orientations, grouped in intervals of 15° . This portion is calculated by dividing the number of fibres in the group, and dividing by the total number of fibres found in the sample.

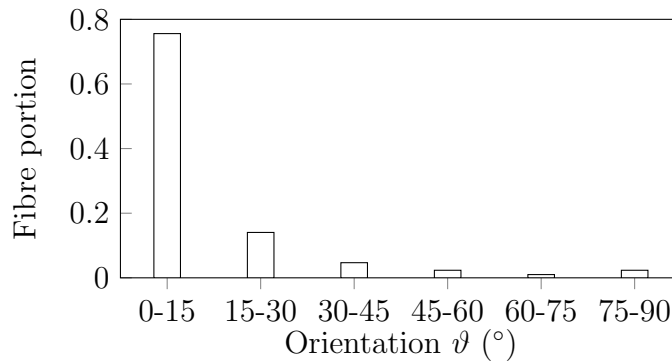


Figure 6.16: Fibre orientations for layering method

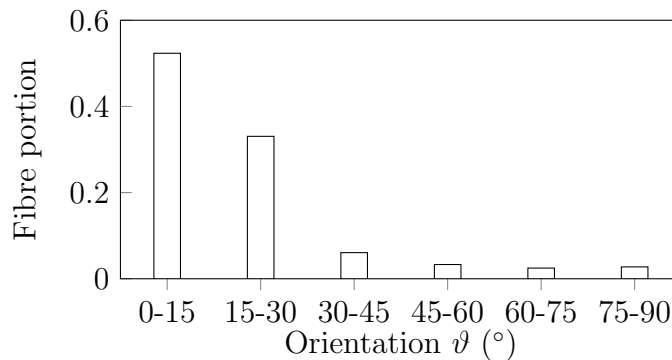


Figure 6.17: Fibre orientations for stirring method

The layering method (Figure 6.16) places almost all of the fibres near the horizontal plane. The sample was divided into six equal layers which were approximately the same height as the fibre length. It is possible that the stirring process caused the fibres to lay horizontally due to the stirrer colliding with the fibres. Additionally, the tamping process may have had a flattening effect.

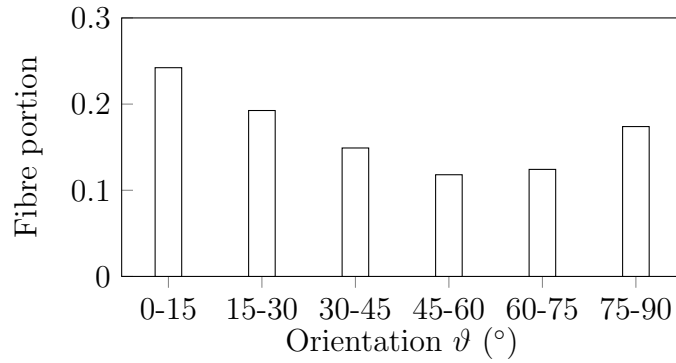


Figure 6.18: Fibre orientations for shaking method

In the triaxial tests (Figure 6.12), samples prepared using the layering method have the highest shear strength. This is consistent with the distribution curve as the horizontal fibres act to resist the expansion of the sample in the horizontal plane. As more of the fibres are near the horizontal plane for this preparation method, then the radial expansion of the sample is resisted more.

The stirring method (Figure 6.17) has a more even distribution of fibres; with a significant portion outside the $0-15^\circ$ range. This method uses no layering in preparation of the sample. The reason for this change in distribution may be due to the method in which the mixture is poured into the mould. With this method, the mould is filled in a single pour.

The triaxial curves for this preparation method (Figure 6.12) show a similar peak shear stress, however there is a drop in shear stress after extensive straining; this effect is also seen in Figures 6.11 and 6.13. One possible explanation for this drop in strength may be due to some inhomogeneity in the sample; this method is somewhat crude in comparison to the layering method and this is reflected in the repeatability in the triaxial test curves.

Samples prepared using the tumbling method show the most uniform distribution of fibre orientations (Figure 6.18). A majority of the fibres are still horizontal, however there is a significant portion in the vertical direction. The triaxial results correlate with this observation such that the samples prepared using the tumbling method tend to be weaker in shear. Similarly to the stirring method (Figure 6.17), the sample is placed into the mould with a single pour, also a residual shear stress is

observed in the 400 kN/m² test (Figure 6.12). Again, poor repeatability is observed, possibly due to the crudeness of the preparation method.

Concluding remarks

This chapter has presented the experimental work of two MSc projects, co-supervised by the author (Chatzopoulos, 2015; Wang, 2015), for the purpose of providing data to compare against a new soil-fibre composite model. A set of characterisation tests allow for the determination of both soil and fibre parameters. A set of triaxial tests give a good basis to understand the influence of fibres in soils and give a benchmark for model calibration.

Chapter 7

A new soil-fibre model

Thus far, a reasonable understanding of soil-fibre behaviour has been established both by a review of the literature in Chapter 5 and directly through the experimentation documented in Chapter 6. With this information, it is possible to establish a mechanical model to capture the behaviour of fibres when mixed throughout a soil.

In this chapter, a new fibre model is formulated which is based on micro-mechanical soil-fibre interactions; experimental observations are also taken into account and used to build some of the more complex behavioural features such as interface debonding. The model formulated is based on the shear lag concept (Cox, 1952), and draws on ideas from several other authors including Maher and Gray (1990) and Diambra and Ibraim (2015). The proposed model also differs previous models in that debonding is considered at the microscopic scale. Calibration against experimental data is also possible through manipulation of several material parameters which have real physical meaning. Prior work on this proposed fibre model has already been documented by Bower et al. (2016b) and Bower et al. (2016a).

The proposed model can be coupled with a range of constitutive soil models, although in this study, it is intended to be used alongside the HS-LC model, as described in Chapter 3. The HS model can easily be calibrated to triaxial stress-strain curves for unreinforced soils. The fibre model is then superimposed onto the HS-LC model by use of the rule of mixtures.

To gain an understanding of the mechanics of fibre behaviour at the fibre scale, a finite element study is conducted in Section 7.1 which analyses the stress transfer mechanism from soil to fibre for an elastic, and an inelastic soil. A model to predict the behaviour of a single fibre is then proposed in Section 7.2, which is based on micro-mechanical interactions between the soil and fibre, taking into consideration the predicted behaviour of the soil-fibre interaction from the finite element study and data from the experimental study conducted in Chapter 6. The stress distribution calculated with the proposed fibre model is then compared against that of the finite element study.

The single fibre model is then transformed into a homogenised model in Section 7.3, which takes an assumed distribution of fibres, as they would be distributed in a soil, and uses the single fibre model to predict the global behaviour of a sand reinforced with randomly distributed fibres. The final model uses parameters which allow the control of fibre volume fraction, geometry, stiffness, bond strength, and orientation distribution. A sensitivity analysis of each parameter is conducted in Section 7.4, where each parameter is adjusted independently, and the effects of these changes are noted in the simulation of triaxial tests.

7.1 A finite element study of soil-fibre interaction

The purpose of this section is to establish an expected stress-strain distribution for a single fibre within a soil. Both fully bonded, and partially debonded cases were considered and the fibre was modelled as a linear elastic material; in order to control the stress level at which debonding occurs, a yield criterion based only on the shear stress was used for the soil; this was the von Mises criterion. From the fibre pullout experimental tests (performed in Section 6.3.2), it was found that after initial debonding, the pullout force reduced to a residual level, therefore softening behaviour was enabled for the yield surface:

$$f_{VM} = \sqrt{J_2} - H_{VM}(\gamma^p) \quad (7.1)$$

where J_2 is the second invariant of the deviatoric stress tensor, and relates to the shear stress by $q = \sqrt{3}\sqrt{J_2}$, and H_{VM} is a linear hardening function which relates directly to the plastic shear strain.

The problem was analysed using finite element software LUSAS. The geometry of the full problem is shown in Figure 7.1, this can be simplified by exploiting the rotational symmetry and was modelled in the finite element model as an axisymmetric domain as shown in Figure 7.2. Note that only half of the fibre was considered due to symmetry. The soil and fibre are modelled as different materials where the fibre was always elastic, and the soil was either modelled as fully elastic or elastoplastic with the von Mises plasticity model. The two materials were attached with linear spring joint elements acting in the horizontal direction only. The soil was then given a uniform tensile force on the end face. The soil and fibre were restrained in the loaded direction on the opposite end to the applied forces; this was to enforce symmetry.

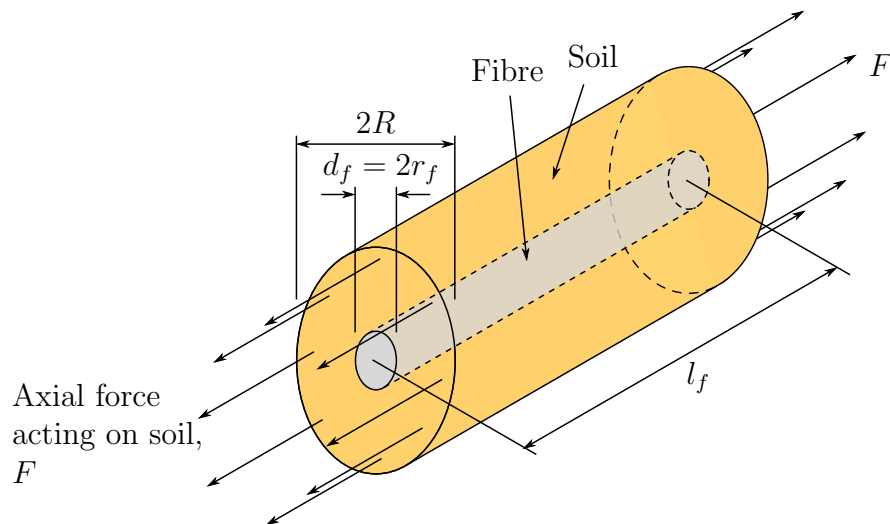


Figure 7.1: Schematic of single fibre pullout model (not to scale)

The problem was modelled using 5100 quadratic, quadrilateral, axisymmetric elements and 61 linear joint elements. As this is a geometrically non-linear problem, the total tensile force was split over several increments; for the fully bonded case

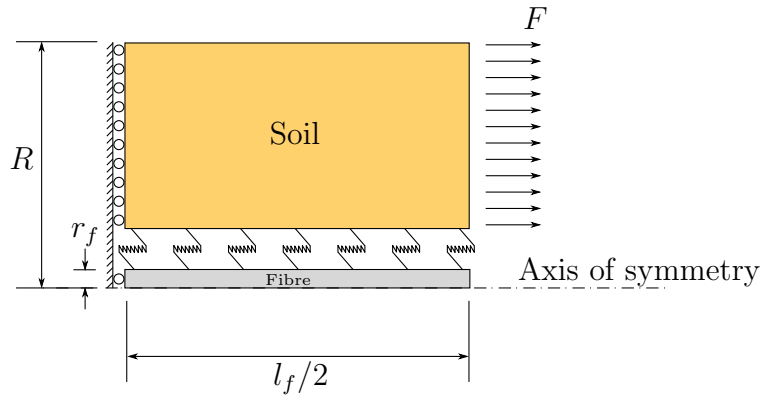


Figure 7.2: Schematic of axisymmetric finite element fibre pullout model (not to scale)

10 increments are used, and 40 increments were used for the debonding case. The primary convergence criteria are the residual force norm which was set to 1.0%, and the incremental displacement norm, which was set to 0.1%. The co-rotational formulation was used in the multi-frontal Newton-Raphson solver to assist with the geometric non-linearity in this problem. A mesh convergence study and step size dependency study were conducted to ensure the results obtained here are reasonable.

7.1.1 Elastic soil and fully bonded fibre

Based on the mechanical properties of the polypropylene (Diambra et al., 2013; Ineos, 2014), the fibre was modelled using a Young modulus of 900 N/mm^2 and Poisson's ratio of 0.42. The soil was modelled using a Young modulus of 20 N/mm^2 and Poisson's ratio of 0.25; this was based on typical properties of sand. The linear joint, which represents the bond between the soil and the fibre, has a horizontal spring stiffness of 10 N/mm^2 . The actual value of this spring stiffness is unimportant, as it is not the purpose of this study to quantify the stress transfer, but to better understand the nature of it, however, a value was chosen that was half of the stiffness of the soil. The total load applied to the face of the soil was 1 N/mm^2 . The radius of the fibre was modelled as 0.5 mm, and the half length of the fibre modelled was 22.5 mm, to match the geometry of the Durus S400 fibre. A 0.5 mm gap was used between the soil and fibre and the total radius of the composite is 41 mm, this is to ensure that the influence region of the fibre is fully contained within the soil

cylinder.

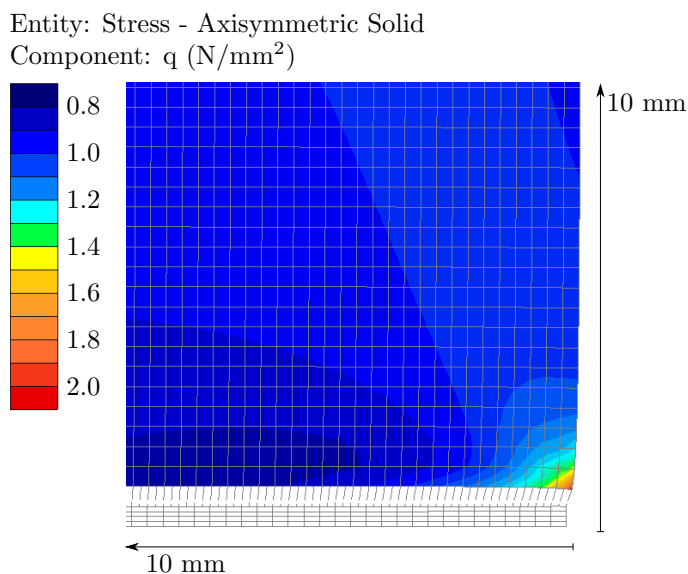


Figure 7.3: The variation of the shear stress in fully elastic soil after loading is applied (image is zoomed to stress concentration at fibre end)

From Figure 7.3, the highest shear stress in the soil occurs adjacent to the fibre ends. Also, the shear stress becomes almost constant at the outside surface of the composite, suggesting that the fibre has very little influence in this region.

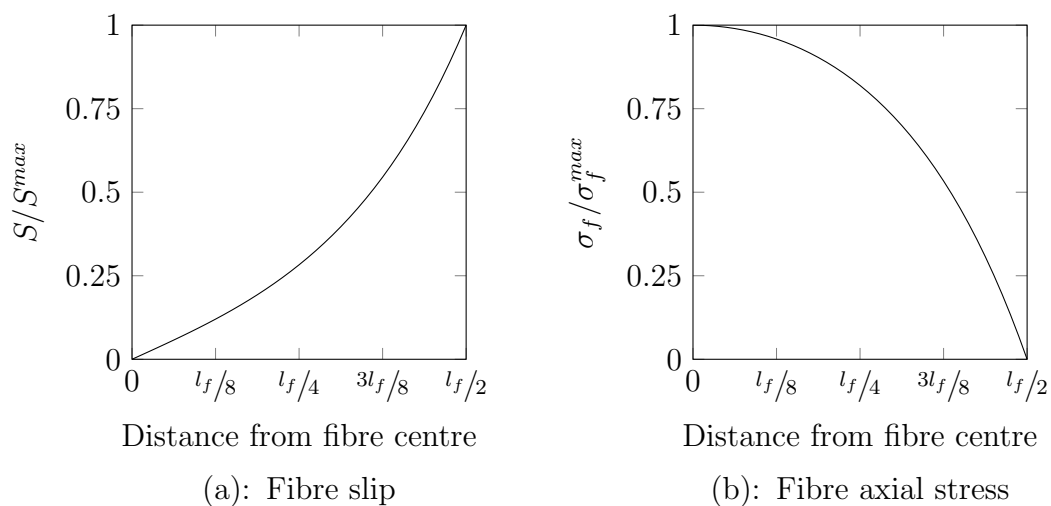


Figure 7.4: Interface slip and fibre axial stress distributions along the length of the fibre with elastic soil (normalised to maximum values)

The slip along the fibre length is also calculated. Slip is defined as the difference in the displacement of the matrix and fibre across the interface. Figure 7.4a shows the interface slip which is zero at the fibre centre, and increases to maximum at the fibre end. This trend is non-linear. The axial stress in the fibre (Figure 7.4b) is also

non-linear and is maximum at the fibre centre. The axial stress decreases to zero at the end of the fibre.

The displacement of the soil at the end of the composite is shown in Figure 7.5. There is very little soil displacement adjacent to the fibre; this is because the fibre is much stiffer than the soil and the bond between the soil and fibre prevents the soil from moving. At the furthest distance from the fibre, the displacement is maximum, this is because there is no restraint in the horizontal direction at the outside of the composite. The gradient profile is also important here, as the gradient close to the fibre is very steep, and the gradient furthest from the fibre is very shallow. This suggests that the fibre has a limited range of influence; at a radius of 20 mm, the horizontal soil displacement is almost uniform.

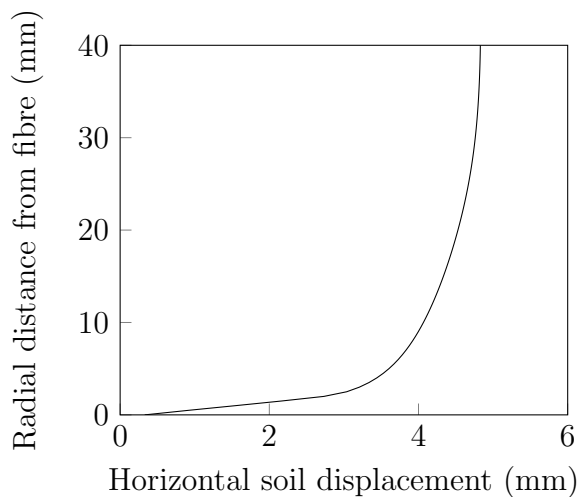


Figure 7.5: Horizontal displacements at the rightmost line of soil

7.1.2 Elasto-plastic soil and fully bonded fibre

A similar analysis was performed for a soil undergoing plastic strains. The same loads were applied to the same materials and geometry, however the von Mises yield criterion was included with the soil with an initial yield stress of 0.1 N/mm^2 and a hardening slope of -0.16 which is active until a residual stress of 0.05 N/mm^2 is reached. These values were chosen such that the soil towards the end of the fibre would yield whereas the soil towards the fibre centre would remain fully elastic. A

negative hardening gradient was included to replicate the softening observed in the experimental pullout tests (Section 6.3.2).

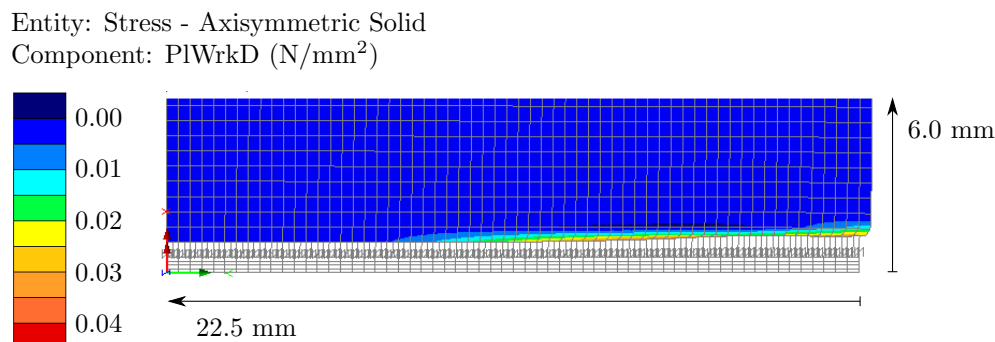


Figure 7.6: Plot of plastic work done for a elasto-plastic soil (image is zoomed to stress concentration at fibre end)

Figure 7.6 depicts the plastic work done in the soil due to the tensile load in the presence of the fibre. The plastic work done represents the amount that the yield surface in the von Mises model has moved, and is therefore synonymous with the plastic shear strains. The highest plastic shear strain is at the fibre end, where the most slip has occurred; this decreases towards zero towards the centre of the fibre. The plastic shear strains are also confined to a band narrower than the radius of the fibre, indicating that the plasticity induced by the fibre inclusion is a localised effect. On a global scale, the plasticity introduced by the presence of the fibre is not spread to the rest of the soil; this is shown by a plastic work done of zero at any distance further than 1.0 mm from the fibre in Figure 7.6. Therefore debonding should be included in the new composite model at a micro-mechanical level.

Applying the same tensile load of 1 N/mm², the slip distribution for the fully loaded soil is shown in Figure 7.7a. There is a clear change in gradient at $x = 3l_f/8$ where soil plasticity starts to take effect. Extrapolating the elastic region, the maximum slip at the fibre end is significantly reduced. The gradient in the yielding region is linear and the steepness of the curve is higher.

The stress distribution in the fibre (Figure 7.7b) is also effected by the soil plasticity. The distribution in the yielding region is linear, and the distribution in the elastic region is curved, but much flatter than the fully elastic results.

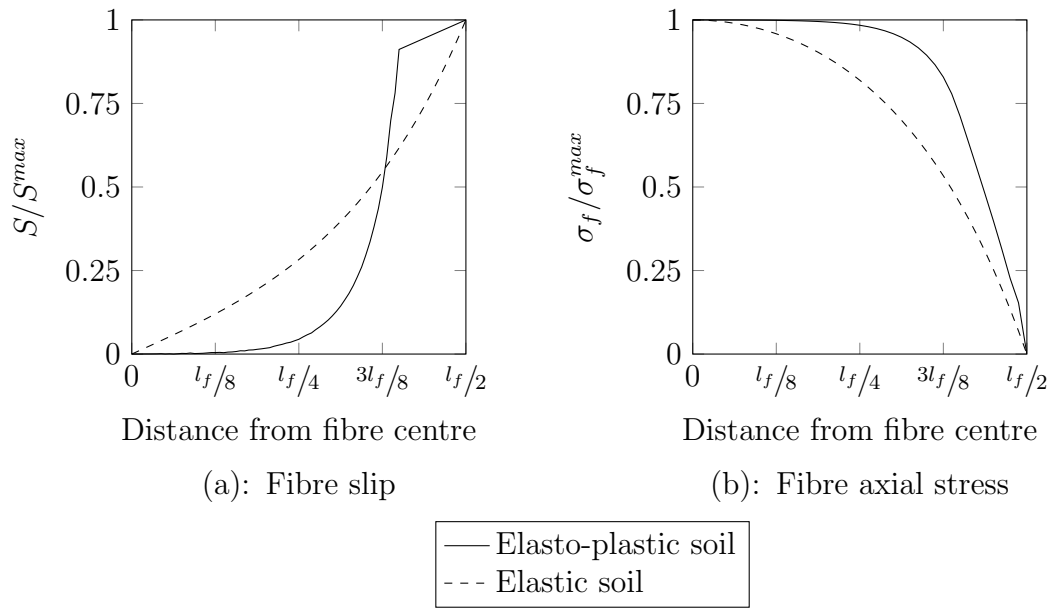


Figure 7.7: Interface slip and fibre axial stress distributions along the length of the fibre with elasto-plastic soil (normalised to maximum values)

Several conclusions may be drawn from this finite element study of soil-fibre interaction:

- For a fully bonded fibre, the distribution of axial stress is non-linear, with the highest tensile stress in the centre of the fibre, and zero stress at the fibre end. This is in agreement with the hyperbolic distribution by Cox (1952).
- The slip between fibre and soil is maximum at the ends of the fibre, and zero at the centre, and is also non-linear.
- Plasticity and softening at the fibre-soil interface reduces the amount of axial stress which can be transferred across the interface. Use of the von Mises plasticity model with linear softening created a linear distribution of slip and fibre stress in the debonded region.
- As plastic strains develop in the soil, and the fibre begins to debond, a higher portion of the axial stress is carried by the central region of the fibre.
- The radius of influence of the fibre was approximately 20 mm, 40 times the radius of the fibre in this case.

The following sections describe the formulation of a constitutive soil-fibre model, which is based on micro-mechanical interactions, physical relationships, and the findings from this finite element study.

7.2 Model formulation

Based on the literature review, experimental study, and finite element study carried out; a new soil-fibre interaction model is formulated in this section. At the smallest scale, the model captures the behaviour of a single fibre; this model is then homogenised to obtain the overall contribution from the full network of fibres in the macro scale.

7.2.1 Behaviour of a single fibre

The model formulated here is first described in terms of a single fibre of radius r_f , and length l_f . This fibre is modelled as a cylinder within a larger cylinder of soil (Figure 7.8). The composite is considered as a cylinder with a radius R_c defined by the fibre packing density. The calculation of this radius is explored later in Section 7.3.1.

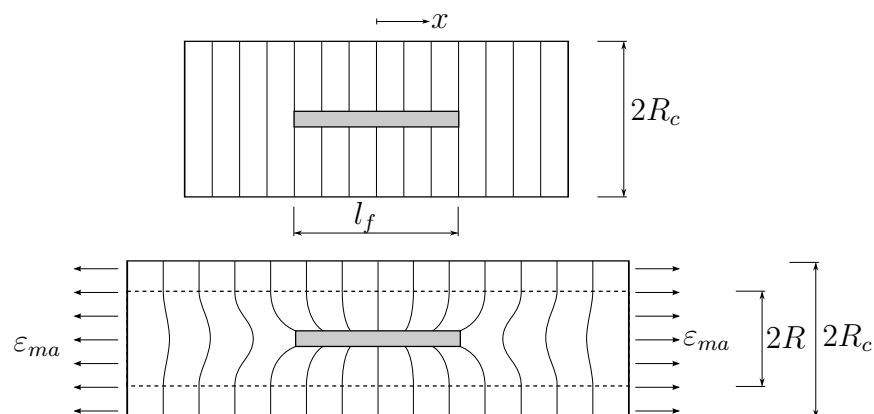


Figure 7.8: Deformation contours due to presence of fibre during axial straining (redrawn from Matthews and Rawlings, 1999)

The shear lag model, originally proposed by Cox (1952), models the elastic slip of a single short fibre within a continuous matrix. As shown in Figure 7.8, the strain

in the matrix is partially transferred to the fibre through friction between the fibre and the matrix. In granular soils this creates a shear stress in the matrix around the fibre, this is named the shear influence zone; outside this zone the strains are assumed to be purely axial in nature. The size of this influence zone is assumed to coincide with the location of average axial displacement (Aveston and Kelly, 1973) as cited in (Diambra and Ibraim, 2015).

$$R = \frac{r_f + R_c}{2} \quad (7.2)$$

The calculated strains in the fibre are reported to be insensitive to the exact value of R (Diambra and Ibraim, 2015).

The cross-sectional area of the matrix and fibre are simply defined as follows

$$a_m = \pi (R^2 - r_f^2) \quad (7.3)$$

$$a_f = \pi r_f^2 \quad (7.4)$$

Based on typical mechanical properties of manufactured fibres and soil, the fibres are assumed to be significantly stiffer than the soil they are reinforcing. Also, the fibre is expected to slip in the soil before the material yields (Diambra et al., 2013; Zhu et al., 2014). Therefore, a linear elastic stress-strain relationship is assumed:

$$\sigma_f = E_f \varepsilon_f \quad (7.5)$$

where σ_f and ε_f are the axial stress and strain at any point along the fibre, and E_f is the uniaxial Young's modulus of the fibre. The fibres are modelled as one dimensional elements, i.e. radial effects are neglected for axial strains.

The stress-strain relationship in the matrix is also assumed to be linear. Although the fibre model is to be used alongside a soil plasticity model, this plasticity will be transferred into the fibre model by applying a limiting bond strength; this will be discussed later in Section 7.2.3.

$$\sigma_m = E_m \varepsilon_m \quad (7.6)$$

In order to maintain equilibrium conditions, the following relationships must be enforced:

$$a_f \frac{d\sigma_f}{dx} + a_m \frac{d\sigma_m}{dx} = 0 \quad (7.7)$$

$$a_f E_f \frac{d\varepsilon_f}{dx} + a_m E_m \frac{d\varepsilon_m}{dx} = 0 \quad (7.8)$$

7.2.2 Fully bonded fibre

To continue development of the formulation, the forces on an infinitesimal length of fibre (Figure 7.9) are considered and the basic shear lag equation is formed:

$$\frac{d\sigma_f}{dx} = -\frac{2\tau}{r_f} \quad (7.9)$$

$$\frac{d\varepsilon_f}{dx} = -\frac{2\tau}{E_f r_f} \quad (7.10)$$

The slip is defined as the difference between the matrix and fibre displacement at any point, as defined in Equation 7.11, and the interface shear stress is assumed to related directly to the amount of slip (Equation 7.12).

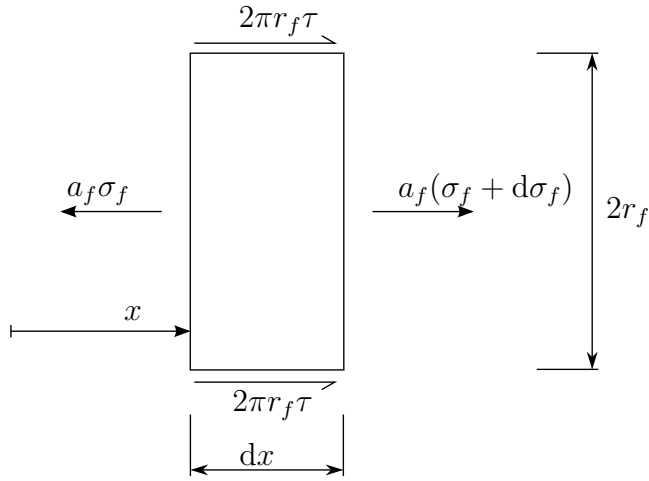


Figure 7.9: Infinitesimal length of fibre; free body diagram

$$S = u_m - u_f \quad (7.11)$$

$$\tau = k_s S \quad (7.12)$$

Differentiating (7.11) gives the following relationships

$$\frac{dS}{dx} + \varepsilon_f = \varepsilon_m \quad (7.13)$$

$$\frac{d^2 S}{dx^2} + \frac{d\varepsilon_f}{dx} = \frac{d\varepsilon_m}{dx} \quad (7.14)$$

Substitution of (7.14), (7.12) and the shear lag equation (7.10) into the equilibrium condition (7.8) gives:

$$(a_f E_f + a_m E_m) \frac{k_s S}{E_f r_f} + a_m E_m \frac{d^2 S}{dx^2} = 0 \quad (7.15)$$

Simplifying leads to:

$$\frac{d^2 S}{dx^2} - \beta^2 S = 0 \quad (7.16)$$

where

$$\beta^2 = \frac{2(a_f E_f + a_m E_m) k_s}{E_f r_f a_m E_m} \quad (7.17)$$

A general solution to this differential equation takes the form:

$$S = A \cosh(\beta x) + B \sinh(\beta x) \quad (7.18)$$

which must be solved by applying known boundary conditions. As the loading condition is assumed to be symmetric, the slip between the matrix and fibre at the centre of the fibre is zero. Applying this condition yields $A = 0$. At the fibre ends, the stress and strain in the fibre are zero, and the matrix strain ε_m is assumed to be equal to the applied composite strain ε_{ma} . Another option for describing the matrix strain is to record elastic and plastic components of the matrix strain, and relate them to elastic and plastic components of interface slip. However, the former of the two methods has been adopted for this study due to its simplicity; one disadvantage of doing this is that unloading cycles may be poorly represented, as all fibre strains are based on the total matrix strain, with no knowledge of loading history.

Equation 7.13 contains each stress component and can be used to solve for this boundary condition. Substituting the condition into (7.13) gives:

$$B\beta \cosh(\beta x) + 0 = \varepsilon_{ma} \quad (7.19)$$

Solving for B then gives the final slip relationship for the fully bonded case as

$$S(x) = \frac{\varepsilon_{ma} \sinh(\beta x)}{\beta \cosh\left(\beta \frac{l_f}{2}\right)} \quad (7.20)$$

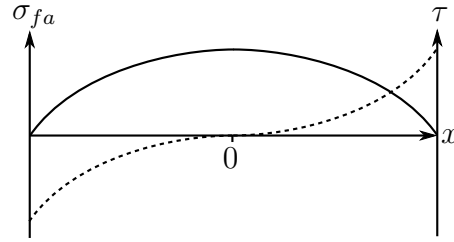


Figure 7.10: Tensile fibre stress σ_f (solid) and interface shear stress τ (dashed) distributions for fully bonded fibre

The stress in the fibre can be obtained by integrating the shear lag relationship in Equation 7.9. Integrating from the fibre end to the position of interest gives the fibre stress at any position.

$$\sigma_f(x) = \frac{-2k_s}{r_f} \int_x^{l_f/2} S(z) dz \quad (7.21)$$

which, when integrated within the given limits becomes:

$$\sigma_f(x) = \frac{2k_s \varepsilon_{ma}}{r_f \beta^2} \left(\frac{\cosh(\beta x)}{\cosh\left(\beta \frac{l_f}{2}\right)} - 1 \right) \quad (7.22)$$

Plotting the fibre axial stress and the interface shear stress with the position in the fibre gives the hyperbolic distributions shown in Figure 7.10.

7.2.3 Debonding fibre

Through extended straining in the composite, the slip between the matrix and fibre will become plastic. From a micro-mechanical perspective, this would correspond to soil particles bonding and debonding with different sections of the fibre.

From the experimental pullout results in Section 6.3.2, a distinct peak load is observed in each of the pullout tests, followed by a drop to a fairly constant residual stress. The residual stress oscillated in the experimental results, however for the purposes of modelling, the mean value is used.

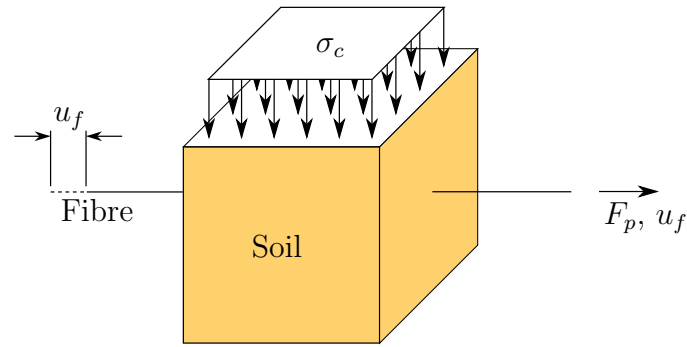


Figure 7.11: Fibre pullout schematic; soil is fully contained in a box, and loaded from the top, the fibre is then pulled from one end and its remains unchanged throughout the test.

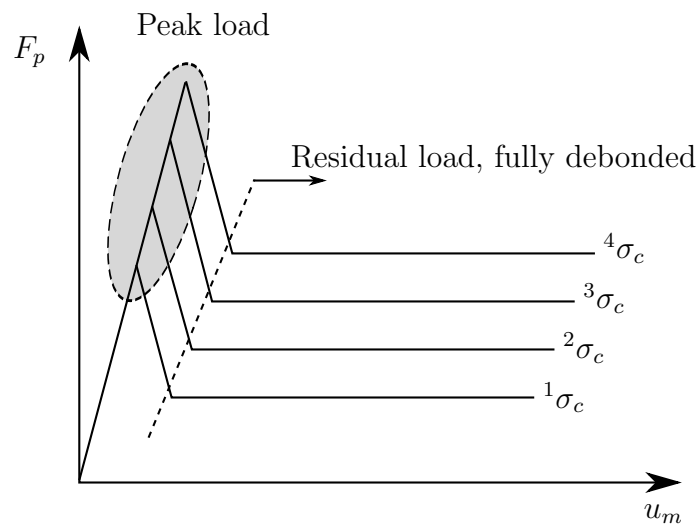


Figure 7.12: Idealised results from fibre pullout test showing distinct loading stages.

There is a clear increase in peak and residual strength with increased confining stress (Figure 6.15). The initial gradient before debonding was found to not be effected by this confining stress. A total of five confining stresses were tested and each test was repeated a total of 3 times. The experimental peak and residual forces are plotted in Figure 6.15. An idealised configuration of the fibre pullout test is shown in Figure 7.11, which relates to an idealised form of the experimental results shown in Figure 7.12.

These values can be converted into pullout shear stresses by dividing by the fibre area in contact with the soil. Assuming a $K_0 = 1 - \sin \varphi$ distribution to horizontal stresses, the radial compressive stress σ_r acting on the fibre can be estimated to the average of the horizontal and vertical stress. With this information, linear

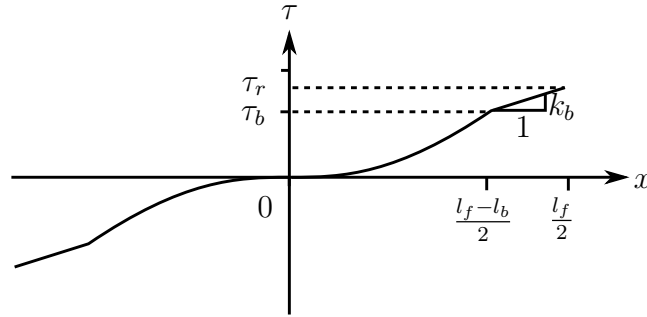


Figure 7.13: Assumed shear stress distribution for a debonding fibre

relationships can be obtained relating the radial stress to the peak pullout shear strength:

$$\tau_b = \kappa_b \sigma_r \quad (7.23)$$

and the residual shear strength:

$$\tau_r = \kappa_r \sigma_r \quad (7.24)$$

Based on results from the finite element study in Section 7.1; an assumption is made regarding the stress distribution in the fibre during debonding. As the shear stress is highest at the fibre ends, the shear stress will debond at the fibre end first, and debonding will progress towards the centre of the fibre with extended strain. It is then assumed the shear stress at the bonding-debonding boundary is τ_b , the shear stress at the fibre end becomes τ_r . A plot of the assumed shear stress distribution is shown in Figure 7.13. With this model it is possible for the residual shear stress τ_r to be lower than, equal to, or higher than the debonding shear stress τ_b . A similar approach was used by Brighenti (2004), whereby the composite was modelled using representative volume elements (RVEs), and the matrix portion was modelled using a bi-linear softening stress-strain curve.

The shear stress in the debonded region is now linear, the gradient of the

debonded region is given by k_b . The equation for shear stress in this region is given by

$$\tau = \tau_b + k_b \left(x - \frac{l_f - l_b}{2} \right) \quad (7.25)$$

The shear-slip relationship in (7.12) still holds, therefore

$$S(x) = \frac{1}{k_s} \left(\tau_b + k_b \left(x - \frac{l_f - l_b}{2} \right) \right) \quad (7.26)$$

The first debonding occurs at the fibre end when the shear stress equals the debonding shear stress. Thus, the debonding slip is defined as

$$S_b = \frac{\tau_b}{k_s} \quad (7.27)$$

Equation 7.27 satisfies the debonding region slip (7.26) for the case of $x = (l_f - l_b)/2$. The stress is calculated similarly to the fully bonded case (7.21), whereby the slip function is integrated from the fibre end. Performing the same integration for the debonded region leads to

$$\sigma_f(x) = -\frac{2}{r_f} \left[\tau_b \left(\frac{l_f}{2} - x \right) + k_b \left(\frac{l_f^2}{8} - \frac{x^2}{2} - \frac{l_f - l_b}{2} \left(\frac{l_f}{2} - x \right) \right) \right] \quad (7.28)$$

The stress at the bonded-debonded interface is found by substituting $x = (l_f - l_b)/2$ into Equation 7.28.

$$\sigma_{fb} = -\frac{l_b}{r_f} \left(\tau_b + \frac{k_b l_b}{4} \right) \quad (7.29)$$

The bonded region follows the same derivation as before, however the new boundary conditions must be applied to the differential equation

$$S(x) = C \cosh(\beta x) + D \sinh(\beta x) \quad (7.30)$$

Similarly to before, the slip at the centre of the fibre ($x = 0$) is zero. This leads to $C = 0$. At the debonding interface, the slip is equal to the debonding slip S_b . Enforcing this boundary condition allows solving for D , and the expression for the slip in the bonded region can be written as:

$$S(x) = \frac{S_b \sinh(\beta x)}{\sinh\left(\beta \frac{l_f - l_b}{2}\right)} \quad (7.31)$$

At this stage, the applied matrix strain which drives the problem is not included in the debonded formulation. Enforcing the third boundary condition requires the matrix strain ε_{ma} to calculate the debonded length. The third boundary condition is that the stress is equal to the debonding stress (7.29) at $x = (l_f - l_b)/2$. This condition should hold for the debonded region (7.28) and the central bonded region.

It is assumed that the central bonded region is unaffected by the debonding of the fibre ends. The equivalent bonded end shear stress τ_e is used to describe the shear stress at the end of the fibre, if the bond strength were infinite.

$$\tau_e = \frac{k_s \varepsilon_{ma} \tanh\left(\beta \frac{l_f}{2}\right)}{\beta} \quad (7.32)$$

Substituting (7.32) into the bonded slip relation (7.31) at the fibre end and rearranging gives

$$\tau_b = \frac{k_s \varepsilon_{ma} \sinh\left(\beta \frac{l_f - l_b}{2}\right)}{\beta \cosh\left(\beta \frac{l_f}{2}\right)} \quad (7.33)$$

Substituting (7.33) into the slip function for the debonded region (7.26) at the fibre end, gives an expression for the residual shear stress.

$$\tau_r = \frac{k_s \varepsilon_{ma} \sinh\left(\beta \frac{l_f - l_b}{2}\right)}{\beta \cosh\left(\beta \frac{l_f}{2}\right)} + \frac{k_b l_b}{2} \quad (7.34)$$

From the linear portion of the curve in Figure 7.13, an expression for the debonded length can be obtained.

$$l_b = \frac{2}{k_b} (\tau_r - \tau_b) \quad (7.35)$$

The variable k_b is not a material parameter and must be eliminated from the problem by substitution. Equations 7.34 and 7.35 are independent and are used to solve for the debonded length l_b . Using the exponential equivalents of the hyperbolic trigonometric functions, and through further algebraic manipulation, a quadratic equation involving l_b can be formed. Solving this quadratic equation gives an expression for the debonded length which relates directly to the applied matrix strain ε_{ma} .

$$l_b = l_f - \frac{2}{\beta} \operatorname{arcsinh} \left(\frac{S_b \beta \cosh\left(\beta \frac{l_f}{2}\right)}{\varepsilon_{ma}} \right) \quad (7.36)$$

One advantage of using this method is that a variety of debonding shear stress distributions can be used, subject to re-solving of the necessary equations. The solution for l_b can also be found by using an iterative procedure such as Newton-Raphson or bisection methods.

7.2.4 Comparison with finite element study

The stress distributions from the micro-mechanical model are compared against the finite element study carried out in Section 7.1. Figure 7.14 shows the slip and stress distributions for the fully bonded, and partially debonded fibre. The fibre length is kept constant and the aspect ratio \mathcal{R} is altered by modifying the fibre radius. An

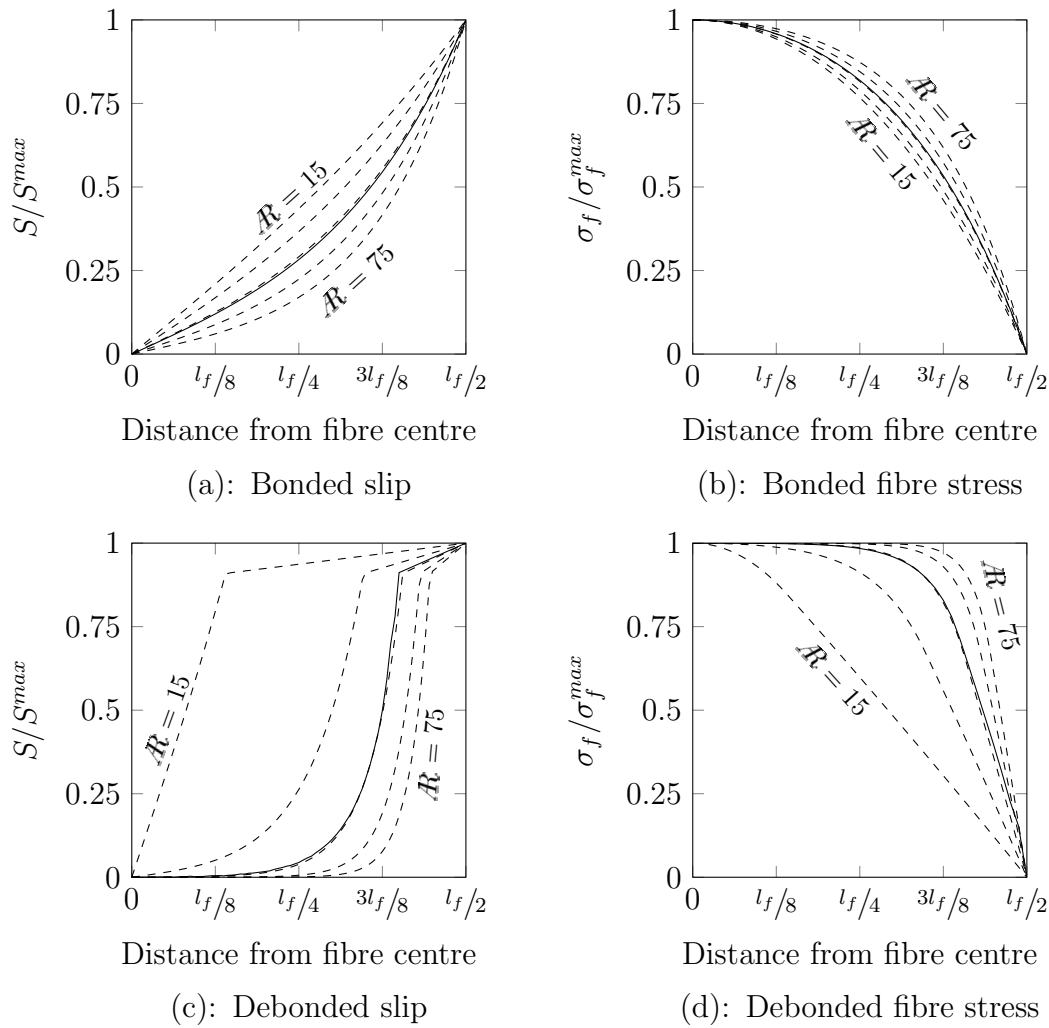


Figure 7.14: Fully bonded fibre slip and stress distributions with different aspect ratios. Comparison of FEA model (solid) and micro-mechanical model (dashed), results have been normalised to the maximum values, aspect ratios are linearly distributed; (a) and (b) show the fully bonded case, (c) and (d) show the debonding case

even distribution of fibre radii are analysed such that the following aspect ratios are used: $\mathcal{R} = 15, 30, 45, 60, 75$, where the aspect ratio is equal to $l_f/2r_f$. The aspect ratio of the fibre analysed in the finite element study was $\mathcal{R} = 45$.

The first observation which can be made is that the slip and stress distributions are able to closely match the results from the finite element study. The distributions corresponding to $\mathcal{R} = 45$ match the FEA results the closest; this is the same geometrical configuration as used in the FEA study.

Focussing on the elastic results in Figures 7.14a and 7.14b, increasing the aspect ratio tends to decrease the slip at the fibre centre, concentrating the slip toward the

fibre ends. The fibre stress results appear to be less sensitive to \mathcal{R} , however the stress is more evenly spread over the fibre with a higher \mathcal{R} .

Regarding the debonding slip distribution in Figure 7.14c, the limiting interface shear stress τ_b and the residual shear stress τ_r were calculated directly from the finite element study. Both the slip and stress results for the debonding case appear to be more sensitive to the change in aspect ratio than in the fully bonded case. In Figure 7.14c, the highest aspect ratio fibre has the slip most concentrated at the fibre end, with a lower aspect ratio, the bonded length decreases, and the distribution becomes more linear in the bonded region.

The debonding stress distribution in Figure 7.14d shows a similar trend, where the lower aspect ratio produces more linear results. The axial stress in the de-bonded region is linear, and becomes non-linear in the bonded region.

7.3 Homogenisation

To include the effects of randomly distributed fibres in a soil, the problem must be homogenised into a representative volume element (RVE); ready for use in the finite element stress space.

7.3.1 Fibre radius of influence

The portion of fibres in the composite affects the spacing between the fibres. Based on data obtained from the finite element study, the radius of influence of the fibre is approximately 40 times the fibre radius. In the literature, fibre concentrations of between $v_f = 0.1\%$ and $v_f = 1.0\%$ are typically investigated (Diambra et al., 2010; Ibraim et al., 2012; Li and Zornberg, 2013). This relates to an average distance of 10 times the fibre radius for a fibre concentration of $v_f = 1.0\%$, and 30 times for a concentration of $v_f = 0.1\%$. From the FEA plot of horizontal soil displacements in the composite (Figure 7.5), the level of influence at this range is low. Therefore

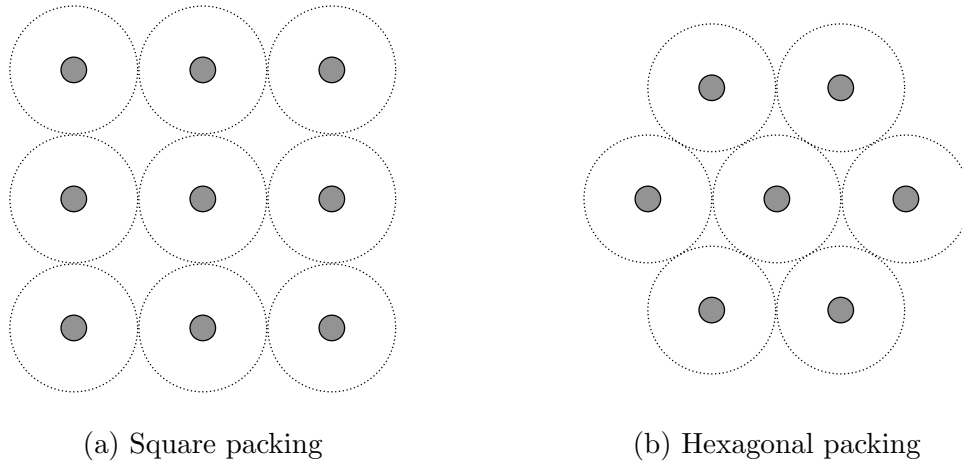


Figure 7.15: Idealised fibre arrangements and their respective composite radii R_c

it is not unreasonable to assume the simplification that the fibres do not influence each-other, as this is unlikely to affect the predicted composite strength.

A simple and convenient method for describing the fibre spacing is to assume a uniform distribution in two dimensions (Figure 7.15); this theory is taken from the field of unidirectional composites. This theory also assumes a uniform packing arrangement as typically applied in uni-directional fibre composites. The actual positioning in the soil is random, not uniform, however an average distribution is assumed for the homogenised model.

Several options for packing arrangements are available. The simplest is the square arrangement (Figure 7.15a) where each fibre is layered in a grid pattern. From a basic geometric calculation, the maximum possible fibre volume fraction (assuming that the fibres are touching and are unidirectional) is $v_f = 0.785$ (Altenbach et al., 2004). The most efficient arrangement is the hexagonal layout (Figure 7.15b); this minimises the distance between fibres and using a similar calculation, the maximum possible volume fraction is $v_f = 0.907$ (Altenbach et al., 2004).

The hexagonal arrangement is to be used in this model, as it appears to more accurately reflect a homogenised random distribution. Whilst this choice is somewhat arbitrary, for the same volume fraction, use of the square packing arrangement produced a negligible difference in strength contribution from the fibres. This is most likely due to the low volume fractions considered in soils. The spacing of fibres R_c

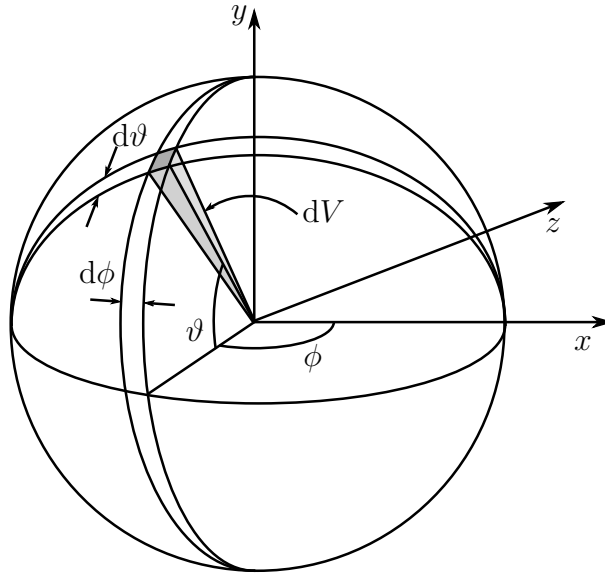


Figure 7.16: Spherical coordinate system and elemental volume used in integration (redrawn from Michalowski and Zhao, 1996)

is related to the fibre volume fraction v_f and the fibre radius r_f

$$R_c = \frac{r_f}{\sqrt{\frac{2\sqrt{3}v_f}{\pi}}} \quad (7.37)$$

for the hexagonal arrangement. This is not to be confused with the radius of influence R , which is calculated using Equation 7.2.

7.3.2 Fibre orientation distribution

It is known that the orientation of the fibres has a significant effect on the response of composites, and that different fibre placement techniques produce different orientations (Wang, 2015; Ibraim et al., 2012); with layering and stirring methods exhibiting a horizontal preference. For most foreseeable civil engineering applications, it can be safely assumed that there is a uniform distribution of fibres on the horizontal plane (i.e. when observed vertically from above).

For the purposes of the homogenisation technique adopted here, the distribution of fibre orientations can be described as a function of the current orientation. It

is also important that the integration of the function over the orientation domain must equal to one, as to not artificially increase the fibre volume fraction. It is also possible to achieve the same effect by dividing a distribution function by the mean value of the function; however this study will enforce the criterion shown in Equation 7.38, which uses the spherical coordinate system from Figure 7.16.

$$\frac{1}{2\pi} \int_0^{2\pi} \int_0^{\pi/2} \rho_{\vartheta}(\vartheta, \phi) \cos(\vartheta) \, d\vartheta \, d\phi = 2\pi \quad (7.38)$$

The horizontal plane has a uniform distribution of fibre orientations, therefore the distribution function with respect to the horizontal is given a constant value of 1; this is why it is not included in Equation 7.38. Therefore, integrating with respect to the vertical plane gives the simplified criterion.

$$\frac{1}{2\pi} \int_0^{\pi/2} \rho_{\vartheta}(\vartheta) \cos(\vartheta) \, d\vartheta = 1 \quad (7.39)$$

Characterisation

The simplest vertical orientation distribution is the uniform distribution. The function takes the form of a fixed value which must satisfy (7.39).

$$\rho_{\vartheta}(\vartheta) = \frac{1}{2\pi} \quad (7.40)$$

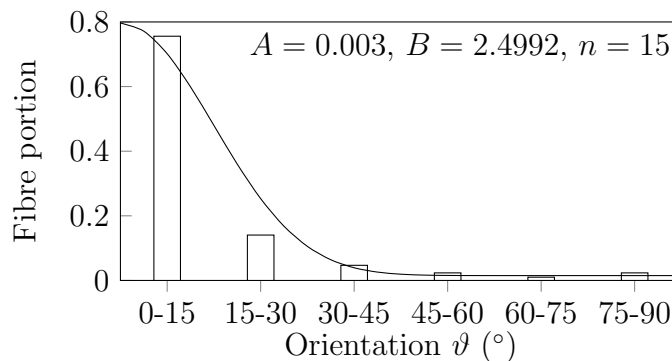


Figure 7.17: Fibre orientations for layering method, showing actual portions (bars) and modelled distribution function (line), markers represent midpoint of each range

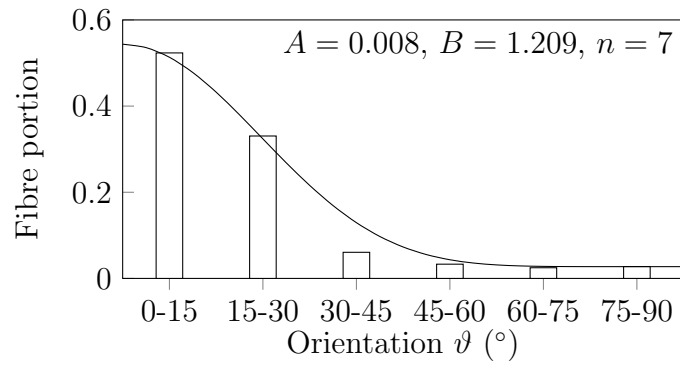


Figure 7.18: Fibre orientations for stirring method

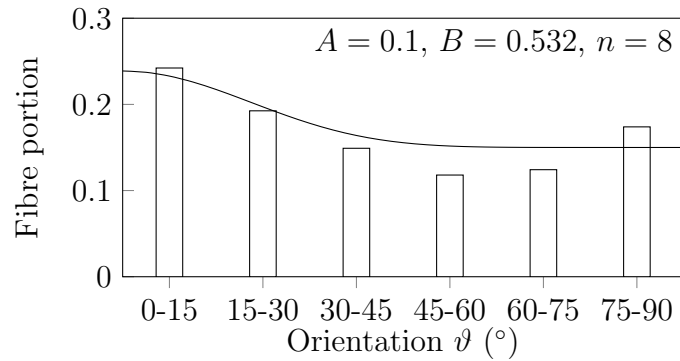


Figure 7.19: Fibre orientations for shaking method

The actual and modelled distributions are shown in Figures 7.17, 7.18, and 7.19 for each preparation method. Both the layering and stirring methods produced distributions with a strong bias towards horizontal fibres; with the layering method this effect is more pronounced. The shaking method produces a more uniform distribution, where a larger portion of the fibres are vertical. Michalowski (1997) proposed the following function to describe the orientation distribution of fibres, assuming axial symmetry on the horizontal plane.

$$\rho_{\vartheta}(\vartheta) = A + B |\cos(\vartheta)|^n \quad (7.41)$$

The parameters A , B , and n can be adjusted to fit the experimental distribution and to satisfy (7.39).

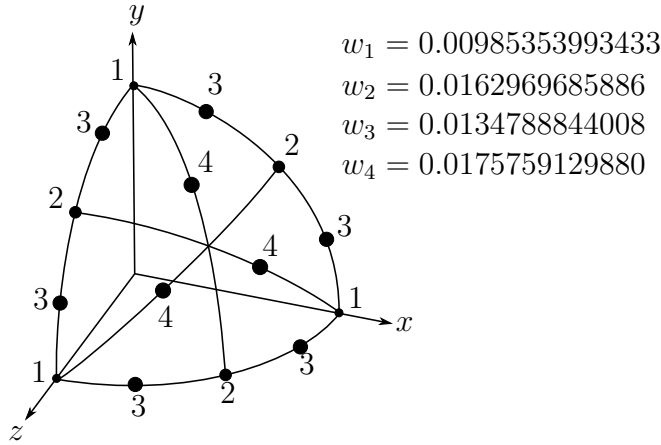


Figure 7.20: Integration points on the unit sphere for the 66 point rule (redrawn from Bažant and Oh, 1986)

7.3.2.1 Spherical integration

Exact integrations of the fibre contribution over the surface of the sphere are computationally expensive. This is why a numerical approach is adopted. Much like a simple Gauss-Legendre integration over a finite element domain, sampling positions on the surface of the sphere are chosen and assigned weights. The points are chosen by finding the position of the corners of regular and irregular polyhedra. Weights are assigned to each point by minimising the errors from a Taylor series expansion of an algebraic function over the integrated domain.

Various integration rules are available with different numbers of sampling positions. Bažant and Oh (1986) provide a comparison of regimes ranging from 20 to 122 sampling positions. As to be expected, the regimes using a higher number of sampling points provided more accurate results, but at a higher computational cost. The 66 point rule (as illustrated in Figure 7.20) is considered for this study, this is an 11th order approximation and it is a good compromise of cost and accuracy (Bažant and Oh, 1986).

Full orthogonal symmetry is also observed in this method. The integration is implemented by looping through each direction, the coordinates of each point represent a direction cosine. The fibre contribution for each direction is multiplied by its direction cosine vector, then added to the running total of the fibre contribution in

the chosen stress space. The symmetry about the horizontal plane is observed and 33 additions are required for the full summation (Equation 7.43). Integration over the length of the fibre is also considered, this is to take into account to the different positions of the fibre relative to the integration point. This distribution is taken as uniform ($2/l_f$). The integration over the fibre length and over the spherical domain is given as:

$$\boldsymbol{\sigma}_f = \frac{1}{2\pi} \int_0^{\pi/2} \int_0^{2\pi} \frac{2}{l_f} \int_0^{l_f/2} (\boldsymbol{\Psi}(\boldsymbol{\vartheta}))^T \rho_\vartheta(\vartheta) \sigma_f(x, \varepsilon_{ma}) dx d\phi d\vartheta \quad (7.42)$$

and in the form for numerical integration as:

$$\boldsymbol{\sigma}_f = \sum_{i_d=1}^{33} w_{i_d} \rho_\vartheta(\vartheta_{i_d}) (\boldsymbol{\Psi}_{i_d})^T \frac{2}{l_f} \int_0^{l_f/2} \sigma_f(x, \varepsilon_{ma}) dx \quad (7.43)$$

where $\boldsymbol{\Psi}$ is a matrix containing the direction cosines for each integration point, and w_{i_d} is the current sampling weight. Note that the integration over ϕ is not included in (7.43) because the orientation distribution is uniform, hence the density function is a constant $\rho_\phi = 2\pi$.

The axial matrix strain ε_{ma} is calculated for each integration direction by transforming the Cartesian strain vector $\boldsymbol{\varepsilon}$ with the current direction cosine vector $\boldsymbol{\Psi}_{i_d}$. The radial stress on the fibre is computed in a similar manner and the average of the two other orthogonal directions is taken as the radial stress on the fibre σ_r .

The total fibre stress is then added to the total matrix contribution using the rule of mixtures.

$$\boldsymbol{\sigma} = v_m \boldsymbol{\sigma}_m + v_f \boldsymbol{\sigma}_f \quad (7.44)$$

The matrix stress $\boldsymbol{\sigma}_m$ is calculated from the given total strain vector $\boldsymbol{\varepsilon}$ using a choice of constitutive soil model; this study considers the use of the fibre model alongside the HS-LC model as described in Chapter 3. However, it is also possible to

use other constitutive soil models such as the Mohr-Coulomb model or the Modified Cam-Clay model.

7.3.2.2 Stiffness tensor

The relationship between incremental stresses and strains (i.e. the D matrix) for the fibre behaviour is defined here. As the fibres are considered to be fully elastic, and the fibre strain is directly related to the applied soil strain, a single definition of the stiffness tensor is required. The fibre stiffness tensor is first calculated in its total form

$$\mathbf{D}_f = \frac{1}{2\pi} \int_0^{\pi/2} \int_0^{2\pi} \frac{2}{l_f} \int_0^{l_f/2} (\boldsymbol{\Psi}(\boldsymbol{\vartheta}))^T \rho_{\boldsymbol{\vartheta}}(\boldsymbol{\vartheta}) \frac{d\sigma_f(x, \varepsilon_{ma})}{d\varepsilon_{ma}} dx \boldsymbol{\Psi}(\boldsymbol{\vartheta}) d\phi d\boldsymbol{\vartheta} \quad (7.45)$$

However, for use in computations, it is calculated from a numerical integration, similarly to the fibre stress tensor.

$$\mathbf{D}_f = \sum_{i_d=1}^{33} w_{i_d} \rho_{\boldsymbol{\vartheta}}(\boldsymbol{\vartheta}_{i_d}) (\boldsymbol{\Psi}_{i_d})^T \frac{2}{l_f} \int_0^{l_f/2} \frac{d\sigma_f(x, \varepsilon_{ma})}{d\varepsilon_{ma}} dx \boldsymbol{\Psi}_{i_d} \quad (7.46)$$

The total stiffness of the composite is calculated using the rule of mixtures. The D matrix from the soil may be elastic, or the 4th order consistent tangent matrix, depending on the current state of the soil model.

$$\mathbf{D} = v_m \mathbf{D}_m + v_f \mathbf{D}_f \quad (7.47)$$

This version of the D matrix is required to preserve the quadratic rate of convergence for the global Newton-Raphson iterative scheme (see Section 3.8 for more details on the Newton-Raphson scheme and the consistent tangent matrix).

7.4 Parametric study

A study of the fibre parameters is performed, where the fibre model is superimposed onto the re-formulated hardening soil model (as discussed in Chapter 3). A series of triaxial tests are simulated and the resulting shear and volumetric behaviour are compared using the parameters shown in Table 7.1. A summary of the soil parameters is also shown in Table 7.2; the parameter $m = 0$ has been chosen to remove stress dependency in the HS model, thus clarifying the effects of the fibres.

As debonding significantly affects the distribution of stress along the fibre, a selection of the basic parameters are repeated for one debonding result; this is why the bond strength parameter κ_b in Table 7.1 has two base values.

The model is run in a single point constitutive driver with a Newton-Raphson solver. The composite is first taken to a confining stress of -0.3 N/mm^2 , then a vertical strain is prescribed to the composite at a rate of $\Delta\varepsilon_y = 0.003$ per step, taking a total of 100 steps to achieve a total vertical strain of 30%.

Table 7.1: Key values used in parametric study

Parameter	Base value	Values studied
R/r_f	5	3, 5, 7, 9, 11
E_f	900 N/mm ²	500, 700, 900, 1100, 1300 N/mm ²
v_f	1.08%	0.36, 0.72, 1.08, 1.44, 1.80%
k_s	0.8 N/mm ²	0.4, 0.6, 0.8, 1.0, 1.2 N/mm
l_f	35 mm	15, 25, 35, 45, 55 mm
r_f	0.05 mm	0.01, 0.03, 0.05, 0.07, 0.09 mm
n	7	3, 5, 7, 9, 11
κ_b	0.05, 0.02	0.002, 0.01, 0.02, 0.03, 0.04, 0.05
κ_r	1.1	0.5, 0.75, 1.0, 1.25, 1.5

The purpose of this study is to analyse both the sensitivity and the effect on strength, for each parameter. Figures 7.22 to 7.33 show shear and volumetric results from triaxial compression simulations. Each figure is then discussed independently and a summary is included at the end of this chapter. The results for an unreinforced

Table 7.2: Assumed soil parameters used in each analysis

Parameter	Value
E_{50}^{ref}	20 N/mm ²
E_{ur}^{ref}	60 N/mm ²
σ^{ref}	-0.1 N/mm ²
m	0
ν	0.25
φ	40°
ψ	10°
c	0.0 N/mm ²
R_f	0.9

soil are also included on each graph with a solid line.

Sensitivity must also be classified in order to quantify descriptions of the parameter dependencies. A low sensitivity is any difference between shear stress results less than 10%, a medium sensitivity is a difference between 11% and 30%, and a high sensitivity is classed as greater than 30% difference in shear stress results. For the differences in volumetric strain, this correlates to classification boundaries of 26% and 57%. This difference is quantified by Equation 7.48, as is accompanied by Figure 7.21 and the following description: As the abscissa points of each set of curves are the same, the difference between the highest and lowest curve is calculated directly at each abscissa point. The mean value of all curves is then calculated and used to weight the difference. The total sensitivity is the sum of all the weighted differences, multiplied by 100, and divided by number of data point sets.

$$\text{sensitivity} = \frac{100}{N} \sum_{i=1}^N \left| y_1^i - y_5^i \right| \sum_{j=1}^5 \frac{5}{y_j^i} \quad (7.48)$$

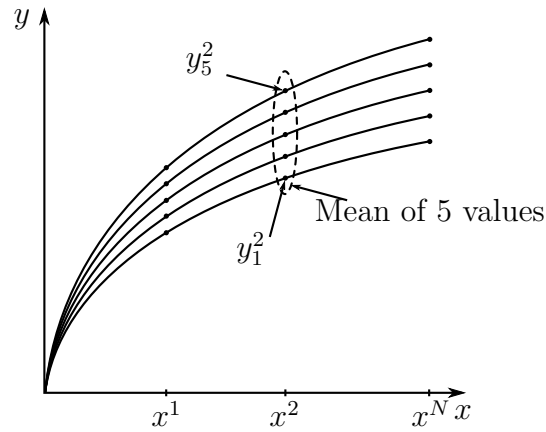


Figure 7.21: Method for the determination of the difference between curves with the same abscissa points

7.4.1 Shear radius R/r_f

A particular assumption was made in Section 7.2.1 for the formation of Equation 7.2. The assumption is that the solution to fibre problems is insensitive to the exact value of the fibre influence radius R . The radius of this zone is calculated as the average of the fibre packing radius (according to a hexagonal distribution array) and the fibre radius.

In Figure 7.22, it appears that some significant variation does exist in the model with the variation of R . Increasing the influence radius increases the shear strength and increases the dilatancy reduction in the model. The dependency from $R/r_f = 3$ to $R/r_f = 5$ is significantly larger than that between $R/r_f = 9$ and $R/r_f = 11$, suggesting that the sensitivity does reduce as the influence radius increases. The sensitivity of this parameter is classed as medium. Comparing to the horizontal displacements calculated in the soil for the finite element study (Figure 7.5), a ratio of $R/r_f = 3$ corresponds to a horizontal soil displacement of 2.23 mm, a ratio of $R/r_f = 7$ corresponds to 3.35 mm, and $R/r_f = 11$ corresponds to a displacement of 3.71 mm. As these values are changing fairly significantly with material properties typically used in soil-fibre composites, it is possible that the assumption made in the formulation of Equation 7.2 may not be valid. This is the assumption that the composite stress in the fibre is insensitive to composite radius.

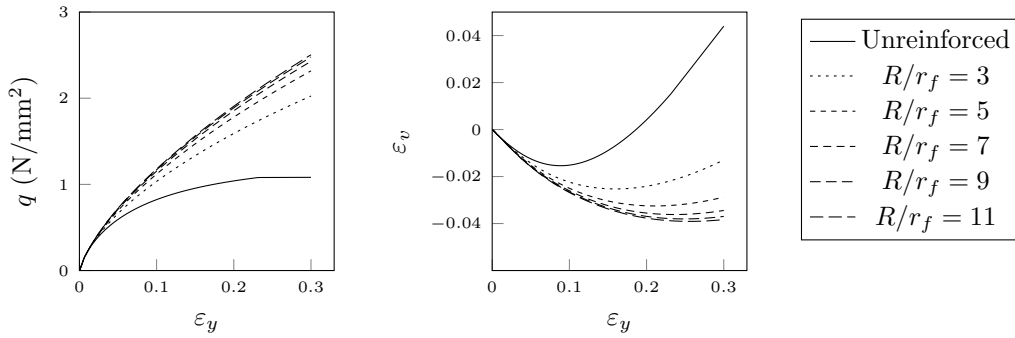


Figure 7.22: Variation of shear radius R/r_f for bonded case $\kappa_b = 0.05$

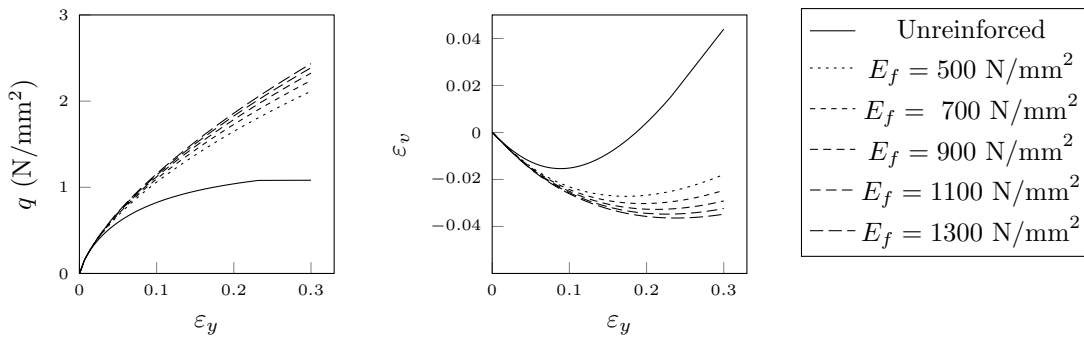


Figure 7.23: Variation of fibre modulus E_f for bonded case $\kappa_b = 0.05$

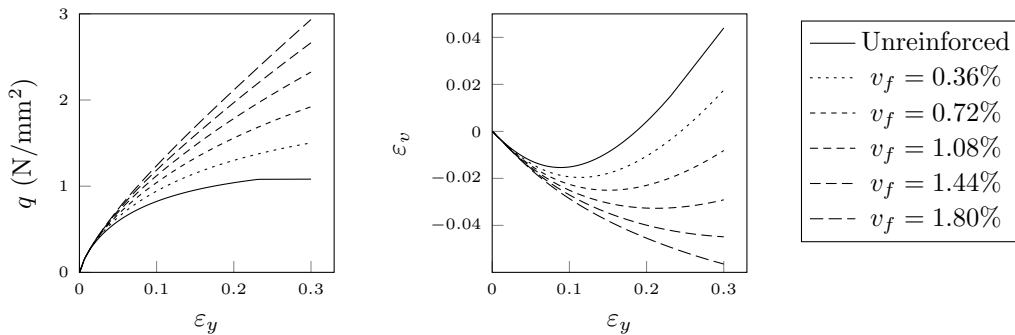


Figure 7.24: Variation of fibre volume fraction v_f for bonded case $\kappa_b = 0.05$

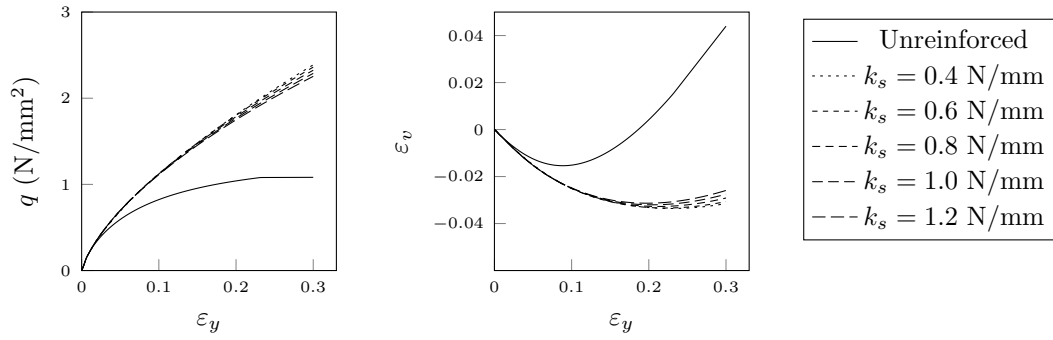


Figure 7.25: Variation of slip stiffness k_s for bonded case $\kappa_b = 0.05$

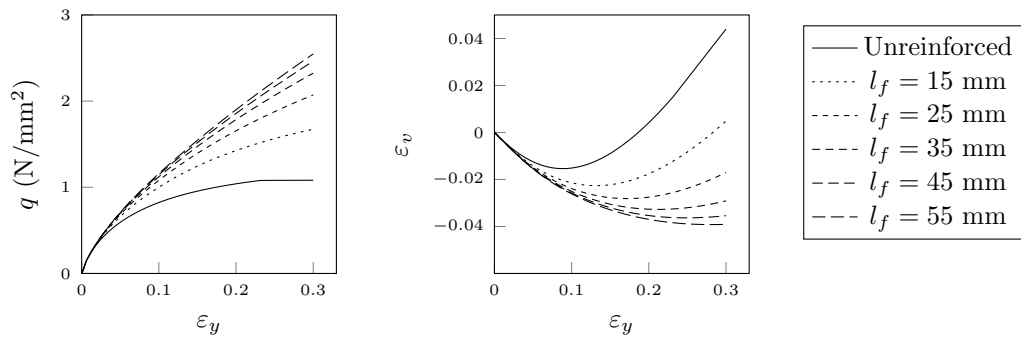


Figure 7.26: Variation of fibre length l_f for bonded case $\kappa_b = 0.05$

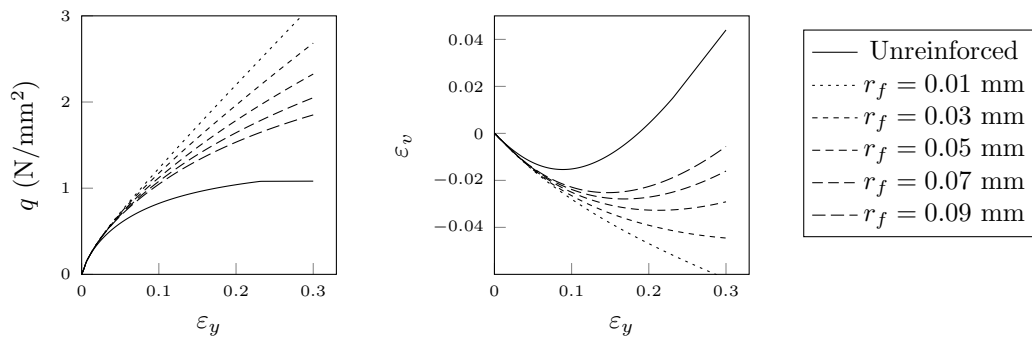


Figure 7.27: Variation of fibre radius r_f for bonded case $\kappa_b = 0.05$

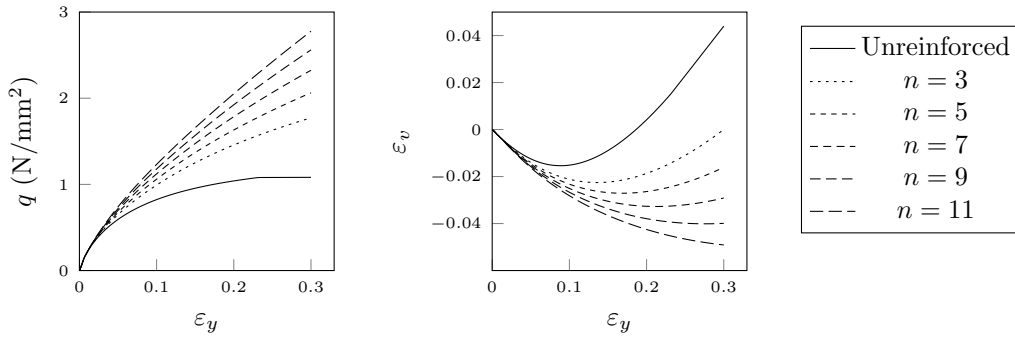


Figure 7.28: Variation of orientation exponent n for bonded case $\kappa_b = 0.05$

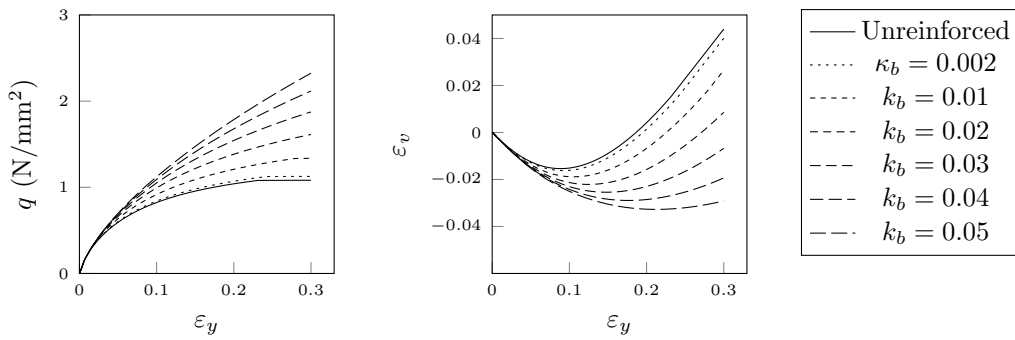


Figure 7.29: Variation of bond strength κ_b

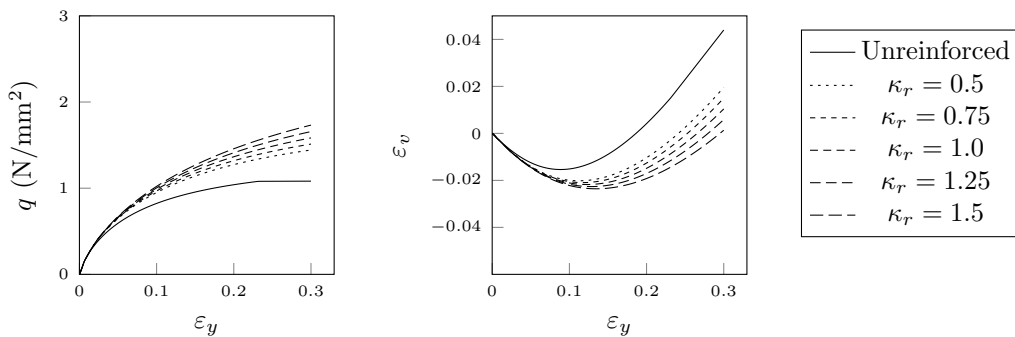


Figure 7.30: Variation of residual strength κ_r for debonded case $\kappa_b = 0.02$

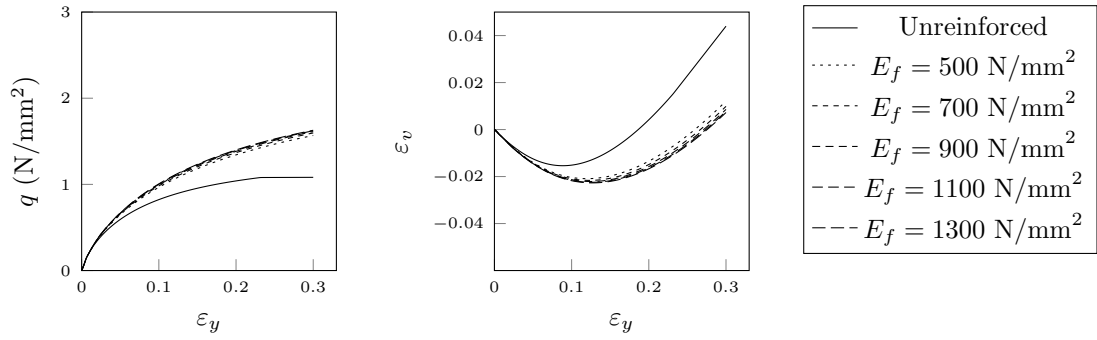


Figure 7.31: Variation of fibre modulus E_f for debonded case $\kappa_b = 0.02$

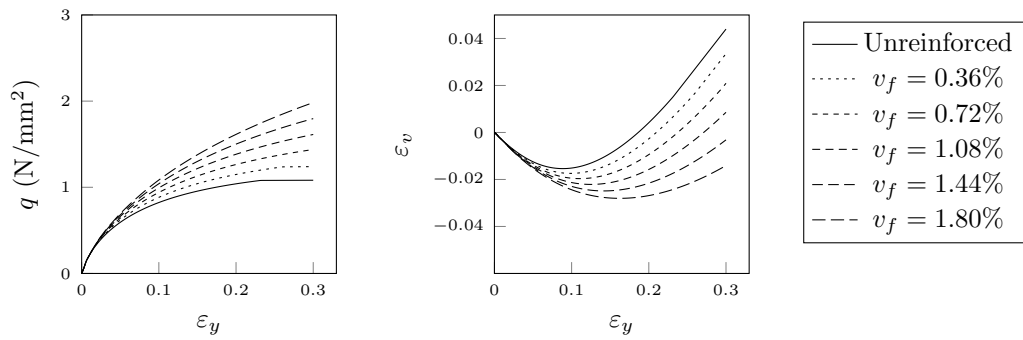


Figure 7.32: Variation of fibre volume fraction v_f for debonded case $\kappa_b = 0.02$

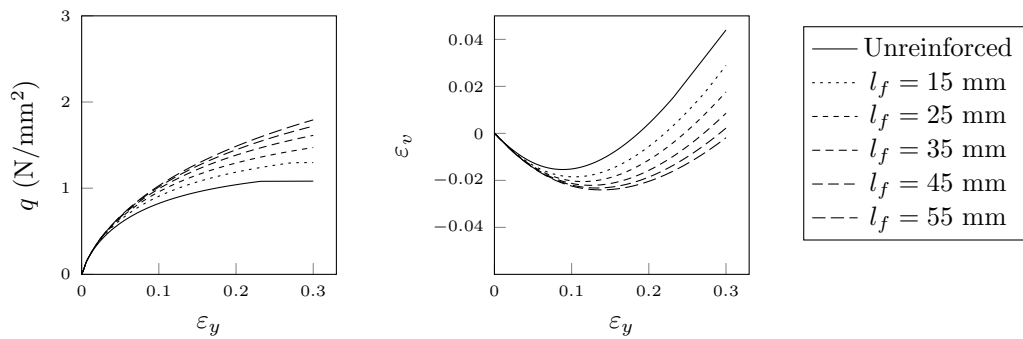


Figure 7.33: Variation of fibre length l_f for debonded case $\kappa_b = 0.02$

7.4.2 Fibre modulus E_f

As might be expected, Figure 7.23 shows that an increase in Young's modulus in the fibre increases the shear strength of the composite. The dilative effects are also increased further. The level of sensitivity is classed as low and decreases with increasing modulus.

7.4.3 Fibre volume fraction v_f

As shown in Figure 7.24, an increase in fibre volume fraction (or fibre content) provides an increase in shear strength and a decrease in dilatancy. The sensitivity of this parameter is high, with a doubling of fibre content leading to a strength increase of 150% and a very high reduction in dilatancy.

7.4.4 Slip stiffness k_s

As the slip stiffness increases, the composite shear strength decreases and the dilatancy also increases (Figure 7.25). This result is perhaps a little counter-intuitive, however it may be attributed to the approaching of debonding; as the slip stiffness increases, debonding commences sooner, hence lowering the overall strength. The sensitivity of this parameter is low and the change observed after 20% strain can be attributed to the premature debonding, where even with the higher debonding constant of $\kappa_b = 0.05$, debonding still initiates.

7.4.5 Fibre length l_f

Figure 7.26 shows that increasing the fibre length creates an increase in shear strength and a decrease in dilatant effects. It is important to note that the fibre volume fraction does not change throughout this test set. In mechanical terms, the strength increase can be largely attributed to an increase in the average length

of fibre on each side of a slip plane for example. The sensitivity is medium and reduces with increasing fibre length.

7.4.6 Fibre radius r_f

Figure 7.27 shows an increase in the fibre radius causes a decrease in the soil strength and an decrease in dilatancy reduction. The sensitivity of this parameter is high and appears to be slightly non-linear. As the fibre radius decreases, the contact area between the soil and fibres increases, thus increasing the frictional component of the fibres.

7.4.7 Orientation exponent n

The orientation exponent controls the portion of fibres which are horizontal. From the Poisson effect, a restriction in horizontal strains will also restrict the vertical strains. As the fibres can only act in tension, they are only active as the triaxial cell radius expands; i.e. near the horizontal plane. Therefore, an increase in the fibre concentration near the horizontal plane should increase the shear strength and reduce the dilatancy. This is reflected in the results as a high sensitivity, with a near linearly proportional relationship shown in Figure 7.28.

7.4.8 Bond strength κ_b

The bond strength limits the amount of shear stress that the fibre-soil interface can carry. As shown in Figure 7.29, decreasing the bond strength limits the shear capacity of the composite and reduces the volumetric influence of the fibres. When the bond strength is reduced to $\kappa_b = 0.002$, the fibres provide very little strength increase, and the soil reaches an ultimate limit state. There is a high sensitivity to this parameter and it shows a linear relationship between the parameter value and the soil strength (and dilatancy reduction).

7.4.9 Residual strength κ_r (debonded)

The residual strength determines the behaviour of the interface after debonding initialises at the fibre ends. If τ_r is lower than τ_b , then softening is modelled, if it is equal to τ_b then a perfectly plastic slip relation is used, and if it is greater than τ_b then hardening is modelled. In Figure 7.30 there is no clear distinction between hardening and softening relationships other than that the shear strength increases along with residual strength, and the dilatancy increases. The effects of debonding for this case seem to begin at an early stage of approximately 8% strain. The sensitivity of this parameter is low for the debonding case and the progression is linear. For a set of fully bonded fibres, this parameter has no effect on the results

7.4.10 Fibre modulus E_f (debonded)

Using the same series of Young moduli for the debonded case (Figure 7.31), the sensitivity has reduced even lower than that of the bonded case (Figure 7.23). It is apparent that the bond strength dominates the results when debonding is in effect.

7.4.11 Fibre volume fraction v_f (debonded)

As shown in Figure 7.32, the sensitivity to volume fraction is also reduced when debonding is active, but to a lesser extent than the Young modulus. The composite has reached failure for the lowest fibre content at a strain of 26%. The sensitivity is still classed as medium and its variation is linear.

7.4.12 Fibre length l_f (debonded)

Similarly to the fibre modulus and volume fraction, as seen in Figure 7.33, the sensitivity of the results to the fibre length has also reduced with debonding present in the model. The sensitivity is now medium but the progression is still reduces slightly with increasing fibre length.

Concluding remarks

The mechanisms behind the strength improvement due to fibres have been explored in a finite element study of a single fibre surrounded a fully elastic soil, and an elasto-plastic soil (based on the von Mises plasticity model with softening). The distribution of fibre stress and interface slip were determined for both cases and this influenced and helped to confirm these distributions calculated using the model proposed in this chapter.

The proposed soil-fibre composite model was formulated based on micro-mechanical relationships at the fibre level, results from the experimental study (discussed in Chapter 6), and results from the finite element study. This model uses concepts from the well known shear lag model (Cox, 1952), and introduces more advanced effects observed in soil such as fibre debonding. The proposed model was then used in a statistical, spherical integration to model the macroscopic behaviour of a soil reinforced with short fibres which are randomly distributed through the soil.

The experimental study indicated that the preparation method used in the fabrication of soil-fibre composites had an impact on the behaviour of the composite due to the change in orientation distribution of the fibres. The proposed soil-fibre model takes this effect into account through an orientation distribution function, which describes and controls the portion of fibres which lay at each vertical orientation.

A sensitivity study was then conducted on each of the material parameters used in the fibre model. This study used the HS-LC model as the constitutive soil model, and modelled the same triaxial test with different fibre parameters. It was found that the model was sensitive to each of the parameters to varying degrees, and many of the general trends (for example with fibre length, and volume fractions) were consistent with the experimental study and findings in the literature (discussed in Chapter 5). The range of parameters explored in the sensitivity study caused results from the model to display a range of features including the increase of strength contribution with fibre content, reduction in dilatancy with fibre content, and the

onset of debonding. The sensitivity to the composite radius R was higher than initially expected, this contradicts one of the assumptions used in the formulation of the model which was that fibres are spaced so sparsely that their influence does not spread across fibres. As this assumption may be invalid to a degree, extra care may be required with use of the model, particularly in the selection of parameters.

Chapter 8

Fibre model validation

The purpose of this chapter is to assess the accuracy of the fibre model proposed in Chapter 7, which is used alongside the new implementation of the HS-LC model described in Chapter 3. To validate the proposed model, results predicted with the model are compared with results obtained in the experimental program detailed in Chapter 6.

In the experimental program, several different fibres were studied. Each of these fibre types, and other parameters used in the fibre model are described in Table 8.1. Several preparation methods were utilised in the experimental program, resulting in different distributions of fibre orientations. Each of the parameters used in the orientation distribution function are described in Table 8.2. The material properties of the sand used in the experimental study were determined from calibration of unreinforced triaxial tests; these are described alongside the prior materials used in the HS-LC model in Table 4.1.

8.1 Unreinforced triaxial tests

The first series of tests is the analysis of unreinforced dense Leighton Buzzard sand at different confining stresses. This series of tests is used to determine the material parameters to use in the HS-LC model. The failure parameters φ and c were cal-

Table 8.1: Material parameters used in fibre model

ID	Fibre name	l_f mm	r_f mm	E_f N/mm ²	k_s N/mm	κ_b	κ_r
F1	Loksand	35.0	0.044	900	0.050	0.06	1.1
F2	Conplus6	6.0	0.009	900	0.050	0.008	1.1
F3	Conplus12	6.0	0.009	900	0.050	0.008	1.1
F4	Conplus18	6.0	0.009	900	0.050	0.008	1.1
F5	Durus S400	22.5	0.500	900	0.534	0.484	1.3

Table 8.2: Fibre orientation distribution parameters used in Equation 7.41

ID	Distribution name	A	B	n
D1	Layered	0.003	2.499	15
D2	Stirred	0.008	1.209	7
D3	Shaken	0.100	0.532	8

culated by plotting the envelope of soil failure at different confining stresses. The secant stiffness parameter E_{50}^{ref} was calculated from the triaxial q - ε curve, and the other stiffness parameters E_{ur}^{ref} and E_{oed}^{ref} were approximated based on standard relationships typically used in the HS-LC model (Schanz et al., 1999; Benz, 2007):
 $E_{ur}^{ref} \approx 3E_{50}^{ref}$, $E_{oed}^{ref} \approx E_{50}^{ref}$.

The volumetric properties ν and ψ were determined from the experimental ε_v - ε plots. The lateral earth pressure coefficient K_0^{NC} is approximated from Jaky's formula $K_0^{NC} \approx 1 - \sin \varphi$ (Jaky, 1948). The auxiliary parameters are adjusted to match the other given parameters, as described in Section 3.6.

Results obtained using the calibrated parameters are shown in Figure 8.1 for different confining stresses; these are compared with experimental data. The shear response is captured very well, the failure shear limit matches the experimental limit closely. The curvature of the shear response is very similar to the experimental curves for the 100 and 300 kN/m² confining stress, however, the 500 kN/m² experimental data reaches failure much later than predicted, this feature of the model is characterised by the failure ratio parameter R_f . The initial gradients of the shear

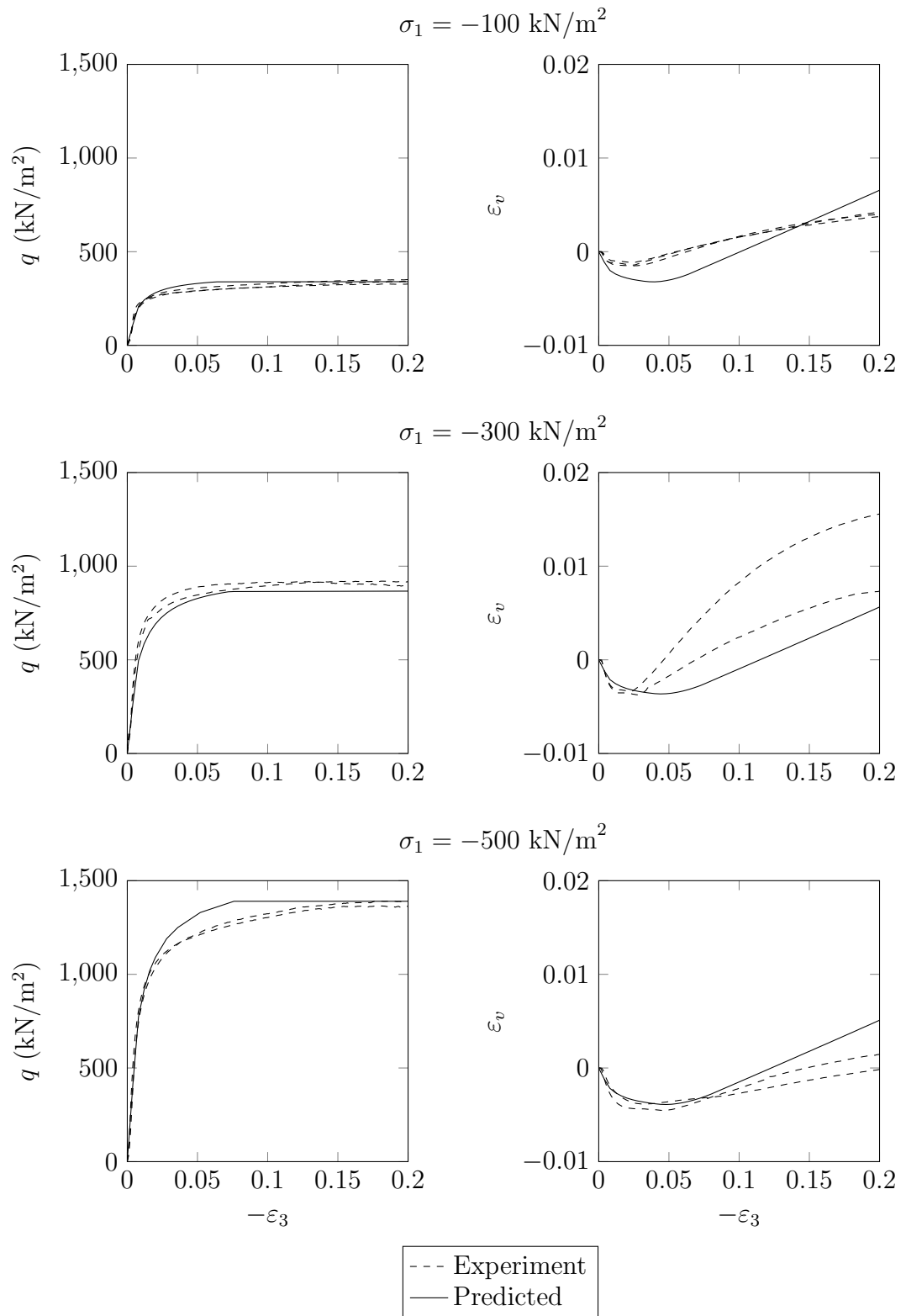


Figure 8.1: Experimental and predicted triaxial test results on unreinforced Leighton Buzzard sand (S2)

curves also match the experimental curves.

The experimental volumetric response shows an initial compressive stage, followed by a dilatant stage where the overall soil volume increases. This is reflected in each predicted result. There is no particular trend in the degree of dilatancy with each confining stress. The 300 kN/m² experimental result shows the highest dilatancy, and the 500 kN/m² test is the least dilatant. The cause of this may be due to experimental variation, or it may be that the sand reaches a critical packing arrangement where the increase in dilatancy peaks at a confining stress of 300 kN/m².

The HS-LC predictions produce volumetric curves similar to all three sets of experimental curves in Figure 8.1. The curves are not repeated precisely, but show the same degree of dilatancy. The predicted results show decreased dilatancy with increasing confining stress, this is also seen in the 100 kN/m² and 500 kN/m² results.

8.2 Triaxial fibre concentration study

The parameters obtained in the study of the unreinforced sand are next used in the HS-LC model alongside the proposed fibre model. Many of the parameters used in the fibre model are obtained directly, this includes the fibre geometry and material properties. The interface parameters for the fibre and sand were not measured directly, except for the Durus S400 fibres, which was investigated with a series of fibre pullout tests (Section 6.3.2). For the Loksand and Conplus fibres, the parameters are calibrated to triaxial data. For the Loksand fibres, the parameters k_s , κ_b , and κ_r are calibrated to the results at 100 and 300 kN/m² confining stress for a fibre concentration of $w_f = 0.3\%$. The Loksand fibres were prepared using the layering method, and the orientation distribution parameters A , B , and n for distribution D1 (Table 8.2) are used in the model.

Triaxial experimental results and predictions of $w_f = 0.3\%$ Loksand fibres for different confining stresses are shown in Figure 8.2. The presence of the fibres has increased the shear strength of the soil, delaying the onset of failure to beyond the

axial strain investigated in this study. The presence of fibres reduced the stiffness of the soil at low strains, a feature not fully captured in the model. The shear strength of the 500 kN/m² reinforced test is also under-predicted slightly.

The experimental volumetric response in Figure 8.2 is significantly less dilatant than unreinforced soil (Figure 8.1). The volumetric response here is more characteristic of a loose sand. The model predicts some loss of dilatancy, however, this is not enough to match the experimental results. The experimental dilatancy decreases with an increasing confining stress, the model predicts behaviour opposite to this.

The next series of tests compares the effect of changing the fibre concentration (Figure 8.3). In these tests, the confining stress remains constant at 300 kN/m². An increase in fibre concentration increases the shear strength, this is captured well in the model predictions. Again, the experimental results show that the presence of the fibres reduces the initial stiffness of the composite, this is most prevalent in the $w_f = 0.9\%$ test. This is captured in the model predictions but to a lesser extent.

The experimental volumetric results show that the fibres cause the soil to only undergo compression during shearing. The mechanism for this may be that the sand particles are held further apart due to the presence of the fibres. The model does predict some decrease in dilatancy, but the effect is not pronounced enough to match the experimental results.

8.3 Triaxial fibre type study

The next study investigates the different behaviours with use of different fibre types. Loksand and Durus S400 fibres are compared directly at the same confining stress and fibre concentration (Figure 8.4). The interface parameters are calculated from the fibre pullout data (Section 6.3.2). The elastic interface gradient k_s is calculated from the initial gradient of each pullout curve; it was found that this gradient was not dependent on the confining stress, therefore a constant value is used in the model. The bond strength parameter κ_b is dependent on the confining stress and is

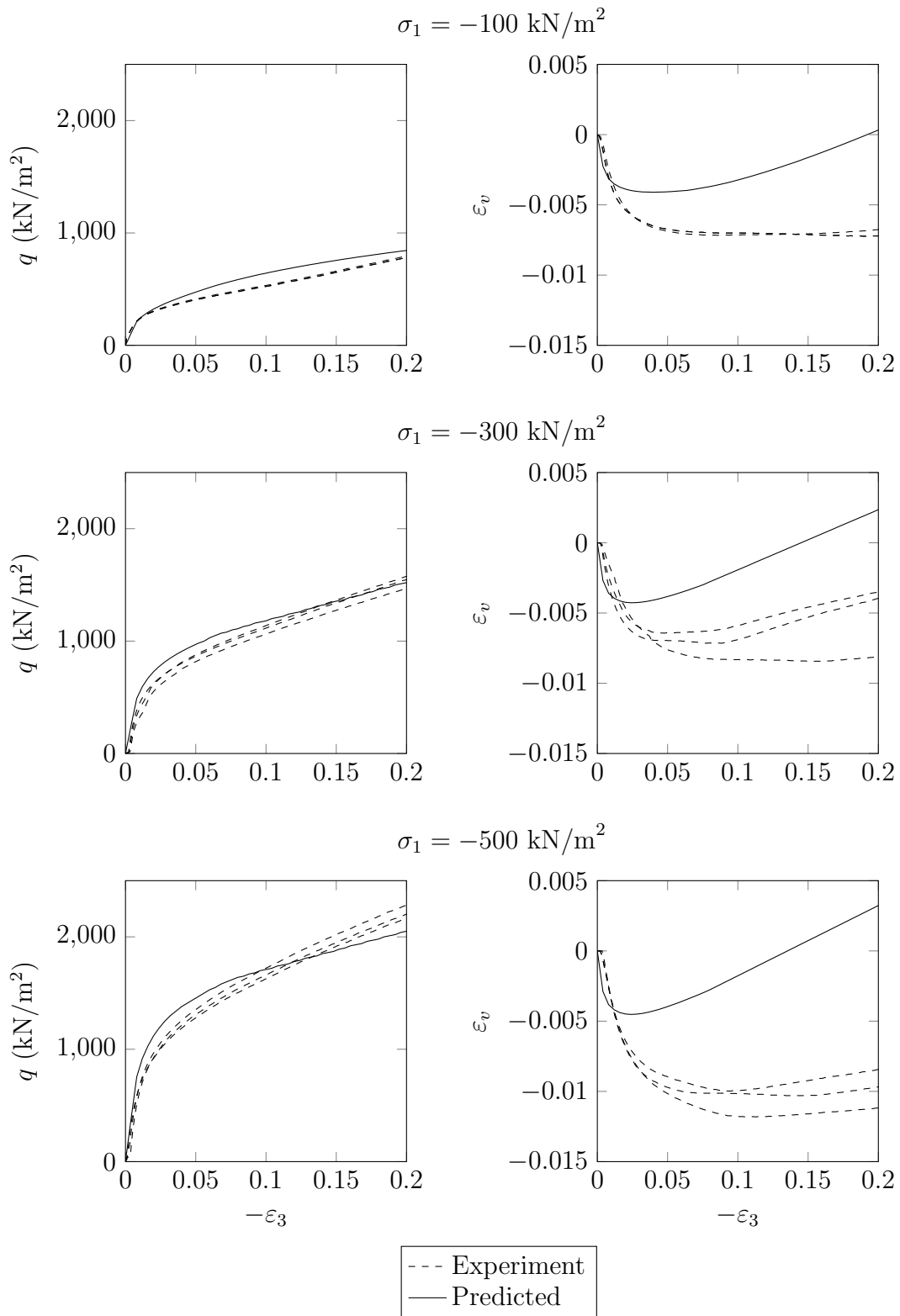


Figure 8.2: Experimental and predicted triaxial test results on Leighton Buzzard sand (S2) reinforced with $w_f = 0.3\%$ Loksand fibres

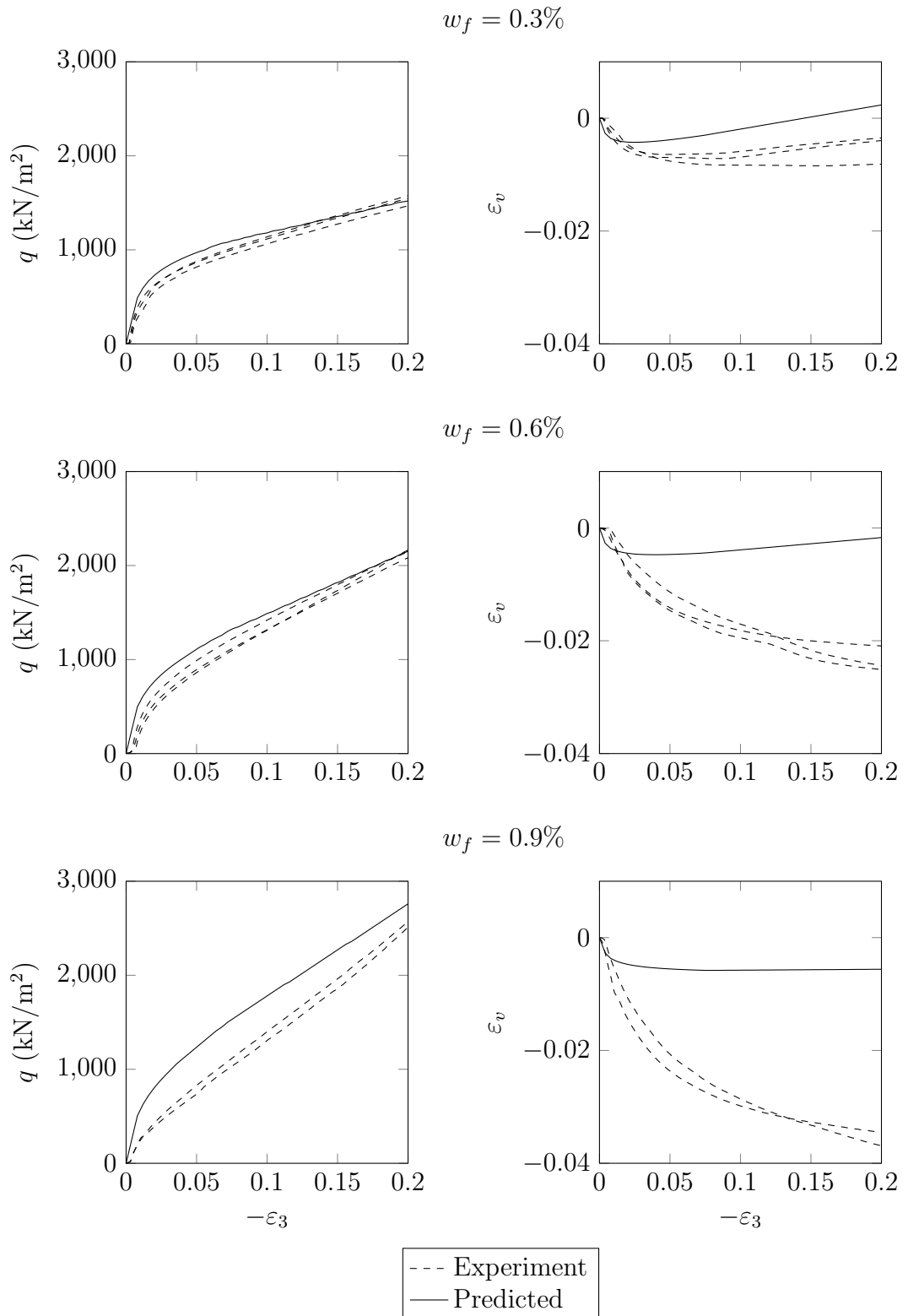


Figure 8.3: Experimental and predicted triaxial test results at 300 kN/m^2 confining stress, on Leighton Buzzard sand (S2) reinforced with different concentrations of Loksand fibres

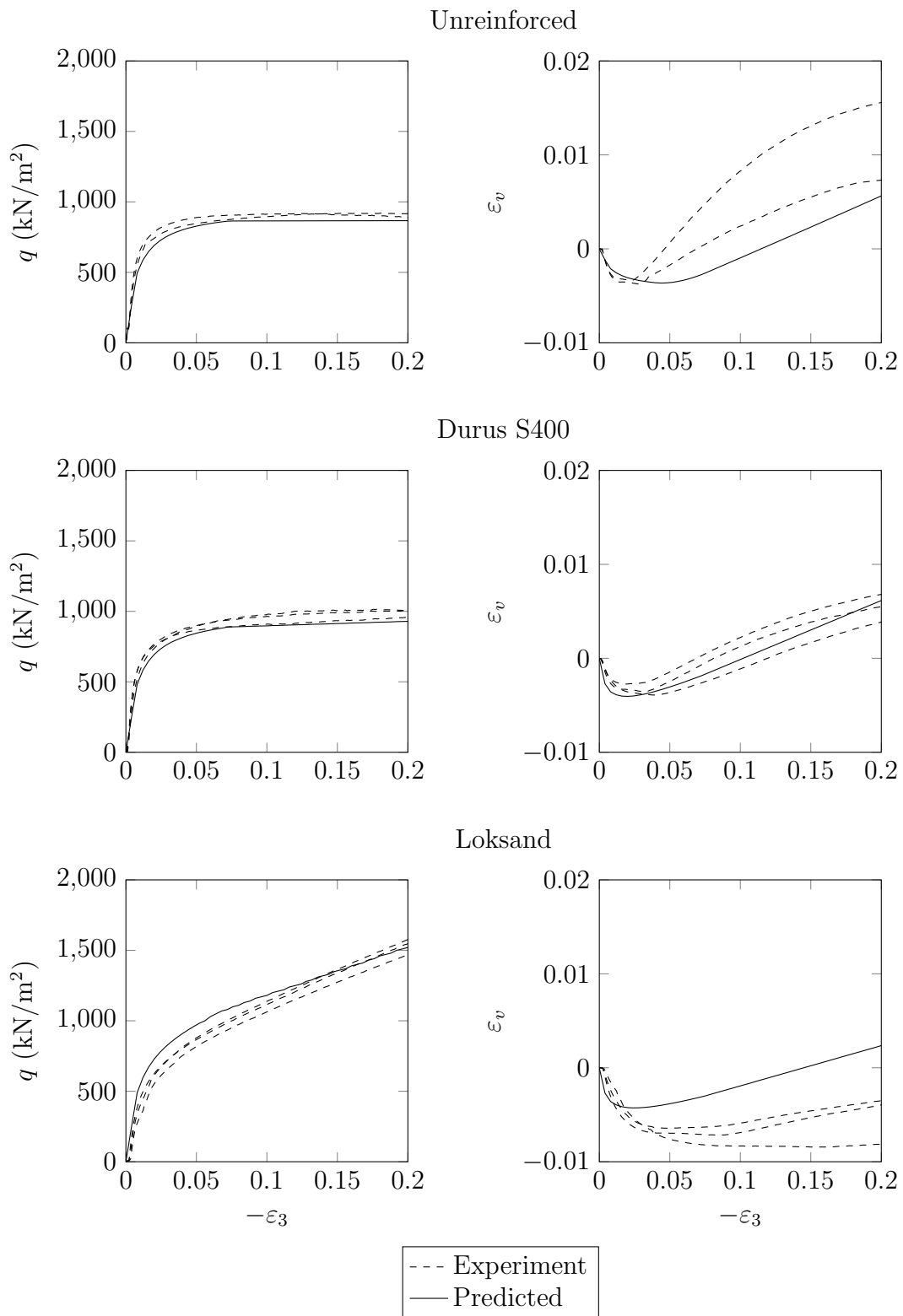


Figure 8.4: Experimental and predicted triaxial test results at 300 kN/m² confining stress, on Leighton Buzzard sand (S2) unreinforced, and reinforced with $w_f = 0.3\%$ concentration of different fibre types, samples prepared using the layering method (D1)

calculated from the peak pullout value. The residual strength must be estimated, as the boundary conditions for the pullout test are different from the *in situ* fibre behaviour. The value of κ_b was chosen to be approximately 20% higher than that of the calibrated Loksand parameter, this value is assumed due to the increased roughness of the Durus fibres.

The experimental data shows that the Durus fibres do not increase the shear strength of the soil significantly, a shear stress increase of approximately 8% was observed. This is reflected in the model results with a nominal shear strength increase predicted. The Loksand fibres appear to increase the shear stress indefinitely within the strain range investigated, this is also predicted with the model.

Presence of either fibre type decreases the amount of dilatancy in the soil. The Loksand fibre decreased the dilatancy the most. This is captured in the model predictions, however, like the other volumetric data presented so far, the actual paths are not predicted closely. The Durus volumetric path is modelled very closely, however this may be a coincidence, as it is the only reinforced volumetric path which is predicted closely.

8.4 Triaxial fibre length study

The next part of the study investigates the effect of fibre length on soils. Conplus fibres are used here, and triaxial results for different lengths of Conplus fibres are shown in Figures 8.5 to 8.7. This series of triaxial tests are performed on the same sand, but samples were prepared to a different void ratio. The properties for this sand are shown in Table 4.1 with the identification LLS.

The experimental data shows that the Conplus fibres do not significantly increase the shear strength of the sand, nor do they significantly alter the volumetric behaviour. Most of the shear curves show a loss in strength after initial failure, this is not captured with the HS model as it does not incorporate shear softening.

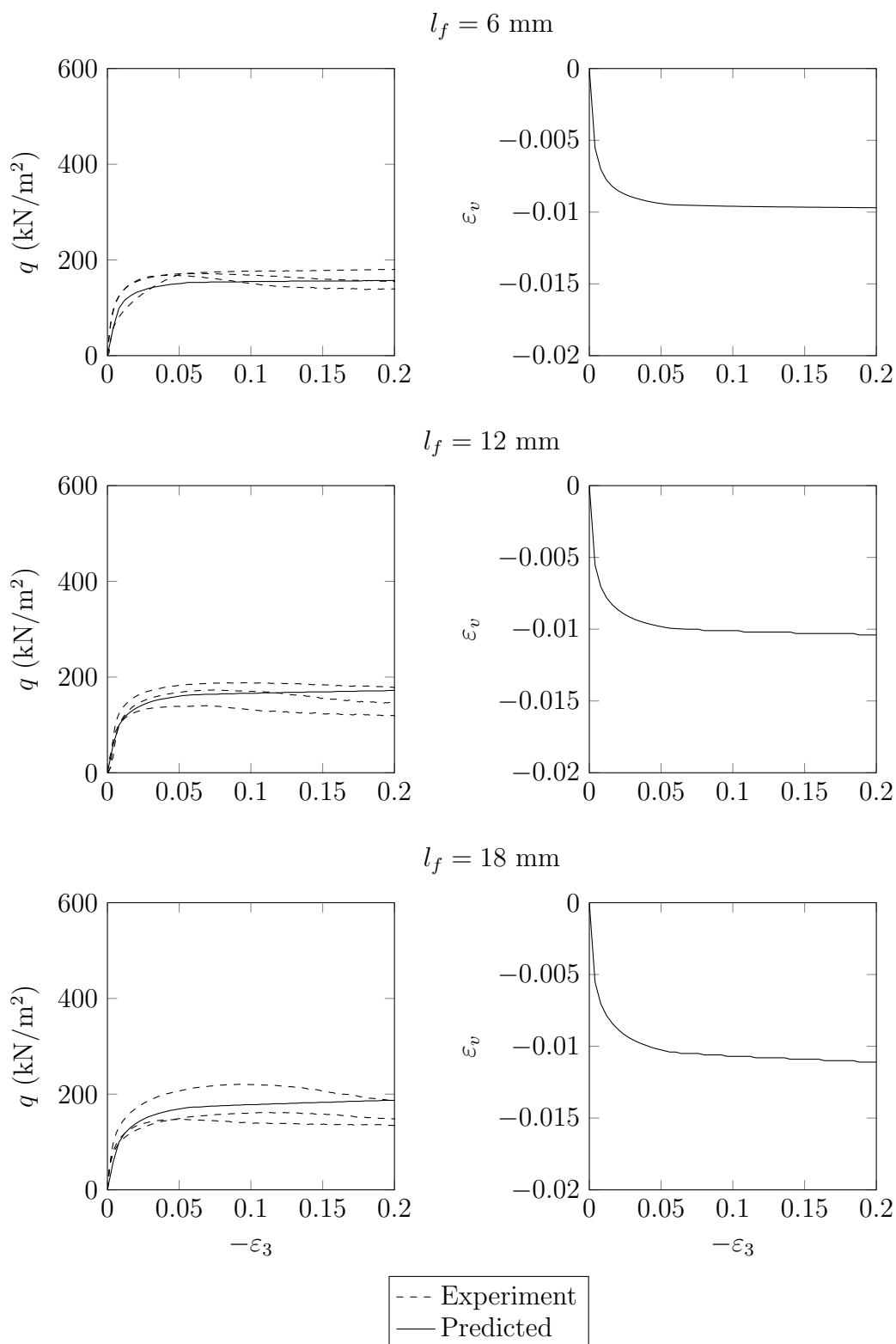


Figure 8.5: Experimental and predicted triaxial test results at 200 kN/m^2 confining stress, on Loose Leighton Buzzard sand (LLS) reinforced with different lengths of Conplus fibres (F2, F3, F4), samples prepared using the stirring method (D2)

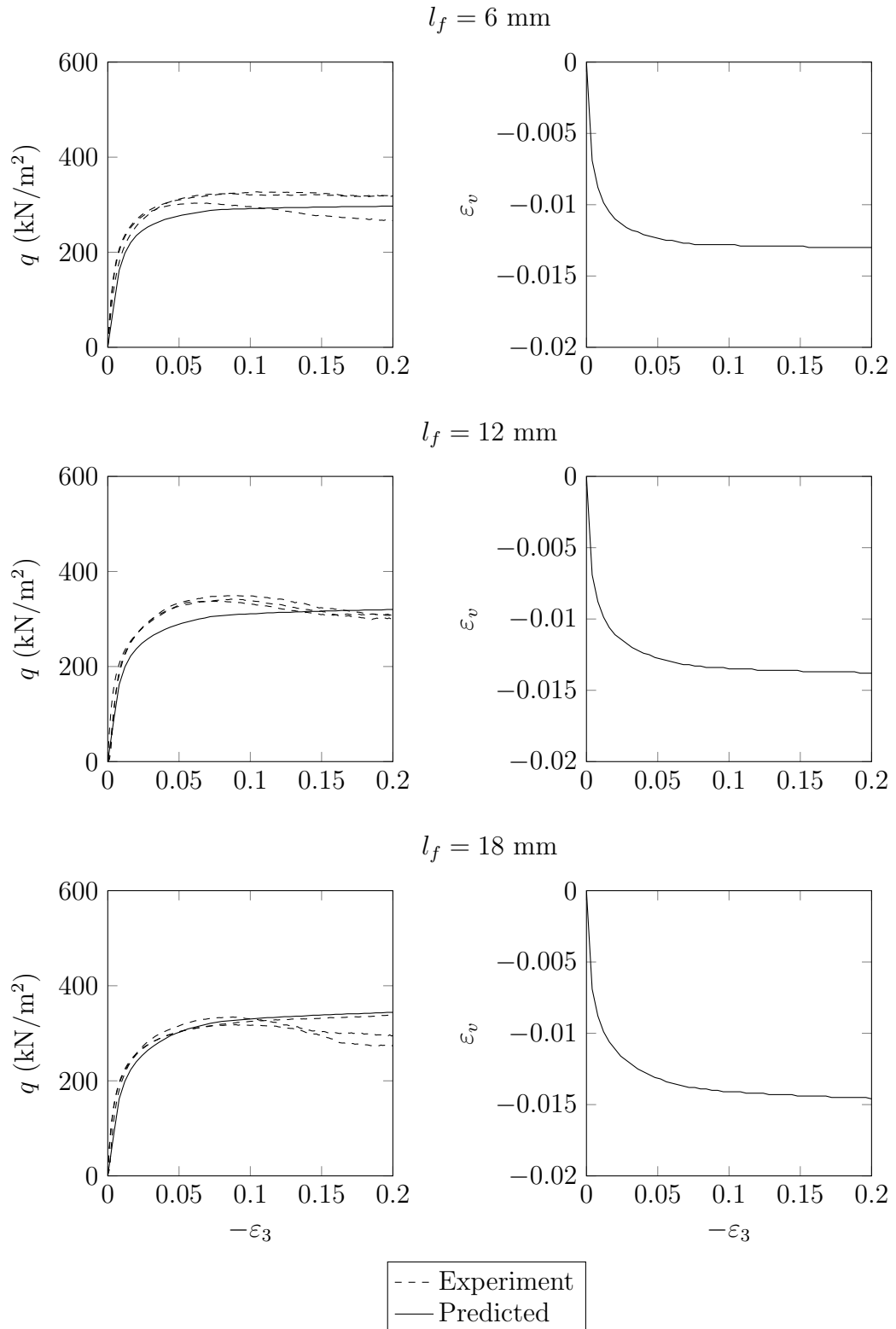


Figure 8.6: Experimental and predicted triaxial test results at 400 kN/m^2 confining stress, on Loose Leighton Buzzard sand (LLS) reinforced with different lengths of Conplus fibres (F2, F3, F4), samples prepared using the stirring method (D2)

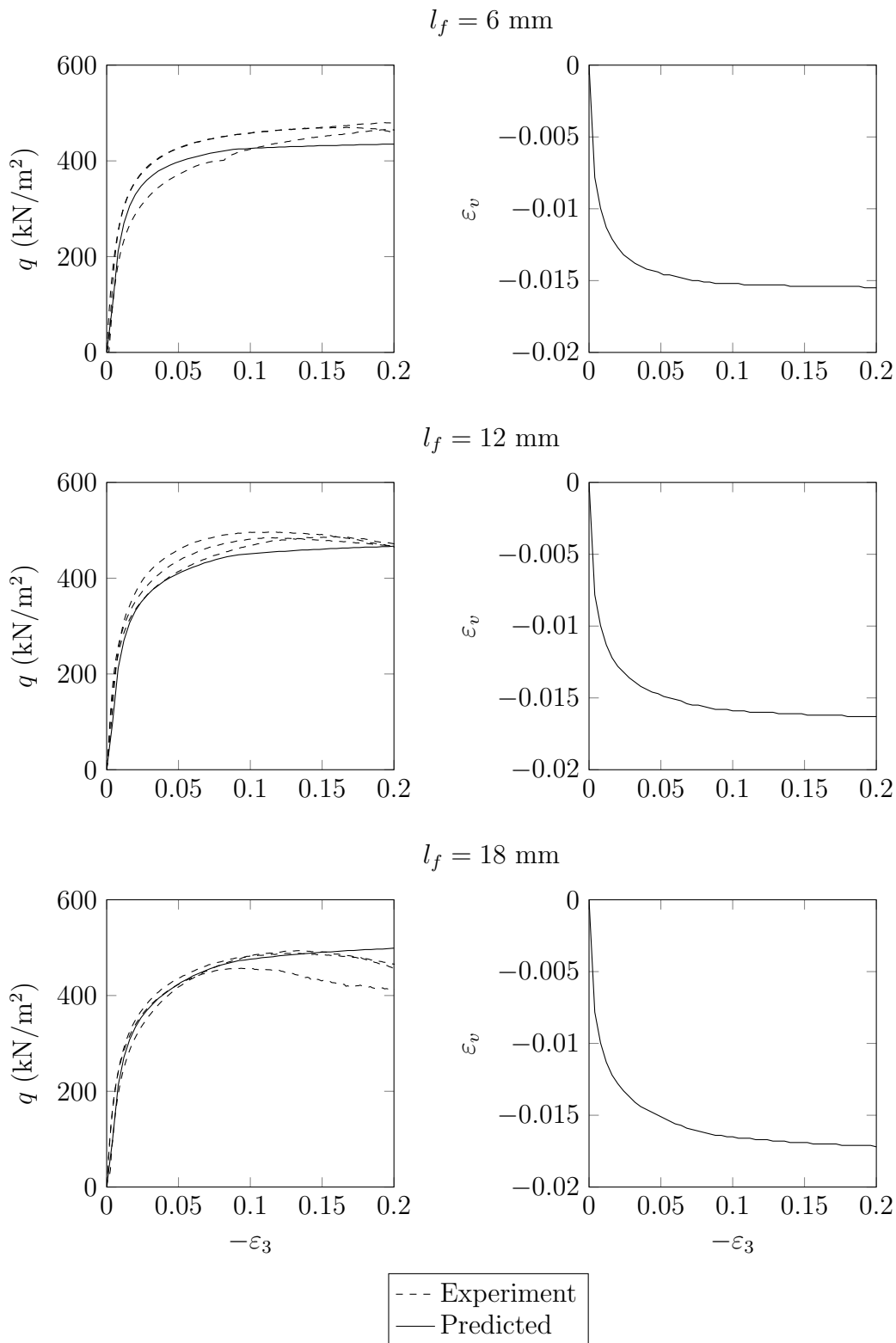


Figure 8.7: Experimental and predicted triaxial test results at 600 kN/m^2 confining stress, on Loose Leighton Buzzard sand (LLS) reinforced with different lengths of Conplus fibres (F2, F3, F4), samples prepared using the stirring method (D2)

A very small strength increase of between 5% and 20% was observed in the experimental results between the 18 mm and 6 mm fibres. A shear strength increase of 14% to 17% was predicted with the proposed model. In general, the shear predictions are within the range of experimental variation.

The volumetric response of the soil was not measured for this series of tests, therefore it is impossible to comment on the accuracy of the predicted volumetric behaviour. With each confining stress, the increase in fibre length increases the amount of compaction in the soil. Between 6 mm and 18 mm fibres, the volumetric strain at the end of the studied strain range ($\varepsilon_3 = -0.2$) is increased by 14.4% at 200 kN/m², 12.3% at 400 kN/m², and 11.0% at 600 kN/m² confining stress.

8.5 Triaxial sample preparation study

The final part of the triaxial study investigates the influence of the sample preparation method. In Section 7.3.2, the orientation parameters for three preparation methods were determined. These parameters are used in the predictions of triaxial tests, which used samples prepared using these methods. The orientation parameters for each preparation method are shown in Table 8.2.

Results from each preparation method are compared in Figures 8.8 to 8.10. 12 mm Conplus fibres are prepared using each method, and tested at different confining stresses. For each shear curve, the layered preparation produced the strongest soil-fibre composites, and the shaking method produced the weakest. The shear strength increase observed was nominal; between 7.5% and 27.3% (for tests undertaken at 600 kN/m² and 200 kN/m² confining stress respectively). The soil-fibre model predicted shear strength increases between 15.0% and 20.0%.

The predicted shear curves are mostly within each range of experimental repeatability for each test. Again, experimental volumetric data is not available for this set of tests. The model predictions show that the layered method increased the amount of compaction in the soil the most; following patterns from the previous tests, this,

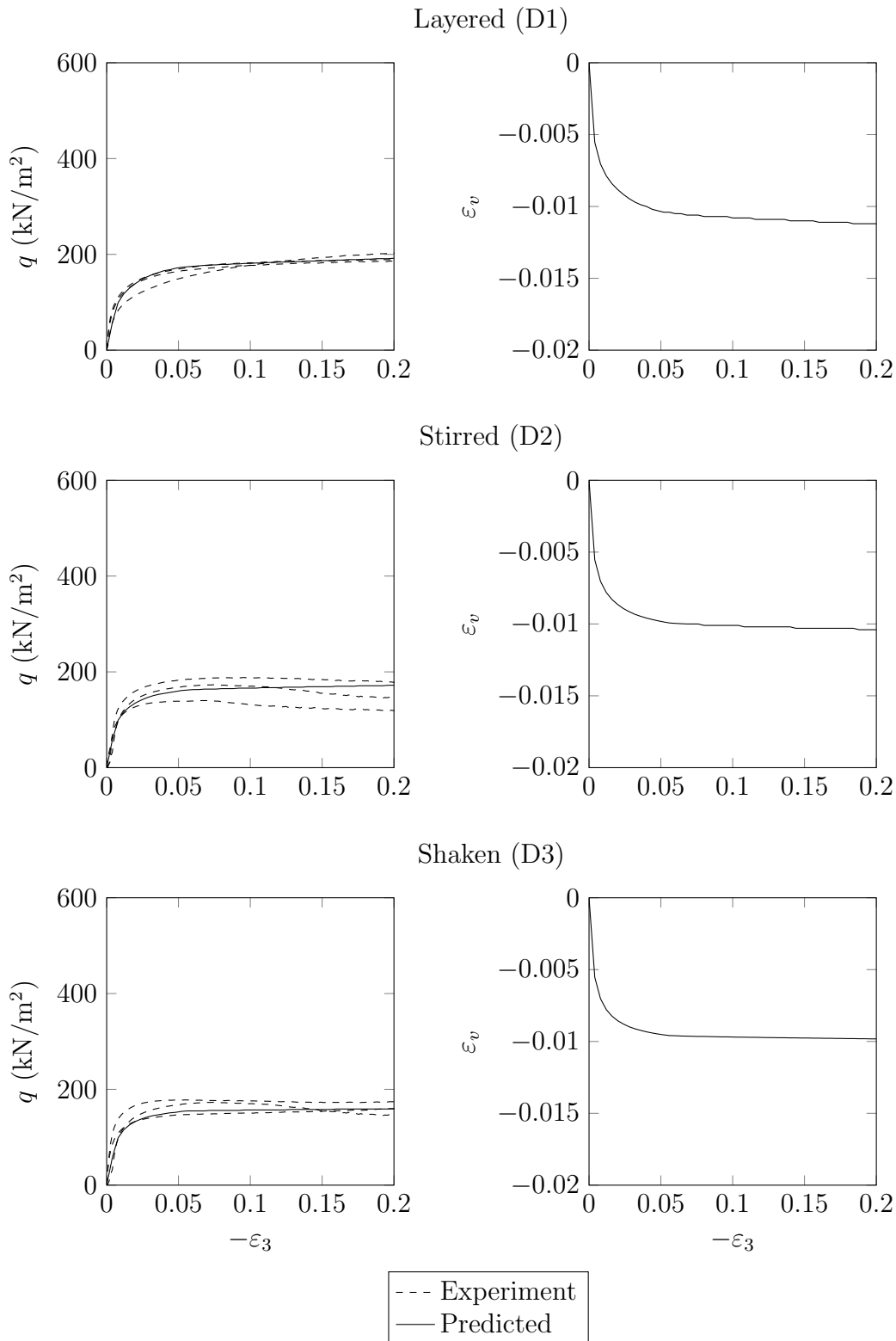


Figure 8.8: Experimental and predicted triaxial test results at 200 kN/m² confining stress, on Loose Leighton Buzzard sand (LLS) reinforced with 12 mm Conplus fibres (F3), samples prepared using the different methods (D1, D2, D3)

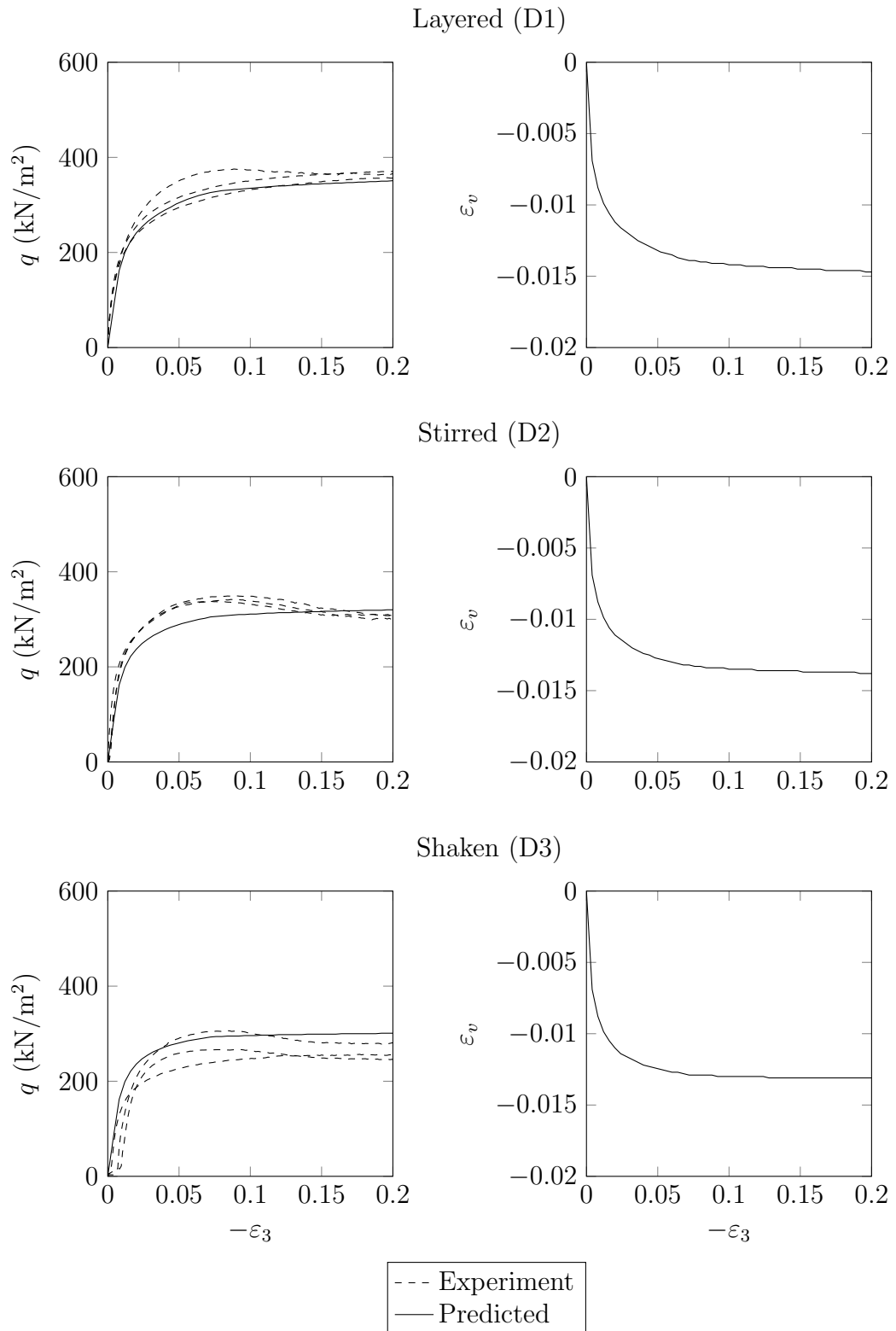


Figure 8.9: Experimental and predicted triaxial test results at 400 kN/m^2 confining stress, on Loose Leighton Buzzard sand (LLS) reinforced with 12 mm Conplus fibres (F3), samples prepared using the different methods (D1, D2, D3)

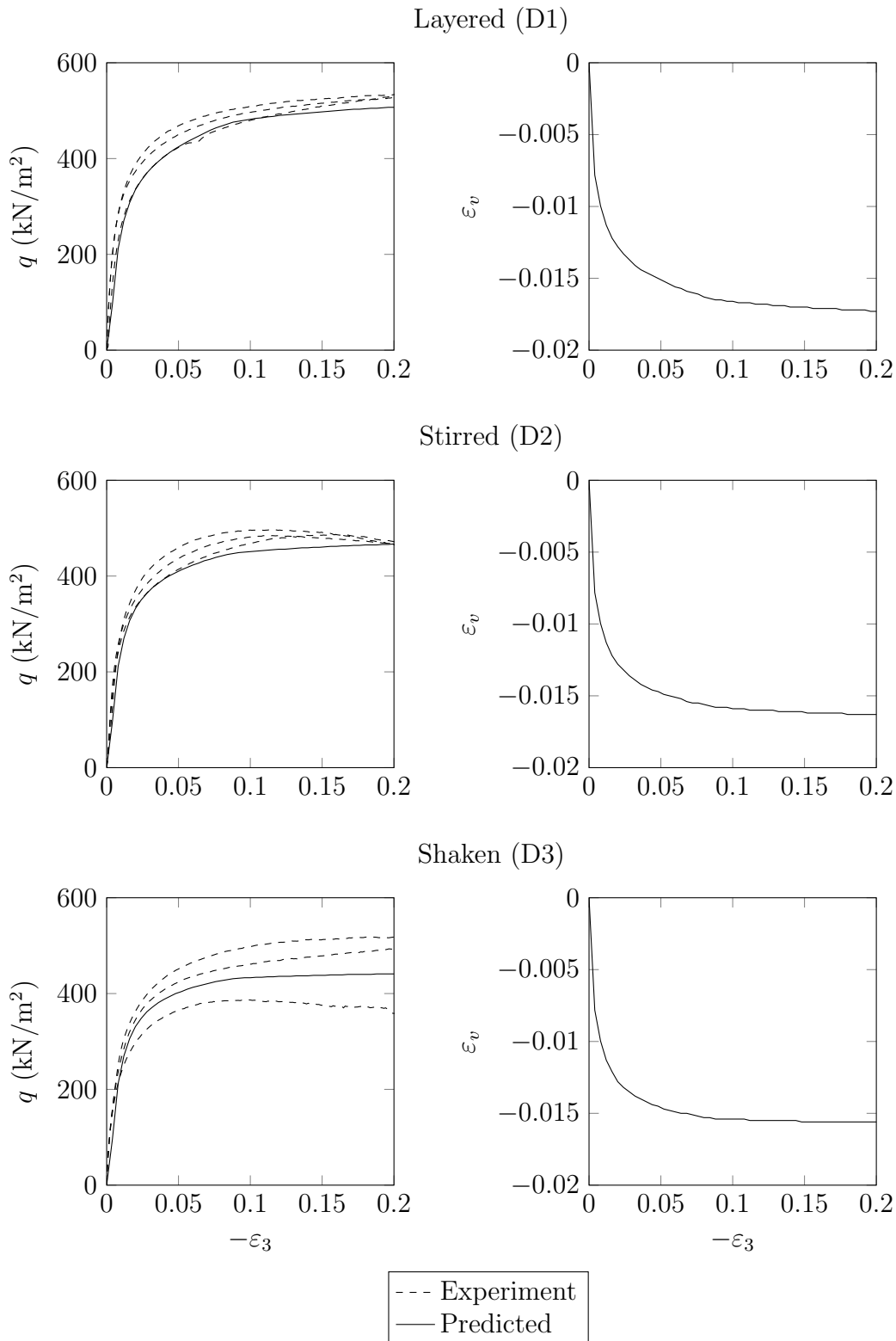


Figure 8.10: Experimental and predicted triaxial test results at 600 kN/m² confining stress, on Loose Leighton Buzzard sand (LLS) reinforced with 12 mm Conplus fibres (F3), samples prepared using the different methods (D1, D2, D3)

along with the shear response, indicates that the layered method reinforces the soil the most effectively.

Concluding remarks

In summary, the first thing to note from the experimental results is that the Durus and Conplus fibres do not significantly improve the strength of soils, in contrast to the Loksand fibres, which are far more effective. This is predicted well in the proposed soil-fibre model. The cause of this is the relation between the sand particle size and the fibre geometry. The Conplus fibres are too thin and short to sufficiently grip to the sand particles. These fibres are designed for use in concrete, which offers different bonding conditions to the granular soil. The Durus S400 fibres also do not significantly improve the strength of the soil. These fibres are much larger, with a diameter similar to the mean particle size of the sand. For a given fibre concentration, the Durus fibres as a whole have a much smaller surface area than the smaller fibre types. The roughness of the Durus fibres provides a surface with a higher friction, which makes up slightly for the lack of surface area.

The Conplus fibres, which only provided nominal strength increase, were more effective at the longer lengths; this is also captured in the model. The post-peak failure behaviour for the Conplus tests is not captured in the model because the base soil model does not incorporate shear softening.

Overall, the volumetric behaviour is not predicted well by the model. Presence of the fibres significantly reduces soil dilatancy, and increases compaction. The model does repeat this trend, however to a much smaller magnitude. It is possible that there is some other mechanism which is not currently captured in the model. One such explanation is that the presence of a fibre restricts the ability of the sand particles to interlock in the same way that they would with no fibre. On a local scale, this would mean that the sand is looser near each fibre. On a macroscopic scale, the loosening of sand around each fibre could sum to a significant global effect,

creating the reduction in dilatancy observed in the experimental results.

Another possible cause for this is one of the assumptions used in the formulation of the model. This is that each fibre is assumed to be independent, and strains are not transferred between fibres. Results from the finite element study indicated that the radius of influence of the fibre was higher than the typical spacing between fibres as observed in prepared reinforced samples. Therefore, it may be possible that this assumption is creating some inaccuracy in the model.

Chapter 9

Conclusions

This thesis is divided into two main areas of study. The first was to produce an improved implementation of the hardening soil model, the second was to produce a suitable constitutive model for the analysis of fibre-reinforced soils.

A literature review of one specific soil model was conducted, this was the hardening soil model, which has had developments and contributions from several authors. The main features and material parameters of the model were explored as well the available optional model components.

Initial research and implementation of the HS model indicated several areas for potential improvement. The first and most major issue identified with the original HS model was the formulation of the hardening shear yield surface. In this formulation of the model (Schanz et al., 1999), and in the updated HS-smooth model (Benz, 2007), the position of the shear surface is related to both the current shear stress, and the state of the hardening variables. Therefore, for a given set of hardening variables, the shear surface is dependent on the stress state, and not fixed.

This issue was addressed in the formulation described in Chapter 3 and involved removing the stress dependency from the yield surface position. The modified yield surface is akin to a more typical cone surface, with a non-linear hardening rule. The

formulation of this surface was derived from the same principles as both previous HS models. The hardening rule was based on Kondner's hyperbola (Kondner and Zelasko, 1963), as implemented in the Duncan-Chang model (Duncan and Chang, 1970).

The second major change to the HS model was the return mapping scheme. All versions of the HS model have used a form of the closest point projection algorithm, which is a type of backward Euler method. The implementation in this study includes residuals of the hardening parameters (or state variables) in the algorithm, and in the convergence criteria; resulting in a robust method.

The third change to the model was the use of a tensile yield surface based on the mean stress only. The previous versions of the HS model both used three Rankine surfaces; which is well suited for these models as they are derived in principal stress space. The model proposed here is derived in general stress space, avoiding the need to perform axis transformations.

It was shown in Sections 4.1 and 4.2 that the new model is able to produce very similar results to the two previous implementations of the HS model (Schanz et al., 1999; Benz, 2007). This is true for both simple laboratory tests, and more complex field simulations.

Due to differences in the formulations of each model, the auxiliary parameters α , K_s/K_c , E_i^{ref} required for each model are different. These auxiliary parameters are not entered by the user, but are calibrated to given values of K_0^{NC} , E_{oed}^{ref} , and E_{50}^{ref} , the procedure for the calculation of these parameters was clarified.

Mesh dependency and step size dependency were also investigated with the HS-LC model. It was shown that results generated using the HS-LC model were not heavily altered by increasing or decreasing the mesh density. Step size dependency can be an issue with the HS-LC model, this is because some of the stress dependent variables are based on the last converged stress, and increasing the step size causes the solution to drift. This issue was addressed by adding an option to allow these

variables to update using a modified Newton-Raphson approach. It is recommended that a step size convergence study and a mesh convergence study are conducted with use of the HS-LC model, particularly when performing design work.

A literature review was undertaken covering the current state of soil-fibre computational modelling. Several models were discussed, including those which model the behaviour of a single fibre, and those which may be used to model soil reinforced with randomly distributed fibres. The main components of each model were explored along with the fundamental mechanisms behind them. The accuracy of each model was discussed, based on results published by each of the respective authors.

An experimental study was conducted to determine the behaviour of soil-fibre composites. This study consisted of a range of tests, including triaxial compression tests, fibre pullout tests, and sample dissection. Within the series of triaxial tests, the effect of changing the fibre length, type, concentration and preparation method were studied. Each of these effects are detailed below:

- An increase in fibre content w_f leads to an increase in strength
- An increase in fibre length l_f leads to an increase in strength
- Sample preparation methods which cause a higher portion of fibres to lay horizontal produce the strongest composites in triaxial tests

It was also found that the radius of the fibre had a significant impact on the composite strength, where too small a radius would fail to bind with the soil particles, and too large a radius would not create enough contact surfaces between the soil particles and fibre. In summary, it appears that there is an optimum fibre radius, for each particular sand, which is effective in reinforcing soil.

A constitutive model was developed to predict the behaviour of soil fibre composites. This model comprised of two levels: the first was to predict the behaviour of a single fibre surrounded by soil, and is driven by strains in the soil. The second

takes the behaviour of the single fibre, and integrates this effect over each orientation to predict the behaviour of soil reinforced with randomly distributed fibres.

The micromechanical model of the single fibre used theory from the shear lag model (Cox, 1952) and was developed further to take into account fibre debonding. Parameters used in this model allowed control of bond stiffness, bond strength, fibre geometry and fibre material. These parameters all have physical meaning, however the bond strength and stiffness are difficult to measure directly as they require a pullout test to be conducted. Instead, these parameters can be calibrated from triaxial tests with the model in its globally integrated form.

The fully integrated model is used to predict the behaviour of fibres randomly distributed in the soil. This was performed through a statistical integration method, as described by Maher and Gray (1990). Computationally, this integration was performed by a numerical approach described by Bažant and Oh (1986). To take into account the effect of different preparation methods, an orientation distribution function was used and included in the global integration.

Results from the proposed soil-fibre model were compared against the experimental results and it was found that the model was reasonably accurate at replicating shear stresses in the triaxial tests. The volumetric behaviour was not fully captured, as dilatancy was not reduced enough by the model. Clearly, a better understanding of soil-fibre composites is required to sufficiently model this behaviour.

9.1 Future work

This thesis has presented two constitutive models for predicting the behaviour of soil and of fibre-reinforced soil. There are several aspects in both models which may be subject to future improvement.

One contribution previously made to the HS model was the development of the HS-small model by Benz (2007); Benz et al. (2009). This model takes into

account the effect of increased stiffness observed in soils under small strains. The HS-LC model currently does not include this advanced feature. The addition of this behaviour to the model requires the modification of the elastic stiffness matrix, where the Young modulus is modified according to the small-strain model by Hardin and Drnevich (1972). In order to implement this change, the hardening rules, and CPP algorithms would also need to be modified to preserve the quadratic rate of convergence of the global Newton-Raphson solution method.

The auxiliary parameters α , K_s/K_c , and E_i^{ref} are currently calculated through calibration of triaxial and oedometer simulations. This process can be time consuming and sometimes very difficult to match predicted results to the calibration parameters K_0^{NC} , E_{oed}^{ref} , and E_{50}^{ref} . Instead of performing this calibration directly it may be possible to use methods such as multivariate regression, or machine learning methods to calculate the auxiliary parameters based on a series of training data obtained from the direct calibration. Such methods would calculate the auxiliary parameters quickly, however at the expense of obtaining the training data.

One of the areas which should be addressed with the fibre model is the prediction of volumetric strains. The model under-predicted the reduction of dilatancy due to the presence of fibres. Two potential explanations for this issue were proposed. One remedy for this issue may be to include some empirical relationship which relates the fibre content to the dilatancy angle used in the soil fraction of the constitutive model. However, in order to gain a full understanding of the mechanisms involved in this behaviour, it may be necessary to investigate the effects of a single fibre in sand in more detail than was conducted in this thesis.

Discrete element modelling of the sand and fibre during pullout may give some clues to the cause of this behaviour. It may also be possible to capture this behaviour experimentally, for example, a single fibre could be placed along one side of a transparent box which is then filled with compacted sand. Using high resolution cameras, it may be possible to track the movement of sand particles as the fibre is pulled through the sand.

Bibliography

- Ahmad, F., Bateni, F., and Azmi, M. (2009). Performance evaluation of silty sand reinforced with fibres. *Geotextiles and Geomembranes*, 28(1):93–99.
- Alamshahi, S. and Hataf, N. (2009). Bearing capacity of strip footings on sand slopes reinforced with geogrid and grid-anchor. *Geotextiles and Geomembranes*, 27(3):217–226.
- Altenbach, H., Altenbach, J. W., and Kissing, W. (2004). *Mechanics of composite structural elements*. Springer–Verlag, Berlin, Germany.
- Amini, Y. and Hamidi, A. (2014). Triaxial shear behavior of a cement-treated sand-gravel mixture. *Journal of Rock Mechanics and Geotechnical Engineering*, 6(5):455–465.
- Aveston, J. and Kelly, A. (1973). Theory of multiple fracture of fibrous composites. *Journal of Materials Science*, 8(3):352–362.
- Bardet, J. P. (1990). Lode dependences for isotropic pressure-sensitive elastoplastic materials. *Journal of Applied Mechanics*, 57(3):498–506.
- Bažant, Z. P. and Oh, B. H. (1986). Efficient numerical integration on the surface of a sphere. *Journal of Applied Mathematics and Mechanics*, 66(1):37–49.
- Benz, T. (2007). *Small-strain stiffness of soils and its numerical consequences*. PhD thesis, Universität Stuttgart, Institut für Geotechnik.
- Benz, T., Vermeer, P. A., and Schwab, R. (2009). A small-strain overlay model. *International journal for numerical and analytical methods in geomechanics*, 33(1):25–44.
- Benz, T., Wehnert, M., and Vermeer, P. A. (2008). A Lode angle dependent formulation of the hardening soil model. In *Proceedings of the 12th International Conference of International Association for Computer Methods and Advances in Geomechanics*, pages 653–660.

- Bergado, D. T., Ruenkraitersa, T., Taesiri, Y., and Balasubramaniam, A. S. (1999). Deep soil mixing used to reduce embankment settlement. In *Proceedings of the Institution of Civil Engineers - Ground Improvement*, volume 3, pages 145–162. Thomas Telford Ltd.
- Bower, T. A. and Duxbury, P. (2014). *Duncan Chang soil model - software development report*. LUSAS.
- Bower, T. A., Jefferson, A. D., Cleall, P. J., and Lyons, P. (2016a). A micro-mechanics based soil-fibre composite model for use with finite element analysis. In *Proceedings of the 24th UK Conference of the Association for Computational Mechanics in Engineering*, pages 146–149.
- Bower, T. A., Jefferson, A. D., Cleall, P. J., and Lyons, P. (2016b). Modelling soil-fibre composite behaviour using a micromechanical approach. In *Proceedings of the 7th European Congress on Computational Methods in Applied Sciences and Engineering*.
- Brighenti, R. (2004). A mechanical model for fiber reinforced composite materials with elasto-plastic matrix and interface debonding. *Computational materials science*, 29(4):475–493.
- British Standards Institution (1990). BS 1377-8:1990 – methods of test for soils for civil engineering purposes. shear strength tests (effective stress). Standard, British Standards Institution, London.
- British Standards Institution (2015). BS 5930:2015 – code of practice for ground investigations. Standard, British Standards Institution, London.
- Cai, Y., Shi, B., Ng, C. W. W., and Tang, C. (2006). Effect of polypropylene fibre and lime admixture on engineering properties of clayey soil. *Engineering Geology*, 87(3):230–240.
- Chatzopoulos, S. (2015). Soil reinforced with discrete polypropylene fibers. Master’s thesis, Cardiff University, Cardiff.

- Consoli, N. C., Prietto, P. D. M., and Ulbrich, L. A. (1998). Influence of fiber and cement addition on behavior of sandy soil. *Journal of Geotechnical and Geoenvironmental Engineering*, 124(12):1211–1214.
- Cotecchia, F. and Chandler, R. J. (2000). A general framework for the mechanical behaviour of clays. *Géotechnique*, 50(4):431–447.
- Cox, H. (1952). The elasticity and strength of paper and other fibrous materials. *British Journal of Applied Physics*, 3(3):72–79.
- Craig, R. F. (2004). *Craig's soil mechanics*. Spon Press, London, 7th edition.
- Das, B. M. (2011). *Geotechnical engineering handbook*. J Ross Publishing Inc, Fort Lauderdale, FL, USA.
- Diambra, A. and Ibraim, E. (2015). Fibre-reinforced sand: interaction at the fibre and grain scale. *Géotechnique*, 65(4):296–308.
- Diambra, A., Ibraim, E., Muir Wood, D., and Russell, A. R. (2010). Fibre reinforced sands: Experiments and modelling. *Geotextiles and Geomembranes*, 28(3):238–250.
- Diambra, A., Ibraim, E., Russell, A., and Muir Wood, D. (2013). Fibre reinforced sands: from experiments to modelling and beyond. *International Journal for Numerical and Analytical Methods in Geomechanics*, 37(15):2427–2455.
- Diambra, A., Russell, A. R., Ibraim, E., and Muir Wood, D. (2007). Determination of fibre orientation distribution in reinforced sands. *Géotechnique*, 57(7):623–628.
- Drucker, D. C., Prager, W., and Greenberg, H. T. (1952). Extended limit design theorems for continuous media. *Quarterly of Applied Mathematics*, 9(4):381–389.
- Dumbleton, M. J. (1981). The british soil classification system for engineering purposes: its development and relation to other comparable systems. Technical Report 1030, Transport and Road Research Laboratory.
- Duncan, J. M. and Chang, C. Y. (1970). Nonlinear analysis of stress and strain in soils. *Journal of the Soil Mechanics and Foundations Division*, 96(5):1629–1653.

- Estabragh, A. R., Bordbar, A. T., and Javadi, A. A. (2011). Mechanical behavior of a clay soil reinforced with nylon fibers. *Geotechnical and Geological Engineering*, 29(5):899–908.
- Estabragh, A. R., Soltannajad, K., and Javadi, A. A. (2014). Improving piping resistance using randomly distributed fibers. *Geotextiles and Geomembranes*, 42(1):15–24.
- Gajo, A. and Muir Wood, D. (1999). Severn–trent sand: a kinematic-hardening constitutive model: the q–p formulation. *Géotechnique*, 49(5):595–614.
- Gray, D. H. and Ohashi, H. (1983). Mechanics of fiber reinforcement in sand. *Journal of Geotechnical Engineering*, 109(3):335–353.
- Gunzburger, M. D. (2012). *Finite element methods for viscous incompressible flows: a guide to theory, practice, and algorithms*. Elsevier, San Diego, CA, USA.
- Harbottle, M. J., Lam, M. T., Botusharova, S., and Gardner, D. R. (2014). Self-healing soil: Biomimetic engineering of geotechnical structures to respond to damage. In *Proceedings of the 7th International Congress on Environmental Geotechnics*, pages 1121–1128. Engineers Australia.
- Hardin, B. O. and Drnevich, V. P. (1972). Shear modulus and damping in soils: Design equations and curves. *Proceedings of the American Society of Civil Engineers: Journal of Soil Mechanics & Foundations Division*, 98(SM7):667–692.
- Hataf, N. and Rahimi, M. M. (2006). Experimental investigation of bearing capacity of sand reinforced with randomly distributed tire shreds. *Construction and Building Materials*, 20(10):910 – 916.
- Hejazi, S. M., Sheikhzadeh, M., Abtahi, S. M., and Zadhoush, A. (2012). A simple review of soil reinforcement by using natural and synthetic fibers. *Construction and Building Materials*, 30:100–116.
- Huang, J. and Griffiths, D. V. (2009). Return mapping algorithms and stress pre-

- dictors for failure analysis in geomechanics. *Journal of Engineering Mechanics*, 135(4):276–284.
- Huang, Y. (1967). Stresses and displacements in nonlinear soil media. *Proceedings of the American Society of Civil Engineers: Journal of Soil Mechanics & Foundations Division*, 94(1):1–20.
- Huebner, K. H., Dewhirst, D. L., Smith, D. E., and Byrom, T. G. (2001). *The Finite Element Method for Engineers*. John Wiley & Sons Ltd, New York, NY, USA, 4th edition.
- Hull, D. and Clyne, T. W. (1996). *An introduction to composite materials*. Cambridge university press, Cambridge.
- Ibraim, E., Diambra, A., Russell, A. R., and Muir Wood, D. (2012). Assessment of laboratory sample preparation for fibre reinforced sands. *Geotextiles and Geomembranes*, 34:69–79.
- Ineos (2014). *Typical engineering properties of polypropylene*. League City, TX, USA.
- Ingold, T. S. (1994). *Geotextiles and geomembranes handbook*. Elsevier Advanced Technology, Oxford.
- Jaky, J. (1948). Pressure in silos. In *Proceedings of the 2nd International Conference on Soil Mechanics and Foundation Engineering*, volume 1, pages 103–107. Harvard University.
- Janbu, N. (1963). Soil compressibility as determined by oedometer and triaxial tests. In *Proceedings of the European Conference on Soil Mechanics and Foundation Engineering*, volume 1, pages 19–25.
- Jewell, R. A. (1980). *Some factors which influence the shear strength of reinforced sand*. University of Cambridge, Cambridge.

- Jiang, Z.-h. and Zhang, Y. X. (2012). Second development of hardening soil constitutive model in FLAC^{3d}. *Electronic Journal of Geotechnical Engineering*, 17(X):3429–3439.
- Khemissa, M. and Mahamedi, A. (2014). Cement and lime mixture stabilization of an expansive overconsolidated clay. *Applied Clay Science*, 95:104–110.
- Khoury, C. N., Miller, G. A., and Hatami, K. (2010). Unsaturated soil-geotextile interface behaviour. *Geotextiles and Geomembranes*, 29(1):17–28.
- Koerner, R. M. and Koerner, G. R. (2011). The importance of drainage control for geosynthetic reinforced mechanically stabilized earth walls. *Journal of GeoEngineering*, 6(1):3–13.
- Kondner, R. L. and Zelasko, J. S. (1963). A hyperbolic stress-strain formulation for sands. In *2nd Panamerican Conference on Soil Mechanics and Foundation Engineering*, Sao Paulo, Brazil.
- Lade, P. V. (1977). Elasto-plastic stress-strain theory for cohesionless soil with curved yield surfaces. *International Journal of Solids and Structures*, 13(11):1019–1035.
- Lambe, T. W. and Whitman, R. V. (1969). *Soil mechanics*. John Wiley & Sons, New York, NY, USA.
- Latha, G. M. and Somwanshi, A. (2009). Bearing capacity of square footings on geosynthetic reinforced sand. *Geotextiles and Geomembranes*, 27(4):281–294.
- Lewis, R. W., Morgan, K., Thomas, H. R., and Seetharamu, K. (1996). *The finite element method in heat transfer analysis*. John Wiley & Sons, Chichester.
- Li, C. and Zornberg, J. J. G. (2013). Mobilization of reinforcement forces in fiber-reinforced soil. *Journal of Geotechnical and Geoenvironmental Engineering*, 139(1):107–115.
- Li, X. S. and Dafalias, Y. F. (2000). Dilatancy for cohesionless soils. *Géotechnique*, 50(4):449–460.

- Maeda, K. and Ibraim, E. (2008). Dem analysis of 2d fibre-reinforced granular soils. In *Proceedings of the 4th International Symposium on Deformation Characteristic of Geomaterials*, volume 2, pages 623–628, Amsterdam, The Netherlands. Academic Press.
- Maher, M. H. and Gray, D. H. (1990). Static response of sands reinforced with randomly distributed fibers. *Journal of Geotechnical Engineering*, 116(11):1661–1677.
- Maliakal, T. and Thiyyakkandi, S. (2013). Influence of randomly distributed coir fibers on shear strength of clay. *Geotechnical and Geological Engineering*, 31(2):425–433.
- Marcher, T. and Vermeer, P. A. (2001). Macromodelling of softening in non-cohesive soils. In Vermeer, P. A., Ehlers, W., Herrmann, H., and Ramm, E., editors, *Continuous and discontinuous modelling of cohesive-frictional materials*, volume 568. Springer Science & Business Media.
- Marto, A., Oghabi, M., and Eisazadeh, A. (2013). The effect of geogrid reinforcement on bearing capacity properties of soil under static load; a review. *The Electronic Journal of Geotechnical Engineering*, 18:1881–1898.
- Matsuoka, H. and Nakai, T. (1974). Stress-deformation and strength characteristics of soil under three different principal stresses. In *Proceedings of Japan Society of Civil Engineers*, volume 9, pages 59–70.
- Matthews, F. L. and Rawlings, R. D. (1999). *Composite materials: engineering and science*. CRC Press, Boca Raton, FL, USA.
- Mayne, P. W., Jones, Jr, J. S., and Dumas, J. C. (1984). Ground response to dynamic compaction. *Journal of Geotechnical Engineering*, 110(6):757–774.
- Michalowski, R. L. (1997). Limit stress for granular composites reinforced with continuous filaments. *Journal of engineering mechanics*, 123(8):852–859.

- Michalowski, R. L. and Čermák, J. (2002). Strength anisotropy of fiber-reinforced sand. *Computers and Geotechnics*, 29(4):279–299.
- Michalowski, R. L. and Čermák, J. (2003). Triaxial compression of sand reinforced with fibers. *Journal of geotechnical and geoenvironmental engineering*, 129(2):125–136.
- Michalowski, R. L. and Zhao, A. (1996). Failure of fiber-reinforced granular soils. *Journal of Geotechnical Engineering*, 122(3):226–234.
- Mitchell, J. K. and Gardner, W. S. (1971). Analysis of load-bearing fills over soft subsoils. *Journal of the Soil Mechanics and Foundations Division*, 97(11):1549–1571.
- Möller, S. C., Vermeer, P. A., and Marcher, T. (2004). NATM-tunnelling in softening stiff clays and weak rocks. In *Numerical Models in Geomechanics: Proceedings of the 9th International Symposium on Numerical Models in Geomechanics*, pages 407–414. Taylor & Francis.
- Muntohar, A. S. (2009). Influence of plastic waste fibers on the strength of lime-rice husk ash stabilized clay soil. *Civil Engineering Dimension*, 11(1):32–40.
- Nakai, T. and Matsuoka, H. (1983). Shear behaviours of sand and clay under three-dimensional stress condition. *Soils and Foundations*, 23(2):26–42.
- Obrzud, R. F. (2010). On the use of the hardening soil small strain model in geotechnical practice. In *Numerics in Geotechnics and Structures*, pages 15–32.
- Owen, D. R. and Hinton, E. (1980). *Finite elements in plasticity*. Pineridge press, Swansea.
- Panteghini, A. and Lagioia, R. (2013). A fully convex reformulation of the original Matsuoka–Nakai failure criterion and its implicit numerically efficient integration algorithm. *International Journal for Numerical and Analytical Methods in Geomechanics*, 38(6):593–614.
- PLAXIS (2016). *Material Models Manual*.

- Rahman, M. M., Mallik, A. K., and Khan, M. A. (2007). Influences of various surface pretreatments on the mechanical and degradable properties of photografted oil palm fibers. *Journal of applied polymer science*, 105(5):3077–3086.
- Reddy, J. N. and Gartling, D. K. (2010). *The finite element method in heat transfer and fluid dynamics*. CRC press, Boca Raton, FL, USA, 3rd edition.
- Roscoe, K. H. and Burland, J. B. (1968). On the generalized stress-strain behaviour of wet clay. *Engineering Plasticity*, pages 535–609.
- Rowe, P. W. (1962). The stress-dilatancy relation for static equilibrium of an assembly of particles in contact. *Proceedings of the Royal Society of London A: Mathematical, Physical and Engineering Sciences*, 269(1339):500–527.
- Sadek, S., Najjar, S. S., and Freiha, F. (2010). Shear strength of fiber-reinforced sands. *Journal of geotechnical and geoenvironmental engineering*, 136(3):490–499.
- Schanz, T., Vermeer, P. A., and Bonnier, P. G. (1999). The hardening soil model: formulation and verification. In *Beyond 2000 in Computational Geotechnics*, pages 281–296, Rotterdam, The Netherlands. Balkema.
- Schofield, A. and Wroth, P. (1968). *Critical state soil mechanics*. McGraw-Hill, Maidenhead.
- Simo, J. C. and Hughes, T. J. R. (2006). Computational inelasticity. In *Interdisciplinary Applied Mathematics*, volume 7. Springer, New York, NY, USA.
- Singh, H. P. and Bagra, M. (2013). Improvement in cbr value of soil reinforced with jute fiber. *International Journal of Innovative Research in Science, Engineering and Technology*, 2(8):3447–3452.
- Sireesh, S., Sitharam, T. G., and Dash, S. K. (2009). Bearing capacity of circular footing on geocell–sand mattress overlying clay bed with void. *Geotextiles and Geomembranes*, 27(2):89–98.

- Sivakumar Babu, G. L., Vasudevan, A. K., and Haldar, S. (2008). Numerical simulation of fiber-reinforced sand behavior. *Geotextiles and Geomembranes*, 26(2):181–188.
- Slocombe, B. C., Bell, A. L., and Baez, J. I. (2000). The densification of granular soils using vibro methods. *Géotechnique*, 50(6):715–725.
- Søreide, O. K. (1990). *Mixed hardening models for frictional soils*. PhD thesis, Norwegian University of Science and Technology, Trondheim, Norway.
- Spagnoli, G., Bellato, D., Doherty, P., and Murphy, G. (2016). Innovative deep-mixing methods for oil & gas applications. In *Proceedings of the 1st International Conference on Energy Geotechnics*, pages 91–98. CRC Press.
- Tafreshi, S. M. and Norouzi, A. (2012). Bearing capacity of a square model footing on sand reinforced with shredded tire—an experimental investigation. *Construction and Building Materials*, 35:547–556.
- Tang, C. S., Shi, B., Gao, W., Chen, F., and Cai, Y. (2007). Strength and mechanical behavior of short polypropylene fiber reinforced and cement stabilized clayey soil. *Geotextiles and Geomembranes*, 25(3):194–202.
- Tang, C. S., Shi, B., and Zhao, L. Z. (2010). Interfacial shear strength of fiber reinforced soil. *Geotextiles and Geomembranes*, 28(1):54–62.
- Terzaghi, K., Peck, R. B., and Mesri, G. (1996). *Soil mechanics in engineering practice*. John Wiley & Sons Ltd, New York, NY, USA, 3rd edition.
- Truty, A. and Obrzud, R. (2015). Improved formulation of the hardening soil model in the context of modeling the undrained behavior of cohesive soils. *Studia Geotechnica et Mechanica*, 37(2):61–68.
- Venkatarama Reddy, B. V. and Latha, M. S. (2014). Influence of soil grading on the characteristics of cement stabilised soil compacts. *Materials and Structures*, 47(10):1633–1645.

- Vermeer, P. A. (1978). A double hardening model for sand. *Géotechnique*, 28(4):413–433.
- Vermeer, P. A. (1980). *Formulation and analysis of sand deformation problems*. PhD thesis, Delft University of Technology.
- Waldron, L. J. (1977). The shear resistance of root-permeated homogeneous and stratified soil. *Soil Science Society of America Journal*, 41(5):843–849.
- Wang, Z. (2015). Fibre reinforced sand: From sample preparation to triaxial tests and orientation investigation. Master's thesis, Cardiff University, Cardiff.
- Wehnert, M. (2006). *Ein Beitrag zur drainierten und undrainierten analyse in der Geotechnik*. PhD thesis, Universität Stuttgart, Institut für Geotechnik.
- Wood, D. M. (1990). *Soil behaviour and critical state soil mechanics*. Cambridge university press, Cambridge.
- Xanthakos, P. P., Abramson, L. W., and Bruce, D. A. (1994). *Ground control and improvement*. John Wiley & Sons Inc, New York, NY, USA.
- Yang, G., Zhang, B., Lv, P., and Zhou, Q. (2009). Behaviour of geogrid reinforced soil retaining wall with concrete-rigid facing. *Geotextiles and Geomembranes*, 27(5):350–356.
- Yetimoglu, T. and Salbas, O. (2003). A study on shear strength of sands reinforced with randomly distributed discrete fibers. *Geotextiles and Geomembranes*, 21(2):103–110.
- Yoo, C. and Jung, H. S. (2004). Measured behavior of a geosynthetic-reinforced segmental retaining wall in a tiered configuration. *Geotextiles and Geomembranes*, 22(5):359–376.
- Zhu, H. H., Zhang, C. C., Tang, C. S., Shi, B., and Wang, B. (2014). Modeling the pullout behavior of short fiber in reinforced soil. *Geotextiles and Geomembranes*, 42(4):329–338.

Zienkiewicz, O. C. and Taylor, R. L. (2000). *The finite element method*, volume 1.
Butterworth-Heinemann, Oxford, 5th edition.

Nomenclature

Acronyms

2-D	Two-dimensional
3-D	Three-dimensional
\mathcal{R}	Aspect ratio
BS	British standards
CPP	Closest point projection
CTM	Consistent tangent matrix
DC	Duncan-Chang
FE	Finite element
FEA	Finite element analysis
FEM	Finite element method
HS	Hardening soil
HS-LC	Hardening soil - Lusas Cardiff
HS-smooth	Hardening soil - smooth
LMN	Lode Matsuoka-Nakai
LVDT	Linear variable differential transformer
MC	Mohr-Coulomb
MN	Matsuoka-Nakai
MNR	Modified Newton-Raphson
OPEFB	Oil palm empty fruit bunch

RVE Representative volume element

VM von Mises

Symbols

β Fibre slip integration constant

χ HS cap shaping function

$\Delta\lambda$ Plastic multiplier

η Shear yield surface shaping parameter

η_ψ Shear plastic potential shaping parameter

γ Shear strain

γ^p Plastic shear strain

κ_b Debonding constant (peak)

κ_r Debonding constant (residual)

ϕ Fibre horizontal orientation

Ψ Vector of direction cosines

ψ Dilatancy angle

ψ_m Mobilised dilatancy angle

ρ Scaled Lode angle dependency function

ρ_ψ Scaled Lode angle dependency function for plastic potential

σ^{ref} Reference stress level

σ_1 Minor principal stress

σ_2 Intermediate principal stress

σ_3 Major principal stress

σ_f	Axial stress in fibre
σ_m	Stress carried by matrix parallel to the fibre axis
σ_n	Normal stress
σ_r	Radial stress acting on fibre from matrix
σ_t	Tension limit
σ_y	Uniaxial yield stress
τ	Shear stress / interface shear stress
τ_b	Debonding interface shear stress
τ_r	Residual interface shear stress
Θ	Lode angle dependency function
θ	Lode angle
Θ_ψ	Lode angle dependency function for plastic potential
ε_f	Axial strain in fibre
ε_m	Axial strain in matrix
ε_v	Volumetric strain
ε_{ma}	Axial strain in matrix at fibre end
ε_{v0}	Initial volumetric strain
φ	Friction angle
φ_c	Critical state friction angle
φ_m	Mobilised friction angle
ϑ	Fibre vertical orientation
$\boldsymbol{\mu}$	Vector representing material state variables

σ_0	Converged stress at start of increment
σ_{LC}	Stress vector from last converged state
σ_{LI}	Stress vector from the last iteration
σ_{tr}	Trial stress vector
σ	Stress vector, made up of Cartesian components $\sigma_x, \sigma_y, \sigma_z, \sigma_{xy}, \sigma_{yz}, \sigma_{zx}$
ε^e	Elastic component of the strain vector
ε^p	Plastic component of the strain vector
ε	Strain vector, made up of Cartesian components $\varepsilon_x, \varepsilon_y, \varepsilon_z, \varepsilon_{xy}, \varepsilon_{yz}, \varepsilon_{zx}$
D_e	Elastic Hookean matrix
D_f	Fibre stiffness matrix
D_m	Matrix (soil) stiffness matrix
D_{ep}	Consistent tangent matrix
ξ	Shear yield surface shaping parameter
ξ_ψ	Shear plastic potential shaping parameter
A	Orientation distribution parameter
a_f	Cross-sectional area of fibre
a_m	Cross-sectional area of matrix
B	Orientation distribution parameter
c	Cohesion
D	Density
e	Void ratio

e_0	Initial void ratio
E_f	Young modulus of fibre
E_i	Initial Young modulus
E_i^{ref}	Initial Young modulus at reference stress level
E_m	Young modulus of matrix
E_{50}	Secant Young modulus
E_{50}^{ref}	Secant Young modulus at reference stress level
E_{change}	Change in Young modulus between iterations
E_{oed}	Oedometer Young modulus
E_{oed}^{ref}	Oedometer Young modulus at reference stress level
E_{tol}	Tolerance for change in Young modulus
E_{ur}	Unload-reload Young modulus
E_{ur}^{ref}	Unload-reload Young modulus at reference stress level
f	Yield function
f_c	HS cap yield function
f_s	HS shear yield function
f_t	HS tension yield function
f_{DP}	Drucker-Prager yield function
f_{MC}	Mohr-Coulomb yield function
f_{MN}	Matsuoka-Nakai yield function
$f_{s,MC}$	Alternative HS shear yield function
f_{VM}	von Mises yield function

g	Plastic potential function
g_c	HS cap plastic potential function
G_f	Post-failure triaxial stiffness
g_s	HS shear plastic potential function
g_t	HS tension plastic potential function
H	HS cap hardening gradient
H_{VM}	von Mises hardening gradient
I_1	First invariant of the stress tensor
I_2	Second invariant of the stress tensor
I_3	Third invariant of the stress tensor
J_2	Second invariant of the deviatoric stress tensor
J_3	Third invariant of the deviatoric stress tensor
K_0	Lateral earth pressure coefficient
k_b	Debonded interface shear stress gradient
K_c	Primary loading bulk modulus
K_s	Unload-reload bulk modulus
l_b	Length of fibre debonded region
l_f	Fibre length
M	Shear yield surface shaping function
m	Stress dependency exponent
M_ψ	Shear plastic potential shaping function
n	Orientation distribution parameter

p	Mean stress
p_a	Atmospheric pressure
q	Shear stress
q_a	Asymptotic shear stress
q_f	Shear stress at soil failure
R	Single fibre radius of influence
r	Stiffness update weight factor
R_c	Single fibre composite radius
R_f	Failure shear stress ratio
r_f	Fibre radius
r_q	Shear stress ratio
r_u	Stiffness ratio
S	Fibre-soil interface slip
v_f	Fibre volume fraction
v_m	Matrix volume fraction
Y_f	Factor for minimum stress dependency

CPP algorithms

Algorithm 1 Closest Point Projection algorithm for HS-LC shear surface

Initialisation

$$\Delta\lambda = 0; \delta\lambda = 0; \Delta\varepsilon^p = 0; \varepsilon^p = \varepsilon^{p,n-1}$$

Trial stress

$$\boldsymbol{\sigma} = \boldsymbol{\sigma}_0 + \mathbf{D}_e \Delta\varepsilon$$

Update yield function

$$f_s = f_s(\boldsymbol{\sigma}, \varepsilon^p)$$

$$f_{s,tol} = |f_s| \cdot 10^{-6}$$

$$i = 1$$

while ($|f_s| > f_{s,tol}$ or $\|\mathbf{R}\| > 10^{-8}$) and $i < 100$ **do**

Calculate derivatives

$$\frac{\partial f_s}{\partial \boldsymbol{\sigma}}; \frac{\partial g_s}{\partial \boldsymbol{\sigma}}; \frac{\partial^2 g_s}{\partial \boldsymbol{\sigma}^2}; \frac{\partial f_s}{\partial \varepsilon^p}$$

Calculate consistent constitutive matrix

$$\mathbf{A}_e = \left(\mathbf{I} + \Delta\lambda \mathbf{D}_e \frac{\partial^2 g_s}{\partial \boldsymbol{\sigma}^2} \right)^{-1} \mathbf{D}_e$$

Calculate residual plastic strain

$$\mathbf{R} = -\Delta\varepsilon^p + \Delta\lambda \frac{\partial g_s}{\partial \boldsymbol{\sigma}}$$

Update plasticity multiplier

$$\delta\boldsymbol{\sigma} = -\mathbf{A}_e \left(\mathbf{R} + \delta\lambda \frac{\partial g_s}{\partial \boldsymbol{\sigma}} \right)$$

$$\mathbf{F}_s^T = \frac{\partial f_s}{\partial \boldsymbol{\sigma}}^T + \Delta\lambda \frac{\partial f_s}{\partial \varepsilon^p}^T \frac{\partial^2 g_s}{\partial \boldsymbol{\sigma}^2}$$

$$\delta\lambda = \frac{f_s - \mathbf{F}_s^T \mathbf{A}_e \mathbf{R} + \frac{\partial f_s}{\partial \varepsilon^p}^T \mathbf{R}}{\mathbf{F}_s^T \mathbf{A}_e \frac{\partial g_s}{\partial \boldsymbol{\sigma}} - \frac{\partial f_s}{\partial \varepsilon^p}^T \frac{\partial g_s}{\partial \boldsymbol{\sigma}}}$$

$$\Delta\lambda = \Delta\lambda + \delta\lambda$$

Update plastic strains

$$\delta\varepsilon_p = \mathbf{R} + \delta\lambda \frac{\partial g_s}{\partial \boldsymbol{\sigma}} + \Delta\lambda \frac{\partial^2 g_s}{\partial \boldsymbol{\sigma}^2} \delta\boldsymbol{\sigma}$$

$$\Delta\varepsilon^p = \Delta\varepsilon^p + \delta\varepsilon_p$$

$$\varepsilon^p = \varepsilon^p + \delta\varepsilon^p$$

Update stress

$$\boldsymbol{\sigma} = \boldsymbol{\sigma} + \delta\boldsymbol{\sigma}$$

Update yield function

$$f_s = f_s(\boldsymbol{\sigma}, \varepsilon^p)$$

$$i = i + 1$$

end while

return $\boldsymbol{\sigma}, \varepsilon^p, \Delta\lambda$

Algorithm 2 Closest Point Projection algorithm for HS-LC cap surface

Initialisation

$$\Delta\lambda = 0; \delta\lambda = 0; \Delta p_p = 0; \Delta\varepsilon^p = 0; p_p = p_p^{n-1}; \varepsilon^p = \varepsilon^{p,n-1}$$

Trial stress

$$\boldsymbol{\sigma} = \boldsymbol{\sigma}_0 + \mathbf{D}_e \Delta\varepsilon$$

Update yield function

$$f_c = f_c(\boldsymbol{\sigma}, p_p)$$

$$f_{c,tol} = |f_c| \cdot 10^{-6}$$

$$i = 1$$

while ($|f_c| > f_{c,tol}$ or $\|\mathbf{R}\| > 10^{-8}$ or $|R_h| > 10^{-8}$) and $i < 100$ **do**

Calculate derivatives

$$\frac{\partial f_c}{\partial \boldsymbol{\sigma}}, \frac{\partial g_c}{\partial \boldsymbol{\sigma}}, \frac{\partial^2 g_c}{\partial \boldsymbol{\sigma}^2}, \frac{\partial f_c}{\partial p_p}, \frac{\partial p_p}{\partial \varepsilon_v^p}, \frac{\partial \varepsilon_v^p}{\partial \boldsymbol{\varepsilon}^p}$$

Calculate consistent constitutive matrix

$$\mathbf{A}_e = \left(\mathbf{I} + \Delta\lambda \mathbf{D}_e \frac{\partial^2 g_c}{\partial \boldsymbol{\sigma}^2} \right)^{-1} \mathbf{D}_e$$

Calculate residual plastic strain and hardening parameter residual

$$\mathbf{R} = -\Delta\varepsilon^p + \Delta\lambda \frac{\partial g_c}{\partial \boldsymbol{\sigma}}$$

$$R_h = -\Delta p_p + \Delta\lambda \frac{\partial p_p}{\partial \varepsilon_v^p} \frac{\partial \varepsilon_v^p}{\partial \boldsymbol{\varepsilon}^p} \frac{\partial g_c}{\partial \boldsymbol{\sigma}}$$

Update plasticity multiplier

$$\delta\boldsymbol{\sigma} = -\mathbf{A}_e \left(\mathbf{R} + \delta\lambda \frac{\partial g_c}{\partial \boldsymbol{\sigma}} \right)$$

$$\mathbf{F}_c^T = \frac{\partial f_c}{\partial \boldsymbol{\sigma}} + \Delta\lambda \frac{\partial f_c}{\partial p_p} \frac{\partial p_p}{\partial \varepsilon_v^p} \frac{\partial \varepsilon_v^p}{\partial \boldsymbol{\varepsilon}^p} \frac{\partial^2 g_c}{\partial \boldsymbol{\sigma}^2}$$

$$\delta\lambda = \frac{f_c - \mathbf{F}_c^T \mathbf{A}_e \mathbf{R} + \frac{\partial f_c}{\partial p_p} R_h}{\mathbf{F}_c^T \mathbf{A}_e \frac{\partial g_c}{\partial \boldsymbol{\sigma}} - \frac{\partial f_c}{\partial p_p} \frac{\partial p_p}{\partial \varepsilon_v^p} \frac{\partial \varepsilon_v^p}{\partial \boldsymbol{\varepsilon}^p} \frac{\partial g_c}{\partial \boldsymbol{\sigma}}}$$

$$\Delta\lambda = \Delta\lambda + \delta\lambda$$

Update plastic strains

$$\delta\varepsilon_p = \mathbf{R} + \delta\lambda \frac{\partial g_c}{\partial \boldsymbol{\sigma}} + \Delta\lambda \frac{\partial^2 g_c}{\partial \boldsymbol{\sigma}^2} \delta\boldsymbol{\sigma}$$

$$\Delta\varepsilon^p = \Delta\varepsilon^p + \delta\varepsilon_p$$

$$\varepsilon^p = \varepsilon^p + \delta\varepsilon^p$$

Update stress

$$\boldsymbol{\sigma} = \boldsymbol{\sigma} + \delta\boldsymbol{\sigma}$$

Update hardening parameter

$$\delta p_p = R_h + \frac{\partial p_p}{\partial \varepsilon_v^p} \frac{\partial \varepsilon_v^p}{\partial \boldsymbol{\varepsilon}^p} \left(\delta\lambda \frac{\partial g_c}{\partial \boldsymbol{\sigma}} + \Delta\lambda \frac{\partial^2 g_c}{\partial \boldsymbol{\sigma}^2} \delta\boldsymbol{\sigma} \right)$$

$$\Delta p_p = \Delta p_p + \delta p_p$$

$$p_p = p_p + \delta p_p$$

Update yield function

$$f_c = f_c(\boldsymbol{\sigma}, p_p)$$

$$i = i + 1$$

end while

return $\boldsymbol{\sigma}, \varepsilon^p, p_p, \Delta\lambda$

Algorithm 3 Closest Point Projection algorithm for HS-LC tension surface

Initialisation

$$\Delta\lambda = 0; \delta\lambda = 0; \Delta\varepsilon^p = 0; \varepsilon^p = \varepsilon^{p,n-1}$$

Trial stress

$$\boldsymbol{\sigma} = \boldsymbol{\sigma}_0 + \mathbf{D}_e \Delta\varepsilon$$

Update yield function

$$f_t = f_t(\boldsymbol{\sigma})$$

$$f_{t,tol} = |f_t| \cdot 10^{-6}$$

$$i = 1$$

while ($|f_t| > f_{t,tol}$ or $\|\mathbf{R}\| > 10^{-8}$) and $i < 100$ **do**

Calculate derivatives

$$\frac{\partial f_t}{\partial \boldsymbol{\sigma}}; \frac{\partial g_t}{\partial \boldsymbol{\sigma}}; \frac{\partial^2 g_t}{\partial \boldsymbol{\sigma}^2}$$

Calculate consistent constitutive matrix

$$\mathbf{A}_e = \left(\mathbf{I} + \Delta\lambda \mathbf{D}_e \frac{\partial^2 g_t}{\partial \boldsymbol{\sigma}^2} \right)^{-1} \mathbf{D}_e$$

Calculate residual plastic strain

$$\mathbf{R} = -\Delta\varepsilon^p + \Delta\lambda \frac{\partial g_t}{\partial \boldsymbol{\sigma}}$$

Update plasticity multiplier

$$\delta\boldsymbol{\sigma} = -\mathbf{A}_e \left(\mathbf{R} + \delta\lambda \frac{\partial g_t}{\partial \boldsymbol{\sigma}} \right)$$

$$\mathbf{F}_t^T = \frac{\partial f_t}{\partial \boldsymbol{\sigma}}$$

$$\delta\lambda = \frac{f_t - \mathbf{F}_t^T \mathbf{A}_e \mathbf{R}}{\mathbf{F}_t^T \mathbf{A}_e \frac{\partial g_t}{\partial \boldsymbol{\sigma}}}$$

$$\Delta\lambda = \Delta\lambda + \delta\lambda$$

Update plastic strains

$$\delta\varepsilon_p = \mathbf{R} + \delta\lambda \frac{\partial g_t}{\partial \boldsymbol{\sigma}} + \Delta\lambda \frac{\partial^2 g_t}{\partial \boldsymbol{\sigma}^2} \delta\boldsymbol{\sigma}$$

$$\Delta\varepsilon^p = \Delta\varepsilon^p + \delta\varepsilon_p$$

$$\varepsilon^p = \varepsilon^p + \delta\varepsilon^p$$

Update stress

$$\boldsymbol{\sigma} = \boldsymbol{\sigma} + \delta\boldsymbol{\sigma}$$

Update yield function

$$f_t = f_t(\boldsymbol{\sigma})$$

$$i = i + 1$$

end while

return $\boldsymbol{\sigma}$, ε^p , $\Delta\lambda$

Algorithm 4 Closest Point Projection algorithm for HS-LC shear and cap surfaces

Initialisation

$$\Delta\lambda_s = 0; \delta\lambda_s = 0; \Delta\varepsilon^p = 0; \boldsymbol{\varepsilon}^p = \boldsymbol{\varepsilon}^{p,n-1}$$

$$\Delta\lambda_c = 0; \delta\lambda_c = 0; p_p = p_p^{n-1}$$

Trial stress

$$\boldsymbol{\sigma} = \boldsymbol{\sigma}_0 + \mathbf{D}_e \Delta\boldsymbol{\varepsilon}$$

Update yield functions

$$f_s = f_s(\boldsymbol{\sigma}, \boldsymbol{\varepsilon}^p)$$

$$f_c = f_c(\boldsymbol{\sigma}, p_p)$$

$$f_{s,tol} = |f_s| \cdot 10^{-6}$$

$$f_{c,tol} = |f_c| \cdot 10^{-6}$$

$$i = 1$$

while ($|f_s| > f_{s,tol}$ or $|f_c| > f_{c,tol}$ or $\|\mathbf{R}\| > 10^{-8}$ or $|R_h| > 10^{-8}$) and $i < 100$ **do**

Calculate derivatives

$$\frac{\partial f_s}{\partial \boldsymbol{\sigma}}, \frac{\partial g_s}{\partial \boldsymbol{\sigma}}, \frac{\partial^2 g_s}{\partial \boldsymbol{\sigma}^2}, \frac{\partial f_s}{\partial \boldsymbol{\varepsilon}^p}$$

$$\frac{\partial f_c}{\partial \boldsymbol{\sigma}}, \frac{\partial g_c}{\partial \boldsymbol{\sigma}}, \frac{\partial^2 g_c}{\partial \boldsymbol{\sigma}^2}, \frac{\partial f_c}{\partial p_p}, \frac{\partial p_p}{\partial \boldsymbol{\varepsilon}^p}, \frac{\partial \boldsymbol{\varepsilon}^p}{\partial \boldsymbol{\varepsilon}^p}$$

Calculate consistent constitutive matrix

$$\mathbf{A}_e = \left(\mathbf{I} + \Delta\lambda_s \mathbf{D}_e \frac{\partial^2 g_s}{\partial \boldsymbol{\sigma}^2} + \Delta\lambda_c \mathbf{D}_e \frac{\partial^2 g_c}{\partial \boldsymbol{\sigma}^2} \right)^{-1} \mathbf{D}_e$$

Calculate residual plastic strain and hardening parameter residual

$$\mathbf{R} = -\Delta\boldsymbol{\varepsilon}^p + \Delta\lambda_s \frac{\partial g_s}{\partial \boldsymbol{\sigma}} + \Delta\lambda_c \frac{\partial g_c}{\partial \boldsymbol{\sigma}}$$

$$R_h = -\Delta p_p + \Delta\lambda_c \frac{\partial p_p}{\partial \boldsymbol{\varepsilon}^p} \frac{\partial \boldsymbol{\varepsilon}^p}{\partial \boldsymbol{\varepsilon}^p} \frac{\partial g_c}{\partial \boldsymbol{\sigma}}$$

Update plasticity multipliers

$$\delta\boldsymbol{\sigma} = -\mathbf{A}_e \left(\mathbf{R} + \delta\lambda_s \frac{\partial g_s}{\partial \boldsymbol{\sigma}} + \delta\lambda_c \frac{\partial g_c}{\partial \boldsymbol{\sigma}} \right)$$

$$\boldsymbol{\Omega} = \begin{bmatrix} \mathbf{F}_s^T \mathbf{A}_e \frac{\partial g_s}{\partial \boldsymbol{\sigma}} - \frac{\partial f_s}{\partial \boldsymbol{\varepsilon}^p} \frac{\partial g_s}{\partial \boldsymbol{\sigma}} & \mathbf{F}_s^T \mathbf{A}_e \frac{\partial g_c}{\partial \boldsymbol{\sigma}} - \frac{\partial f_s}{\partial \boldsymbol{\varepsilon}^p} \frac{\partial g_c}{\partial \boldsymbol{\sigma}} \\ \mathbf{F}_c^T \mathbf{A}_e \frac{\partial g_s}{\partial \boldsymbol{\sigma}} & \mathbf{F}_c^T \mathbf{A}_e \frac{\partial g_c}{\partial \boldsymbol{\sigma}} - \frac{\partial f_c}{\partial p_p} \frac{\partial p_p}{\partial \boldsymbol{\varepsilon}^p} \frac{\partial g_c}{\partial \boldsymbol{\sigma}} \end{bmatrix}$$

$$\boldsymbol{\Omega}_f = \begin{bmatrix} f_s - \mathbf{F}_s^T \mathbf{A}_e \mathbf{R} + \frac{\partial f_s}{\partial \boldsymbol{\varepsilon}^p} \mathbf{R} \\ f_c - \mathbf{F}_c^T \mathbf{A}_e \mathbf{R} + \frac{\partial f_c}{\partial p_p} R_h \end{bmatrix}$$

$$\begin{bmatrix} \delta\lambda_s \\ \delta\lambda_c \end{bmatrix} = \boldsymbol{\Omega}^{-1} \boldsymbol{\Omega}_f$$

$$\Delta\lambda_s = \Delta\lambda_s + \delta\lambda_s$$

$$\Delta\lambda_c = \Delta\lambda_c + \delta\lambda_c$$

Update plastic strains

$$\delta\boldsymbol{\varepsilon}^p = \mathbf{R} + \delta\lambda_s \frac{\partial g_s}{\partial \boldsymbol{\sigma}} + \delta\lambda_c \frac{\partial g_c}{\partial \boldsymbol{\sigma}} + \left(\Delta\lambda_s \frac{\partial^2 g_s}{\partial \boldsymbol{\sigma}^2} + \Delta\lambda_c \frac{\partial^2 g_c}{\partial \boldsymbol{\sigma}^2} \right) \delta\boldsymbol{\sigma}$$

$$\Delta\boldsymbol{\varepsilon}^p = \Delta\boldsymbol{\varepsilon}^p + \delta\boldsymbol{\varepsilon}^p$$

$$\boldsymbol{\varepsilon}^p = \boldsymbol{\varepsilon}^p + \delta\boldsymbol{\varepsilon}^p$$

Update stress

$$\boldsymbol{\sigma} = \boldsymbol{\sigma} + \delta\boldsymbol{\sigma}$$

Update yield functions

$$f_s = f_s(\boldsymbol{\sigma}, \boldsymbol{\varepsilon}^p)$$

$$f_c = f_c(\boldsymbol{\sigma}, p_p)$$

$$i = i + 1$$

end while

return $\boldsymbol{\sigma}, \boldsymbol{\varepsilon}^p, p_p, \Delta\lambda_s, \Delta\lambda_c$

Algorithm 5 Closest Point Projection algorithm for HS-LC shear and tension surfaces

Initialisation

$$\Delta\lambda_s = 0; \delta\lambda_s = 0; \Delta\epsilon^p = 0; \epsilon^p = \epsilon^{p,n-1}$$

$$\Delta\lambda_t = 0; \delta\lambda_t = 0$$

Trial stress

$$\boldsymbol{\sigma} = \boldsymbol{\sigma}_0 + \mathbf{D}_e \Delta\boldsymbol{\epsilon}$$

Update yield functions

$$f_s = f_s(\boldsymbol{\sigma}, \epsilon^p)$$

$$f_t = f_t(\boldsymbol{\sigma})$$

$$f_{s,tol} = |f_s| \cdot 10^{-6}$$

$$f_{t,tol} = |f_t| \cdot 10^{-6}$$

$$i = 1$$

while ($|f_s| > f_{s,tol}$ or $|f_t| > f_{t,tol}$ or $\|\mathbf{R}\| > 10^{-8}$ and $i < 100$ **do**

Calculate derivatives

$$\frac{\partial f_s}{\partial \boldsymbol{\sigma}}, \frac{\partial g_s}{\partial \boldsymbol{\sigma}}, \frac{\partial^2 g_s}{\partial \boldsymbol{\sigma}^2}, \frac{\partial f_s}{\partial \epsilon^p}$$

$$\frac{\partial f_t}{\partial \boldsymbol{\sigma}}, \frac{\partial g_t}{\partial \boldsymbol{\sigma}}, \frac{\partial^2 g_t}{\partial \boldsymbol{\sigma}^2}$$

Calculate consistent constitutive matrix

$$\mathbf{A}_e = \left(\mathbf{I} + \Delta\lambda_s \mathbf{D}_e \frac{\partial^2 g_s}{\partial \boldsymbol{\sigma}^2} + \Delta\lambda_t \mathbf{D}_e \frac{\partial^2 g_t}{\partial \boldsymbol{\sigma}^2} \right)^{-1} \mathbf{D}_e$$

Calculate residual plastic strain and hardening parameter residual

$$\mathbf{R} = -\Delta\epsilon^p + \Delta\lambda_s \frac{\partial g_s}{\partial \boldsymbol{\sigma}} + \Delta\lambda_t \frac{\partial g_t}{\partial \boldsymbol{\sigma}}$$

Update plasticity multipliers

$$\delta\boldsymbol{\sigma} = -\mathbf{A}_e \left(\mathbf{R} + \delta\lambda_s \frac{\partial g_s}{\partial \boldsymbol{\sigma}} + \delta\lambda_t \frac{\partial g_t}{\partial \boldsymbol{\sigma}} \right)$$

$$\boldsymbol{\Omega} = \begin{bmatrix} \mathbf{F}_s^T \mathbf{A}_e \frac{\partial g_s}{\partial \boldsymbol{\sigma}} - \frac{\partial f_s}{\partial \epsilon^p} \frac{\partial g_s}{\partial \boldsymbol{\sigma}} & \mathbf{F}_s^T \mathbf{A}_e \frac{\partial g_t}{\partial \boldsymbol{\sigma}} - \frac{\partial f_s}{\partial \epsilon^p} \frac{\partial g_t}{\partial \boldsymbol{\sigma}} \\ \mathbf{F}_t^T \mathbf{A}_e \frac{\partial g_s}{\partial \boldsymbol{\sigma}} & \mathbf{F}_t^T \mathbf{A}_e \frac{\partial g_t}{\partial \boldsymbol{\sigma}} \end{bmatrix}$$

$$\boldsymbol{\Omega}_f = \begin{bmatrix} f_s - \mathbf{F}_s^T \mathbf{A}_e \mathbf{R} + \frac{\partial f_s}{\partial \epsilon^p} \mathbf{R} \\ f_t - \mathbf{F}_t^T \mathbf{A}_e \mathbf{R} \end{bmatrix}$$

$$\begin{bmatrix} \delta\lambda_s \\ \delta\lambda_t \end{bmatrix} = \boldsymbol{\Omega}^{-1} \boldsymbol{\Omega}_f$$

$$\Delta\lambda_s = \Delta\lambda_s + \delta\lambda_s$$

$$\Delta\lambda_t = \Delta\lambda_t + \delta\lambda_t$$

Update plastic strains

$$\delta\epsilon_p = \mathbf{R} + \delta\lambda_s \frac{\partial g_s}{\partial \boldsymbol{\sigma}} + \delta\lambda_t \frac{\partial g_t}{\partial \boldsymbol{\sigma}} + \left(\Delta\lambda_s \frac{\partial^2 g_s}{\partial \boldsymbol{\sigma}^2} + \Delta\lambda_t \frac{\partial^2 g_t}{\partial \boldsymbol{\sigma}^2} \right) \delta\boldsymbol{\sigma}$$

$$\Delta\epsilon^p = \Delta\epsilon^p + \delta\epsilon_p$$

$$\epsilon^p = \epsilon^p + \delta\epsilon^p$$

Update stress

$$\boldsymbol{\sigma} = \boldsymbol{\sigma} + \delta\boldsymbol{\sigma}$$

Update yield functions

$$f_s = f_s(\boldsymbol{\sigma}, \epsilon^p)$$

$$f_t = f_t(\boldsymbol{\sigma})$$

$$i = i + 1$$

end while

return $\boldsymbol{\sigma}, \epsilon^p, \Delta\lambda_s, \Delta\lambda_t$
